A Search for QCD Exotics Using a Beam of Photons

The Hall D Collaboration

R. Clark, P. Eugenio, G. Franklin, C. A. Meyer (Deputy Spokesperson), B. Quinn, R. Schumacher
Carnegie Mellon University (Pittsburgh,PA)

H.Crannell, D.Sober
Catholic University of America (Washington, D. C.

D. Doughty, D. Heddle
Christopher Newport University (Newport News, VA)

R. Jones
University of Connecticut (Storrs, CT)

W. Boeglin, L. Kramer, P. Markowitz, B. Raue, J. Reinhold
Florida International University (Miami,FL)

L. Dennis, P. Dragovitch, G. Riccardi
Florida State University (Tallahassee,FL)

J. Annand, I. Anthony, D. Ireland, J. Kellie, K. Livingston, D. MacGregor, C. McGeorge, B. Owens, G. Rosner, D. Watts
University of Glasgow (Glasgow, Scotland)

A. Dzierba (Spokesperson), J. T. Londergan, M. Pichowsky, E. Scott, P. Smith, T. Sulanke, A. Szczepaniak, S. Teige
Indiana University (Bloomington,IN)

S. Denisov, N. Fedyakin, A. Gorokhov, V. Samoilenko, A. Schukin
Institute for High Energy Physics (Protvino, Russia)

D. Abbott, I. Bird, R. Carlini, H. Fenker, G. Heyes, C. Sinclair,
E. Smith (Hall D Group Leader), D. Weygand, E. Wolin
Jefferson Lab (Newport News,VA)

R. Mischke, A. Palounek, J. C. Peng
* *Los Alamos National Lab (Los Alamos,NM)*

V. A. Bodyagin, A. M. Gribushin, N. A. Kruglov, V. L. Korotkikh,
M. A. Kostin, A. I. Demianov, O. L. Kodolova, L. I. Sarycheva,
A. A. Yershov
Nuclear Physics Institute, Moscow State University, Moscow, Russia

M. Khandaker, V. Punjabi, C. Salgado
Norfolk State University (Norfolk,VA)

E. Solodov
Budker Institute of Nuclear Physics (Novosibirsk, Russia)

A. Klein
Old Dominion University (Newport News,VA)

D. Carman, K. Hicks
Ohio University (Athens,OH)

S. Dytman, J. Mueller
University of Pittsburgh (Pittsburgh, PA)

E. J. Brash, G. M. Huber, G. J. Lolos, Z. Papandreou
University of Regina (Regina, Saskatchewan,Canada)

G. Adams, J. Cummings, R. Davidson, A. Empl, N. Mukhopadhyay,
J. Napolitano, P. Stoler
Rensselaer Polytechnic Institute (Troy,NY)

J. M. Laget, M. Garçon
* *Saclay (France)*

Theory Group

D. Leinweber, W. Melnitchouk (and JLab), A. Thomas, A. Williams
CSSM and University of Adelaide (Adelaide, Australia)

S. Godfrey
Carleton University (Ottawa, Ontario,Canada)

R. Kaminski, L. Lesniak
* *Institute for Nuclear Theory (Cracow, Poland)*

J. Goity
Hampton University (Hampton,VA)

J. T. Londergan, M. Pichowsky, A. Szczepaniak
Indiana University (Bloomington,IN)

P. Page
Los Alamos National Lab (Los Alamos, NM)

A. Afanasev
North Carolina Central University (Durham, NC)

E. Swanson
University of Pittsburgh (Pittsburgh, PA)

T. Barnes
University of Tennessee (Knoxville, TN)
Oak Ridge National Lab (Oak Ridge, TN)

(*) Insitutions not yet committed but involved in workshops and planning

Contents

1 Introduction **7**
- 1.1 History of the project . . . 7
- 1.2 Cassel Review report summary . . . 8
- 1.3 PAC-18 review of the energy upgrade white paper . . . 11
- 1.4 More information . . . 13

2 Executive Summary **15**
- 2.1 Physics and overview . . . 15
- 2.2 Photon beam and choice of energy . . . 20
- 2.3 Detector . . . 22
- 2.4 Civil construction . . . 24
- 2.5 Rates,trigger and DAQ . . . 24
- 2.6 Data handling . . . 25
- 2.7 Monte Carlo simulations . . . 25
- 2.8 Partial wave analysis . . . 25
- 2.9 Management plan . . . 25
- 2.10 Costs . . . 26

3 Scientific Goals of the Hall D Project **27**
- 3.1 Introduction . . . 27
- 3.2 Spectroscopy of gluonic excitations . . . 29
  - 3.2.1 Flux tubes . . . 29
- 3.3 Photoproduction of gluonic excitations . . . 36
  - 3.3.1 Why photoproduction? . . . 36
  - 3.3.2 PWA and photon polarization . . . 39
- 3.4 Theoretical considerations . . . 45
  - 3.4.1 Overview . . . 45
  - 3.4.2 Strong QCD and the role of glue . . . 47
  - 3.4.3 Phenomenology . . . 51
  - 3.4.4 Conventional light quark mesons - theory . . . 53

3.4.5 Hybrids - theory 54
3.4.6 Glueballs - theory 56
3.4.7 Multiquark systems - theory 57
3.4.8 $s\bar{s}$ states - theory 57

4 Photon Beam **61**
4.1 Choice of technique 62
4.1.1 Compton back-scatter 63
4.1.2 Tagged bremsstrahlung 65
4.1.3 Coherent bremsstrahlung 66
4.2 Photon source 68
4.2.1 Essential features 70
4.2.2 Use of collimation 71
4.2.3 Choice of radiator 79
4.2.4 Crystal thickness 82
4.2.5 Crystal mount 85
4.2.6 Crystal alignment and monitoring 87
4.2.7 Crystal quality and lifetime 88
4.3 Electron beam 91
4.3.1 Beam polarization 93
4.3.2 Beam emittance 94
4.3.3 Electron beam line optics 95
4.3.4 Electron beam dump 97
4.3.5 Beam containment and shielding 100
4.4 Tagging spectrometer 101
4.4.1 Specifications 101
4.4.2 Magnet 102
4.4.3 Spectrometer optics 103
4.4.4 Tagger detectors 104
4.4.5 Beam dump optics 107
4.5 Polarimetry instrumentation 107
4.6 Operating beam intensity 108

5 The Hall D Detector **111**
5.1 Overview 111
5.2 The solenoid 112
5.3 The target 115
5.4 Barrel calorimetry 115
5.4.1 Design considerations 116
5.4.2 Pb/SciFi barrel calorimeter 117

5.5 Tracking chambers 120
5.5.1 Design considerations 121
5.5.2 Central drift chamber 127
5.5.3 Forward drift chambers 129
5.5.4 Vertex chamber and start counter 130
5.5.5 Chamber infrastructure and alignment 133
5.5.6 Electronics 134
5.6 Particle identification 134
5.6.1 Time-of-flight 137
5.6.2 dE/dx in the chambers 138
5.6.3 Čerenkov counter 138
5.6.4 Acceptance of the particle identification system 141
5.7 Forward calorimetry 144
5.7.1 Calorimeter performance 144
5.7.2 The RADPHI experience 145

6 Civil Construction 151
6.1 General requirements 151
6.1.1 Compatibility with future upgrades 153
6.2 Personnel protection 153
6.2.1 Failure scenarios 153
6.2.2 Beam containment proposal 154
6.3 Environmental and radiation concerns 155
6.3.1 Site dose limits 155
6.3.2 Beam on radiator 155
6.3.3 Tagger building 156
6.3.4 Tagger hodoscope 156
6.3.5 Electron beam dump 156
6.3.6 Collimator enclosure 156
6.3.7 Detector building 157
6.3.8 Photon beam dump 158
6.3.9 Ground water activation 158
6.4 Geotechnical analysis 158
6.5 Costs 159
6.6 Schedule 159

7 Rates, Trigger and Data Acquisition 161
7.1 Expected rates 161
7.1.1 Overview 161
7.1.2 Trigger elements 162

7.1.3 Accidental rates . . . 163
7.1.4 Rates in tracking chambers . . . 165
7.2 Trigger . . . 169
7.2.1 Overview . . . 169
7.2.2 Level 1 trigger . . . 170
7.3 Data acquisition . . . 173
7.3.1 Overview . . . 173
7.3.2 Data flow . . . 173
7.3.3 Level 3 trigger . . . 176
7.3.4 Monitoring and control . . . 177

8 Data Handling and Offline Computing 179
8.1 Overview . . . 179
8.2 Data acquisition hardware requirements . . . 180
8.2.1 Computer center support for data acquisition and storage 182
8.2.2 Software development for data acquisition . . . 182
8.3 HALL D Offline Computing . . . 183
8.3.1 Detector calibration . . . 185
8.3.2 First-pass event analysis . . . 185
8.3.3 Event simulations . . . 186
8.3.4 Physics analysis . . . 186
8.3.5 HALL D portal (myHallD.org) . . . 187
8.3.6 Project timeline . . . 187
8.4 Conclusions . . . 187

9 Monte Carlo Simulations 189
9.1 Introduction . . . 189
9.2 Monte Carlo framework . . . 189
9.3 Acceptance studies . . . 191
9.3.1 Detector geometry . . . 192
9.3.2 Acceptance performance . . . 193
9.4 Monte Carlo Study of Photon Energy Resolution . . . 195
9.4.1 Photon Detector Energy Resolution . . . 195
9.5 Physics Event Weighters . . . 203

10 Partial Wave Analysis 205
10.1 Introduction . . . 205
10.2 Beam and final state normalizations . . . 207
10.3 A partial wave analysis study . . . 207
10.3.1 The Role of Linear Polarization . . . 208

10.3.2 The PWA Formalism and Results 210
10.3.3 Joint production of excited baryons and mesons 219
10.4 Summary 221

11 Management Plan **223**
11.1 Principles of the management plan 223
11.2 The HALL D collaboration membership 224
11.3 The HALL D governance structure 225
11.3.1 The HALL D collaboration membership structure 225
11.3.2 The working groups 226
11.3.3 The technical review committee 227
11.3.4 The executive group 228
11.3.5 The collaboration board 230
11.4 Summary 232

A The report of the Cassel committee **233**

B The superconducting solenoid **249**
B.1 Introduction 249
B.2 Present condition 249
B.3 Dismantling and relocation 250
B.4 Summary of proposed modifications 251
B.5 Discussion of Magnetic modifications required by the experiment 253
B.6 TOSCA simulations 254
B.6.1 Introduction 254
B.6.2 TOSCA Model 254
B.7 Initial results 256

C Detailed Cost Estimates **261**
C.1 Overview 262

Chapter 1

Introduction

The HALL D project will study the photoproduction of unusual mesons and gluonic excitations at Jefferson Lab (JLab) using a hermetic 4π detector. When the gluonic degree of freedom of mesons is excited, a new kind of particle results. The smoking gun characteristic of these new states is a spin, parity and charge conjugation (J^{PC}) combination not allowed for ordinary $q\bar{q}$. Photon beams are expected to be particularly favorable for the production of such states. These states are required by the quark confining mechanism of QCD. Mapping out the spectrum and decay modes of these gluonic excitations is the necessary first step in understanding the nature of confinement.

This HALL D project also includes a beamline and an above-ground tagger building and detector building to be located off the stub at the east end of the north linac of the CEBAF accelerator. This project assumes that the energy of CEBAF will be increased to 12 GeV by about 2005.

1.1 History of the project

The HALL D plans have evolved over the last three years, starting with a workshop held in July 1997 at Indiana University and the formation of a working group. There then followed workshops at North Carolina State University (November 1997), Carnegie Mellon University (March 1998), Florida State University (October 1998), Rensselaer Polytechnic Institute (March 1999) and at the University of Adelaide (February 2000).

A Preliminary Design Report appeared in January, 1999 and was presented to the JLab Program Advisory Committee (PAC-15) at its meeting in January, 1999 as a Letter of Intent (LOI). PAC-15 enthusiastically endorsed the physics and recommended the formation of a committee to review the project.

The second version of the Design Report was prepared in August 1999 for the review committee which met in December 1999 to review the HALL D project. Its finding are summarized in the next section. The collaboration held a series of collaboration meetings in 1999 and 2000 and recently adopted a management plan which includes a collaboration spokesperson (Alex Dzierba - Indiana), deputy spokesperson (Curtis Meyer) and Hall D JLab group leader (Elton Smith - JLab) and a collaboration board and technical review board. The process of filling the membership of the two boards has begun. This document (Design Report - version 3) summarizes the progress of the HALL D project to date.

1.2 Cassel Review report summary

A committee chaired by David Cassel (Cornell) and consisting of Frank Close (Rutherford Lab), John Domingo (Jefferson Lab), William Dunwoodie (SLAC), Donald Geesaman (Argonne), David Hitlin (Caltech), Martin Olsson (Wisconsin) and Glenn Young (Oak Ridge) reviewed the project plans in December 1999. The Committee was asked to address three principal questions, whose answers were to be based on the answers to more detailed questions. The full report is contained in Appendix A.

In order to provide some background to the review report summary below, we briefly point out the following about the beam and detector.

Linearly polarized photons from 8 to 9 GeV will be produced using a 12 GeV electron beam via coherent bremsstrahlung. The coherent bremsstrahlung technique involves passing an electron beam from the CEBAF accelerator though a wafer-thin diamond crystal: at special settings for the orientation of the crystal, the atoms of the crystal can be made to recoil together from the radiating electron leading to an enhanced emission at particular photon energies and yielding linearly polarized photons.

This photon beam energy range is sufficiently high to access the desired meson mass range and is ideal for a solenoidal spectrometer. The use of a solenoidal spectrometer allows for the measurement of charged particles with excellent efficiency and momentum resolution while at the same time containing the shower of unwanted electron-positron pairs associated with the photon beam.

One of the two largest components of the detector is the superconducting solenoid originally used in the LASS experiment at SLAC and later moved to LANL for the MEGA experiment. This magnet is available for use in HALL D and is free of any major funding obligations. Plans are underway for the move.

The other component is the 3000-element lead glass detector originally built for the E852 experiment at the Brookhaven AGS. This detector was moved to JLab in July, 2000 for use in HALL D.

The charges to the review committee and the committee's conclusions are:

1. **Evaluate the Scientific Opportunities Presented by the Hall D Project.** This collaboration proposes to explore systematically the light mesons (with masses up to about 2.5 GeV) with capabilities far beyond those of previous experiments. The copious spin and flavor initial states produced by photon beams will be an extremely useful tool in this endeavor. Thorough study of the masses, spins, parities, and charge conjugation states of these light mesons will require a complete partial wave analysis. This will provide a much deeper understanding of quark-antiquark states, and will as well permit a definitive search for mesons with exotic quantum numbers, particularly hybrid states and glueballs. This search is very high priority physics, since the states involving excited glue, as well as quarkless glueball states, must exist if QCD is the correct theory of the strong interactions. JLab is unique in being able to provide the high quality, low emittance, CW photon beams that are required for this experiment. In addition, JLab and a significant segment of the JLab physics community are committed to this physics program. Together these provide a unique opportunity for exploring light meson states and making definitive searches for exotic states in this mass region.

2. **Review the Collaboration's Approach to the Realization of that Facility.** The general design of the detector is technically sound. This is verified by a detailed comparison of the capabilities of the proposed Hall D detector with those of the successful LASS detector. This comparison leads to the conclusion that the proposed detector and beam combination will be able to realize the physics goals of the Project.

   However, substantial effort must be invested to optimize the detector design and minimize the cost. The items requiring optimization that we have identified are described in detail in the Report. These optimizations are part of the R & D required to prepare a Conceptual Design Report for the Hall D Project. Preparation of a CDR with the associated WBS and resource-loaded cost and schedule will require a Project Office at JLab with a Project Director and a well-structured organization designed to address the necessary R & D and optimization efforts.

3. **Recommend R & D Needed to Optimize the Facility Design and to Minimize the Overall Project Cost.** The R & D item of greatest

> concern is ensuring that the magnet is still functional, particularly the fourth coil, which has not been used for at least 15 years. R & D should also include construction of prototypes to optimize detector design; to validate mechanical, electronic, and software choices; and to ensure the feasibility of the proposed coherent bremsstrahlung system.

The committee commented on the uniqueness of JLab for carrying out this search using the coherent bremsstrahlung beam:

> JLab, with the energy upgrade, will be uniquely suited for providing such a beam. In particular, the excellent emittance of the JLab electron beam allows for strong collimation of the coherent bremsstrahlung radiation to enhance the polarization and ratio of tagged to untagged photons in the tagged photon beam. No other facility in the world will be able to provide a beam of this quality, with this combination of energy, duty factor, and emittance. If such a project were pursued at other existing high-energy facilities, either the data taking rate would be dramatically reduced, compromising the physics goals, or a much more complicated detector would be required. We do not see any project at an existing accelerator complex (e.g., SLAC, CESR, DESY) which is likely to be able to compete with the Hall D initiative in this area.

Since the report was issued in January 2000, the HALL D collaboration has started on an active R & D program to address issues of optimization and design. Work is currently underway in electronics, particle identification and tracking. The lead glass detector is now being moved from Brookhaven Lab to JLab.

Two areas of concern raised by the committee have now been addressed. An assessment team visited the Los Alamos National Laboratory (LANL) in March 2000 to examine the superconducting magnet and fourth coil. That team included the two engineers who originally designed, built and tested the magnet for its use in the LASS spectrometer at SLAC and were also involved in the transfer of the magnet to LANL. The team found the magnet and fourth coil to be in excellent condition based on visual inspection, interviews with users (engineering and technical staff) and a review of written records. More recent information about the magnet is included in Appendix B.

Another concern was the ability to obtain synthetic diamonds of sufficiently small thickness ($\approx$ 15 microns) needed to obtain the necessary collimation. Recently the group from the University of Glasgow has joined the HALL D

collaboration. They have acquired sufficiently thin crystals and are currently making measurements of rocking curves with these crystals.

In summary, the review committee recognized the uniqueness of an energy-upgraded CEBAF accelerator at JLab to carry out the *definitive searches* for the states required by QCD. The major concerns they raised have already been addressed. The program of R & D recommended for optimization and/or technology choices has started.

1.3 PAC-18 review of the energy upgrade white paper

In July 2000, the JLab PAC-18 was asked to review the draft of the 12 GeV white paper. Here is a summary of the PAC-18 report of that review regarding the physics of the HALL D project which was listed as the first of three primary areas of study.

> The white paper draft presented three primary areas where a 12 GeV upgrade would make a major impact on our understanding of hadronic physics and its QCD substructure. The PAC reviewed each of these areas in turn and found all of them sound. The following comments summarize these deliberations.
>
> *The experimental verification of the origin of quark confinement by QCD flux tubes.*
>
> For the first time in three millennia of reductionism, science has encountered a degree of freedom that cannot be isolated. The properties of strong QCD and the nature of confinement are among the outstanding unresolved problems in physics. At the turn of the 21st century there is strong evidence from theory and computation that confinement of quarks is intimately due to the development of flux tubes between them. This seminal insight awaits experimental confirmation; its wider implications are yet unknown. As matter is heated, theory predicts that the gluonic degrees of freedom in the flux tubes must be excited, the first manifestations of which will be the appearance of "hybrid" states in the hadron spectrum. Predictions for the energy scale of their production have now converged, and estimates of their characteristics and production rates in electromagnetic processes are now rather precisely predicted. In par-

ticular the existence of exotic combinations of spin-parity-charge conjugation J^{PC} quantum numbers among the hybrid mesons will aid their identification. These particular exotic states have their valence quark-antiquark content coupled to spin-1 and are thereby especially suited to production by photons, both real and virtual, in diffractive processes. A 12 GeV upgrade at CEBAF will provide unique means to produce these states, separate them from background and establish a new spectroscopy in QCD.

The following is the entire summary of the PAC-18 review:

The Program Advisory Committee concludes that an outstanding scientific case has been identified which requires the unique capabilities of the JLab 12 GeV upgrade. The results of these experiments are likely to significantly change the way we think about nuclear physics and the strong limit of quantum chromodynamics. Major thrusts to identify the properties of low lying QCD states beyond the well-known quark-antiquark states and to measure the single quark wave functions of the hadrons are expected to produce definitive results. If nature does not match our current expectations, the quality of the data will be such that our field will likely be forced to undergo a significant rethinking of strong QCD.

We find that this experimental program can be carried out with the Jefferson Lab upgrade. The proposed experimental equipment is well suited to the research program and appears to involve proven technological choices. While the major research thrusts are well served by these choices, in some instances, the initial program will be exploratory and concepts for new equipment will naturally evolve.

The PAC would like to acknowledge the major effort the user community and laboratory have devoted to coming to grips with the best science that can be addressed with electromagnetic probes in the 12 GeV regime and thoroughly exploring the physics alternatives. The few additions suggested by the PAC are more speculative in nature and involve legitimate open issues about their usefulness at this time.

1.4 More information

More information about the physics of the HALL D project can be found in articles in the September/October 2000 issue of *American Scientist* [1] and in the September 2000 issue of the *CERN Courier* [2].

The HALL D home page on the world wide web is located at:
http : //dustbunny.physics.indiana.edu/HallD/.

Chapter 2

Executive Summary

2.1 Physics and overview

In the early 1970's, evidence that the masses of strongly interacting particles increased without limit as their internal angular momentum increased led the Japanese theorist Yoichiro Nambu to propose that the quarks inside of these particles are "tied" together by strings. Today the string theories which emerged from this idea are being examined as candidates for the ultimate theory of nature.

Meanwhile we have learned that the strong interactions are described by quantum chromodynamics (QCD), the field theory in which quarks interact through a "color" force carried by gluons. Although it is not fundamentally a string theory, numerical simulations of QCD ("lattice QCD") have demonstrated that Nambu's conjecture was essentially correct: in chromodynamics, a string-like chromoelectric flux tube forms between distant static color charges, leading to quark confinement and a potential energy between a quark and the other quarks to which it is tied which increases linearly with the distance between them. The phenomenon of confinement is the most novel and spectacular prediction of QCD.

The ideal experimental test of this new feature of QCD would be to directly study the flux tube of Figure 2.1 directly by anchoring a quark and antiquark several femtometers apart and examining the flux tube that forms between them. In such ideal circumstances one of the fingerprints of the gluonic flux tube would be the model-independent spectrum characterized by the two degenerate first excited states, which are the two longest wavelength vibrational modes of this system. Their excitation energy is π/r (r is the separation between the quarks) since both the mass and the tension of this "relativistic

string" arise from the energy stored in its color force fields.

Such a direct examination of the flux tube is of course not possible. In real life we have to be content with systems in which the quarks move. Fortunately, we know both from general principles and from lattice QCD that an approximation to the dynamics of the full system which ignores the impact of these two forms of motion on each other works quite well - at least down to the charm quark mass.

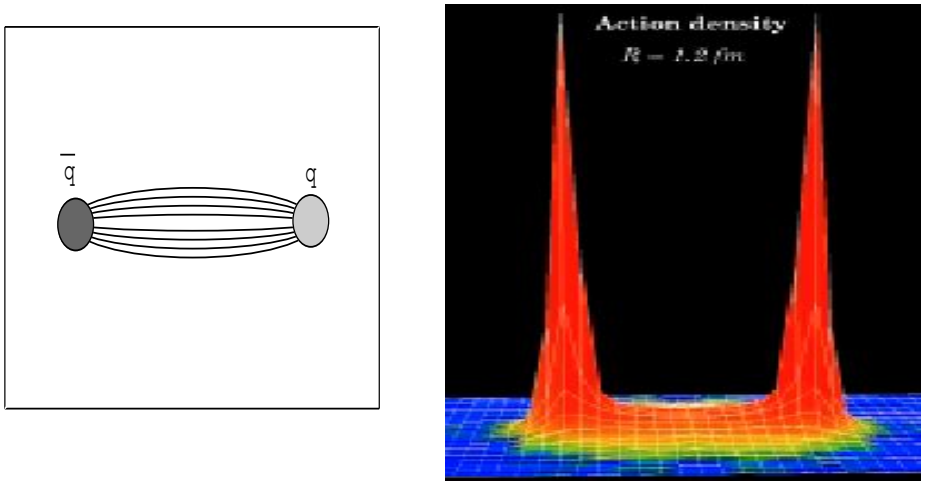

Figure 2.1: Evidence for flux tubes from lattice QCD. (left) The color field lines between a $q\bar{q}$ separated by distance r. (right) Action density (energy density) in the space surrounding a $q\bar{q}$ pair [3].

To extend the flux tube picture to yet lighter quarks models are required, but the most important properties of this system are determined by the model-independent features described above. In particular, in a region around $2\,GeV/c^2$, a new form of hadronic matter must exist in which the gluonic degree of freedom of mesons is excited. The unique characteristic of these new states is that the vibrational quantum numbers of the string, when added to those of the quarks, can produce a total angular momentum J, a total parity P, and a total charge conjugation symmetry C not allowed for ordinary $q\bar{q}$ states. These unusual J^{PC} combinations, like 0^{+-}, 1^{-+}, and 2^{+-}, are called exotic, and the states are referred to as exotic hybrid mesons.

Not only general considerations and flux tube models, but also first-principles lattice QCD calculations, require that these states are in this $2\ GeV/c^2$ mass region, while also demonstrating that the levels and their orderings will provide experimental information on the mechanism which produces the flux tube. Moreover, tantalizing experimental evidence has appeared over the past sev-

eral years for exotic hybrids as well as for gluonic excitations with no quarks (glueballs).

Photon beams are expected to be particularly favorable for the production of the exotic hybrids. The reason is that the photon sometimes behaves as a virtual vector meson (a $q\bar{q}$ state with the quark spins parallel, adding up to total quark spin $S = 1$). When the flux tube in this $q\bar{q}$ system is excited to the first excited levels, both ordinary and exotic J^{PC} are possible. In contrast, when the spins are antiparallel ($S = 0$), as in pion or kaon probes, the exotic combinations are not generated. Thus photons are expected to produce exotics more directly than other meson probes. To date, most meson spectroscopy has been done with incident pion or kaon probes. High flux photon beams of sufficient quality and energy have not been available, so there are virtually no data on the photoproduction of mesons below 3 GeV/c^2. Thus, experimenters have not been able to search for exotic hybrids precisely where they are expected to be found.

The Hall D detector, as shown in Figure 2.2, is optimized for incident photons in the energy range from 8 to 9 GeV in order to access the desired meson mass range. The use of a solenoidal spectrometer allows for the measurement of charged particles with excellent efficiency and momentum determination while at the same time containing the shower of unwanted electron-positron pairs associated with the photon beam. Photons will be produced using a "coherent bremsstrahlung" technique by passing an electron beam from the CEBAF accelerator though a wafer-thin diamond crystal. At special settings for the orientation of the crystal the atoms of the crystal can be made to recoil together from the radiating electron leading to an enhanced emission at particular photon energies and yielding linearly polarized photons. Even with only 10% of the eventual photon fluxes of 10^8/sec and the continuous CEBAF beam, the experiment will accumulate statistics during the first year of operation which will exceed extant published data with pions by at least an order of magnitude. With the HALL D detector, high statistics, and the linear polarization information, it will be possible to map out the full spectrum of these gluonic excitations.

In order to achieve the required photon energy and flux with coherent bremsstrahlung, an electron beam of 12 GeV is required. Figure 2.3 shows the current accelerator complex with the existing three experimental Halls (A, B and C) and the planned HALL D. The addition of state of the art accelerating units ("cryomodules") in the existing space in the linear sections of the accelerator, along with upgrading of magnets in the arcs, will bring the electron energy up from the current maximum of 5.5 GeV to 12 GeV.

When the spectrum and decay modes of these gluonic excitations have

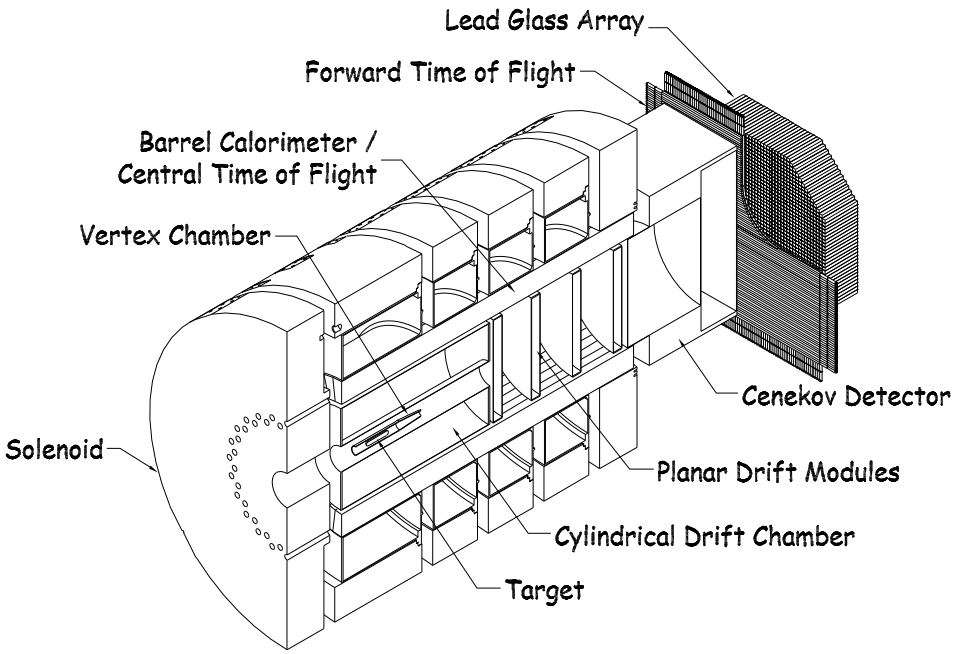

Figure 2.2: The Hall D detector.

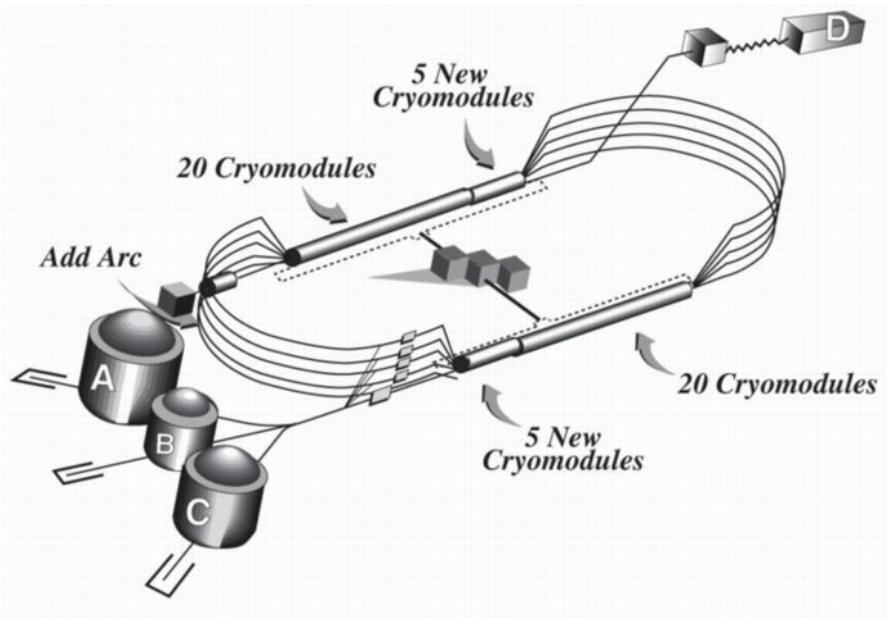

Figure 2.3: The current CEBAF multipass electron accelerator at JLab, showing the three existing experimental Halls (A, B and C) and the planned Hall D.

been mapped out experimentally, we will have made a giant step forward in understanding the confinement mechanism in QCD.

In this Design Report we will expand on:

1. *The role of glue in QCD.* This will include a discussion of how the gluons form flux tubes, and how their excitations lead to QCD mesons, in particular, exotic hybrids. This general picture is not restricted to a particular model but follows from the first principles of QCD. This is discussed in Chapter 3.

2. *The current evidence for gluonic excitations.* The evidence comes from overpopulation of conventional nonets and from possible glueball and exotic hybrid sightings in $\bar{p}p$ annihilations and π-induced interactions. This is also discussed in Chapter 3.

3. *Why the light-quark sector is the most fruitful venue for these searches.* We will compare this to searches in the charm quark or beauty quark sectors or e^+e^- annihilations. This is also discussed in Chapter 3.

4. *Why photons are expected to be particularly effective in producing exotic hybrids.* Its spin structure makes the photon a qualitatively different probe from π and K beams. In addition, there are meager data in hand on the photoproduction of light quark mesons. This is also discussed in Chapter 3.

5. *The importance of the partial wave analysis (PWA) technique in uncovering exotic mesons.* The PWA is a powerful analysis tool which has been successfully employed in experiments to uncover states which are not evident from a simple examination of mass spectra (bump-hunting). The importance of a hermetic detector with excellent resolution and rate capability and sensitivity to a wide variety of decay modes will be explored. This is discussed in Chapters 3 and 10.

6. *Why linear polarization of the photon beam is important for this search.* Linear polarization aids in determination of the J^{PC} quantum numbers, is essential in determining the production mechanism and can be used as a filter for exotics once the production mechanism is isolated. This is discussed in Chapters 3 and 10.

7. *Why the ideal photon energy range is from 8 to 9 GeV.* In order to reach the desired mass range we need to be far enough above threshold to avoid line-shape distortions. We also want to be high enough in

energy to separate kinematically the production of baryon resonances from production of meson resonances. This need for higher energies, however, has an upper limit driven by other considerations: the desire for a solenoid-only-based detector and increased flux and degree of linear polarization for a fixed electron energy. We discuss this in more detail below. Beam considerations and design are described in Chapter 4. The detector is discussed in Chapter 5 and more details about the solenoid magnet are provided in Appendix B.

8. *The desired electron energy.* Having established the desired range of photon beam energies, an electron energy of 12 GeV provides sufficient flux and degree of linear polarization. Again, the beam is discussed in Chapter 4.

2.2 Photon beam and choice of energy

The PWA technique will be used to extract information about the spin and parity of produced states. In a photon beam this process is greatly aided by using photons which are linearly polarized. Linear polarization can be achieved by using Compton backscattering or coherent bremsstrahlung off a crystal. The electron energies required and other practical technical limitations involving mirrors and lasers preclude the former for the photon fluxes and energies required. The latter option will be employed and is possible because the stringent requirements placed on the electron beam are realizable with the CEBAF accelerator. The details of how the tagged and collimated coherent beam will be produced are discussed in Chapter 4 of this Design Report.

What is the optimal photon beam energy to carry out the HALL D physics goals ? The goal of this experiment is to search for mesons in the mass range up to 2.5 GeV/c^2. An incident photon energy of just under 8 GeV is sufficient to produce a meson of mass 3 GeV/c^2. However, we also want to produce mesons with sufficient yield.

The momentum-transfer-squared (t) between the incident photon (γ) and the produced meson (X) in the reaction $\gamma p \to Xp$ is given by:

$$t = (p_\gamma - p_X)^2 \tag{2.1}$$

and at incident photon energies of several GeV and above, the distribution in t is given by:

$$dN/dt = e^{\alpha t} \tag{2.2}$$

The yield is determined by the value of $|t|_{min}$ and the exponential falling distribution in $|t|$. The relative yield for four meson masses for a slope parameter of $\alpha = 8\ (GeV/c)^{-2}$ is shown in Figure 2.4a. Another consideration is the ability to kinematically separate meson resonance production from baryon resonance production. As an example, we considered various reactions leading to a final state: $\pi^+\pi^-\pi^+n$. We enumerate the possibilities:

$$\gamma p \to X^+ n \to \rho^0 \pi^+ n \to \pi^+\pi^-\pi^+ n \tag{2.3}$$

$$\gamma p \to \rho^0 \Delta^+ \to \rho^0 \pi^+ n \to \pi^+\pi^-\pi^+ n \tag{2.4}$$

$$\gamma p \to \pi^+ N^{*0} \to \pi^+\pi^-\pi^+ n \tag{2.5}$$

The first of these is the reaction of interest. We can reduce the other two by requiring that the effective mass of any πn or $\pi\pi n$ combination be outside the baryon resonance region. In this exercise we define the baryon region to include πn or $\pi\pi n$ mass combinations below 1.7 GeV/c^2. The fraction of events for which we are able to reduce the offending reaction, as a function of beam momentum and for various m_X masses is shown in Figure 2.4b.

Whereas the considerations mentioned thus far favor larger photon beam energies, other considerations favor a lower photon beam energy. For the tagged and collimated coherent photon beam the variation in flux, for constant total hadronic rate in the detector, is plotted in Figure 2.5a as a function of photon beam energy for three different values of electron energy. In Figure 2.5b the degree of linear polarization is plotted as a function of photon beam energy for three different values for the electron energy as well.

Finally, in Figure 2.6 we plot an overall figure-of-merit which folds in the variation of beam flux and degree of linear polarization with beam energy, as well as the effective yield taking into account $|t|_{min}$ effects and the ability to separate meson resonances from baryon resonances kinematically.

From this and other considerations we conclude that the optimum photon beam energy is between 8 and 9 GeV. Those other considerations include the fact that for beam energies significantly below 8 GeV the line shape for resonances at the upper end of of our mass range of interest is severely distorted while above 9 GeV the momentum resolution of charged particles from two-particle decays of mesons at the lower end of our meson mass range is degraded since the transverse momentum of the decay products is small.

There then is a clear *sweet spot* for the photon beam energy of 8 to 9 GeV. It is equally important to have an electron energy as close as possible to the

maximum energy achievable with the proposed upgrade. The plots of Figure 2.5 show the price of dropping this electron energy in terms of flux and polarization.

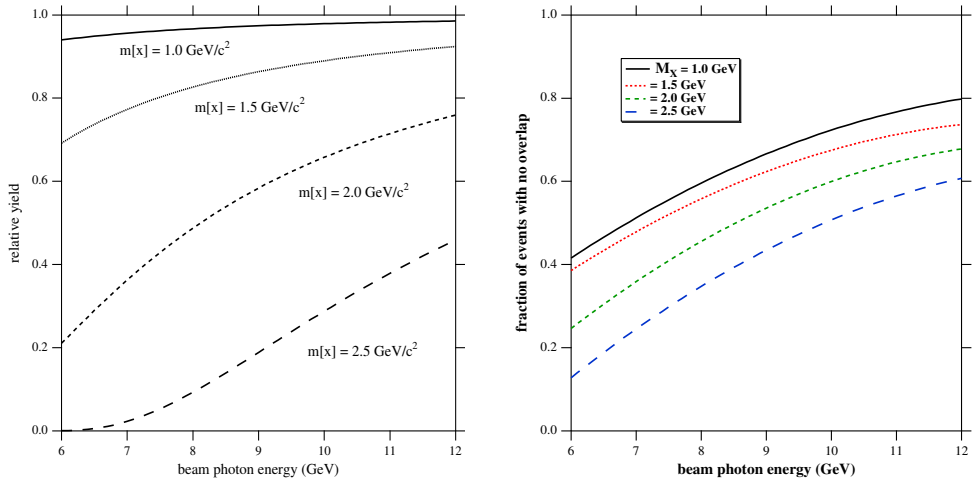

Figure 2.4: Various figures of merit to choose optimal photon beam energy. (left) Relative meson yield as a function of photon beam energy for various meson masses. (right) Fraction of events in which meson and baryon resonances are separated as a function of photon beam energy for various meson masses.

2.3 Detector

The physics goals of the HALL D project require a full PWA of kinematically identified exclusive reactions producing mesons. The decay products of produced mesons must be identified and measured with good resolution and with full acceptance in decay angles. In many cases, the decays of mesons involve a chain of particle decays. The HALL D detector must therefore be hermetic with 4π coverage with the capability of measuring energies of neutral particles (γ, π^0, η) and momenta of charged particles with good resolution. Particle identification is also required.

The HALL D detector described in Chapter 5 is optimized for photon beam energies between 8 and 10 GeV. The detector consists of a large aperture superconducting solenoid filled with a target, tracking chambers and calorimetry. The calorimetry will also provide time-of-flight information for particle identification. The solenoid will be followed with a threshold Čerenkov counter, particle tracking, a forward TOF and a lead glass electromagnetic calorimeter.

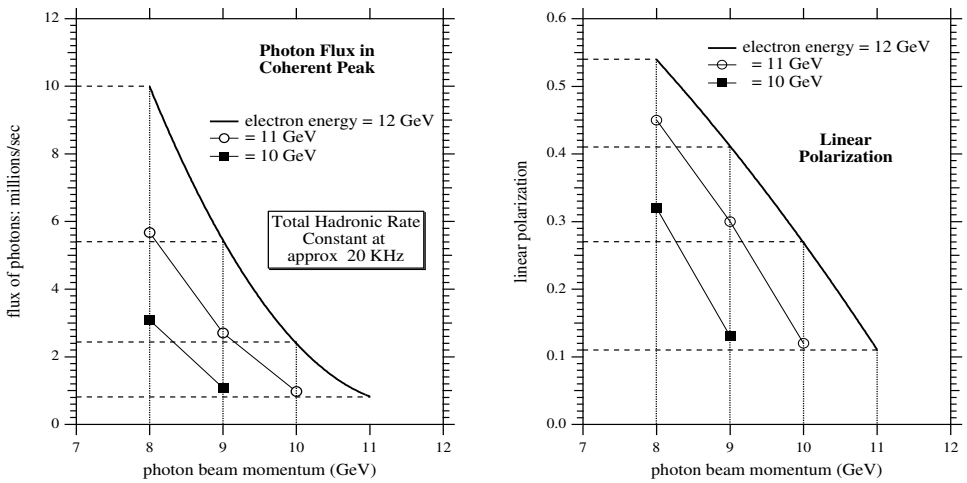

Figure 2.5: Photon beam flux and degree of linear polarization for various values of electron energy. (left) Flux dependence on photon beam energy. (right) Degree of linear polarization dependence on photon beam energy.

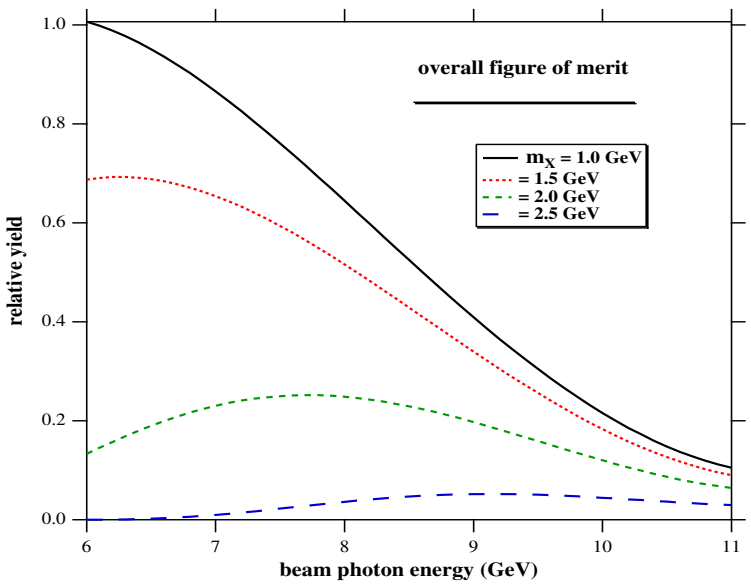

Figure 2.6: Figure of merit: relative meson yield as a function of photon beam energy for various meson masses.

The superconducting solenoidal magnet is the LASS/MEGA magnet. This magnet was built for the Large Aperture Superconducting Solenoid Spectrometer (LASS) at SLAC and later transferred to LANL for use in the MEGA experiment. It will be transferred to JLab for use in HALL D. The forward electromagnetic calorimeter will be a modified version of the lead glass detector used in Brookhaven experiment E852. That detector has already been moved to JLab.

2.4 Civil construction

The plan is to site the meson spectrometer in a new experimental hall (HALL D) to be located at the end of a new beamline which would come off the stub at the east end of the north linac of CEBAF. The civil construction includes work associated with breaking through the stub, delivering beam above ground to a tagging spectrometer, a tagger building, HALL D, the counting house, roads, and a parking area. Members of the HALL D collaboration have been meeting with members the JLab civil construction team to arrive at a cost estimate and milestones for civil construction. Details are given in Chapter 6.

2.5 Rates,trigger and DAQ

Initially the HALL D detector will run with tagged photon fluxes of 10^7 photons/sec and data archive rates of 15K events/sec. Estimates of the hadronic and electromagnetic tagged and untagged rates have been made along with estimates of accidental rates. These rate estimate calculations are backed by measurements made in Hall B and while technically challenging, are within the capabilities of a state-of-the art electronics system.

The trigger system will be implemented from the outset in a pipeline fashion to provide maximum flexibility for sophisticated triggers. This will allow us to gradually increase the incident flux to 10^8 photons/sec – greatly opening the scope of physics, in both meson spectroscopy and rare decays.

The proposed data acquisition (DAQ) system system is based on an upgrade of the existing CODA-based DAQ system already in use at Jefferson Lab. Details about rates, the trigger and DAQ are given in Chapter 7.

2.6 Data handling

In Chapter 8 we discuss the data handling, which will be based on the tools in existence at JLab and their upgrades to handle higher data rates and volumes. It is important to note that the data volumes expected in this experiment are within a factor of two of those currently handled by the CLAS collaboration at JLab.

We also plan to work with computer scientists at collaborating institutions to explore modern information technologies in data mining and movement. Various such applications to the HALL D project were discussed at a workshop on "HALL D and Modern Information Technology" held at Carnegie Mellon University in September 2000 which included HALL D collaborators and computer scientists from Carnegie Mellon, Florida State University, Indiana University and Rensselaer Polytechnic University.

2.7 Monte Carlo simulations

Chapter 9 describes the Monte Carlo work done to date on event generators and on simulating the response of the current detector design.

2.8 Partial wave analysis

Chapter 10 describes recent upgrades to the partial wave formalism to take into account photon beam polarization. Double-blind tests have been done in which events were generated according to particular mixes of partial waves. These events were then passed through software which introduced resolution smearing and acceptance cuts. The resulting events were then reconstructed and analyzed with a PWA fitter. The conclusion is that with a year's worth of data at photon fluxes of 10^7/sec, exotic signals corresponding to a few percent of copiously produced states can be easily extracted.

2.9 Management plan

The HALL D collaboration has adopted a management plan based on the experience of other collaborations at JLab and collaborations in high energy physics. This plan is described in Chapter 11.

2.10 Costs

The total cost for the HALL D project is $\approx$ \$35.6 M (including contingencies). The cost of the detector is $\approx$ \$22.2 M The civil and beamline costs total $\approx$ \$13.4 M and include the tunnel from the accelerator to the HALL D tagger, beamline elements, the HALL D building, control room, parking and roads. Further details of the costs for the various subsystems of the detector, the civil construction, beamline and tagger are given in Appendix C.

Not included in the HALL D cost estimate is the cost of the additional arc in the CEBAF accelerator which would allow 5.5 passes for the electron beam in HALL D.

Also not included in the HALL D cost estimates are all the computer upgrades planned at JLab as part of the overall energy upgrade project.

Chapter 3

Scientific Goals of the Hall D Project

3.1 Introduction

The goal of the HALL D project is the definitive and detailed measurement of the spectrum of exotic hybrid mesons. These manifestations of the gluonic degrees of freedom in the spectroscopy of hadrons will lead to an understanding of the most novel and spectacular feature of QCD – confinement. The most fruitful place to search for these mesons is in the light quark sector and the optimal probe is the photon, which is expected to be far more effective in uncovering these states than beams of π or K mesons have been. The power of the photon probe lies in its virtual $q\bar{q}$ structure: the quark spins are aligned as opposed to π or K mesons in which the quark spins are anti-parallel. Almost all data on the spectroscopy of mesons below 3 GeV/c^2 come from π and K induced reactions, central production in p-induced reactions and $\bar{p}p$ annihilations. Tantalizing indications for gluonic excitations have emerged from these studies but the evidence is far from solid and the details needed for a full understanding are missing. The data in hand on the photoproduction of light mesons are sparse indeed, essentially non-existent. Spectroscopy experiments rely on detecting complicated decays of produced mesons and on the full reconstruction of the reactions in which they are created. Large statistical sample sizes are also required. Up to now, photon beams of sufficient energy, flux and other requisite beam characteristics could not be produced. The determination of quantum numbers of mesons is also greatly aided by using photon beams which are linearly polarized. The superb electron beam

characteristics (spot size and emittance) of the CEBAF accelerator at JLab make possible the employment of the coherent bremsstrahlung technique for producing photon beams with a high degree of linear polarization. Hybrid mesons, including those with exotic quantum numbers, are expected to lie in the range from 1.5 to 2.5 GeV/c^2. To reach these masses requires photons in the energy range from 8 to 10 GeV. This is based on the requirement that mesons are produced sufficiently above threshold so that line shapes are not distorted. This band of photon energies also allows for a solenoid- based detector which, particularly for high-flux photon beams, is optimal in achieving 4π hermiticity. With an electron beam energy of 12 GeV, photon fluxes of up to 10^8 photons/sec with 50 % linear polarization in the desired energy range are achievable. Even with initial fluxes of 10^7 photons/sec, the statistical sample size collected after the first year of running will exceed those collected with incident hadron beams by at least an order of magnitude. With this sample size collected using a hermetic and well-understood detector, the application of the partial wave analysis (PWA) technique will be able to uncover the exotic states, even if they are produced with cross sections only a few percent of those for conventional mesons. Indeed theoretical considerations [4] lead us to believe that the exotic hybrids will be produced with cross sections which are nearly comparable to those of conventional mesons.

In this Design Report we expand on:

1. *The role of glue in QCD.* This will include a discussion of how the gluons form flux tubes, and how their excitations lead to QCD mesons, in particular exotic hybrids. This general picture is not restricted to a particular model but follows from the first principles of QCD.

2. *The current evidence for gluonic excitations.* The evidence comes from overpopulation of conventional nonets and from possible glueball and exotic hybrid sightings in $\bar{p}p$ annihilations and π-induced interactions.

3. *Why the light-quark sector is the most fruitful venue for these searches.* We will compare this to searches in the charm quark or beauty quark sectors or e^+e^- annihilations.

4. *Why photons are expected to be particularly effective in producing exotic hybrids.* Its spin structure makes the photon a qualitatively different probe from π and K beams. In addition, there are meager data in hand on the photoproduction of light quark mesons.

5. *The importance of the PWA technique in uncovering exotic mesons.* The PWA is a powerful analysis tool which has been successfully employed in

experiments to uncover states which are not evident from a simple examination of mass spectra (bump-hunting). The importance of a hermetic detector with excellent resolution and rate capability and sensitivity to a wide variety of decay modes will be explored.

6. *Why linear polarization of the photon beam is important for this search.* Linear polarization aids in determination of the J^{PC} quantum numbers, is essential in determining the production mechanism and can be used as a filter for exotics once the production mechanism is isolated.

7. *Why the ideal photon energy range is from 8 to 9 GeV.* In order to reach the desired mass range we need to be far enough above threshold to avoid line-shape distortions. We also want to be high enough in energy to kinematically separate production of baryon resonances from production of meson resonances. This need for higher energies, however, has an upper limit driven by other considerations: the desire for a solenoid-only-based detector and increased flux and degree of linear polarization for a fixed electron energy.

8. *The desired electron energy.* Having established the desired range of photon beam energies, an electron energy of 12 GeV provides sufficient flux and degree of linear polarization. This was already discussed in Chapter 2.

This then is the overview of the major physics thrust of the HALL D project. In addition to studying hybrid mesons, both with exotic as well as non-exotic quantum numbers, we will also now have the opportunity to study the $s\bar{s}$ sector as well. Little is known about $s\bar{s}$ mesons. Knowledge about this spectroscopy will allow us to bridge from the light quark (u and d) to the heavy (c and b) sectors.

3.2 Spectroscopy of gluonic excitations

3.2.1 Flux tubes

Quantum Chromodynamics (QCD) describes the interactions of quarks and gluons, and along with the electroweak theory they form the successful Standard Model of elementary particles. At short distances, where perturbative techniques are applicable, QCD describes high energy experimental phenomena and data both qualitatively and quantitively. QCD is distinct from QED

in that the force carriers of the former (gluons) carry color charge whereas for the latter the photons are electrically neutral. The gluonic degrees of freedom are experimentally evident at high momenta and manifested in the observation of gluon jets and the details of their production.

At the large distance scale, the situation is far different. Here the successful calculational techniques of the perturbative regime cannot be used. We must rely on first-principles lattice QCD calculations or QCD-inspired models. On the experimental side there is little or no evidence of gluonic degrees of freedom as epitomized in the spectroscopy of hadrons. However, there are many indications that all this is about to change. Developments on the theoretical and experimental fronts give rise to optimism that these gluonic degrees of freedom will be observed, measured and understood in detail. The prize in understanding these new manifestations of gluonic degrees of freedom (glueballs and hybrid mesons) is grand indeed: an understanding of the confinement mechanism of QCD. The phenomenon of confinement is the most novel and spectacular prediction of QCD - unlike anything seen before.

How can we observe the gluonic degrees of freedom in the spectroscopy of mesons? At large distances, a meson consists of a quark and antiquark pair held together by a flux-tube or relativistic string. This model-independent picture of a meson originally emerged in the 1970's when Yoichiro Nambu pointed out the observation of a linear relationship between the spins of hadrons and the square of their masses. This relationship falls out by assuming that the quarks are tied to the ends of a relativistic string with constant mass per length. This also leads to a linearly rising potential.

The confinement mechanism is related to the fact that gluons carry the color charge and becomes evident when we realize that we cannot separate the quarks in a hadron from each other. The field lines of an electic dipole arrange themselves as shown in Figure 3.1a. As we separate the two charges, the potential energy falls off like $1/r$ and the force like $1/r^2$. Consider now a quark and antiquark as shown in Figure 3.1b. Because of the self-interaction of the gluons the field lines form flux tubes as we increase the separation between the quarks. If we compute the number of field lines intersecting an area perpendicular to the flux tube we notice that this number stays constant as we increase r, suggesting a constant force or linear potential. This leads to confinement since infinite energy is then required to separate the quarks. Recent lattice QCD calculations support this notion of the formation of flux tubes as shown in Figure 3.2a where the action density (energy density) is plotted for a $q\bar{q}$ pair. The formation of the flux tube is evident. These lattice calculations also show that the potential for the $q\bar{q}$ pair is linear (Figure 3.2b) for r greater than about 0.2 fm. Indeed the energy levels observed for heavy

quarkonium are in agreement with a linear potential.

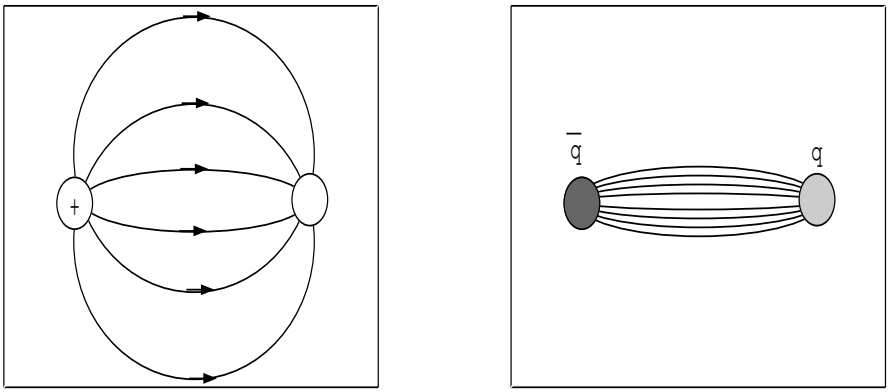

Figure 3.1: Comparing force field lines for QED and QCD. (left) The field lines for an electric dipole. (right) The color field lines for a quark and anti-quark.

Conventional mesons

The conventional mesons of the original quark model correspond to the flux-tube being in its ground state. The conventional mesons made from the u, d and s quarks are grouped in nonets, each characterized by a given J^{PC} determined by the relative orientation of the spins of the quarks and their orbital angular momentum. The rules for allowed values of J^{PC} follow from the requirements of a fermion–antifermion system: the quark spins can be parallel ($S = 1$) or antiparallel ($S = 0$) with relative orbital angular momentum (L), $\vec{J} = \vec{L} + \vec{S}$, $P = (-1)^{L+1}$ and $C = (-1)^{L+S}$. For these $q\bar{q}$ systems $J^{PC} = 0^{--}$, 0^{+-}, 1^{-+}, 2^{+-}, $\cdots$ are not allowed and are referred to as *exotic* quantum numbers. The range of masses of the known conventional meson nonets and their radial excitations extend from the π mass up to about 2.5 GeV/c^2.

Figure 3.4 shows our current knowledge of conventional $q\bar{q}$ states. The exact association of an observed meson with a particular $q\bar{q}$ state within a nonet depends on a good understanding of the various decay modes of the meson as well as its mass, width and production characteristics.

There is also now clear evidence that the observed meson spectrum includes states which cannot be accommodated within the naive quark model. For example, there are at least five scalar states reported with masses below 2 GeV/c^2 suggesting that among these may be a scalar glueball. Lattice Gauge

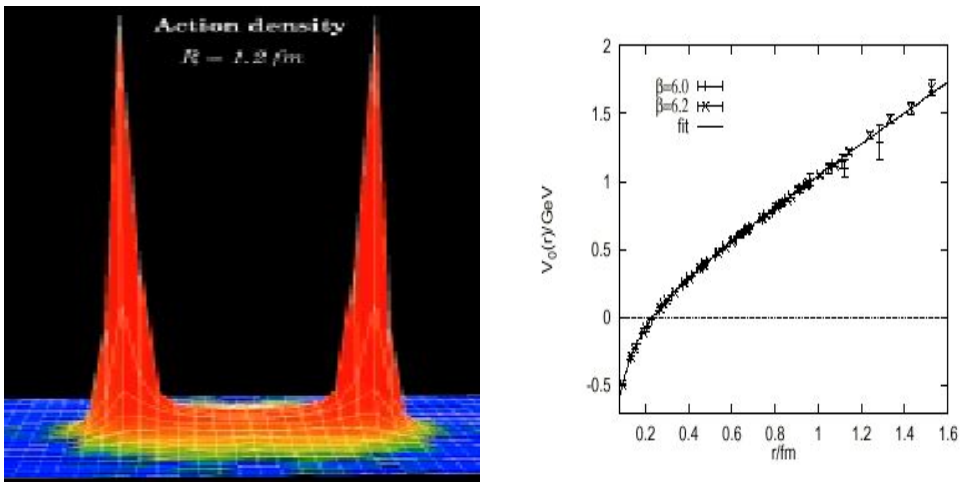

Figure 3.2: Evidence for flux tubes and linear potentials from lattice QCD. (left) Action density (energy density) in the space surrounding a quark and antiquark [3]. (right) The interquark potential [3].

Theory calculations indicate that the lightest scalar glueball should have a mass in the range from 1.5 to 1.7 GeV/c^2, which is consistent with two of the observed states. There exists strong evidence for states with exotic quantum numbers, (the $q\bar{q}$ quantum number restrictions do not apply to gluonic mesons or molecules), although their exact interpretation is unclear. Finally, we have possible evidence for molecular states in the $f_0(980)$ and $a_0(980)$.

More details about the current status of light quark spectroscopy can be found in two recent reviews [5, 6].

Mesons and gluonic excitations

Mesons can also be generated when the flux tube or string is *plucked* or excited. The two degenerate first excited states of the string are the two longest wavelength vibrational modes of this system and π/r is their excitation energy since both the mass and the tension of this "relativistic string" arise from the energy stored in its color force fields. The vibrational quantum numbers of the string, when added to those of the quarks, can produce mesons with exotic J^{PC} – *exotic hybrids* – hybrids because the mesons manifest both their quark and gluonic content. Because the gluons carry color charge it should also be possible to form bound states of glue with no quarks present. Such mesons are called *glueballs*.

Figure 3.3 shows a level diagram giving the range of masses for the con-

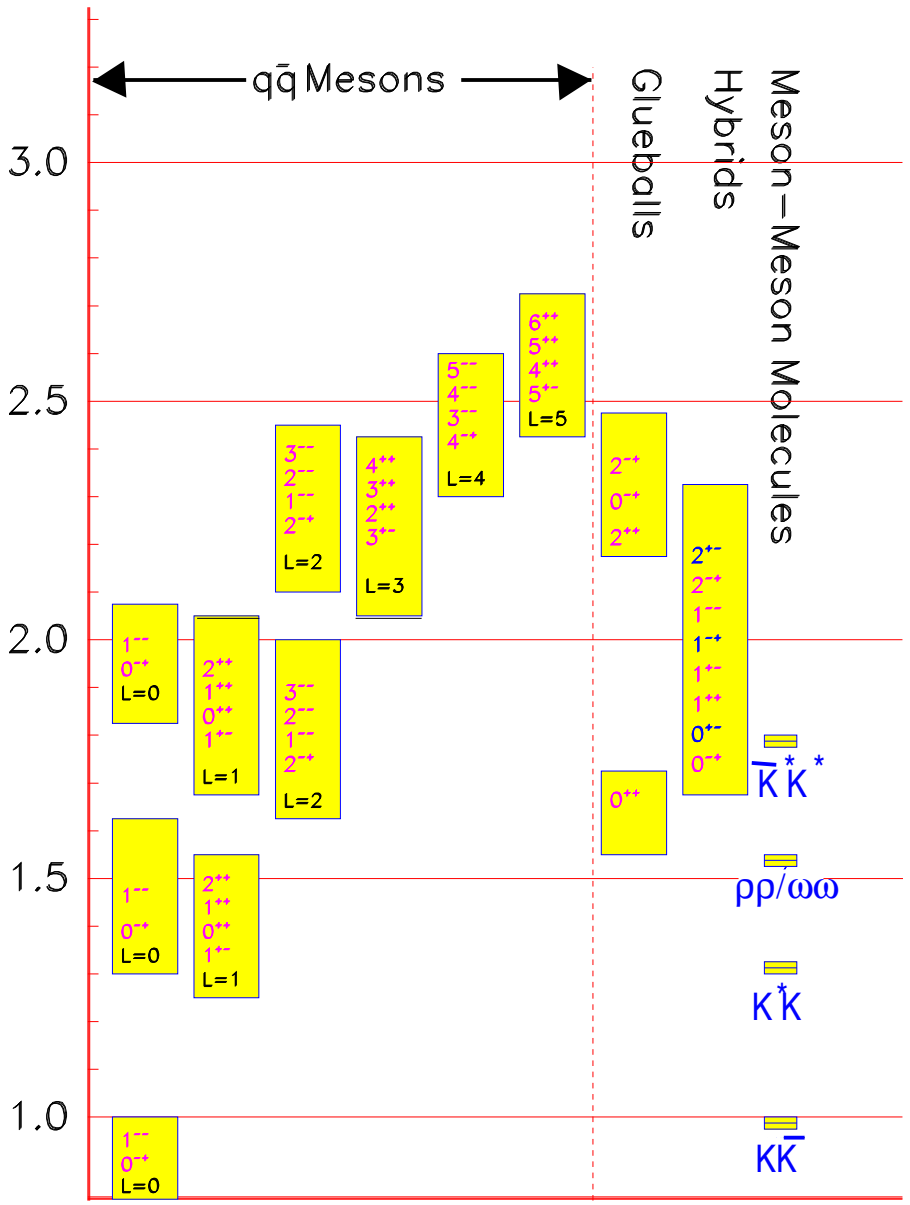

Figure 3.3: A level diagram showing conventional nonets and expected masses of glueballs, hybrids and molecular thresholds. The vertical axis is in units of GeV/c^2. For the $q\bar{q}$ boxes the L refers to the angular momentum between the quarks and each J^{PC} refers to a nonet of mesons. Note also that exotic J^{PC} occur only among the hybrids for the range of masses shown.

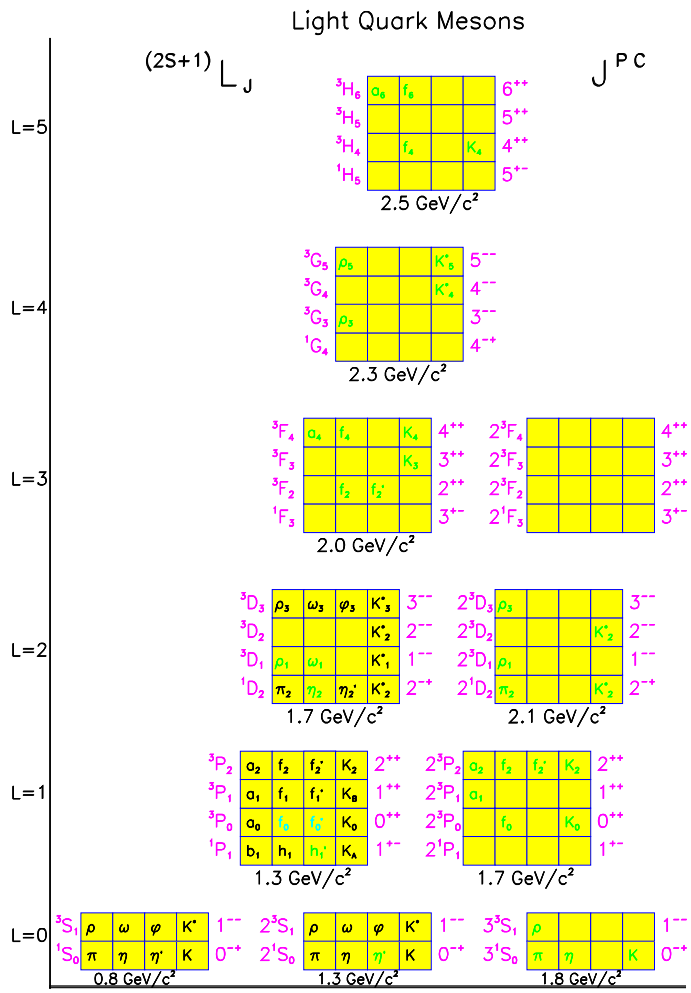

Figure 3.4: The $q\bar{q}$ spectrum of states. The assignments of the light colored states are speculative, while the empty boxes are missing states. The orbital angular momentum of the nonet is plotted on the vertical axis, while the towers of radial excitations are shown along the horizontal axis.

ventional $q\bar{q}$ nonets and estimates of the masses of the lightest glueballs and hybrids, and thresholds which might have nearby associated molecular meson-meson bound states.

Focusing on light-quark exotic hybrids

The focus of the HALL D project is in the light-quark hybrid sector. The initial benchmark states will be the exotic hybrids, which cannot mix with $q\bar{q}$ and which therefore have a *smoking gun* signature. Although there is strong circumstantial evidence for glueballs, the possibility of mixing with $q\bar{q}$ complicates the analysis. Lattice QCD predictions about heavy-quark exotic hybrids are at least as reliable as for the light-quark hybrids but the experimental situation is far more problematic. The production cross-sections are a few orders of magnitude lower. At the higher energies needed to produce these more massive states many other uninteresting processes can contribute to background. Finally, to unambiguously tag a charm or beauty hybrid one must identify detached vertices, further complicating the experimental challenge. Another venue for exotic vector hybrids is production in e^+e^- collisions. The angular momentum barrier (the excited flux-tube carries $J = 1$) suppress this production mode.

From every point of view, photoproduction of light-quark hybrids is expected to be our best handle for providing the information we need to understand confinement.

Observation of gluonic excitations

Lattice QCD and flux-tube model calculations are in agreement that the range of masses of light-quark hybrids is from 1.5 to 2.5 GeV with the lightest exotic hybrid ($J^{PC} = 1^{-+}$) having a mass about 2 GeV/c^2 [7, 8]. After about 15 years of searching we have in hand two candidates for exotic hybrids: one with a mass of 1.4 GeV decaying into $\eta\pi^-$ [9, 10] – the evidence for this state is not without controversy – and a perhaps a more firmly established state at 1.6 GeV/c^2 decaying into $\rho^0\pi^-$ [11]. Both have the assignment: $J^{PC} = 1^{-+}$. These states were reported by the E852 collaboration which studied $\pi^- p$ interactions using the AGS at Brookhaven National Lab. Both states have also been independently confirmed. It is noteworthy that the two candidates in hand have masses below the expectations from lattice QCD and the flux-tube model for the lightest exotic hybrid [12]. In addition, the decay modes observed are not those favored by the flux-tube model. In this model, the exotic hybrid's favored decay mode is into $S + P$ where S indicates a conventional $q\bar{q}$ meson

with $L = 0$ while P indicates a conventional $q\bar{q}$ meson with $L = 1$. This comes about from how the exotic hybrid gives up its spin to the decay daughters and possibly explains why exotic hybrids have not yet been observed – the decay modes are complicated. For example, a favored mode is into $b_1\pi \rightarrow \omega 2\pi \rightarrow 5\pi$.

Lattice QCD calculations indicate that lightest glueball is a scalar with a mass in the range from 1.5 to 1.7 GeV/c^2 [13, 14, 15, 16]. Indeed there is evidence from the Crystal Barrel experiment, which studied $\bar{p}p$ annihilations at CERN, that the $f_0(1500)$ is a leading candidate for a glueball [17, 18]. There are, however, indications that this state is not a pure glueball but has some mixing with conventional $q\bar{q}$ [19]. There are strong indications that the scalar meson sector contains one or more glueballs since there are several more observed states than can be accommodated in the simple $q\bar{q}$ model. However, the unique identification of a glueball is exacerbated by the possibility of mixing with $q\bar{q}$. Lattice QCD indicates a rich spectrum of glueballs, all with non-exotic quantum numbers, from 1.5 to 2.5 GeV/c^2. The lightest glueball with exotic quantum numbers is predicted to have $J^{PC} = 2^{+-}$ and to have a mass of 4 GeV/c^2 [13].

This then is the tantalizing evidence in hand for gluonic excitations. In the case of the exotic hybrids, the range of masses of putative states observed is significantly lower than expectations and the observed modes of decay are not those expected to be favored [20, 21]. Lattice QCD calculations are being refined and significant progress on reducing the theoretical errors on masses and more information on decay modes is expected in the next five years as computational techniques improve and computer power increases. Flux-tube model calculations are in hand for both masses and decay modes [12, 22]. Given the state of current observations, with their uncertainties and limitations, the flux-tube model has not been ruled out. Clearly more data are needed. As will be shown below, photoproduction reactions are expected to be a rich source of hybrids – exotic and non-exotic. Once these states are discovered and mapped out, we will have the data needed to constrain our theoretical understanding of the details of confinement. Without more data, there will be little progress.

3.3 Photoproduction of gluonic excitations

3.3.1 Why photoproduction?

The photon is expected to be particularly effective in producing our *smoking gun* signature for gluonic excitations: hybrids with exotic J^{PC}. In this

regard, we will compare the effectiveness of the π or K as a probe with that of the photon. In the former case, the meson is a $q\bar{q}$ with spins anti-aligned ($S = 0$) and in the latter, the photon is a virtual $q\bar{q}$ with spins aligned ($S = 1$). In both cases, the relative orbital angular momentum is zero ($L = 0$) and the flux tube connecting the quarks is in its gound state.

Consider what happens when the beam probe approaches a target proton and scatters. A possible outcome is a transfer of energy which excites the flux-tube to its lowest excited state. Lattice QCD and flux-tube models both indicate that the lowest excited flux-tube has $J = 1$ [7, 20, 23]. The flux-tube, or string, can be spinning clockwise or counter-clockwise around the $q\bar{q}$ line leading to two degenerate states – degenerate since the energy should not depend on which way the flux-tube is spinning. The states which are linear combinations of these two rotations are eigenstates of parity and charge conjugation leading to two possibilities for the excited flux-tube: $J^{PC} = 1^{-+}$ or $J^{PC} = 1^{+-}$. Suppose we start with the $q\bar{q}$ in the $S = 0$ and $L = 0$ (or $J^{PC} = 0^{-+}$ – the π or K) configuration. Combining this with $J^{PC} = 1^{-+}$ or $J^{PC} = 1^{+-}$ of the excited flux-tube results in hybrid mesons with $J^{PC} = 1^{++}$ or $J^{PC} = 1^{--}$. These are non-exotic. If, however, we start with $q\bar{q}$ in the $S = 1$ and $L = 0$ (or $J^{PC} = 1^{--}$ – the vector photon) configuration, the resulting hybrid can have $J^{PC} = [0, 1, 2]^{+-}$ for the flux-tube with $J^{PC} = 1^{-+}$ and $J^{PC} = [0, 1, 2]^{-+}$ for the flux-tube with $J^{PC} = 1^{+-}$. So we see that in the case of the vector probe, the resulting hybrids can have six possible J^{PC} of which half are exotic combinations whereas, for π or K probes, the exotic combinations are not generated.

In the next section, we will discuss how the technique of PWA will be used to extract information about the spin and parity of produced states. In a photon beam this process is greatly aided by using photons which are linearly polarized. Linear polarization can be achieved by using Compton backscattering or coherent bremsstrahlung from a crystal. The electron energies required and other practical technical limitations involving mirrors and lasers preclude the former for the photon fluxes and energies required. The latter option will be employed and is only a possibility because the stringent requirements placed on the electron beam are realizable with the CEBAF accelerator. The details of how the tagged and collimated coherent beam will be produced are discussed later in this report.

Current photoproduction data

Table 3.1 is a partial compilation of known photoproduction cross sections

Reaction	E_γ *GeV*	σ (μb)	*Events*	*Ref.*
$\gamma p \to p\pi^+\pi^-$	9.3		3500	[24]
$\gamma p \to p\pi^+\pi^-$	19.3		20908	[25]
$\gamma p \to p\pi^+\pi^-\pi^\circ$	2.8		2159	[24]
$\gamma p \to p\pi^+\pi^-\pi^\circ$	4.7		1606	[24]
$\gamma p \to p\pi^+\pi^-\pi^\circ$	9.3		1195	[24]
$\gamma p \to p\pi^+\pi^-\pi^\circ$	4.7–5.8	$13.5 \pm 1.5\,\mu b$	3001	[26]
$\gamma p \to p\pi^+\pi^-\pi^\circ$	6.8–8.2	$11.8 \pm 1.2\,\mu b$	7297	[26]
$\gamma p \to n\pi^+\pi^+\pi^-$	4.7–5.8	$4.6 \pm 1.4\,\mu b$	1723	[26]
$\gamma p \to n\pi^+\pi^+\pi^-$	6.8–8.2	$4.0 \pm 1.2\,\mu b$	4401	[26]
$\gamma p \to n\pi^+\pi^+\pi^-$	16.5–20		3781	[27]
$\gamma p \to p\pi^+\pi^-\pi^\circ$	20–70		14236	[28]
$\gamma p \to p\pi^+\pi^-\pi^+\pi^-$	4–6	$4.0 \pm 0.5\,\mu b$	~ 330	[29]
$\gamma p \to p\pi^+\pi^-\pi^+\pi^-$	6–8	$4.8 \pm 0.5\,\mu b$	~ 470	[29]
$\gamma p \to p\pi^+\pi^-\pi^+\pi^-$	8–12	$4.5 \pm 0.6\,\mu b$	~ 470	[29]
$\gamma p \to p\pi^+\pi^-\pi^+\pi^-$	12–18	$4.4 \pm 0.6\,\mu b$	~ 380	[29]
$\gamma p \to p\pi^+\pi^-\pi^+\pi^-$	15–20		6468	[30]
$\gamma p \to p\pi^+\pi^-\pi^\circ\pi^\circ$	20–70		8100	[31]
$\gamma p \to p\pi^+\pi^+\pi^-\pi^-\pi^\circ$	19.5		2553	[32]
$\gamma p \to \Delta^{++}\pi^-\pi^+\pi^-$	4–6	$1.65 \pm 0.2\,\mu b$	~ 200	[29]
$\gamma p \to \Delta^{++}\pi^-\pi^+\pi^-$	6–8	$1.8 \pm 0.2\,\mu b$	~ 200	[29]
$\gamma p \to \Delta^{++}\pi^-\pi^+\pi^-$	8–12	$1.1 \pm 0.2\,\mu b$	~ 200	[29]
$\gamma p \to \Delta^{++}\pi^-\pi^+\pi^-$	12–18	$1.15 \pm 0.2\,\mu b$	~ 200	[29]
$\gamma p \to p\omega$	4.7–5.8	$2.3 \pm 0.4\,\mu b$	< 1600	[26]
$\gamma p \to p\omega$	6.8–8.2	$2.0 \pm 0.3\,\mu b$	< 1200	[26]
$\gamma p \to p\omega$	4.7	$3.0 \pm 0.3\,\mu b$	1354	[24]
$\gamma p \to p\omega$	9.3	$1.9 \pm 0.3\,\mu b$	1377	[24]
$\gamma p \to p\phi$	4.7	$0.41 \pm 0.09\,\mu b$	136	[24]
$\gamma p \to p\phi$	9.3	$0.55 \pm 0.07\,\mu b$	224	[24]
$\gamma p \to n a_2^+$	4.7–5.8	$1.7 \pm 0.9\,\mu b$		[26]
$\gamma p \to n a_2^+$	6.8–8.2	$0.9 \pm 0.9\,\mu b$		[26]
$\gamma p \to n a_2^+$	19.5	$0.29 \pm 0.06\,\mu b$	~ 100	[27]

Table 3.1: A sample of measured photoproduction cross sections from several references. Note the small numbers of events in any given channel.

and the numbers of events from the existing experiments. The typical cross sections range from of order $0.1\,\mu$b up to of order $10\,\mu$b, with most measurements involving rather small numbers of events, typically on the order of a few thousand. The extant data from photoproduction are far too meager to perform the analysis necessary to unambiguously identify gluonic excitations.

3.3.2 PWA and photon polarization

Kinematics

The technique for identifying meson states (masses, widths and J^{PC}) is the partial wave analysis. Consider a specific exclusive process:

$$\gamma p \to Xp \tag{3.1}$$

The center-of-mass energy squared, s, and the momentum-transfer-squared, t, between the incoming beam and outgoing X are defined in terms of the four-vectors of the particles:

$$s = (p_\gamma + p_p)^2 \tag{3.2}$$

$$t = (p_\gamma - p_X)^2 \tag{3.3}$$

The dependence of cross section on s and t depend on the production mechanism, which is usually described in terms of the particle or particles which can be exchanged as shown in Figure 3.5. For example, if the exchange particle is the pomeron (diffractive process) the cross section is nearly constant in s. For meson-exchange processes, cross sections typically fall off like $1/s^2$. The dependence on t is typically exponential:

$$\frac{dN}{dt} \propto e^{-\alpha|t|} \tag{3.4}$$

For the process (3.1) at high enough photon beam energy, E_γ, we can make the approximation $s \approx 2 \cdot E_\gamma$ where E_γ is in GeV and s is in GeV^2. For fixed s, and mass of X, m_X, there is a minimum value of $|t|$, or $|t|_{min}$, needed to produce X. This $|t|_{min}$ increases with increasing m_X for fixed E_γ and decreases with increasing E_γ for fixed m_X. Coupled with the steep dependence implied in equation (3.4), the dependence of $|t|_{min}$ on m_X will affect event yields. In addition, the line shape of a resonance can be distorted if there is too rapid a variation of $|t|_{min}$ across the width of a resonance.

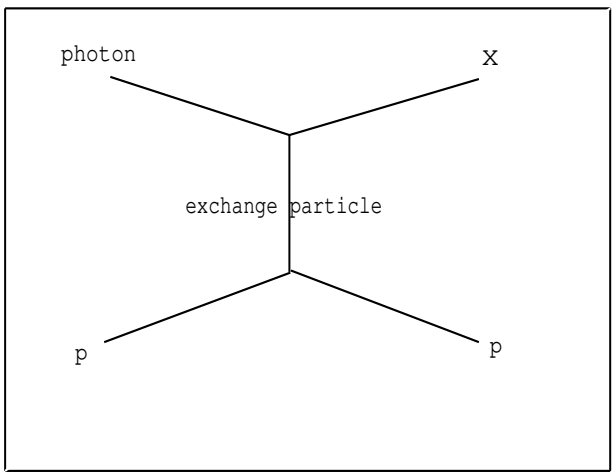

Figure 3.5: The process $\gamma p \to Xp$ proceeding via the exchange of a particle

PWA goals

The goal of the PWA is to extract information about the line shape of a resonance with mass m_X and to determine the production mechanism as well. This necessitates doing the PWA in fine bins in mass and $|t|$. Our criteria are to do the PWA in mass bins of 10 MeV/c^2, with roughly 10 equally populated bins in $|t|$. With the statistical sample expected after one year of running with 10^7 photons/sec, the statistical error in the central peak of an exotic meson for a given bin in $|t|$ will be of order 3%, assuming the exotic is produced with a probability of the order of 5% of conventional mesons.

It is important to stress here that the detector design focuses on hermeticity and resolution to insure nearly uniform coverage with well-understood acceptance functions for various decay angles. Kinematic fitting will also be used to identify exclusive processes. The design focuses on the requirements of the PWA. The existence of well established resonances will be used as benchmarks for the PWA. They also provide benchmarks for the phase variation of candidate exotic states. Furthermore, candidate exotics can appear with multiple decay modes which should give consistent results. As an example, a meson which decays into $\eta\pi$ should be observed in channels where $\eta \to \pi^+\pi^-\pi^0$, $\eta \to 3\pi^0$, and $\eta \to 2\gamma$. Each of these modes leads to different acceptances and systematics. This provides a powerful check on PWA results.

This is all nicely illustrated by the PWA performed by the E852 collabo-

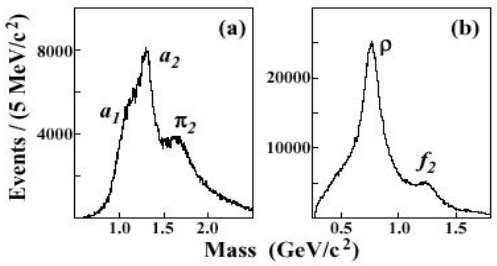

Figure 3.6: Acceptance corrected effective mass distributions for the (left) $\pi^+\pi^-\pi^-$ combination and (right) $\pi^+\pi^-$ combination (two entries per event) from E852 [11].

ration which reported the J^{PC} $\rho^0\pi^-$ exotic state [11] in the reaction $\pi^- p \to \pi^+\pi^-\pi^- p$ at a beam momentum of 18 GeV/c. In Figure 3.6, the acceptance-corrected (average acceptance was 25%) distributions of the $\pi^+\pi^-\pi^-$ and $\pi^+\pi^-$ effective masses are shown. The positions of well-established meson states are shown, even though the $a_1(1260)$, for example, does not show up prominently. The PWA assumes a parent decaying into a $\pi\pi$ state and an unpaired π followed by the decay of the $\pi\pi$ state. The resulting decomposition into various waves is shown in Figure 3.7. The decomposition now clearly shows the $\pi(1800)$ in the 0^{-+} wave, the $a_1(1260)$ in the 1^{++} wave, the $\pi_2(1670)$ in the 2^{-+} wave, and the $a_2(1320)$ in the 2^{++} wave. Evidence for the exotic 1^{-+} $\rho\pi$ is shown in Figure 3.8. Also shown in this figure is the effect of leakage of non-exotic waves. Finally in Figure 3.9 a coupled fit to the wave intensities and phase difference between the 1^{-+} and 2^{-+} waves is shown.

We point here that impressive as these data are, the statistics expected for HALL D will far exceed those of the E852 experiment and the detector will be far better designed and understood since the HALL D project is focused on optimizing the design for this sort of analysis.

A discussion of the PWA technique for specific processes within the context of the HALL D detector is included in the discussion of the apparatus and its design criteria.

Linear and circular polarization

We start with a review of the relationship between linear and circular polarization. A right-handed-circularly ($|R\rangle$) polarized photon has $m = 1$ while for a $|L\rangle$ photon $m = -1$. These are related to the linear polarization states, $|x\rangle$ (in production plane) and $|y\rangle$ (perpendicular to production plane) by:

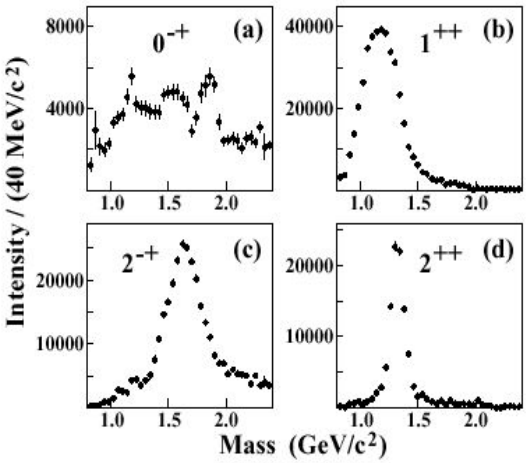

Figure 3.7: Combined intensities for all (a) 0^{-+} waves; (b) 1^{++} waves; (c) 2^{-+} waves; and 2^{++} waves from E852 [11].

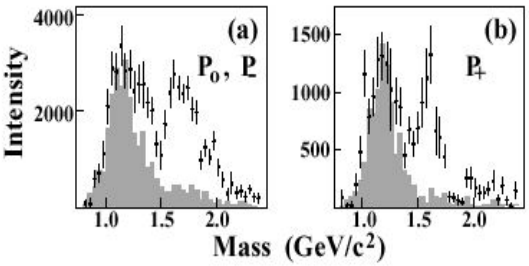

Figure 3.8: The intensities for the waves corresponding to 1^{-+} into $\rho\pi$. The shaded distributions are an estimate of leakage due to non-exotic waves – from E852 [11].

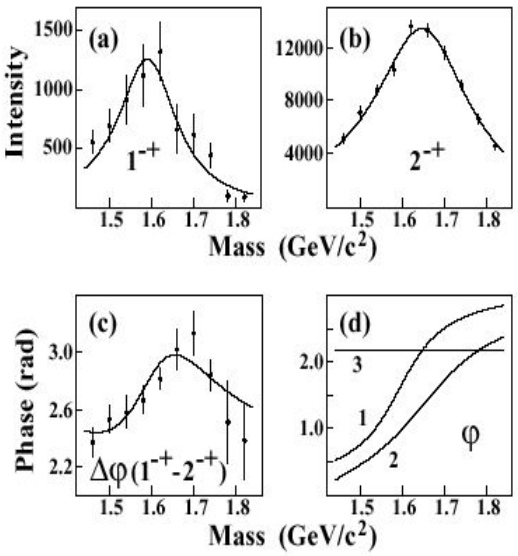

Figure 3.9: Results of a coupled mass-dependent Breit-Wigner fit of the 1^{-+} and 2^{-+} waves showing the phase difference as well – from E852 [11].

$$|x\rangle = \frac{1}{\sqrt{2}}\left(|R\rangle + |L\rangle\right) \tag{3.5}$$

$$|y\rangle = \frac{-i}{\sqrt{2}}\left(|R\rangle - |L\rangle\right) \tag{3.6}$$

We will use these relations in several straightforward cases to show how linear polarization:

1. can provide information on decays in lieu of statistics,

2. is essential in isolating production mechanisms, and

3. can be used as an exotics filter if the production mechanism is known.

Linear polarization and statistics

To illustrate how linear polarization provides useful information in the PWA, consider the case of the photoproduction of a vector meson which subsequently decays into two pseudoscalar mesons. Possible examples are $\rho \to \pi\pi$ or $\phi \to K\bar{K}$. Suppose the production mechanism produces the vector with the same

helicity as the incident photon (or *s-channel helicity conservation*). In the rest frame of the vector the two-pseudoscalar wave function is described by

$$Y_1^m(\theta, \phi) \propto \sin\theta \cdot e^{im\phi} \tag{3.7}$$

For circularly polarized photons (either $m = 1$ or $m = -1$) the square of this amplitude carries no ϕ information while for in-plane photons there is a $\cos^2\phi$ dependence and out-of-plane a $\sin^2\phi$ dependence in the decay angular distribution, since in these cases we have the sum or difference of Y_1^{+1} and Y_1^{-1} according to equations (3.5) and (3.6). Although not essential in determining spin, a gain of statistics is needed to recover a drop in the degree of linear polarization. Indeed our Monte Carlo simulation studies indicate that the increase in statistics is proportional to the decrease in polarization.

Linear polarization and production mechanism

This is best illustrated by considering a specific example. Suppose we produce a vector particle ($J^P = 1^-$) by the exchange of a scalar particle ($J^P = 0^+$ – natural parity exchange) or a pseudoscalar particle ($J^P = 0^-$ – unnatural parity exchange). We wish to determine whether the vector is produced by natural (amplitude A_N) or unnatural (amplitude A_U) parity exchange. In the center-or-mass of the vector particle, the momentum vectors of the beam photon and exchange particle are collinear. For circularly polarized photons, the m of the vector is the same as that of the photon. From parity conservation, the orbital angular momentum between the photon and exchange particle is $L = 0$ or $L = 2$ for natural parity exchange and $L = 1$ for unnatural parity exchange. So for circularly polarized photons, with $m = +1$, the total amplitude is $A_N + A_U$ whereas for $m = -1$, the total amplitude is $A_N - A_U$. This follows simply from the addition of angular momenta. Circularly polarized photons allow us to measure only the sum or difference of the two exchange amplitudes. If however, we have linearly polarized photons along the x-direction, we extract A_N using equation (3.5) and for polarization along the y-direction, we extract A_U using equation (3.6).

Linear polarization as an exotics filter

Using arguments similar to those above, it has been shown [33] that linear polarization can be used as a tool to filter exotics. For example, a $\rho\pi$ system with $I = 1$ has $C = +$. Suppose that one can determine the naturality of the exchange particle by selecting data within a range of $|t|$. For a produced $C = +$ particle with spin one we can have natural parity ($J^{PC} = 1^{-+}$ – exotic)

or unnatural parity ($J^{PC} = 1^{++}$ – non-exotic). In the case of natural parity exchange the in-plane polarization selects the $J^{PC} = 1^{-+}$ wave while out-of-plane polarization selects $J^{PC} = 1^{++}$. For unnatural parity exchange the reverse is true. Note that in this case, we are specifying the naturality of the exchange and using linear polarization to select the naturality of the produced particle. In the previous section, we specified the naturality of the produced particle and used linear polarization to select the naturality of the exchanged particle.

More detailed PWA studies are described in Chapter 10 of this Design Report which also discusses the interplay between statistics and polarization and the need for polarization to extract information on production mechanisms.

3.4 Theoretical considerations

3.4.1 Overview

Strongly-interacting QCD is the most poorly understood regime of the standard model. Whereas conventional perturbation theory can be applied to the physics of high energies, strong QCD is essentially nonperturbative, and the study of this field has required the use of models and the development of new theoretical techniques.

The crucial feature of QCD that dominates the physics of this regime is the phenomenon of confinement. This is a nonperturbative result of gluon self-interactions, which, for example, leads to an interquark potential that grows approximately linearly with distance. Confinement implies that the isolated states we see in the spectrum are color-singlet hadrons rather than individual quarks and gluons, and the masses, interactions and decays of hadrons are for the most part problems in nonperturbative quantum field theory.

The challenge of describing strong QCD has led to the development of LGT, which continues to see wide application in QCD and in many other field theory and condensed matter contexts. The presence of confinement in pure-glue QCD is easily observed in LGT. Similarly, the spectrum of low-lying $q\bar{q}$ mesons and qqq baryons in the stable-hadron "quenched" approximation is relatively easily determined, and after about two decades of improved statistics and computer capabilities the agreement is quite good. LGT is also the preferred theoretical method for investigating strong QCD at finite temperatures (which will be studied at RHIC) and the interplay between finite temperatures and chiral symmetry breaking.

LGT makes some rather dramatic predictions for the spectrum of states

that arise as a result of confinement. One prediction is that there should be a spectrum of glueballs, flavor-singlet states composed only of gluons. (An as yet unknown amount of configuration mixing with $q\bar{q}$ will take place in the physical states.) LGT methods are now sufficiently advanced for the predictions of the spectrum of glueballs to be rather precise. The lightest glueball is expected to be a scalar near 1.6 GeV/c^2, followed by a pseudoscalar and tensor at about 2.3 GeV/c^2, and many additional states at higher masses. There should also be a spectrum of quark-and-gluon hybrid states, which are more attractive experimentally because of their exotic quantum numbers. LGT has only very recently been applied to these states, and confirms that the lightest of these ($J^{PC} = 1^{-+}$ exotic) hybrid mesons should be found at about 2.0 GeV/c^2.

Theorists have also developed various models of these hadrons. In the conventional $q\bar{q}$ and qqq sectors, Coulomb plus linear potential models have proven to be the most useful. These give very good descriptions of the spectrum of conventional hadrons and their couplings and decays, and for $q\bar{q}$ and qqq are more accurate and of wider applicability than LGT. There are several models of hybrids, which we shall discuss subsequently. The flux tube model is the best known, and gives detailed predictions of the spectroscopy and decay modes of hybrids; the unusual decay modes predicted by this model have motivated several experimental studies of $f_1\pi$ and $b_1\pi$ channels in particular. In this proposal we favor a more conservative approach, and plan to search all accessible two body modes, in addition to those suggested by the flux tube model.

How can experiment improve our theoretical understanding of the physics of strong QCD? Determination of the spectrum of exotic states will be the most important new contribution; the LGT results assume stable hybrids, and this *may* lead to an important bias in mass predictions. Similarly, the various models of hybrids differ in the details of the spectrum of states, and identification of several exotics will be crucial in determining which model describes the physics of hybrids most accurately. Decay modes will also provide critical information on hybrid wave functions and dynamics.

The experimental determination of the exotic spectrum is already in progress. At present there are two candidate exotics, the $\pi_1(1400)$ and $\pi_1(1600)$; note that the reported masses are rather far from the LGT and flux-tube predictions of about 1.8-2.0 GeV/c^2. One pion exchange photoproduction (through $\rho\pi$) is a straightforward method for producing states with these quantum numbers, and since the $\pi_1(1600)$ was first reported in $\rho\pi$, photoproduction is an ideal way to search for this state.

Finally, to date there have been no LGT predictions of hybrid decay widths, although these are expected to be determined in future work. Hybrid decay

predictions have come exclusively from models, and the unusual branching fractions predicted by the models will require experimental measurements of branching fractions and relative amplitudes for comparison. Since LGT cannot easily treat decays or radial excitations, models will continue to be important in describing the physics of exotics.

Progress in understanding the gluonic degree of freedom in strong QCD should therefore follow from experimental studies of the conventional and exotic spectrum, improved LGT studies, and improved models of these states.

3.4.2 Strong QCD and the role of glue

Eliminating quark degrees of freedom in principle allows one to focus on gluon dynamics. To date, the main source of information about confinement are the phenomenology and lattice analyses of heavy (static) quark systems. However, the light quark systems are particularly useful for studies of strong QCD. The enormous success of the quark model indicates that after dynamical chiral symmetry breaking, the effective constituent quarks behave as heavy, nonrelativistic particles. Spectroscopy and data on the residual interactions of ordinary, and in particular light, gluonic mesons will therefore provide us with crucial information about the connection between the two main features of low energy QCD.

In this section we briefly summarize the current models of strong QCD. These models present very different concepts of the behavior of soft glue, and an extensive and high quality experimental effort will be needed to clarify this situation.

Flux tube model

The flux tube model is an explicit realization of the string picture of glue [21]. The model is based on the strong coupling expansion of the lattice QCD Hamiltonian. One works with the basis of gauge invariant states and organizes the strong coupling eigenstates into sectors of differing *topologies*. By assuming that the inter–sector couplings are weak, one is able to restrict considerations of the dynamics to the $q\bar{q}$ valence sector. The next step is to model the dynamics of the links as N point-like spinless *beads* of mass ba, where a is the lattice spacing. Finally, adiabatic and small oscillation approximations of the flux tube dynamics are made to arrive at an N–body discrete string–like model Hamiltonian for gluonic degrees of freedom. This is meant to be operative at intermediate scales $a \sim b^{-1/2}$ where the strong coupling is order unity.

It is widely believed that at large distances glue must behave as a sort of string, so that the model is probably reasonably accurate at large scales [34]. However, the authors have relied strongly on intuition to derive the final form of the string Hamiltonian and the efficacy of their approximations is largely unknown. Nevertheless, the validity of the adiabatic and small oscillation approximations has been checked in a simple (one-bead) version of the flux tube mode [12]. It was found that neither approximation is accurate; however, the errors tend to cancel and the final hybrid mass estimates do not shift a great deal. Light hybrids are found to have a mass of roughly 1.9 GeV/c^2.

Lattice gauge theory

At present, LGT offers the greatest hope for determining the low energy properties of QCD. In principle, LGT is an exact representation of the QCD path integral which employs a lattice regulator. This is achieved by explicitly writing the path integral on a discrete four dimensional space-time lattice. The path integral is then numerically evaluated using sophisticated Monte Carlo techniques.

Unfortunately, the lattice must be Euclidean to ensure the tractability of the numerical computations leading to problems with the definition of some quantities. Furthermore, it is very difficult to include all of the physical effects due to quarks and these are often truncated (the *quenched approximation*). Two prominent effects of this truncation are a distortion of the chiral nature of the theory and shifts in the properties of hadrons due to the neglect of coupled channel effects.

Very successful computations have been made in spite of these uncertainties. For example, the nucleon and delta masses are computed within 10% of their experimental values. Great strides in computational power and algorithm efficiency have been made in recent years. As a result reliable quenched low lying glueball masses are available. Estimates of the strengths of the scalar glueball decay modes have also been made. Finally, the masses of heavier hybrids have been determined and light hybrid masses are being calculated. Present estimates for light hybrid masses are 2.0 GeV/c^2 with an error of several hundred MeV [7]. There have also been measurements of several of the lowest lying adiabatic hybrid glue potentials [8], which are useful for heavy hybrid mass estimates and for comparison to analytic models.

Instanton models

An instanton is a specific topological vacuum gauge field configuration which is thought to dominate the QCD vacuum. They have since been widely employed to explain many properties of strong QCD. For example, instantons induce an effective interaction between quarks which may account for chiral symmetry breaking. Calculations of hadronic masses proceed in much the same way as with lattice gauge theory – the correlation function of interpolating fields is evaluated in the instanton vacuum ensemble and the leading behavior is extracted to obtain the mass. While technical problems remain in the application of these ideas to instanton physics, initial results for the scalar glueball are in approximate agreement with lattice calculations [35]. Light hybrid masses have also been estimated with a result of roughly 1.3 GeV/c^2.

Schwinger–Dyson models

The Schwinger–Dyson equations are a set of infinitely many coupled functional equations which are equivalent to the quantum field theory from which they were derived. They are of interest in modeling strong QCD because they may be truncated in a non-perturbative manner and because they are easy to organize in a way which provides information about bound states. In particular, one typically truncates the equations, assumes a confining form for the gluon propagator, solves the resulting gap equation for the quark propagator, and solves the Bethe-Salpeter equations for the properties of the bound state in question [36].

This approach has the benefits of being covariant, of being close to the underlying field theory, and of being capable of describing spontaneous chiral symmetry breaking. Many successful calculations of light hadron (in particular, pion) properties are extant. The methodology may also be easily extended to finite temperatures. Unfortunately, the Schwinger-Dyson program must be considered a model of QCD because of truncations and assumptions about the gluon propagator. Furthermore, it is technically difficult to obtain information on heavy states. Recently Schwinger-Dyson calculations of hybrid masses have appeared. The study employs a separable model for the nonperturbative gluon propagator which provides an algebraic relation between the quark and gluon propagators, the forms of which are fit to pion and kaon observables. A numerical solution of the Bethe-Salpeter equation with these propagators reproduces the pseudoscalar, vector and axialvector meson spectra to within 9% of accepted values and yields two exotic 1^{-+} mesons with masses of 1.44 and 1.50 GeV/c^2 [37].

Potential models

Potential models of hadrons date to the 1960's when they were introduced in an attempt to place Gell–Mann/Zweig's quark model on firm phenomenological ground. The introduction of QCD was crucial to providing the modern framework upon which modern quark potential models are built. These models are in large part non-relativistic or semi-relativistic and incorporate a phenomenological quark-quark interaction – usually with a linear confinement term, a short range one gluon exchange term, and perhaps terms reflecting meson loop effects (pion exchange terms). Potential models are well known for correlating vast amounts of hadronic data, from meson and baryon masses, to baryon magnetic moments, to radiative decays, to transition form factors.

Among the more severe flaws with potential models are their lack of covariance, their phenomenological character, and the lack of glue as a dynamical degree of freedom. The latter problem implies that potential models must be extended in order to describe hybrids. Several approaches have been taken in this regard. The earliest is due to Horn and Mandula [38] who postulated a massless gluon interacting with quarks via a linear potential. Other models assume massive gluons, incorporate glue-glue interactions, or abandon the idea of a glue-quark potential altogether.

Because these models rely heavily on a nonexistent phenomenology, there are relatively few predictions regarding hybrid properties. One group finds non-exotic light hybrids in the 1.3 – 1.8 GeV/c^2 range and 1.8 – 2.2 GeV/c^2 for light exotic hybrids [39]. A more recent calculation is based on a relativistic, many-body, Coulomb gauge, QCD-based model which generates an effective gluon mass by assuming a BCS–like QCD vacuum and solving the resulting gap equation. Linear confinement is assumed between color current densities which allows one to write and solve a relatively simple Salpeter equation [40]. This approach is in modest agreement with lattice results for heavy hybrids [8]. It has not yet been applied to light hybrids.

Bag models

The simplest bag models assume that colored partons are confined in a spatial region of varying (typically spherical) shape [41]. Calculating hadronic masses then becomes similar to calculating electromagnetic resonance modes in a cavity. A great advantage of this approach is that it may be formulated relativistically and hence the model is of particular use in providing qualitative information on such quantities as the nuclear equation of state. However, it does not appear to provide as consistent a picture of hadronic masses as,

for example, potential models. Bag models also suffer from parameter uncertainties and theoretical problems such as spurious center of mass degrees of freedom and gluon self energies.

Hybrid calculations typically place a noninteracting quark, antiquark, and gluon in the confining region. Spin splittings may be incorporated by allowing the quarks and gluons to interact perturbatively. Because of the problems developing a consistent picture of the low mass spectrum, most bag calculations date from the early 1980's; typical masses for light hybrids are in the 1.3 – 1.8 GeV/c^2 range [42, 43, 44, 45]. More recent calculations have used the adiabatic bag model of Ref. [46] to calculate gluonic potential surfaces in heavy hybrids [47], with quite good results.

QCD sum rules

QCD sum rules are an analytical method for determining nonperturbative properties of QCD. The formalism involves equating the perturbative expression for a correlation function (say) to a spectral representation of the same function [48]. Nonperturbative information on the perturbative side of the equation is contained in unknown condensates. One may obtain the condensates by equating to well known spectra. These may then be used to predict spectral properties in other channels, such as hybrid masses and couplings. Unfortunately, this approach is not robust and a consensus on hybrid masses has not been achieved. Estimates for lightest hybrid masses are in the 2.1 – 2.5 GeV/c^2 region [49, 50, 51], however, older results and one current group [52] predict a light hybrid mass of roughly 1.5 GeV/c^2.

3.4.3 Phenomenology

With a few exceptions, such as spin splitting of quarkonia and the phenomenology of strong two body decays, we have had to rely on lattice calculations to provide information on confinement. Most notable are LGT predictions for hybrid masses [7, 8, 23, 53, 54], convergence in the low lying glueball spectrum [13, 14, 15, 16], and the calculation of the potential surfaces for excited glue configurations with static quarks[8]. The latter is especially useful for comparison with model predictions. For example it has recently been compared to the bag model [55], the flux tube model [34], Nambu-Goto inspired models [56], and to a relativistic constituent glue model[40].

Several interesting features have emerged. Although it is believed that glue must behave in a string-like fashion at large quark separation, this behavior is not being seen on the lattice. There are now indications that it may be

occurring at very large distances[34]. Alternatively, constituent models have been shown to either contain the wrong degrees of freedom (and so are unable to describe all of the possible gluonic excitations seen on the lattice) or to approach the linear confining regime too quickly[40]. The latter is interesting because it implies that more degrees of freedom than a single constituent gluon are required to describe hybrids at moderate to large interquark separation.

Although the lattice is useful for obtaining static information about hadrons, it is very difficult to calculate hadronic decays or interactions numerically. Thus the experimental explication of this important area of hadronic physics is crucial. At present there are very few models of hybrid decays. These comprise older perturbative gluon-based models[57, 58, 59], the well-known flux tube decay model[20, 22], and a new flux tube-based decay model[60, 61]. The importance of understanding this aspect of hybrids cannot be overstated. For example, simply detecting hybrids will be difficult without some guidance as to how they decay. We stress that models of hybrid decays are built upon assumptions of hybrid structure and decay mechanisms. As an example of this point we note that in the flux tube model, vector hybrids contain quarks in a spin singlet. In constituent models, however, the quarks may be in a spin triplet. This simple difference in structure may lead to large differences in the decay characteristics of vector hybrids because it is widely held that states with quarks in a singlet cannot decay to mesons which also have their quarks in spin singlets.

Although the prospects of constructing a reliable model of hybrid decay seems daunting without extensive input from experiment, an interesting phenomenon has been observed in all hybrid decay models considered to date: hybrids couple weakly to identical S-wave mesons[1]. Thus for example a hybrid with the quantum numbers of the ρ will not decay to $\pi\pi$ and only weakly to $\omega\pi$ but strongly to πa_1. This expectation can be used to distinguish hybrids from the conventional spectrum. Even though the hierarchy of hybrid decays have been found to be rather insensitive to the details of the underlying dynamics, as illustrated in Table 3.2, if there is more than one wave present in a given decay mode the relative strengths are highly sensitive probes of hybrid structure. It is apparent that a detailed partial wave analysis will be crucial in discriminating between models of hybrids.

[1]The model of Ref.[60] generalizes this: hybrids couple weakly to all pairs of identical mesons.

Decay Mode	Flux–tube [61]		Constituent Glue		QCD sum rules		
	PSS	IKP	[62]	[57]	[63]	[64]	[65]
$b_1\pi$	24	59	144	3			
$f_1\pi$	5	14		0	100 ± 50		
$\rho\pi$	9	8	36	2	40 ± 20 †	274	600
K^*K	1	0		2		8	300
$\eta^{'}\pi$	0	0		28		3	3
$\eta(1295)\pi$	2	1					
$\eta\pi$	0	0		44			0

Table 3.2: Predicted partial widths (in all partial waves) of the 1^{-+} exotic hybrid in MeV. The hybrid mass is 1.6 GeV/c^2 [61, 57, 63, 65], 1.5 GeV/c^2 [64] or 1.4 GeV/c^2 [62]. $\rho\omega$ and $f_2\pi$ is 0 MeV/c^2 [61]. The D– to S–wave width ratio of $b_1\pi$ and $f_1\pi$ is much smaller in the PSS than in the IKP model [61]. Other constituent gluon models quote ratios of widths [66]. † $10 - 100$ [51].

3.4.4 Conventional light quark mesons - theory

The conventional $q\bar{q}$ light meson spectrum is reasonably well understood theoretically up to masses of about 1.5 GeV/c^2. Electromagnetic transitions, which are clearly relevant to studies of photoproduction, are known for many of the light S-wave mesons and for several P-wave states, and are in good agreement with simple electric and magnetic dipole transition rate formulas. Strong decays are much less well understood, indeed the mechanism of strong decays is one of the most important open questions in the field of conventional light hadron spectroscopy. There is a phenomenological model of light hadron decays, known as the $^3\mathrm{P}_0$ model, which assumes that decays take place through pair production of a $q\bar{q}$ pair from the vacuum, with $S = 1$, $L = 1$, $J = 0$ (hence $J^{PC} = 0^{++}$) quantum numbers. Other decay models are generally simple modifications of the spatial strength of pair production that do not change this basic decay mechanism. Although the relationship between this phenomenological decay model and the quark-gluon and gluon-gluon interactions of QCD has not been established, the model can be related to QCD for nonrelativistic quark pair production in the strong coupling limit [67].

This $^3\mathrm{P}_0$ decay model is especially useful in searches for exotica because it gives reasonably accurate predictions for partial widths and relative decay amplitudes of well established $q\bar{q}$ states. An accurate description of decay amplitudes of conventional $q\bar{q}$ mesons is important because we expect that the anomalous strong decay amplitudes of non-exotic glueballs and hybrids will

distinguish them from non-exotic $q\bar{q}$ states with identical quantum numbers and similar masses. Indeed, strong decay amplitudes and quantum numbers may be the only experimental information we will have for most higher-mass meson resonances.

The spectrum of conventional light $q\bar{q}$ resonances is discussed in detail by Godfrey and Isgur [68] in the most cited and most successful work on meson spectroscopy, which uses a relativised Coulomb-plus-linear potential model. One should note however that there are recent experimental indications that their model has overestimated the masses of radial excitations [69], so an updated theoretical study of higher-mass states may be required. Mukhopadhyay [70, 71] has also given detailed predictions of $q\bar{q}$ spectroscopy, and more recent addenda regarding decays of $s\bar{s}$ states have been given by Godfrey *et al.* [72, 73]. An exhaustive calculation of all allowed quasi-two-body strong decay amplitudes in the $^3\mathrm{P}_0$ model for all $n\bar{n}$ mesons ($n = u$ or d quarks) expected up to 2.1 GeV/c^2 has been published recently by Barnes, Close, Page and Swanson [74]. These theoretical results should suffice to distinguish between plausibly $q\bar{q}$ and non-$q\bar{q}$ mesons in the mass regime of greatest current interest, provided that the $^3\mathrm{P}_0$ model remains accurate for these higher-mass states.

3.4.5 Hybrids - theory

The area of greatest interest in recent studies of meson spectroscopy has been the subject of hybrids. Hybrids are formally defined as mesons that have both $q\bar{q}$ and glue in their dominant *valence* basis state; clearly this is a working definition, and complications such as large levels of $q\bar{q} \leftrightarrow q\bar{q}g$ mixing in physical resonances might require a more careful classification. One can at least be confident that there will be more states than expected by the naive quark model, since the presence of both $q\bar{q}$ and $q\bar{q}g$ basis states will lead to more physical resonances than would follow given only $q\bar{q}$ basis states. As with glueballs, confirmation of this "overpopulation" of the spectrum is one of the strategies used in searching for hybrids.

There is a much more striking signature for hybrids, (which is a principal reason they are so attractive experimentally), in that they can have exotic quantum numbers (forbidden to $q\bar{q}$). The discovery of a resonance with exotic J^{PC} would be convincing evidence of a non–$q\bar{q}$ meson. The search for exotic hybrids is the most exciting topic in modern meson spectroscopy as no such states have been universally accepted as confirmed, although there are now two candidates. The $J^{PC} = 1^{-+}$ channel, especially $I = 1$, is of greatest current interest since this is expected theoretically to contain one of lightest and most stable of the light–quark hybrids.

Theorists have given detailed predictions of the spectrum of hybrids and their strong couplings. Many techniques have been used in these calculations, beginning with the bag model and constituent gluon models, and continuing with QCD sum rules and the flux tube model. Common conclusions of these studies were that there should be a relatively light $J^{PC} = 1^{-+}$ exotic in the lowest multiplet (where determined), with a mass in the 1.5 to 2.0 GeV/c^2 region. These estimates have been improved recently by lattice gauge theory, which presumably lacks most of the systematic uncertainty of the models. Recent LGT calculations [7, 75] find that the $J^{PC} = 1^{-+}$ is indeed the lightest hybrid exotic, with a mass close to 2.0 GeV/c^2. Although this appears to vindicate the flux tube model of Isgur, Kokoski and Paton [20], which estimated the mass of the $J^{PC} = 1^{-+}$ exotic to be 1.9 GeV/c^2, one should note that the $J^{PC} = 0^{+-}$ exotic which the flux tube predicts to be degenerate with 1^{-+}, is found by the MILC LGT collaboration to be about 0.7 GeV/c^2 higher in mass! Evidently we still have much to learn about the spectrum of hybrids.

Calculations of strong decay modes of hybrids are of great interest, since these should help us to distinguish between non-exotic hybrids and quarkonia, and also because they may indicate which hybrids are most accessible in photoproduction (for example those with large $\rho^o\pi$ couplings). The more recent decay calculations have relied exclusively on the flux tube model, which may or may not be accurate for these novel states. The first detailed study of hybrid decays in the flux tube model was that of Isgur, Paton and Kokoski [20], who found the now famous hybrid selection rule that the lightest hybrids should decay dominantly to S+P meson pairs rather than the simpler S+S modes. This implies for example that a search for an $I = 1$ $J^{PC} = 1^{-+}$ hybrid should concentrate on unfamiliar quasi-two-body modes such as $\pi f_1(1285)$ and $\pi b_1(1235)$ rather than the more easily accessible $\pi\eta$ and $\pi\rho$. This paper found that the total widths of several hybrids should be relatively narrow ($\Gamma_{tot} \approx$ 150 MeV/c^2, notably including the $I = 1$ $J^{PC} = 1^{-+}$.

The Isgur *et al.* reference considered only the exotic hybrids, whereas the flux tube predicts 5 non-exotic J^{PC} nonets, 0^{-+}, 1^{+-}, 1^{++}, 1^{--} and 2^{-+}, at the same mass as the 3 exotics 0^{+-}, 1^{-+} and 2^{+-}. With this many states, overpopulation could be apparent if any of the non-exotic hybrids is narrow. The calculation of decays of these non-exotic hybrids in the flux tube model was carried out by Close and Page [22], who found that several of these hybrids are indeed predicted to be quite narrow. Especially attractive non-exotic hybrids are relatively narrow 2^{-+} states in both $I = 0$ and $I = 1$, and a remarkably narrow $I = 0$ 1^{--} state, with a total width of 100 MeV/c^2. Close and Page anticipate that the dominant mode of the $I = 1$ 2^{+-} exotic should be $a_2\pi$; a comparative study of photoproduction of the $a_2^{\pm}\pi^{\mp}$ and $a_2^o\pi^o$ channels should

especially interesting, since production by exchange of different C-parities in t-channel can be separated in this manner. Finally, perturbative QCD signatures of hybrids have been theoretically investigated by Carlson and Mukhopadhyay [76].

3.4.6 Glueballs - theory

There has been tremendous interest in finding glueballs, as they are conceptually the furthest removed from the conventional $q\bar{q}$ of all the mesons expected in QCD. Although many anticipated properties of glueballs may be strongly model dependent, there are reliable LGT predictions [13, 14, 15, 16] of a lightest scalar glueball mass of 1.5 to 1.7 GeV/c^2. The next glueballs found above this scalar in LGT studies are 0^{-+} and 2^{++}, both expected at a mass of about 2.2 to 2.3 GeV/c^2, with all other J^{PC} found at higher masses.

Since these lighter glueballs are non-exotic, one can hope to identify them through *overpopulation*, as anomalous extra states in the background of conventional $I = 0$ $q\bar{q}$ mesons. Here we are unfortunate, since $I = 0$ 0^{++} is probably the most obscure sector in the entire light meson spectrum, with broad states $f_0(1300)$ and $f_0(1700)$, the narrow $K\bar{K}$ candidate $f_0(980)$, and the relatively narrow CERN glueball candidate $f_0(1500)$. Conventional $I = 0$ $n\bar{n}$ and $s\bar{s}$ states are expected at about 1.3 and 1.5 GeV/c^2 in the quark model; these are likely to be rather broad, although the $^3P_0$ model predictions for their width are quite sensitive to their radial wave functions.

Several experiments at the LEAR $p\bar{p}$ facility at CERN have found the rather narrow $f_0(1500)$ scalar [77, 78], with a total width of 112 ± 10 MeV/c^2; this has been widely cited as a scalar glueball candidate. There are complications with this identification, however. The reduced decay couplings to pseudoscalar pairs do not follow the naive 3:4:1 $\pi\pi$:$K\bar{K}$:$\eta\eta$ ratio expected for a flavor singlet, instead the $K\bar{K}$ mode appears quite weak. Recent LGT studies of the $\mid k \mid$ dependence of glueball–Ps–Ps couplings finds the opposite result [15], that heavier mesons should be produced preferentially from scalar glueball decay, and for this reason the $f_0(1700)$ might instead be the scalar glueball. In either case these are rather narrow states, so one might also hope to find the 0^{-+} and 2^{++} glueballs as unusually narrow states. Of course the spectrum around 2.2 and 2.3 GeV/c^2 is poorly known, so this cannot be investigated without higher statistics high–mass data.

3.4.7 Multiquark systems - theory

The best known *multiquarks* are nuclei, which are weakly bound associations of largely unmodified color-singlet nucleons. Similarly we know of many examples of hypernuclei, in which a nucleon has been replaced by a Λ, and the famous $\Lambda(1405)$ appears plausible as a weakly bound $\bar{K} - N$ meson-baryon nucleus. The $f_0(980)$ and $a_0(980)$ are likely cases of weakly bound meson pairs, and if so are our first examples of mesonic nuclei. There are many arguments in favor of this interpretation (see Weinstein and Isgur [79, 80]), most obviously that they are just below $K\bar{K}$ threshold, have S-wave $K\bar{K}$ quantum numbers, are 0.2 to 0.3 GeV/c^2 lighter than expectations for 0^{++} nnbar states, and are very narrow compared to expectations for scalar quarkonia at this mass.

Although the $f_0(980)$ and $a_0(980)$ can be explained as dominantly $K\bar{K}$ molecules, earlier predictions of four-quark states with these quantum numbers at light masses has resulted in persistent speculations that these might actually be $q^2\bar{q}^2$ clusters, once known as *baryonia* [81, 82]. These issues can be tested through photoproduction of an initial $\phi(1020)$ and a measurement of radiative transition rates. Preliminary experimental results from Novosibirsk [83] are closer to the theoretical $q^2\bar{q}^2$ branching fraction, although they may include important non- $f_0(980)/a_0(980)$ backgrounds.

There is likely to be a rich spectrum of meson-meson molecules in other sectors, such as vector-vector, so confirmation (or disproof) of the $K\bar{K}$ molecule hypothesis would be a very important step in the study of multiquark systems.

3.4.8 $s\bar{s}$ states - theory

The quark model describes conventional light mesons as bound states of quarks and antiquarks, interacting through perturbative gluon exchange at short distance and a nonperturbative confining interaction at large distances. Four "flavor" types are distinguished according to the type of quark and antiquark in the meson; in the light $q\bar{q}$ mesons we can have any of the three light quarks u, d, s and their antiquarks. If both q and $\bar{q}$ are of u, d type we have a "nonstrange meson", which we refer to generically as $n\bar{n}$. With one chosen from $n = u, d$ and the other s, we have an $n\bar{s}$ or $s\bar{n}$ "kaonic state". The remaining possibility, $s\bar{s}$, is called "strangeonium".

The nonstrange $n\bar{n}$ mesons are fairly well established experimentally at lower masses, *albeit* with notable exceptions such as the scalar states. Taking 2.2 GeV/c^2 as a current frontier of light meson spectroscopy, the quark model anticipates 44 $n\bar{n}$ states up to this mass. (These are the 1S, 2S, 3S, 1P, 2P, 1D, 1F = 22 J^{PC} levels, with a doubling for $I = 0$ and $I = 1$.) About half these

mesons have been identified experimentally. Similarly we anticipate 22 kaonic J^{PC} levels ($n\bar{s}$ and $s\bar{n}$), and about 2/3 of these are known. In comparison the $s\bar{s}$ "strangeonium" states are a *terra incognita*; we consider only 5 $s\bar{s}$ states to be well established. These are the $\eta(547)$ and $\eta'(958)$ (counted as one $s\bar{s}$ state), $\phi(1019)$ $f_2'(1525)$, $\phi(1680)$ and the $\phi_3(1854)$. Other more controversial possibilities are $\eta(1295)$, $h_1'(1380)$, $f_1(1420)$ and $\eta(1440)$.

Although sectors such as 2^{++} clearly have almost flavor pure $n\bar{n}$ and $s\bar{s}$ resonances, there are counterexamples such as the famous $\eta - \eta'$ mixing and perhaps evidence for strong $n\bar{n} - s\bar{s}$ mixing in the scalar sector, which has complicated the identification of the scalar glueball. This *Zweig rule violation* is another interesting and poorly understood aspect of QCD, and an experimental search for $s\bar{s}$ states should clarify the level of Zweig violation in other J^{PC} sectors. The various flavor mixing angles could be established experimentally by comparing branching fractions of nominally $n\bar{n}$ and $s\bar{s}$ partners to $(n\bar{n})(n\bar{n})$ $(s\bar{n})(n\bar{s})$ and $(s\bar{s})(s\bar{s})$ final states, for example $\pi\pi$, $K\bar{K}$, $\eta\eta$ and $\eta\eta'$.

Photoproduction is an excellent technique for producing $s\bar{s}$ mesons, because the incident photon is in effect a vector meson beam with a large ϕ-meson component. Much of the photon–hadron interaction takes place through vector dominance, in which the incident photon becomes a vector meson. The relative probability of interacting through the different light meson types ρ°:ω:ϕ is 9:1:2 according to the quark model, and this relative coupling strength is approximately confirmed by the diffractive cross sections for vector meson photoproduction. (There is an additional suppression of the $s\bar{s}$ cross section by about a factor of two that is not well understood.) Thus in photoproduction we have the opportunity to produce mesons with vector meson beams of all diagonal light flavors $u\bar{u}$, $d\bar{d}$ and $s\bar{s}$, with a known relative luminosity between the flavors. In addition to diffractive photoproduction, which produces C=$(-)$ states, other mechanisms such as t–channel vector exchange may lead to significant photoproduction of C=$(+)$ $s\bar{s}$ states. In contrast, hadronic production of $s\bar{s}$ states is suppressed because the initial hadrons provide at most one strange valence quark (for example in KN experiments such as LASS).

The $s\bar{s}$ sector is also attractive because some decay modes should be very *clean*. These include channels such as $\phi\eta$, $\phi\eta'$ and $\phi\phi$, which according to the Zweig rule should only arise from $s\bar{s}$ initial states. One may also study channels such as $\phi\pi$, which are *not* expected as decays of $q\bar{q}$ states. One might find evidence for molecular states or Zweig–rule violation in this channel. Observation of both the $n\bar{n}$ and $s\bar{s}$ partners of a flavor nonet would be useful for establishing the $q\bar{q}$ (and $q\bar{q}g$ hybrid) spectrum, since the relative photoproduction amplitudes can be estimated. This would distinguish a $q\bar{q}$ or hybrid flavor nonet from a meson–meson molecule or a glueball, as molecules and glueballs

do not span nonets.

The total widths of $s\bar{s}$ states are predicted on average to be comparable to the widths of $n\bar{n}$ states. Detailed calculations in the $^3P_0$ model [84, 85] do however find some rather narrow states. Four of the $s\bar{s}$ states anticipated in the 1.6-2.2 GeV/c^2 region are predicted to have widths in the 100-200 GeV/c^2 range. These are the $^3D_3$ $\phi_3(1854)$ (predicted total width 104 MeV/c^2, observed $\approx$ 90 MeV/c^2), the $^3D_2$ (predicted 214 MeV/c^2), the $^1D_2$ $\eta_2(1850)$ (predicted 129 MeV/c^2) and the $^3F_4$ $f_4(2200)$ (predicted 154 MeV/c^2, possibly observed by LASS [86] with a total width of roughly 100 MeV/c^2. Since the $\rho_3(1690)$ has been reported in diffractive photoproduction, the $\phi_3(1850)$ should also be observed, with a known cross section. Comparison of photoproduction amplitudes of the various ϕ_J states will be interesting as a test of the quantum number dependence of the photoproduction mechanism. It might also be produced through $\phi\eta$ collisions in η exchange (a strong coupling to $\phi\eta$ is predicted), and could be observed in the $\phi\eta$ final state. Studies of these narrower states, especially the as yet unknown levels, will be useful as tests of our decay models, photoproduction mechanisms, and mixing with non-$s\bar{s}$ components.

The vector sector provides an example of the paucity of information on $s\bar{s}$ spectroscopy. As in the $n\bar{n}$ case one expects both $L = 0$ and $L = 2$ vectors, a 2^3S_1 and a $^3D_1$. In the $I = 1$ $n\bar{n}$ sector there has been progress recently in separating these states [87, 88]. Experimentally there are somewhat overlapping $\rho(1450)$ and $\rho(1700)$ states, which both appear to be present in diffractive photoproduction. Usually the 1450 state is assumed to be 2^3S_1 and the 1700 is $^3D_1$, since the nonrelativistic quark model anticipates approximately this mass splitting between spectroscopically pure $n\bar{n}$ levels. The $^3P_0$ decay model predicts that these states should have very different couplings to the S+P modes πh_1 and πa_1; these should couple very strongly to $^3D_1$ but quite weakly to 2^3S_1. A recent study of 4π modes by the Crystal Barrel has confirmed this result. In the $s\bar{s}$ sector only one higher-mass vector state has been reported, the $\phi(1680)$. This is seen in e^+e^- annihilation and in photoproduction, and apparently decays to KK but dominantly to K^*K. Can one similarly confirm that this state is the 2^3S_1 level as the mass suggests? If so, should the unknown higher-mass $^3D_1$ be observable in any particular final states? The experimental situation is summarized in Table 3.4.8 ; it is consistent with the 2^3S_1 $\phi(1680)$ identification, but only qualitative information on branching fractions is available, and the crucial $K_1(1273)K$ mode has not been investigated. Both states should appear in the clean $\phi\eta$ mode, but again this has not been studied. Thus we have the beginnings of $s\bar{s}$ spectroscopy, but quantitative studies of interesting and characteristic modes such as $\phi\eta$ and the "$s\bar{s}$ workhorse" modes KK,

	KK	K^*K	K^*K^*	$K_1(1273)K$	$\phi\eta$
expt.(1680 region)	seen	dominant	-	-	-
theor. 2^3S_1(1680 assumed)	89	245	0	0	44
theor. $^3D_1$(1850 assumed)	65	75	5	465	29

Table 3.3: Predicted and observed partial widths (in MeV/c^2) of the two 1^{--} $s\bar{s}$ states $2^3S_1(1680)$ and $^3D_1(1850)$.

K^*K, K^*K^* and K_1K simply have not been carried out. We may find many surprises in the $s\bar{s}$ sector, especially as regards mixing with non-$s\bar{s}$ states.

If these $s\bar{s}$ states were expected to be simple copies of the $n\bar{n}$ states, with a mass higher by approximately 250 MeV/c^2, establishing the $s\bar{s}$ spectrum might be considered a mundane exercise. However even the lightest $s\bar{s}$ system, the η and η', show a remarkable and poorly understood strong mixing with $n\bar{n}$; the physical states are close to the maximally mixed $(|n\bar{n}\rangle \pm |s\bar{s}\rangle)/\sqrt{2}$ combinations. This is due to a large $q\bar{q}$ annihilation amplitude in the 0^{-+} channel, which has been attributed to various perturbative and nonperturbative QCD mechanisms but has never been convincingly explained. This large mixing is presumably due to annihilation through the gluonic sector, but why 0^{-+} shows such a large annihilation amplitude, whereas others such as vector and tensor are relatively unmixed, remains a mystery. The discovery of the CERN glueball candidate has added more information to this puzzle [14, 15, 89, 90, 91, 17, 18]. The observed decays of the $f_0(1500)$ are far from the flavor–symmetric pattern of $\pi\pi : KK : \eta\eta : \eta\eta' = 3 : 4 : 1 : 0$ (for branching fraction divided by phase space) that one would expect from a simple model of glueball decay, and instead strongly favor $\pi\pi$. This may be due to an intrinsic quark mass dependence of these couplings (as suggested by the LGT results of Weingarten et al), or (as suggested by Close and Amsler) it may be due to a large $n\bar{n} \leftrightarrow G \leftrightarrow s\bar{s}$ mixing similar to the $n\bar{n} \leftrightarrow s\bar{s}$ mixing in the η–η' system. While all J^{PC} channels will provide important information regarding $n\bar{n} \leftrightarrow s\bar{s}$ mixing, the most likely *a priori* to show a significant effect are the radial pseudoscalars (perhaps the $\eta(1295)$ and the $\eta(1440)$) and the 2^{-+} pseudotensors). The 2^{-+} states are interesting because some models predict this to be one of the lighter glueball channels In addition, there are η_2 states at about 1.65 and 1.87 GeV/c^2 (reported by Crystal Barrel [92]), both of which couple strongly to modes forbidden to decay into $s\bar{s}$ by the Zweig rule.

Chapter 4

Photon Beam

One of the unique opportunities presented by a CEBAF upgrade to energies of 12 GeV and beyond is the possibility of generating high-intensity c.w. photon beams for high-energy photoproduction experiments. In this regime, photon beams represent an interesting extension to the meson spectroscopy program that has been actively pursued using beams of pseudoscalar mesons at hadron accelerator laboratories: with high energy photons one has essentially a beam of *vector* mesons. It is difficult, in fact, to conceive of any other way to obtain such a vector beam.

The requirements for photon beam energy and polarization were described in Chapter 3. This chapter describes a design for a real photon facility that meets these requirements. Starting with a beam of monochromatic electrons, it provides an intense beam of high-energy photons with an energy spectrum that is dominated by a single peak. A significant fraction of the total power in the beam is concentrated inside this peak, which has a width of less than 10% f.w.h.m. At a fixed electron beam energy E_0, the peak energy of the photon beam can be varied anywhere up to 90% E_0 simply by rotating a crystal. The photon spectrum inside the intensity peak has a large degree of linear polarization. The precise energy of an individual photon inside the peak is determined ("tagged") from the momentum of the recoil electron measured in a dedicated "tagging" spectrometer. The design is formed around the expected parameters for the CEBAF beam following the energy upgrade to 12 GeV, although nothing prevents its operation at lower energies before the time that 12 GeV beams are available.

This chapter begins with a survey of the techniques for producing high-energy photons that were considered in the development of this design, and the reasons for the choice of coherent bremsstrahlung. The coherent bremsstrahlung source is then described in greater detail, followed by a discussion of the re-

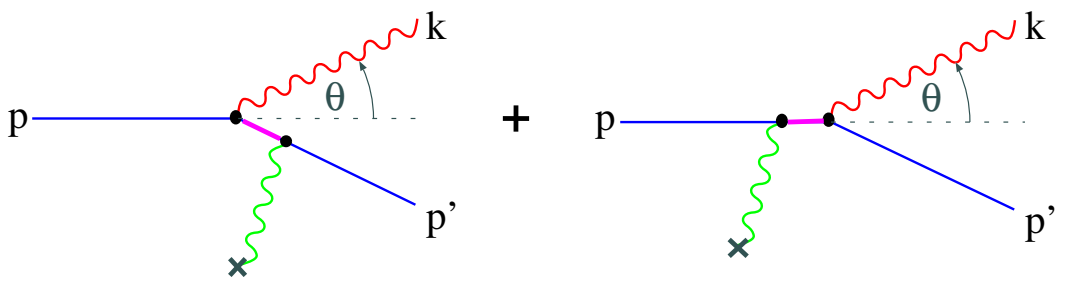

Figure 4.1: Generic diagrams for hard photon production from a high energy electron beam. The symbol × represents either a static charge distribution, in the case of virtual photons in the initial state (i.e. bremsstrahlung), or an optical cavity, in the case of real photons in the initial state (i.e. Compton scattering).

quirements that the design places on the electron beam that feeds the source. The tagging spectrometer design is described next, and the chapter concludes with a discussion of the considerations that govern the choice of beam intensity for particular measurements.

4.1 Choice of technique

Two basic methods have been considered for producing photons of the highest possible energy, flux and polarization from electrons of 12 GeV. The methods are bremsstrahlung and Compton scattering of light. Both are well-established methods of producing photon beams. Both techniques are actually described by the same Feynman diagrams, shown in Fig. 4.1. In the case of Compton scattering the incoming photon is real, whereas it is virtual for the case of bremsstrahlung.

Each of these techniques has its own limitations and advantages. In order to be suitable for HALL D, the photon source must be capable of producing photons of energy at least 80% E_0. The photon beam should have linear polarization. The energy resolution for individual photons in the beam should be as good as possible, *i.e.* on the order of the energy spread of the electron beam itself. It should be capable of producing fluxes up to 10^8/s. The contamination of the beam with photons outside the desired energy band should be as low as possible. It is also important that the source should be reliable and require a minimum of down-time for maintenance. The suitability of each approach is discussed below in the light of these criteria.

4.1.1 Compton back-scatter

A Compton source begins with a beam of visible or ultraviolet light, typically from a laser that is aligned to intersect the incident electron beam at close to 180°. Some of the photons undergo Compton scattering with the beam electrons. In the lab frame, the scattered photons come out in a narrow cone about the incident electron direction and carry a significant fraction of the electron energy.

The basic design of the Compton back-scatter source for this study was put forward by C. Keppel and R. Ent [93]. The design entails the use of a four-mirror high-gain cavity pumped by a 10kW argon-ion laser putting out $2\,ps$ pulses at a frequency of $100\,MHz$. The pulses in the cavity are synchronized so that the light pulses intercept an electron bucket each time they pass through the beam. The total length of the cavity is $2\,m$ with a crossing angle of 1°. Both cavity and electron beam are focused to a tiny spot of 10 μm r.m.s. radius at the crossing point. A small spot size is necessary in order to get as high a scattering rate as possible. The gain of the cavity is 10^4, which is conservative in view of recent advances in mirror technology. The wavelength of the light is $514\,nm$. The rate spectrum of the back-scattered beam from this source is shown in Fig 4.2a for a 1μA electron beam at 12 GeV.

From the point of view of flux, this source is marginal. With a few μA of beam and mirror improvements, it might produce 10^8 photons/s in the upper 1/3 of its energy spectrum. However, its maximum photon energy of 3.7 GeV is far short of the 80% E_0 needed for HALL D. To remedy this one must decrease the wavelength of the laser beam. This can be done by the use of a frequency-doubling crystal that absorbs the green light from the laser and produces ultraviolet light at $257\,nm$. Storing this light in a cavity of similar design to that described above yields the back-scatter rate spectrum shown in Fig. 4.2b. The major reason for the drop in rate is the decrease in the cavity gain from 10000 to 250. This is imposed by the diminished reflectivities of mirrors in the UV. Other factors are the inefficiency of the doubling crystal, a factor of two in rate from the doubling itself, and the decreasing Compton cross section with energy. The maximum photon energy is still under 50% E_0 and the flux is three orders of magnitude below the desired rate.

In order to reach photon energies of 80% E_0, initial photons of 20 eV are needed. The brightest sources of these would be a synchrotron light source or a free electron laser (FEL). Mirrors that operate at these wavelengths typically have reflectivities around 70%. With these one could conceive of a scheme that uses a wiggler to extract energy from the 12 GeV beam before it enters the dump. This light would have the same time structure as incident beam, and

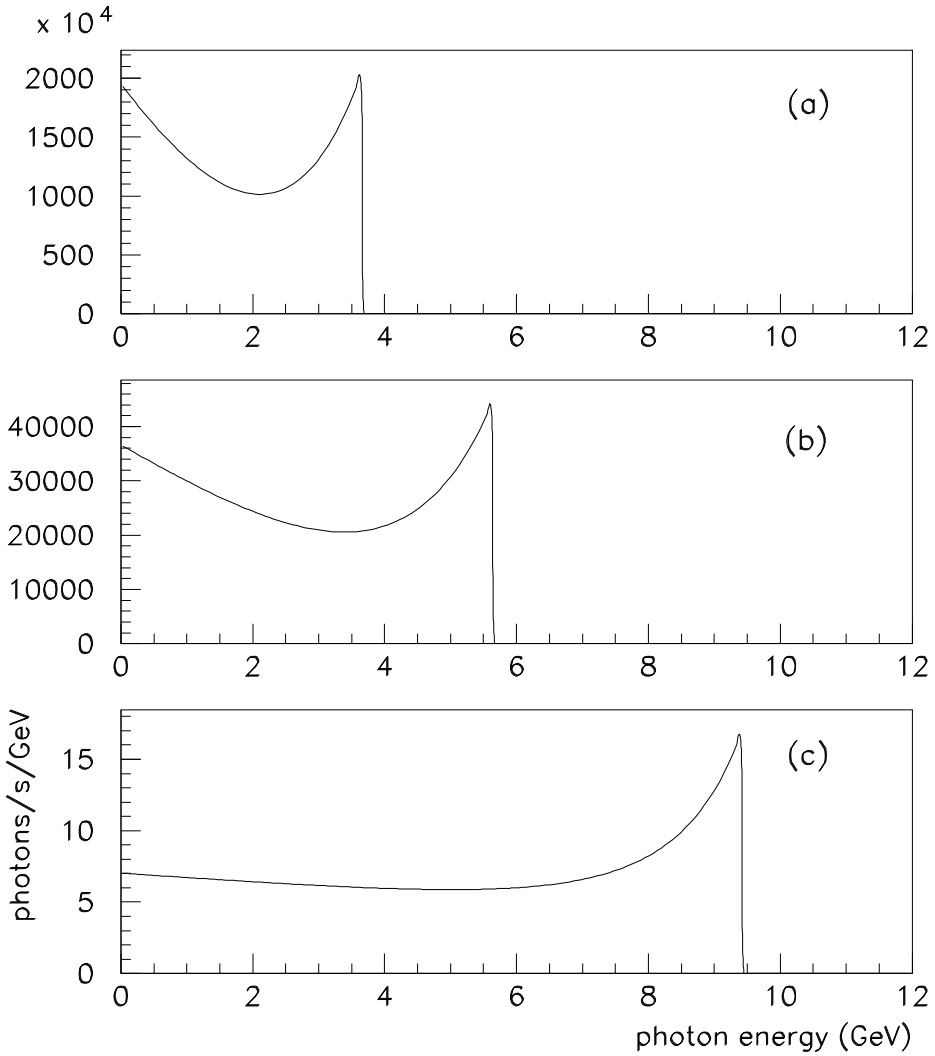

Figure 4.2: Photon energy spectrum from the Compton back-scatter source described in the text and a 12 GeV electron beam at 1μA. (a) cavity of gain 10000 driven by a 10kW Argon-ion laser (514 nm) pulsed at 100 MHz. (b) cavity of gain 250 driven by 3kW frequency-doubler (257 nm) pulsed at 100 MHz. (c) cavity of gain 1 driven by a hypothetical FEL source operating at 20 eV with the same time structure as CEBAF beam, peak power 1kW.

so it could be reflected back and made to cross the incident beam at a small angle for a Compton back-scatter source. An indication of the level of flux that could be achieved with such a source can be obtained by using the laser cavity model described above, setting the gain to 1, the wavelength to 62 nm, and assuming 1kW peak (1W average) of synchrotron light. The back-scatter rate is shown in Fig 4.2c. This plot shows that even if the full power of a 1 μA 12 GeV beam were converted into 20 eV photons and back-scattered from the incoming beam, the rate would still fall far short of the requirements for HALL D.

From the point of view of polarization, the Compton back-scatter source would be ideal. The polarization of the back-scattered beam is controlled by that of the laser, and can be essentially 100%. This source is also virtually background-free because the spectrum below any desired cutoff can be eliminated by collimation. The energy of the remaining beam can be measured to within the resolution of the electron beam by tagging. However the the combination of sufficient energy and sufficient flux for the purposes of HALL D cannot be achieved using this source.

4.1.2 Tagged bremsstrahlung

A bremsstrahlung source consists of a thin piece of material (the radiator) that is placed in the electron beam and converts part of the energy of the beam into bremsstrahlung radiation. Bremsstrahlung offers the only practical way, starting with an electron beam at CEBAF energies, to produce a photon beam with a significant flux in the vicinity of the end point. It produces a naturally collimated photon beam with a characteristic angular spread of m/E_0. This allows the low emittance of the CEBAF beam to be effectively transfered into the secondary photon beam.

Bremsstrahlung does not suffer from the kind of flux limitations that were encountered in the examination of Compton back-scatter sources. The radiator thickness must be kept below 1% of a radiation length in order to maintain good energy resolution in the tagger. Keeping the thickness below 10^{-3} radiation lengths ensures that multiple scattering in the radiator does not significantly broaden the divergence angle of the photon beam. A 10^{-3} radiator and 1μA of electrons would produce much more than sufficient flux for HALL D.

A bremsstrahlung source is, however, deficient in some other respects. Averaged over the bremsstrahlung cone, the photon beam has zero linear polarization. Circular polarization can be achieved by polarization transfer from a circularly polarized electron beam, but for the purposes of HALL D it is linear

polarization that is desired. A bremsstrahlung source also suffers from a large low-energy flux in the beam. The power spectrum of a bremsstrahlung beam is approximately uniform from zero up to the energy of the incident electrons. This means that an experiment that uses the high-energy part of the beam must operate in a background of low-energy photons that are many times more frequent. The tagger is helpful in eliminating many of the false starts in the detector that arise from the background, but this technique becomes ineffective at rates above a few 10^7 tagged photons/s. For the typical experiment using tagged bremsstrahlung and open detector geometry, background from low-energy beam particles limits the rate at which the experiment can run to less than $5 \cdot 10^7$ tagged photons/s. The goal for HALL D pushes that limit to 10^8/s by employing tagged *coherent* bremsstrahlung.

4.1.3 Coherent bremsstrahlung

The source described in the previous section meets most of the requirements for HALL D, but is deficient in the areas of polarization and backgrounds. Both of these deficiencies can be remedied by replacing the conventional amorphous or polycrystalline radiator with a thin mono-crystalline wafer. At special settings for the orientation of the crystal, the atoms in the radiator can be made to recoil together from the radiating electron. When they do this they produce a coherent enhancement at particular energies in the radiation spectrum, which correspond to the reciprocal lattice vectors of the crystal. The kinematics are such that a randomly oriented lattice vector would make a tiny peak located up at the end point of the energy spectrum, where the coherent gain factor is negligible. By careful orientation of the crystal, however, one of the lattice vectors can be aligned with the favored kinematics for bremsstrahlung, at which point its coherent peak appears well below the end point, and its coherent gain can be large enough that it contributes a large fraction of the total radiated power.

This is illustrated in Fig. 4.3. This plot shows the intensity (dP/dE) or power spectrum of the coherent bremsstrahlung beam after collimation. The sequence of secondary peaks above the primary correspond to integral multiples of the primary reciprocal lattice vector and so they are always present. By careful choice of orientation angles it is possible to suppress all other vectors and isolate just one primary peak. By rotating the crystal, the position of the peak can be moved from one end of the spectrum to the other. Note that the coherent peaks appear on top of the incoherent bremsstrahlung continuum.

Unlike the underlying continuum, the photons in the coherent peak have significant net linear polarization in the plane given by the beam direction

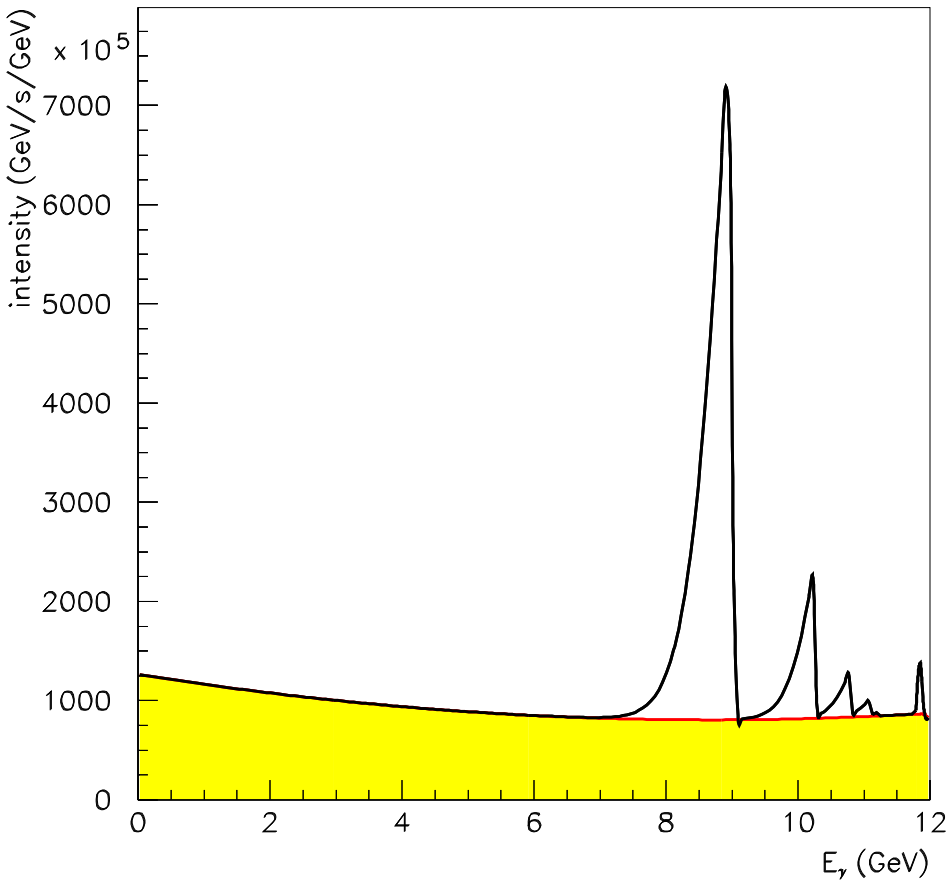

Figure 4.3: Photon power spectrum from an oriented diamond radiator. The y axis is dP/dE with power P expressed in $GeV/$s and E in GeV. The radiator thickness is 10^{-4} radiation lengths and the electron beam current is 1 μA. Shown is what emerges after the photon beam passes through a collimator 3.4 mm in diameter located 80 m downstream from the radiator.

and the crystal lattice vector. This polarization is enhanced by collimating the photon beam beyond its intrinsic angular spread, as discussed in the next section. The loss in flux from collimation can be recovered by increasing the electron beam current. As will be shown in the following section, even in the case of very thin crystals and severe collimation, only modest electron beam currents are needed to produce the required photon flux.

The use of coherent bremsstrahlung improves the background conditions by increasing the ratio of hard to soft photons in the beam. For measurements that do not require polarization, a crystal radiator can be used without collimation to reduce the amount of low-energy background for a given rate of tagged photons. Where polarization is required, coherent bremsstrahlung is indispensable.

4.2 Photon source

A horizontal plan view of the photon beam line is shown in Fig. 4.4 with the major components labelled. The electron beam enters the figure from below ground at the left and is bent into the horizontal plane to enter the tagger building. There it passes through two small dipoles to impinge upon the bremsstrahlung radiator. After its exit from the radiator, the electron beam passes into the tagging spectrometer where the primary beam is bent in the direction of the electron beam dump. The radiator crystal is thin enough that the average energy loss by the electrons in traversing the radiator is less than the intrinsic energy spread of the incident beam. Those electrons which lose a significant fraction of their initial energy inside the radiator do so by emitting a single bremsstrahlung photon. These degraded electrons are bent out of the primary beam inside the tagger magnet and exit the vacuum through a thin window, passing through air for a short distance to strike the focal plane of the spectrometer. The primary electron beam is contained inside vacuum all the way to the dump.

The photons that are produced in the radiator pass through a small hole bored in the return yoke of the tagger magnet in the forward direction. They then pass into an evacuated photon beam pipe and travel to the experimental hall. Just before entering the hall the photon beam passes through a system of collimators and sweeping magnets. In the figure they are shown in a separate enclosure for shielding purposes. The primary collimator is first. It defines the part of the photon beam that is allowed to reach the target. Debris from interactions along the inside surface of the collimator bore forms a halo around the photon beam that exits the primary collimator. The charged component of

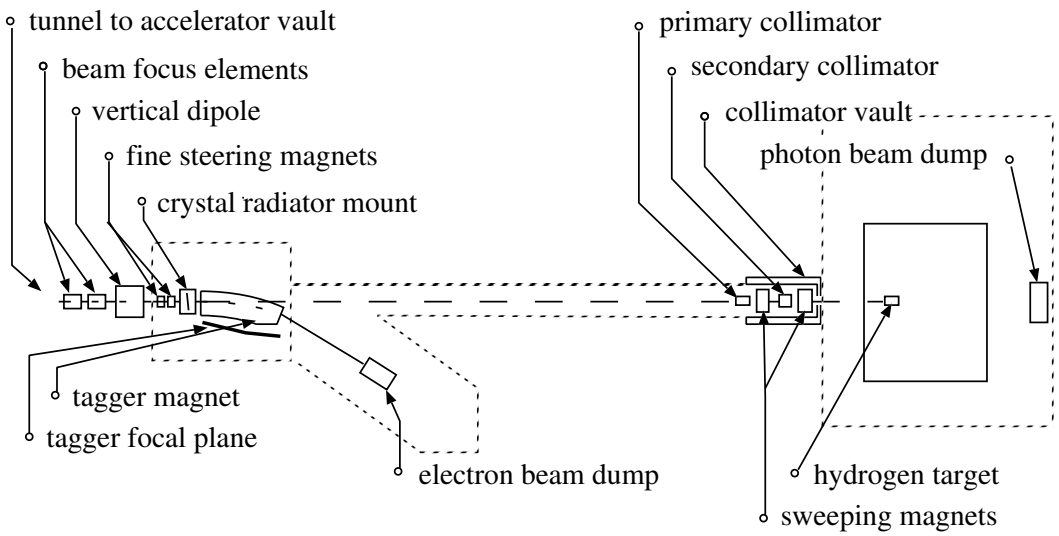

Figure 4.4: Schematic plan view of the photon beam line, shown in the horizontal plane as viewed from above. The objects in this figure are not drawn to scale.

the halo is deflected away from the beam axis by a dipole "sweeping" magnet just downstream of the collimator. A secondary collimator follows the sweeping magnet to stop the deflected shower particles and block the halo of secondary photons generated by the first collimator. The secondary collimator is of a larger diameter than the primary and so sees a reduced rate of secondary interactions on the inner surface of the hole. What new showers are generated there are cleaned up by a second sweeping magnet. The beam then passes through a final collimating aperture into the experimental hall. This triple-collimation system was copied from the setup developed at SLAC [94].

The collimated photon beam, now only a few mm in diameter, is delivered to the experimental target. After passing through of order 3% radiation lengths of target, the photon beam passes through the detector and into the photon beam dump at the back of the hall. Based upon a design upper limit of 60kW (5μA at 12 GeV) being delivered to the electron beam dump, the total power in the photon beam is not more than 1.5W in the experimental hall and not more than 15W in the collimator enclosure.

4.2.1 Essential features

The adjective 'coherent' in coherent bremsstrahlung does not indicate that the photons in the beam are in a coherent state, as is light from a laser. Rather it refers to the coherent effect of multiple atoms in a crystal lattice in absorbing the recoil momentum from a high energy electron when it radiates a bremsstrahlung photon. In X-ray spectroscopy one encounters the same thing in the Mössbauer effect, except in that case the chief physical consequence is the disappearance of the recoil Doppler shift from the photoabsorption/emission spectrum. Here the chief consequence is the enhancement of bremsstrahlung at those particular kinematics for which the recoil momentum matches one of the reciprocal lattice vectors of the crystal.

Another useful way to view the process of coherent bremsstrahlung is as virtual Compton scattering. To the high energy electron, the atoms in the radiator appear as clouds of virtual photons. For a disoriented radiator material, the virtual photon spectrum is given simply by the atomic form factor, averaged over the different species in the material. If the radiator is a single crystal, however, the atomic form factor gets multiplied by the form factor of the crystal, which in the ideal case looks like a series of delta-functions located at the sites of the reciprocal lattice. In effect, the crystal provides a set of virtual laser beams, each one a standing wave tuned to a specific reciprocal lattice vector. In this view the process of hard bremsstrahlung is seen to be the same as Compton back-scattering of laser light. For a more detailed discussion of the physics of coherent bremsstrahlung there are a number of good references [94, 95, 96, 97].

The use of Compton back-scattering of laser light as a photon source was earlier noted as ruled out by the limitation of high-power lasers and cavities to wavelengths above 100 μm. The characteristic wavelength of the crystal photons is a few Angstroms, three orders of magnitude shorter. In this case, 180° scattering would result in essentially 100% of the electron beam momentum being transfered to the photon in the lab frame. However, the Compton cross section contains a factor of $1/(\vec{q} \cdot \vec{p})^2$ where $\vec{q}$ is the virtual photon momentum and $\vec{p}$ is that of the electron, which strongly favors incident photons with $\vec{q}$ nearly orthogonal to $\vec{p}$. With reciprocal lattice vectors pointing in almost every direction, only those nearly perpendicular to the beam contribute appreciably to the scattering rate. This fact applies equally to ordinary bremsstrahlung; in fact, to a first approximation the bremsstrahlung spectrum from a single crystal is the same as from a disoriented radiator. The reason is that, if the sum over crystal momenta were replaced with a continuous integral, one would recover the ordinary bremsstrahlung result for isolated

atoms. Beyond a few unit cells from the origin in reciprocal lattice space, the atomic form factor and kinematic factors become slowly varying on the scale of the lattice spacing, and the sum becomes indistinguishable from the integral. Besides that, the uncertainty principle requires that atoms localized at the sites in a crystal undergo fluctuations about their mean position. This has the effect of attenuating the discrete peaks in the crystal form factor at progressively higher-order crystal momenta, eventually washing them out and filling in the gaps between them, so that the sum deforms smoothly into the integral at high momentum transfer. Hence, the sum over crystal indices that yields the final photon spectrum can be separated into two parts: a discrete sum over a limited set of small crystal indices and an integral over the continuum of momentum transfer values beyond. The latter appears in the coherent bremsstrahlung beam as an ordinary $1/k$ bremsstrahlung spectrum, while the former appears as a set of peak structures superimposed upon it. The $1/k$ continuum, referred to as the incoherent component, is invariant as the crystal is rotated, whereas the coherent peaks change in position and intensity, depending on crystal orientation.

A typical coherent bremsstrahlung spectrum is shown in Fig. 4.5. The distinction between incoherent and coherent components in the figure is artificial; it is there to show the part of the spectrum that shifts as the crystal is rotated. The vertical scale in the figure gives the photon rate for the given beam current and crystal thickness. Note that the intensity of the incoherent background is less than what would be obtained with an amorphous carbon radiator of the same thickness, because a part of the momentum transfer integral in the Bethe-Heitler formula has been moved into the discrete sum and contributes to the coherent part. The radiation length of diamond is actually an average over all orientations of the crystal. In the calculation for Fig. 4.5 the leading 400 lattice sites were included in the discrete part of the calculation, although it can be seen that only two or three of them contribute with sufficient intensity to be individually visible in the spectrum.

4.2.2 Use of collimation

The presence of the large incoherent flux in Fig. 4.5 presents a significant handicap to a photoproduction experiment. Not only do the low energy photons produce background in the detector, but they diminish the polarization of the beam. The entire beam polarization appears in the coherent component; the underlying incoherent flux only serves to dilute the polarization. There is another difference between the two components that allows them to be separated to some extent. The kinematics of bremsstrahlung confines most of the inten-

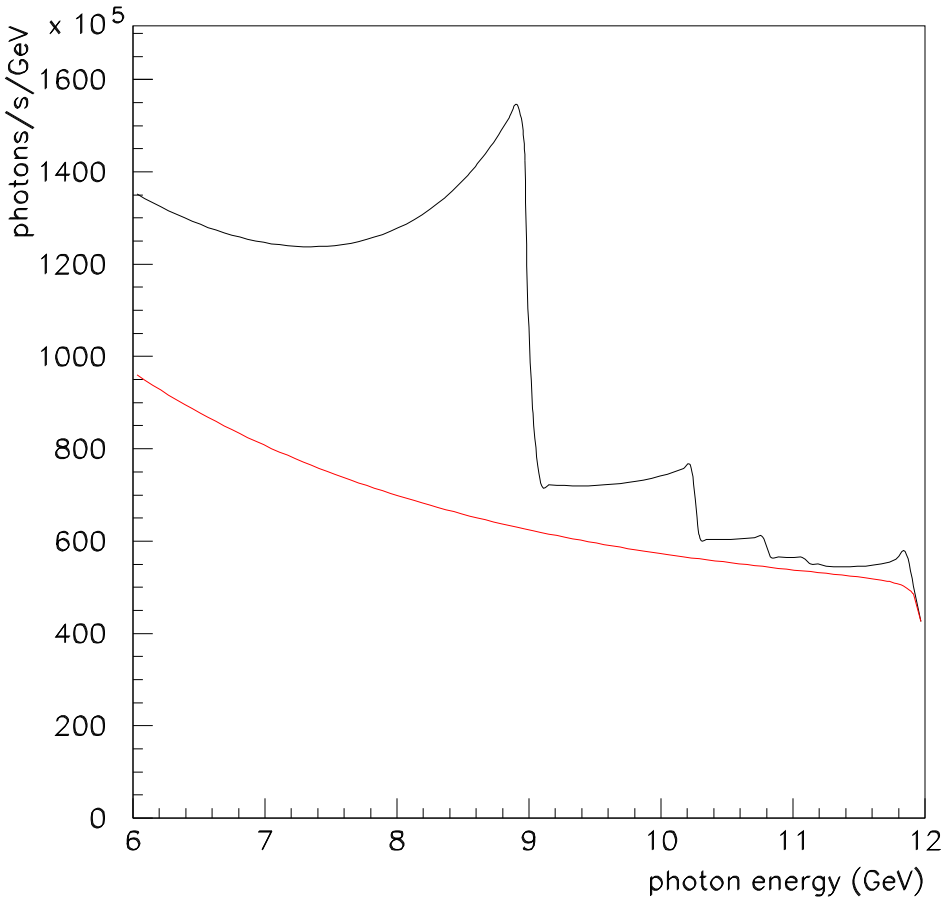

Figure 4.5: Coherent bremsstrahlung spectrum, calculated for a diamond crystal radiator 15 μm thick and a 1 μA electron beam of 12 GeV energy. Typical values were used for beam emittance and crystal mosaic spread.

sity of the photon beam to forward angles within m/E radians of the incident electron direction. In the lab this is a small angle, but in the rest frame of the electron-photon system it subtends all angles in the forward hemisphere. A peak in the coherent component that corresponds to a single reciprocal lattice vector has two-body kinematics, so there is a well-defined relation between the emission angle and the energy of the emitted photon in the lab: emission at 0° yields a maximum energy photon, with energy decreasing with increasing angle. This accounts for the shape of the coherent peaks in Fig. 4.5, with the sharp right-hand edge corresponding to 0° emission and the tail to lower energies corresponding to scattering into higher angles.

The incoherent component, because it comes from a sum over momentum transfers at all angles, has essentially no correlation between photon energy and emission angle. This means that collimating away all photons beyond some angle $\theta_{max} < m/E$ uniformly attenuates the incoherent spectrum at all energies, whereas it preserves all of the coherent photons from the maximum energy for the given peak down to some cutoff. The kinematic relations for coherent bremsstrahlung are as follows,

$$\theta^2 + 1 = \left(\frac{1-x}{x}\right)\left(\frac{x_{max}}{1-x_{max}}\right) \tag{4.1}$$

$$x_{max} = \frac{2\vec{p}\cdot\vec{q}}{2\vec{p}\cdot\vec{q} - m_e^2} \tag{4.2}$$

where x is the photon energy in units of the incident electron energy and θ is the lab emission angle of the photon relative to the incident electron momentum axis, in units of m/E .

The effects of collimation are demonstrated in the calculated spectra shown in Fig. 4.6. First, note that the collimation angles are very small, which requires a long flight path of order $100\,m$ in order that the collimator can be larger than the intrinsic beam spot size, otherwise the collimator is cutting in transverse coordinate instead of in angle. This distance is, in fact, a sensitive function of the electron beam emittance from the machine, and must be increased in inverse proportion to the beam emittance if the effectiveness of collimation is held constant. This issue, along with the associated demands placed on beam alignment and position stability, are taken up in more detail in the following section on the electron beam line.

Second, note that the cut imposed on the coherent peak by collimation does not produce a perfectly sharp edge as would be expected from two-body kinematics. This is because the collimator cuts on radius at some fixed distance which translates into a cut on emission angle only in an approximate way,

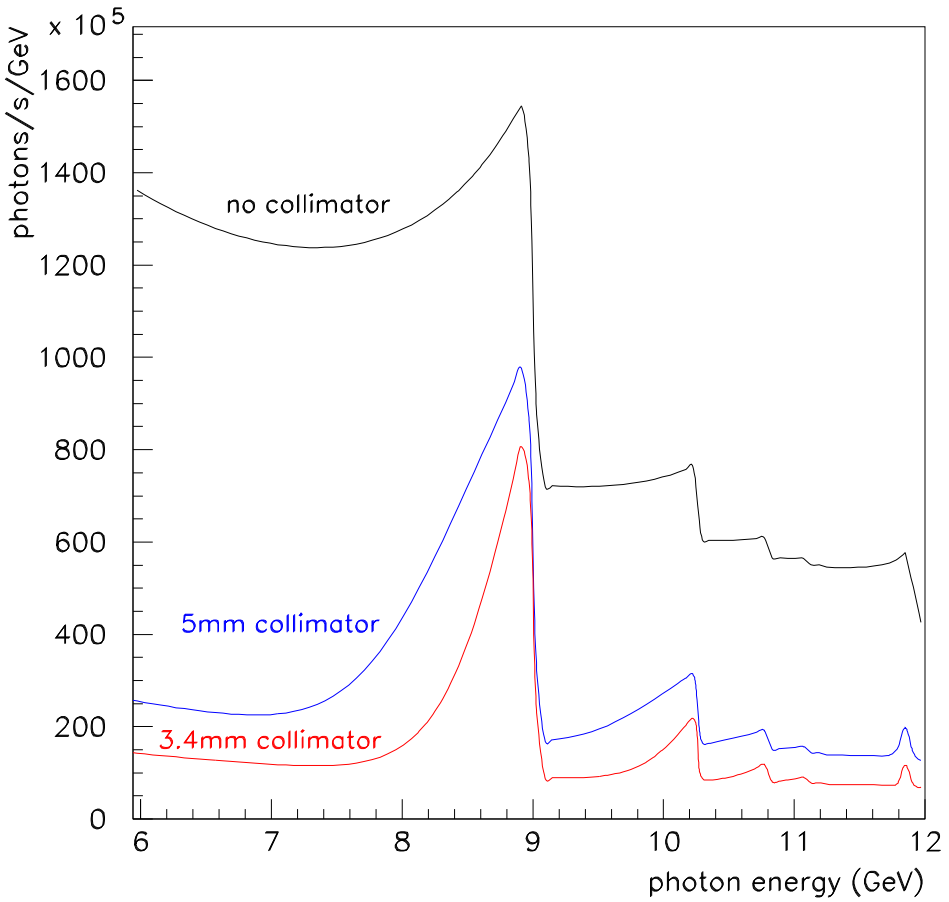

Figure 4.6: Coherent bremsstrahlung spectrum, calculated under the same conditions as in Fig. 4.5 , after collimation. The upper curve is the uncollimated spectrum from Fig. 4.5. The middle curve corresponds to a 5 mm diameter collimator placed 80 m downstream of the radiator, or approximately 0.75 m/E in collimator half-angle. The lower curve corresponds to a 3.4mm collimator in the same position, approximately 0.50 m/E. For the 3.4 mm collimator there are approximately $3.3 \times 10^7 \gamma/s$ in the primary peak.

thus the curves in Fig. 4.6 are labelled by their collimator size and distance individually rather than their ratio which is the nominal collimation angle. Multiple scattering by the electron in the radiator prior to emission and beam spot size and divergence are the major contributors to the error involved in translating a collimator radius into a cut on emission angle. All of these effects have been incorporated into the analytical calculation of the yields from a collimated coherent bremsstrahlung source that has been used in preparing this report. Crystal imperfections, which amount to an intrinsic spread in the direction of the incoming virtual photon, are also taken into account in the calculation.

Third, note that the relatively weak collimation at $5\,mm$ reduces the incoherent background without significantly affecting the coherent flux near the maximum, and thereby almost doubling the polarization of the beam at the peak relative to the uncollimated case. Further reducing the collimator diameter continues to narrow the peak and reduce the incoherent flux relative to the peak, albeit at some cost in peak intensity.

The $3.4\,mm$ collimator diameter has been chosen for this design because it provides for a maximum reduction in the incoherent flux while transmitting 95% of the coherent flux at the peak. Most of the net photon beam energy, however, is being absorbed by the collimator. For this reason the collimator is located in a separate enclosure outside the experimental hall, and must be surrounded by a considerable amount of shielding. The peak in Fig. 4.6 for a $3.4\,mm$ collimator contains 33M photons/s for an electron beam current of 1μA, which will be increased by a factor of 3 for full-intensity running in HALL D.

Fourth, note that the rate seen in the focal plane of the tagging spectrometer corresponds to the upper curve in Fig. 4.6, regardless of the collimation. This means that collimating the bremsstrahlung beam increases the rate in the tagger focal plane relative to what is seen at the detector. For full-intensity running at 10^8 photons/s on target in the coherent peak, Fig. 4.6 implies a rate of 240 MHz in the focal plane within a 600 MeV window around the peak. Combining this rate with the beam pulse spacing of 2ns leads to an accidental tagging rate of about 50% and to a fraction of ambiguous tags of 40%. In an ideal detector the per-second yield of single-tag events does not saturate until the fraction of ambiguous tags reaches 63%; however detector rate and trigger considerations will lower this figure somewhat. The detector and tagging spectrometer design are based upon a maximum rate of 10^8 photons/s on target and 400 MHz per GeV in the tagger. A novel focal plane design is currently under study, to be discussed below in section 4.4, which may enable the focal plane rate to be reduced by about a factor of two without any decrease in the

collimated flux.

The linear polarization of the photons in the coherent peak is shown in Fig. 4.7 as a function of the energy of the electron beam. This figure demonstrates why it is essential to have electrons of as high energy as possible, even though photon energies of no more than $9GeV$ are required. The intensity of the coherent peak, not shown in the figure, has a similar dependence on the electron beam energy in this region.

Shown in Fig. 4.8 is the linear polarization of the photon beam *vs* photon energy for fixed electron beam energy. The dashed curves show how the maximum polarization in the primary peak varies as the peak energy is changed by rotating the crystal. The polarization in all cases is zero at the endpoint. Without collimation it rises as $(E_0 - k)^2$, one power coming from the intensity of the coherent peak relative to the incoherent component going to zero linearly at the endpoint, and the other from the intrinsic polarization of the coherent photons also behaving like $(E_0 - k)$ near the endpoint. Collimation allows one to essentially isolate the coherent component, so that the polarization available to the experiment rises from zero at the endpoint in a linear fashion. The dashed curves in Fig. 4.8 demonstrate this point.

In order to obtain the full polarization enhancement from collimation, it is necessary to have a distance between the radiator and collimator on the order of $100\,m$. This distance scale is set by the requirement that the collimator aperture must be large compared to the virtual electron beam spot on the collimator but small compared to the actual photon spot size.

The size of the virtual spot at the collimator is controlled by the beam emittance coupled with a limit of 20μr on the angular spread of the electron beam at the radiator. The latter value was chosen to match the spread in the beam incidence angle to the mosaic spread of the crystal because it is the combination of the two that limits the definition of the coherent peak. Taking this value together with an emittance of 10^{-8}m·r, which has been projected for the CEBAF beam at 12 GeV leads to a virtual spot size of $0.5\,mm$ r.m.s. ($1.2\,mm$ f.w.h.m.). Note that this scale does not depend on the radiator-collimator distance. The size of the real photon spot is given by one characteristic angle m/E which defines a circle on the collimator containing approximately 50% of the total photon intensity. The real spot size is proportional to the radiator-collimator distance. At a distance of 80m the ratio of spot sizes is 6, sufficient to allow collimator sizes that satisfy both of the above inequalities.

Fig. 4.9 shows the peak polarization of the beam as a function of radiator-collimator distance for a coherent peak at 9 GeV. In this calculation the collimator diameter is held constant at $3.4\,mm$ to make sure that the virtual beam spot of $1.2\,mm$ f.w.h.m. is well-contained, which is the main condition

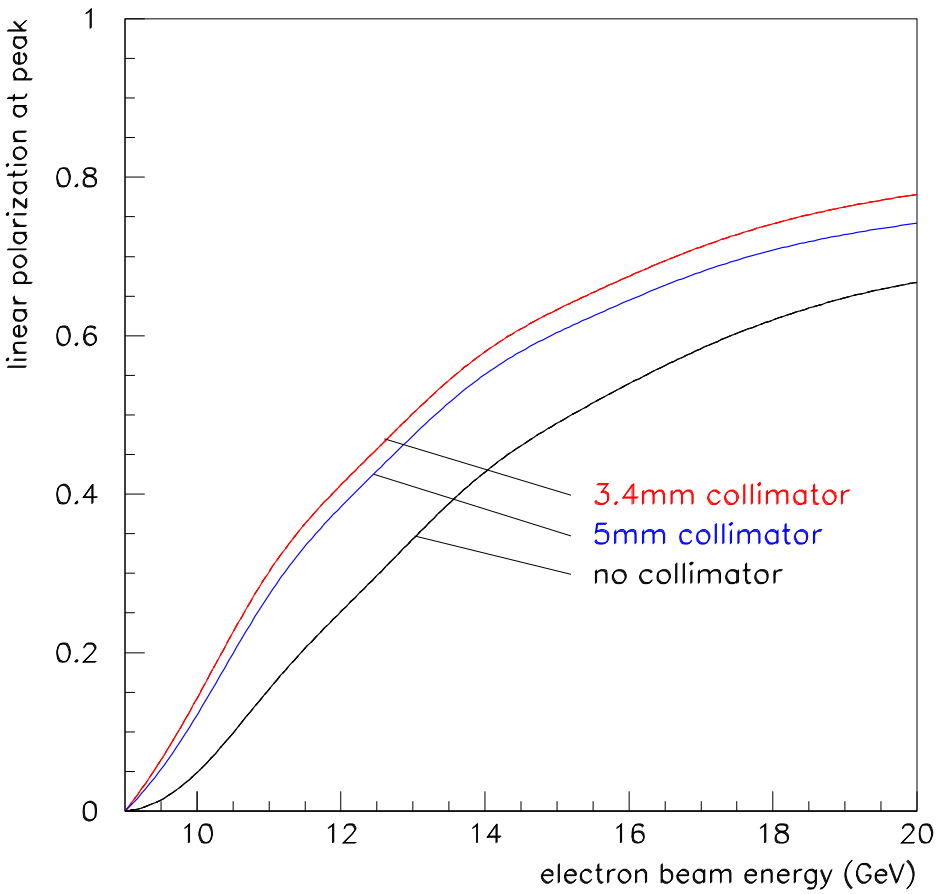

Figure 4.7: Linear polarization in the coherent bremsstrahlung peak as a function of electron beam energy keeping the energy of the coherent peak fixed at 9 GeV. The calculation is performed under the same conditions as in Fig. 4.6.

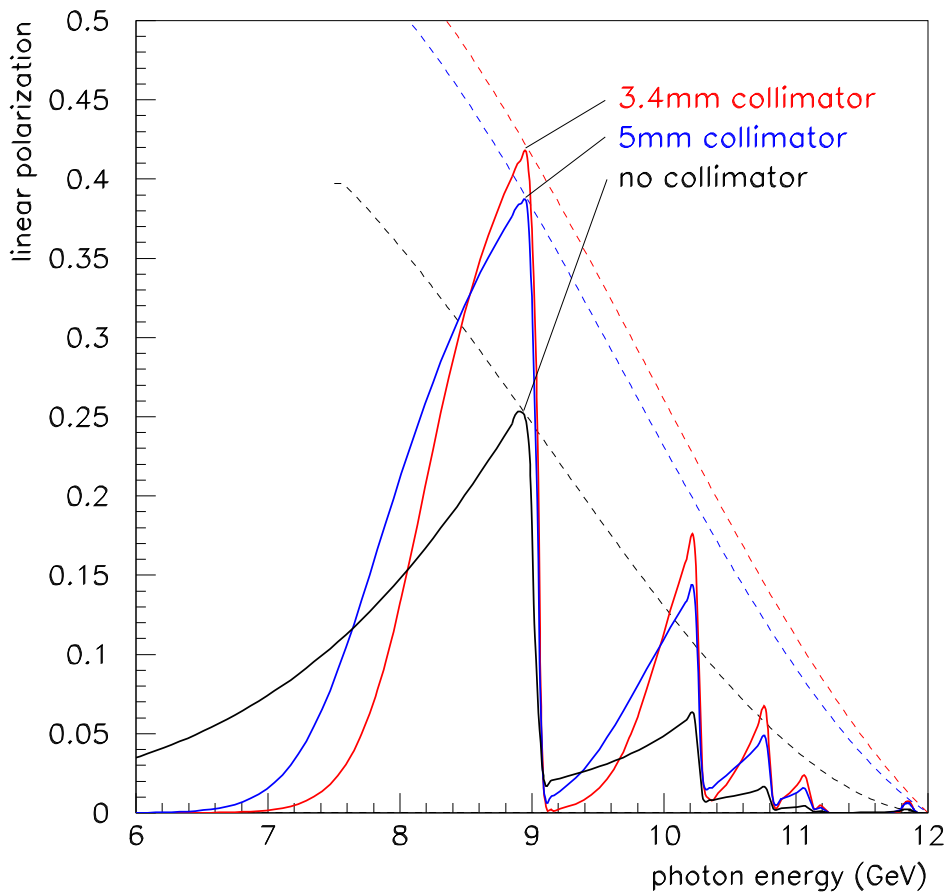

Figure 4.8: Linear polarization of the coherent bremsstrahlung beam for a fixed electron beam energy of 12 GeV calculated under the same conditions as in Fig. 4.6. The dashed lines indicate the trajectory of the peak polarization as the peak energy is swept across the focal plane by rotating the crystal.

crystal	best reciprocal vector	$P/P_{diamond}$
diamond	2,-2,0	1.00
beryllium	0,0,2	0.86
boron	2,0,8	0.38
silicon	2,-2,0	0.19
Be_2C	2,2,0	1.10

Table 4.1: Figure of merit of various materials that might be used as a coherent bremsstrahlung radiator. This table is reproduced from Table 2 in Ref. [95].

for effective collimation. At zero distance the collimator has no effect except to attenuate the beam, and so the uncollimated polarization from coherent bremsstrahlung is obtained. At 100m separation distance the polarization enhancement from collimation has saturated. The design for HALL D calls for a radiator-collimator distance of approximately 80 m. However from the figure one can see that the performance of the photon source is not a very sensitive function of this variable.

4.2.3 Choice of radiator

The ideal radiator would be a layered structure with strong transverse fields that alternate between layers spaced about 50 nm apart, thus simulating the standing wave in a cavity driven by a 15 eV laser. While it is possible to construct ordered materials with unit cells as large as this, the self-shielding of atoms means that beyond the atomic length scale the residual fields are comparatively weak. Hence heterogeneous structures are not viable for use as a coherent radiator. Since the strong fields inside a solid are revealed at the atomic scale, the first requirement for a good radiator is that the unit cell be compact and closely packed. The best radiators are those with the smallest unit cells because these provide the best match between the atomic and the crystal form factors. This match is best for the light elements, and essentially prohibits the effectiveness of any materials heavier than carbon. An extensive survey of possible radiator materials is presented in Ref. [95]. In Table 4.1 is shown the figure of merit that those authors report for favored crystalline materials. The figure of merit is the product of the atomic times the crystal form factor evaluated at the leading peak, normalized to the value for diamond.

Table 4.1 shows that the list of viable materials for a crystal radiator is

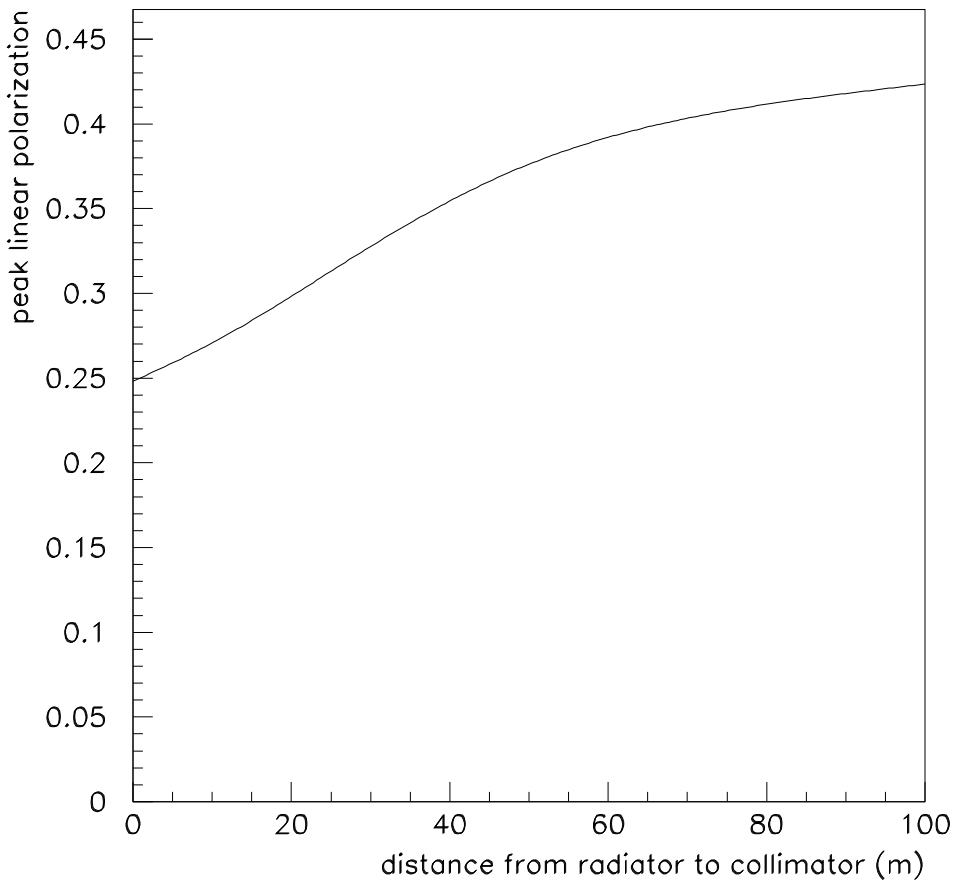

Figure 4.9: Maximum polarization *vs* radiator-collimator distance for a coherent peak at 9 GeV. The collimator diameter is held fixed in this calculation to keep a constant ratio between the sizes of the virtual electron spot and the collimator.

relatively short. Silicon would be an excellent choice from the point of view of price and fabrication, but unfortunately it is far inferior in terms of performance. Beryllium carbide is not a material that is familiar to the crystal growth industry, and nothing is known at present concerning its suitability for the growth of single crystals of large area. In general compound materials are more susceptible to radiation damage than are pure elements, which would argue in favor of diamond and beryllium metal. These two materials are comparable in terms of their performance.

Most of the experience to date with coherent bremsstrahlung has been with diamond radiators. Extensive expertise for handling large diamond crystals exists within the gem industry. Recently, since it has become necessary to find some new diamond radiators for the coherent bremsstrahlung tagged photon facility in Mainz, members of the Glasgow group have established good contacts within the gem industry for procuring diamonds and have developed techniques for assessing the quality of the diamonds [98].

Currently, there is a need for diamonds with areas greater than 5 mm $\times$ 5 mm for X-ray windows on synchrotron light sources. Ideally, the diamonds should have a perfect crystal structure. In general terms, diamonds are classified as type I or type II, where type II have been subjected to greater stresses during their formation than type I. Commonly, type II exhibit substantial plastic deformation. Diamonds are also classified according to the form in which nitrogen atoms are present in the crystal lattice. In type a the nitrogen is aggregated into clusters of atoms, whereas in type b the nitrogen is almost uniformly distributed throughout the crystal. For coherent bremsstrahlung radiators, type Ib diamonds are the most suitable. Unfortunately, type Ib natural diamonds are very rare and probably the most reliable source of Ib diamonds will be synthetics. At present synthetic diamond monocrystals typically have nitrogen concentrations around 100 ppm.

Synthetic diamonds are made using either vapour deposition (CVD) or high pressure high temperature (HPHT) techniques. CVD diamonds have an extensive mosaic and are unsuitable for coherent bremsstrahlung. However HPHT synthetics look very promising, and the Glasgow group have recently acquired a $5\,mm \times 5\,mm$ synthetic diamond less than 18μm thick which has a [100] orientation. It produces a very good coherent bremsstrahlung spectrum and X-ray measurements show it has rocking curve widths of less than 10μr, quite close to the ideal value for diamond.

Beryllium is another material that might be used as a crystal radiator. Beryllium metal is widely used in industry, being preferred for its high strength-to-weight ratio and robustness, in addition to its transparency to X-rays. Thin films of high-purity beryllium are routinely produced for vacuum window ap-

plications, which use some of the same vacuum deposition techniques that would be used for the growth of single crystals. As a radiator material, beryllium is distinguished as the metal with the highest Debye temperature, around 1400°K . The Debye temperature measures the temperature at which the thermal motion of the atoms in the lattice reaches the level of the zero-point motion due to their confinement in the lattice, as dictated by the uncertainty principle. A high Debye temperature indicates a stiff crystal lattice, in which the atoms have little liberty to move and so have large momentum fluctuations, as dictated by the uncertainty principle.

A high Debye temperature is important for a bremsstrahlung radiator material for three reasons. First, the cross section for coherent bremsstrahlung from a discrete crystal momentum vector $\vec{q}$ contains a factor $e^{-q^2/4M\theta_D}$ which reflects the fact that position fluctuations of atoms in the lattice diminish the coherent effect. This factor is near unity for the low-order crystal momenta provided that θ is sufficiently large. Second, the Debye temperature is, roughly speaking, a measure of the stability of the crystal structure and hence its readiness to form as a single crystal and to survive significant doses of radiation. Third, the radiator material will inevitably be heated by the beam, and will normally operate in vacuum well above the ambient temperature. A high Debye temperature means that there is a large range of temperatures over which the material may operate without degraded performance as a crystal radiator. The Debye temperature of diamond is about 2200° K. Past experience has shown that diamond meets all of the requirements for a good crystal radiator.

Beryllium remains therefore a second choice, to be investigated further in the case that affordable sources of large-area diamond crystals at some point are no longer available. The growing need for such crystals for use at synchrotron light sources gives reason for confidence that this is not likely to happen any time soon.

4.2.4 Crystal thickness

The range of permissible thicknesses for a crystal radiator is bounded both from above and below. It is bounded from above by multiple scattering of the electron beam as it passes through the radiator, which causes the divergence of the incident beam to grow, thereby enlarging the photon beam spot on the collimator face and degrading the degree to which collimation discriminates against the incoherent component in favor of the coherent part. It is bounded from below by the fact that the crystal must be of some minimum thickness in order to achieve the full coherent gain. In the calculation of the coherent bremsstrahlung process one begins by assuming an infinite crystal, although

practically it is presumed to mean only that the crystal is large compared to the some characteristic scale. It is important to identify what the characteristic scale is in this problem in order to know how thin one can make the crystal without hurting performance. In the analogous case of the Mössbauer effect, one can estimate the number of atoms participating in the collective absorption by looking at the emission time of the photon (lifetime of the radiating transition) and asking how many nuclei lie within the envelope of the photon wave packet. In the coherent bremsstrahlung process, the lifetime of the radiating system is given in the lab system by the uncertainty principle and by how far the electron energy deviates from its on-shell value between absorbing the virtual photon and emitting the real one. The latter quantity is almost exactly given by q_z , the virtual photon momentum component along the incident electron axis, which means that the electron travels a distance $\lambda = \hbar c/q_z$ during the interaction. For a given coherent peak at normalized energy x in the photon spectrum, the coherence length is given by

$$\lambda = \frac{2E(1-x)}{xm^2} \tag{4.3}$$

in units of $\hbar c$. From this simple argument one sees that the coherent gain goes linearly to zero at the endpoint, a result that is borne out by the full QED calculation. One also sees that the lower limit on crystal thickness imposed by the coherence length depends upon both the electron beam energy and the photon energy. For a 12 GeV beam energy and a 6 GeV coherent photon the coherence length is 18 nm, or about 50 unit cells for diamond. This shows that the coherence length does not impose a practical limit on how thin the radiator should be.

The effects of multiple scattering are best presented by showing the calculated spectra for various radiator thicknesses. In Fig. 4.10 is shown the photon spectrum for a 10^{-4} and a 10^{-3} radiation-lengths radiator to demonstrate the effect. The 10^{-3} radiator spectrum is scaled down by a factor of 10 to facilitate the comparison. The calculation assumed a 3.4 mmcollimator located 80 m downstream of the radiator. The loss in normalized intensity with the thicker radiator, as well as the broadening of the left edge of the peak, is due to the enlarging of the photon beam spot on the collimator face from multiple scattering of the electron beam in the crystal prior to radiation. A 10^{-4} diamond radiator is 15 μm thick. The goal for HALL D is to run with crystals of thickness in the range 10 μm to 20 μm.

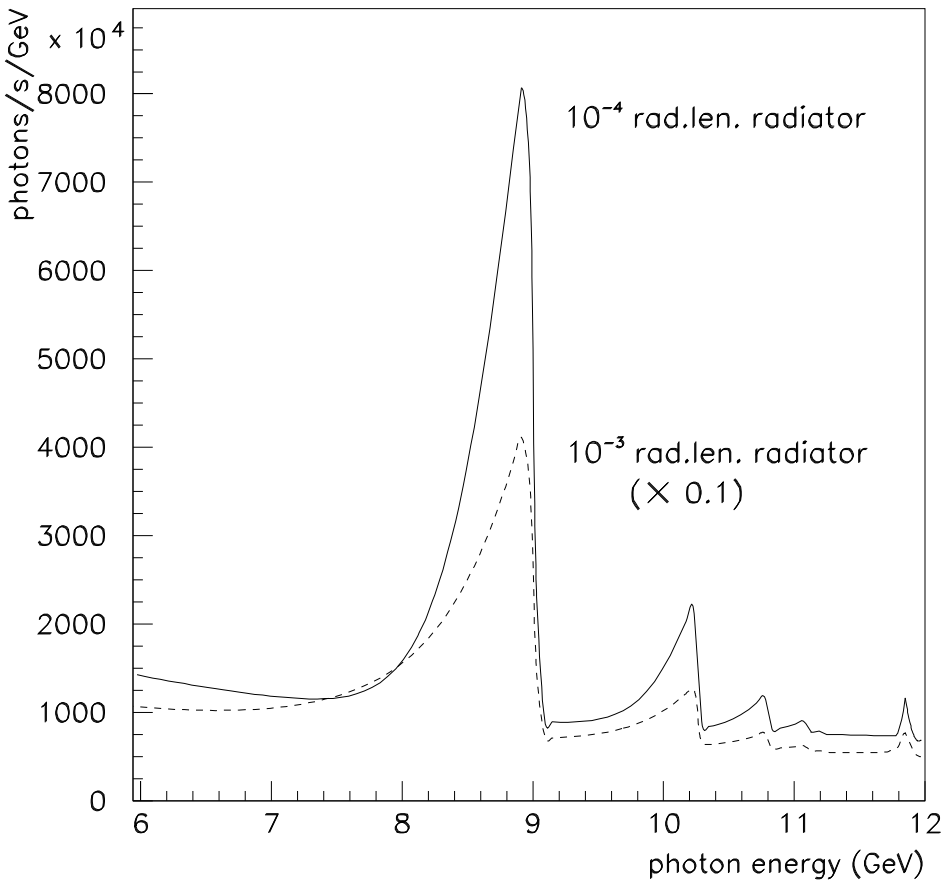

Figure 4.10: Collimated coherent bremsstrahlung spectrum from a 1μA electron beam at 12 GeV using diamond radiators of two different thicknesses. The calculation assumes a 3.4 mm collimator located 80 m from the radiator, and typical values for beam emittance and crystal quality.

Axis	Motion	Range	Step size
x	horizontal translation	-50 mm – +50 mm	0.01 mm
y	vertical translation	-20 mm – + 20 mm	0.01 mm
θ_v	vertical rotation	-100mr – +100mr	10μr
θ_h	horizontal rotation	-100mr – +100mr	10μr
ϕ	azimuthal rotation	-100° – +100°	0.01°

Table 4.2: Requirements for goniometer axes

4.2.5 Crystal mount

It has already been shown that in order to achieve appreciable coherent gain the crystal must be oriented so that the coherent peaks appear well below the end point. Equation 4.2 then implies that the orientation must be such that the crystal momentum dotted with the beam momentum be of order m^2 . Given a p of 12 GeV and q of 10keV, this requires that the two vectors must be within 100μr of perpendicular to each other and that, within a range of angles of that order, the coherent peak sweeps out nearly the full range in x from 0 to 1.

Hence, to have a stable photon beam with the coherent peak positioned at the right energy, the angle between the incident electron beam and the crystal radiator must be adjustable in steps of a few μr and remain stable at this level. Since the angle of the incident beam is fixed by the beamline optics and the position of the photon collimator, all adjustments must be made by changing the orientation of the crystal. This is achieved with a precision goniometer (shown schematically in Fig. 4.11) which should provide motion on at least 5 axes. Rotation about the azimuthal axis ϕ sets the orientation of the polarization plane, rotations about the θ_v, θ_h axes set the angle of the crystal relative to the beam, and x, y translations select the position of the beam spot on the crystal. Estimates of the approximate range and step size for each of the axes are given in Table 4.2.

In practice several targets need to be mounted in the goniometer. The minimum requirement is a diamond crystal, an amorphous radiator, and a blank. It is also desirable to have a screen to show the position of the beam spot and a spare diamond. This means either mounting some targets off-axis on the azimuthal plate (as in the Mainz setup), or having a sixth axis to allow a target ladder to sit inside the azimuthal plate (as in the Jlab Hall B setup). A goniometer with the required precision can be obtained commercially, and

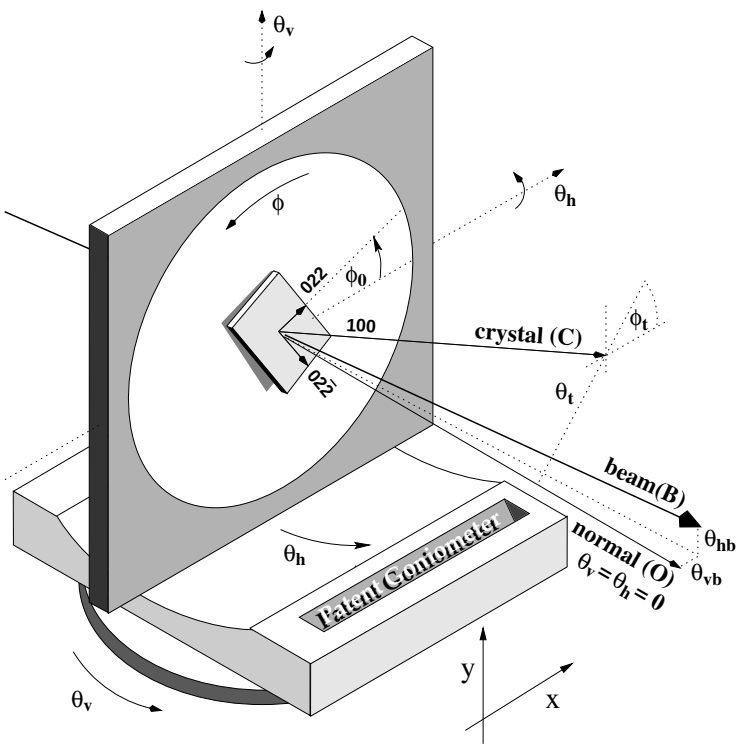

Figure 4.11: Schematic illustration of crystal mounted in goniometer

would be controlled with the slow control system.

4.2.6 Crystal alignment and monitoring

As can be seen in Fig. 4.11 the goniometer setting θ_v,θ_h defines the direction of the normal to its inner plate (O). Ideally at its zero setting $\theta_v = \theta_h = 0$ this would coincide with the electron beam direction (B), but in practice there are small offsets θ_{vb}, θ_{hb} which may vary according to the stability of the electron beam. There will also be a misalignment of the crystal lattice with respect to the inner plate due to imperfections in the mounting and in the cutting from the original stone. The 100 axis (C) will be tilted with respect to the inner plate at an angle θ_t with this maximum tilt occurring at an azimuthal angle ϕ_t. In addition, the 022 vector will be offset by ϕ_0 with respect to the horizontal. Any motion about the azimuthal axis ϕ changes the angle of the 100 axis (C) relative to the beam. The angle of the polarization plane is set by adjusting the azimuthal angle of the crystal ϕ. Hence when a new crystal is installed, the default value ϕ_0 needs to be measured. Furthermore, to position the coherent peak at the required photon energy, the angle (or *offsets*) between the beam and 100 crystal axis (C) at the chosen value of ϕ must also be established.

Feedback on the relative angle between the crystal and the beam is obtained from a photon energy spectrum derived from the tagger focal plane counters, either via scalers or a TDC hit pattern. The scaler spectrum does not show the effect of collimation (unless the scalers are gated with a downstream photon detector), but can be obtained very quickly since it does not require a triggered data acquisition system. The scaler readout is essential for the alignment process, where the offsets are measured by carrying out a series of scans in which 2d histograms of photon energy vs. crystal angle are built up by moving the goniometer in a sequence of small angular steps and reading the tagger scalers. In addition to providing the feedback required for alignment, the focal plane counters provide essential online diagnostics to monitor drifts in angles caused by the beam tuning, or thermal effects in the crystal mount. If necessary a feedback system could be implemented via the slow control system, where any drift in the position of the coherent peak could be corrected by periodically adjusting the goniometer within predefined limits.

The spectrum obtained from the tagger focal plane can also provide online monitoring of the photon polarisation to within 5% by fitting with an analytic bremsstrahlung code.

4.2.7 Crystal quality and lifetime

There are two considerations that fall under the heading of crystal quality. The first respects the quality of the original crystal, and the second is with regard to degradation from radiation damage. In the calculation of the coherent bremsstrahlung spectrum a perfect single crystal was assumed, but even the very best crystals have some dislocations and other defects. Besides locally disrupting the regularity of the crystal, these defects impose stresses which produce small ripples in the crystal planes. If these ripples were amplified, the surface of a crystal would appear like a mosaic of planar regions with approximately parallel surfaces. The scale of deviations from planarity across the face of a single crystal is termed the *mosaic spread* of the crystal. The mosaic spread contributes in the same way as beam divergence to the smearing in the exact energy-angle relation for coherent photons.

In section 4.2.3 it was mentioned the Glasgow group have developed techniques for assessing the quality of diamond radiators. Two stages are involved. Firstly the diamonds are examined under a microscope with polarized light. This reveals any stresses in the crystal lattice and is particularly useful for eliminating diamonds with plastic deformation. Then any diamond which looks as if it could be used as a radiator is examined with one of the X-ray beams from the Synchrotron Radiation Source at Daresbury in England. Three types of measurements are performed.

i. Rocking curves widths which, for a selected set of crystal planes, measure quantitatively how any defects or dislocations distort the crystal lattice. Using rocking curves it is possible to measure how close to ideal is the lattice structure of the diamond being investigated. At Daresbury, the X-ray beam can be collimated so that an area as small as $0.25\,mm$ by $0.25\,mm$ can be sampled.

ii. Projection topographs which reveal any large-scale imperfections in the crystal. Here the diamond is set at the Bragg angle for a particular set of planes and a photograph is taken of the scattered X-rays. It is possible to sample the whole volume of the crystal, and the photograph will reveal dislocations, growth boundaries and any feature which prevents Bragg scattering at the selected angle taking place.

iii. Section topographs which show the depth profile of the imperfections of the crystal. By collimating the X-ray beam to a narrow strip a few μm wide, the effects of dislocations and boundaries within the lattice

through the thickness of the diamond can be examined. Hence, by measuring projection and section topographs, a 3-dimensional picture of the diamond can be obtained. It is also possible to differentiate between screw and edge dislocations.

These techniques were used to examine a diamond which had been used at Mainz for several years for providing linearly polarized photons. The electron beam on the diamond had a diameter of about 100μm and it was estimated that around 10^{20} electrons had passed through the diamond. There was a small greenish black spot where the beam had hit the diamond.

The X-ray rocking curve measurements showed that considerable damage had occurred to the integrity of the crystal structure in the center of the beam spot. However 2 mm away from the damage center the width of the diffraction peak was the same as it had been for the pristine crystal, which indicates that the lifetime of the crystal could be extended by occasionally moving the beam spot on the face of the crystal.

At Mainz the area of the beam spot on the radiator is two orders of magnitude smaller than what is being planned for Hall D. A larger spot means a longer crystal lifetime before radiation damage substantially degrades its crystal properties. Appropriately scaled, the exposure of the Mainz crystal would correspond to 15 straight years of running in Hall D at the full intensity of 3μA without a spot move. Plans for the Hall D source are to keep the exposure about three orders of magnitude less than this. The SLAC group found that the performance of their diamonds had degraded noticeably after a total charge of 3 Coulombs had been accumulated over a spot of size roughly 2 mm r.m.s., leading to a limit of about 0.25 Coulomb/mm^2. Taking this as a conservative estimate for the allowed exposure, the source can run at a full intensity of 3μA for 60 hours before it is necessary to move the spot on the crystal. If it had no bad zones, a square crystal of 5 mm $\times$ 5 mm would accomodate 5 spot moves before the crystal would need to be replaced. SLAC researchers were able to recover a good performance for the damaged crystals by putting them through an annealing process. Further research and development will be required to determine whether this is an effective way of reducing the operating costs of the Hall D source.

Another issue to be addressed is that of heat dissipation for very thin crystals. The heat comes from the ionization energy loss of the beam as it passes through the crystal. Although this is small compared to the bremsstrahlung energy loss, it is not entirely negligible at these beam currents. It can be calculated using the restricted energy loss formula, which yields 21mW for a 15 μm (10^{-4} radiation lengths) crystal at a current of 3 μA. This is not much power,

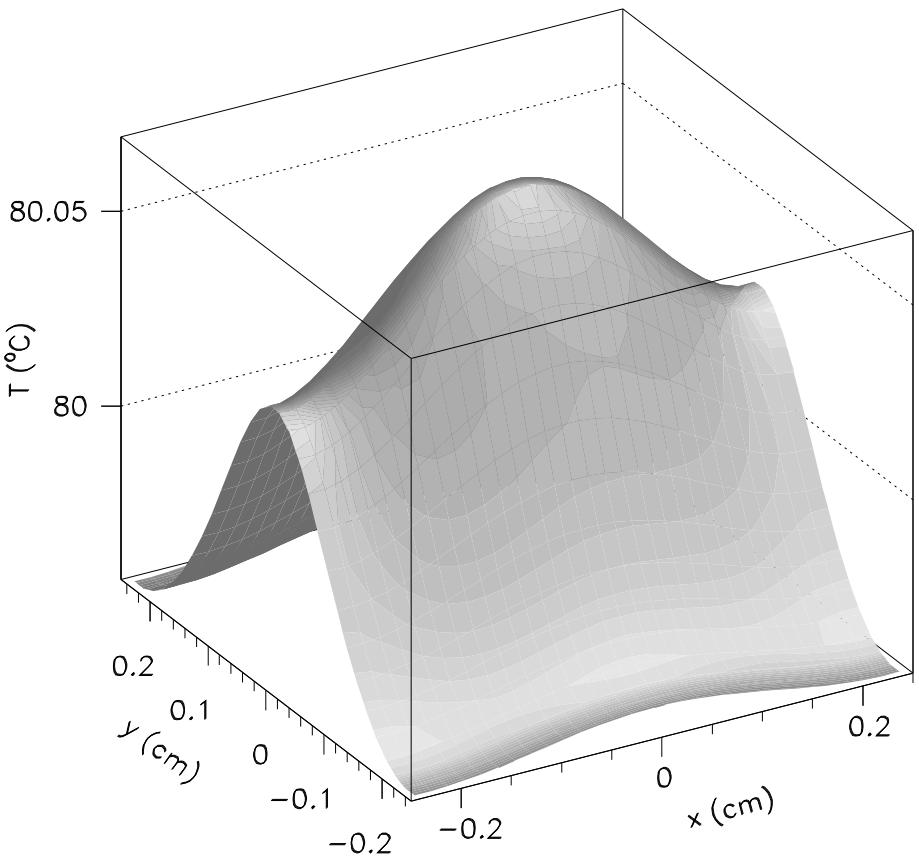

Figure 4.12: Calculated temperature profile of diamond crystal with a 12 GeV beam at 3μA. The crystal dimensions are 5 $mm \times 5\,mm \times 15\mu$m. The ambient room temperature was taken to be 27^oC (300 K).

but the crystal is very thin. Heat dissipation is through radiation and conduction. Diamond has a very high melting point; at low pressures it sublimates at about 4027 ^{o}C. However at normal pressures it begins to transform into graphite above 707 ^oC, at a rate that depends on temperature. It is therefore important that the crystal at the center of the beam spot stay well below this limit.

The diffusion equation including a heating term and one for radiative cooling can be written as

$$C_P\, a\, \frac{dT}{dt} = h(x,y) - 2\sigma\left(T^4 - T_0^4\right) + \kappa\, a \nabla^2 T$$

where the heating term $h(x,y)$ has units of power/area, σ is the Stefan-Boltzmann constant, C_P is the heat capacity and κ the coefficient of conduction for diamond, and a is the thickness of the crystal. T_0 is the ambient temperature of the environment and T is the local crystal temperature, a function of space and time coordinates. After a certain time, T converges to the steady-state solution shown in Fig. 4.12. The calculation used a crystal of dimensions $5\,mm \times 5\,mm \times 15\mu$m and a beam current of 3μA. This calculation shows that the conductivity of diamond is sufficient to prevent significant temperature gradients across the crystal even for very thin wafers, and that radiative cooling alone is sufficient to dissipate the heat being generated by the beam passing through the crystal so that the crystal mount does not need to act as a heat sink.

4.3 Electron beam

The performance of the photon source is dependent upon the parameters of the electron beam in several important areas. These parameters are listed in Table 4.3. The first column of numbers gives the set of parameters that have been adopted as the design goals for the source. These are the values that have been taken as input in calculating the characteristics of the coherent bremsstrahlung source for HALL D. The second column of numbers was obtained from a concrete design of the HALL D beam line [99] that was carried out by members of the Jefferson Lab Accelerator Division. The exact choice of the final parameters has not yet been made, but the preliminary design shows that all of the design goals can be met within the available real estate.

The following sections highlight the particular properties of the electron beam which have a special impact on the performance of the source.

parameter	design goals	design results
energy	12 GeV	12 GeV
electron polarization	not required	unknown
minimum useful current	100 pA	100 pA
maximum useful current	3 μA	3 μA
r.m.s. energy spread	< 10 MeV	7 MeV
transverse x emittance	10 $mm{\cdot}\mu$r	10 $mm{\cdot}\mu$r
transverse y emittance	2.5 $mm{\cdot}\mu$r	2.3 $mm{\cdot}\mu$r
x-dispersion at radiator	none	negligible
y-dispersion at radiator	none	$<$ 1cm
x spot size at radiator	1.7 mm r.m.s.	1.55 mm r.m.s.
y spot size at radiator	0.7 mm r.m.s.	0.55 mm r.m.s.
x image size at collimator	0.5 mm r.m.s.	0.54 mm r.m.s.
y image size at collimator	0.5 mm r.m.s.	0.52 mm r.m.s.
distance radiator to collimator	80 m	80 m
position stability	$\pm$200 μm	

Table 4.3: Electron beam properties that were asked for (column 2) and obtained (column 3) in a preliminary optics design for the transport line connecting the accelerator to the HALL D photon source.

4.3.1 Beam polarization

It has already been stated that to generate bremsstrahlung photons with linear polarization it is necessary to use an oriented crystal radiator. However photons with circular polarization are produced by ordinary incoherent bremsstrahlung any time the incident electrons are longitudinally polarized. In fact for 9 GeV photons produced by 12 GeV electrons, the polarization transfer from electron to photon beam is almost 90%. This raises the question of what happens when one has longitudinally-polarized electrons incident on an oriented crystal radiator. What happens in this case is that the photon beam is elliptically polarized; it carries both circular and linear polarization. There is a sum rule that limits the sum of the squares of the linear plus circular polarizations to be no greater than 1. Hence one sees the linear polarization in coherent bremsstrahlung going to zero as one approaches the end-point energy (see Fig. 4.8) while at the same time the circular polarization goes to 1 at the end-point (assuming electrons of 100% longitudinal polarization).

Thus the statement in Table 4.3 that electron beam polarization is not required for HALL D is correct, but it is not correct to assume that the photon source is independent of the state of polarization of the electron beam. The presence of a non-zero circular polarization in the HALL D photon beam will, in principle, produce observable effects in the angular distributions measured in photoproduction reactions. This means that there will be an important coupling between the HALL D program and the other experimental halls whose programs sometimes require them to have control over the beam polarization. This coupling can be eliminated by setting up the tune of the electron beam line to HALL D such that the longitudinal component of the electron beam polarization is rotated to zero at the crystal radiator. Whether the decision is made to rotate it away or simply to measure its value periodically, this consideration underlines the importance of having a means to measure photon beam polarization in a way that does not rely on *a priori* knowledge of the properties of the electron beam.

Although the ability of the source to produce photon beams with both circular and linear polarization complicates operation when one of them is desired without the other, it does increase the versatility of the source. The two kinds of polarization are controlled independently of one other, and together they give access to a more complete set of polarization observables than would be possible with only one or the other.

4.3.2 Beam emittance

The values for the electron beam emittances shown in Table 4.3 are estimates based upon the parameters of the current machine projected to 12 GeV[99]. The definition of emittance used here is the product of the r.m.s. widths of the beam in transverse position and divergence angle. Because synchrotron radiation inside the accelerator occurs mainly in the horizontal plane , the emittance values in x are generally larger than those for y. The two vertical bends required for bringing the 12 GeV beam from the level of the accelerator up to beam height in HALL D do increase the vertical emittance a small amount over its value inside the machine; this effect has been included in computing the vertical emittance shown in Table 4.3.

The longitudinal emittance of the beam is important as it is the limiting factor in determining the ultimate energy resolution of the tagger. The design goal of 0.1% photon energy resolution is well matched to the energy spread expected for the CEBAF beam at 12 GeV.

The place where transverse emittance plays a critical role is at the photon collimator. For optimum effectiveness in collimation it is important that the electron beam spot at the collimator position be as small as possible. The electron beam does not actually reach the photon collimator, being bent into the dump by the tagger magnet shortly after the radiator . But considering the optics of the electron beam as if the tagger dipole were switched off, the electron beam at the radiator can be projected forward to form a virtual image on the collimator entrance plane. The position and size of this virtual spot determines the definition of 0° emission angle for the photons. If this spot is small compared to the collimator aperture and is correctly centered then the bremsstrahlung photons of a given emission angle α intersect the entrance plane of the collimator in a well-defined ring of radius $D\alpha$ concentric with the collimator aperture, where D is the distance between the radiator and the collimator entrance plane. In this way a collimator of diameter d passes only those photons of emission angle $\alpha \leq d/2D$. If however the size of the virtual spot is comparable to or larger than the collimator aperture then the ring image of photons of a given emission angle α is smeared out, so that the effect of collimation is simply to reduce the intensity of the pre-collimated beam but not to enhance the coherent component.

Note that this analysis does not place any specific limits on the size of the beam at the radiator. The beam spot can and should be larger there to increase the lifetime of the crystal between spot moves. For the SLAC coherent bremsstrahlung source the beam spot at the radiator was about 3 mm r.m.s. focused down to a 1 mm r.m.s. virtual spot at the primary collimator positioned

91 m downstream of the radiator.

The superior emittance characteristics of the CEBAF beam allow the transverse dimensions to be somewhat smaller than this for the HALL D source, more so in the vertical than the horizontal dimension. The difference between the horizontal and vertical emittance of the CEBAF beam implies that making the spot round at the radiator implies an elliptical virtual spot at the collimator, and *vice versa*. The collimator aperture is circular, so the choice was made to make the virtual spot round. This is why the beam spot on the radiator is asymmetric.

Figure 4.13 shows how the collimated photon spectrum depends upon the transverse emittance of the electron beam. To generate this plot the increases in emittance were simply translated into an increased virtual spot size on the collimator. This was done because it was assumed that the spot size of the electron beam on the radiator, already close to 2 mm r.m.s., cannot be further inflated and stay contained within the limits of the crystal. When the virtual spot size becomes comparable with the collimator aperture then the collimation is rendered ineffective, and the photon spectrum and polarization revert to their uncollimated values. There is another connection between focal spot size and beam emittance that is connected with the requirement that all electrons enter the radiator at the same incidence angle with respect to the planes of the crystal. Practically, the divergence does not broaden the coherent peak provided that it is kept below the mosaic spread of the crystal. A conservative value for the allowable angular divergence δ in the electron beam at the radiator would then be 20 μr . Taken together with a 500 μm r.m.s. spot size at the focus, this leads to an emittance of 10 $mm{\cdot}\mu$r at 12 GeV. This corresponds to the upper curve in Fig. 4.13.

4.3.3 Electron beam line optics

Translating the beam emittance into a r.m.s. values for the beam radius and divergence requires the knowledge of the β function of the transport line between the accelerator and the radiator. Beta is defined as the ratio of the r.m.s. beam size to its angular divergence.

The preliminary optics design [99] of the HALL D beam line (see Table 4.3) is shown in Fig. 4.14. The horizontal and vertical beta functions are shown in the upper and lower panels, respectively. Between the two panels is shown a schematic of the transport lattice. The design begins at the exit of the beam from the end of the linac and ends at HALL D. The z coordinate is measured along the axis of the linac, with its origin at the mid-point of the accelerator. Fig. 4.15 shows the beta functions translated into r.m.s. beam size and shifted

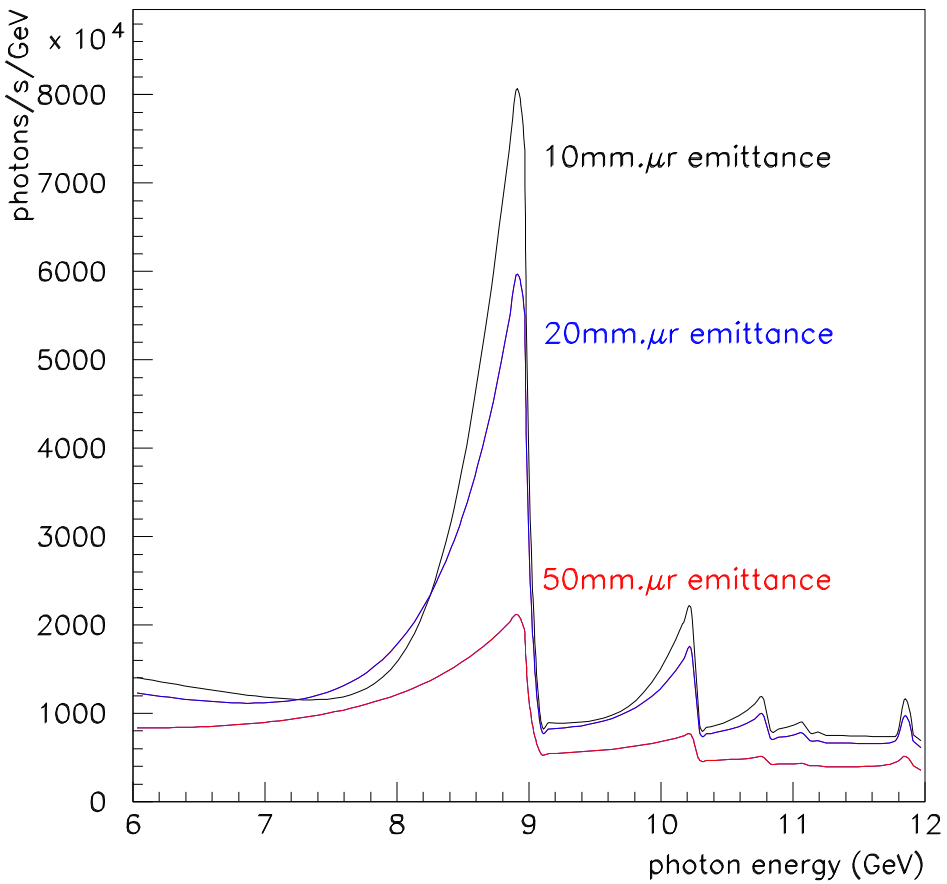

Figure 4.13: Coherent photon spectrum for three different values of the electron beam transverse emittance. The horizontal (shown on the plot) and vertical emittances are assumed to scale together. A 3.4 mm collimator located 80 m from the radiator was used for this calculation.

to place the radiator at the origin. The design allows the ratio of the spot sizes at the radiator and collimator to be adjusted over about an order of magnitude simply by changing the current in the beam line elements. In this way it will be possible to optimize the optics for a given size of crystal and collimator after beams are delivered to the hall, and more precise values for the emittances are in hand.

Not only must the virtual electron spot be small enough to fit within the collimator aperture, but it must also be centered on the aperture and stable. In order to maintain a stable beam position on the collimator, the SLAC experiment [94] instrumented the collimator with a secondary-emission detector (SEQ). The detector was of the "pin-cushion" design and was installed as a segment of the collimator near the position of the shower maximum. The readout was divided into four quadrants, which read equal currents when the beam was properly aligned on the collimator. The SEQ was connected via a feedback loop to the last steering elements on the electron beam line prior to the radiator. From that distance a bend of only $10\mu r$ results in a shift of $1\,mm$ at the collimator position. Hence the beam alignment feedback system is effectively decoupled from the crystal orientation controls.

The small deflections that are necessary to keep the beam centered on the collimator do not produce appreciable walk in the beam-crystal angle. This means that an active feedback system can be set up between the instrumented collimator and deflection coils just upstream of the radiator, that can operate independent of the crystal alignment system to keep the electron beam aimed at the center of the collimator.

The experimental program in parity violation at Jefferson Lab has already demonstrated a position stabilization circuit that is able to keep the beam position steady to within $20\mu m$ over a 20 m lever arm. A less sophisticated version of this circuit will meet the position stability requirements for the HALL D photon source.

4.3.4 Electron beam dump

The electron beam is dumped in the horizontal plane, as shown in figure 4.4. The horizontal bend offers several advantages over dumping the beam into the ground. The tagger magnet is easier to support if it sits in the horizontal position. It is also easier to mount and service the focal plane in this position. The dump itself is also more accessible in case it needs to be serviced. An above-ground dump also affords the possibility of running parasitic beam dump experiments that do not interfere with the operation of the experimental hall.

The primary design requirement for the electron beam dump is that it has

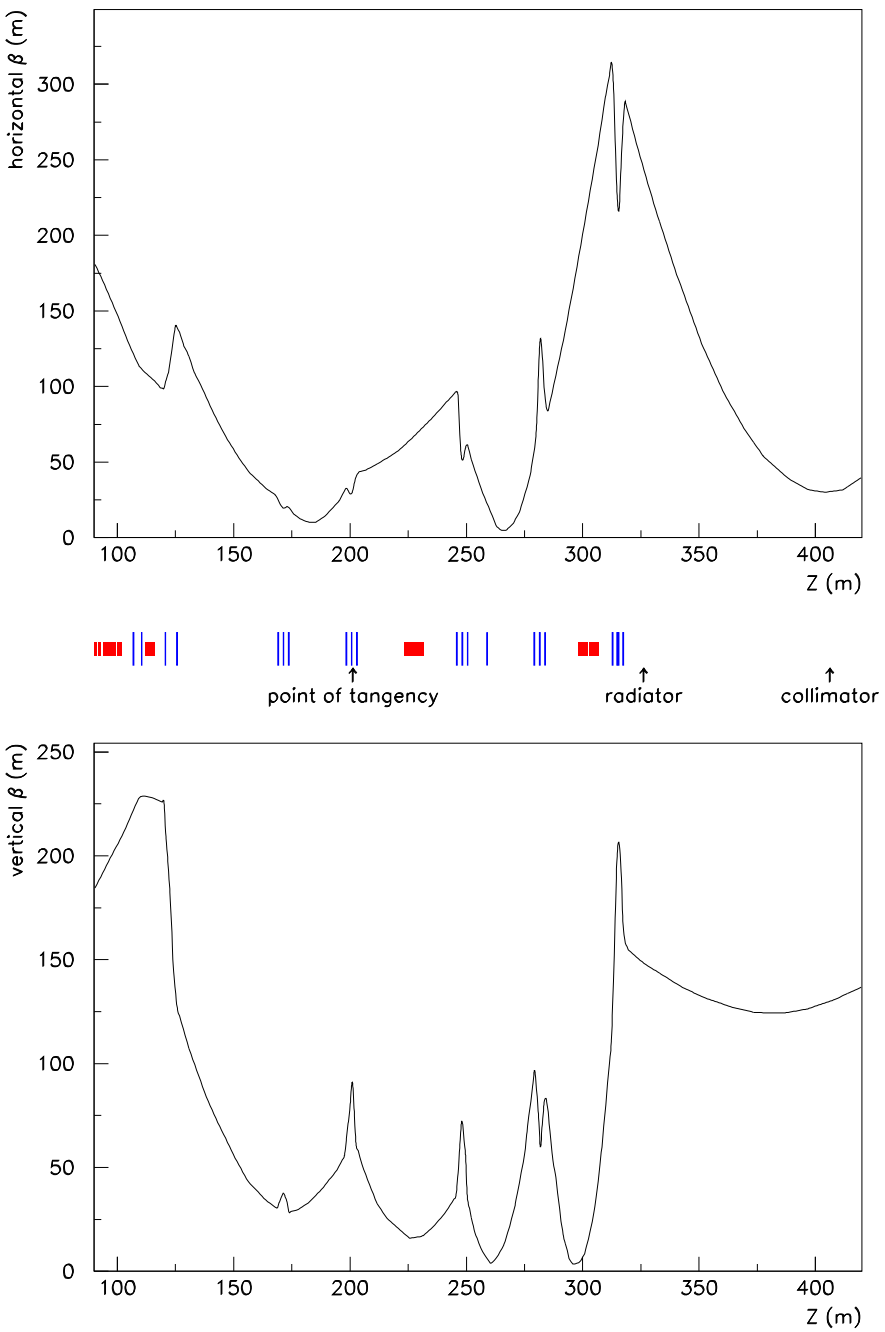

Figure 4.14: Horizontal (upper panel) and vertical (lower panel) beta functions from the preliminary optics design for the transport line from the accelerator to the HALL D photon source. The beam line lattice is shown schematically between the two panels, with dipole magnets represented by the short boxes and quadrupoles by the taller lines. The z coordinate is equal to the flight path length of the electrons starting at the center of the linac, up to an error of a few cm from the vertical motion of the beam.

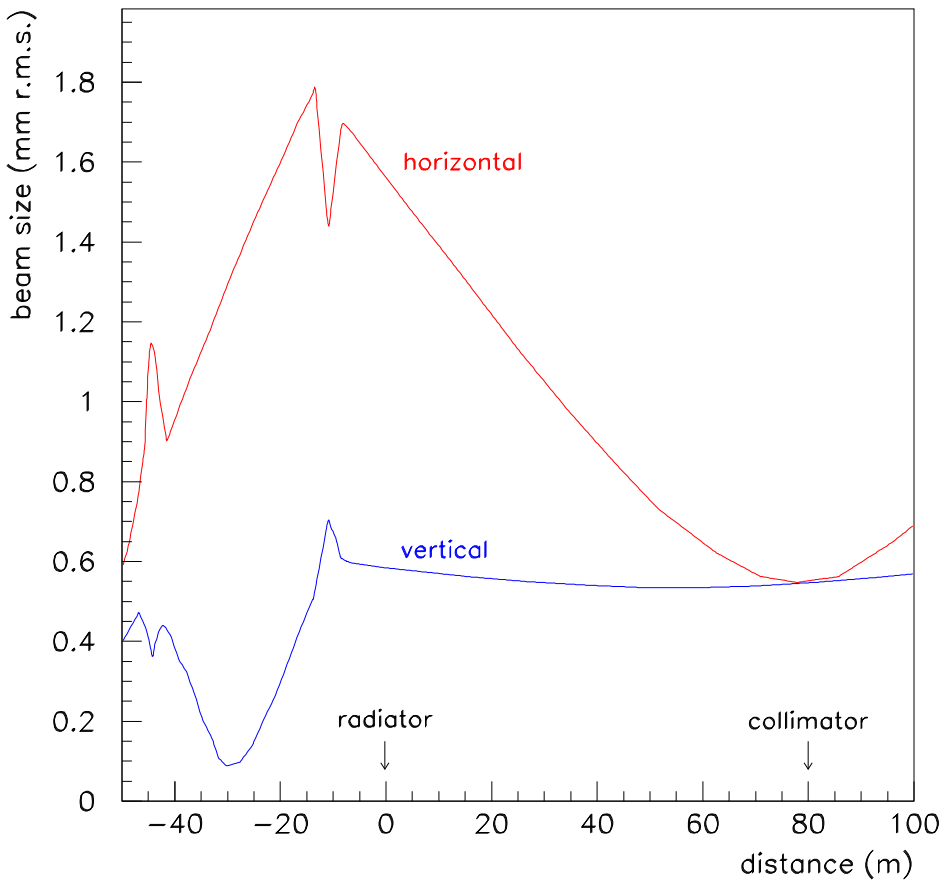

Figure 4.15: Horizontal and vertical r.m.s. envelopes for the electron beam in the region of the photon source, as derived from the beam emittance and beta functions of Fig. 4.14. The origin of the z coordinate has been placed at the radiator. In the region between the radiator and the collimator the envelope refers to the projected image of the electron beam, and does not describe the size of a physical beam that exists in that region.

a sufficiently high capacity to handle beams of the highest intensities foreseen for HALL D. A 60KW design would provide a a healthy margin for operation of a 12 GeV beam at 3μA and sufficient capacity to handle 3μA at 20 GeV in the case of a further upgrade.

4.3.5 Beam containment and shielding

There are three factors that must be taken into account in the design of the shielding for the HALL D beam line. The first is the constraint on the background radiation level that is allowed outside the beam enclosure. The second factor is the level of radiation in the experimental hall which can generate background in the detector during normal running. The third factor is the control of hazards which may occur in the event of a failure of one or more of the beam delivery systems. The first issue has been studied by the Jefferson Laboratory Radiation Controls Group, and will be discussed further in the chapter on Civil Construction. The latter two considerations have been studied by a working group headed by L. Keller (SLAC). A summary of their recommendations [100] follows.

Assuming that the electron beam dump is shielded to the requirements of radiation safety, the next source of background radiation in the experimental hall is the photon collimator. The most penetrating forms of radiation from the collimator are muons and neutrons. A Monte Carlo simulation, assuming a 13 radiation lengths tungsten collimator followed by a sweeping magnet and 5 m of iron shielding, predicted a flux of $1.4 \times 10^3 \mu$/s incident on the detector at full operating beam intensity. This is a negligible rate compared with the trigger rate from photon interactions in the target. The flux of neutrons from the collimator is more difficult to calculate, but some fraction of 1m of concrete shielding will be needed surrounding the collimator enclosure to shield the hall from energetic neutrons.

With regard to hazards associated with the accidental failure of beam line elements or controls, the following measures were recommended in the Keller study [100] and have been incorporated into the HALL D design. The dipole string that bends the electron beam up towards the surface from the below ground and then bends it back horizontal will be connected in series so that failure of a magnet supply or current control electronics cannot result in a beam being steered into the ceiling of the tagger building. The power supply feeding this string of magnets will be protected by a meter relay that shuts off if the current varies from its desired value outside a predefined tolerance. A similar meter relay will also be used on the power supply of the tagger magnet. An electron beam collimator with a burn-through monitor will be located just

upstream of the radiator to prevent a mis-steered beam from using radiator support structures as a bremsstrahlung target. Permanent magnets will be located in the upstream region of the photon beam line to bend an errant electron beam into the ground in the case that beam is present while the tagger magnet is off. An emergency beam stop will be installed in the bottom of the photon beam line to catch the errant beam deflected by the permanent magnets. It will be equipped with a current monitor to shut down the primary beam any time electrons are sensed in the photon beam line. Ion chambers located upstream of the photon collimator, and also at the entrance to the photon beam dump behind the experiment, will monitor the total flux in the photon beam and shut off the beam if the flux exceeds a safe value.

4.4 Tagging spectrometer

4.4.1 Specifications

To satisfy the needs of the HALL D physics program, the tagged photon spectrometer should meet the following specifications:

1. Photon energy detection from 70% to 75% of E_0 with energy resolution of about 0.1%. Percentages refer to the primary beam energy E_0, i.e. "0.1%" means 12 MeV energy resolution for a 12 GeV beam.

2. A detector system which allows a counting rate of at least 5×10^6 electrons per second per 0.1% over this range of photon energies.

3. An additional capability for photon energy detection from 25% to 90% of E_0, with less stringent resolution and count rate requirements .

4. A quadrupole magnet between the radiator and dipole spectrometer which images the beam spot on the radiator onto a line on the focal plane. This feature makes it possible to envision the use of focal plane counters with two-dimensional readout, with which one could enhance the tagging efficiency and linear polarization of the source. Focal plane detectors with two-dimensional readout are considered as a possible upgrade beyond the baseline design presented in this chapter. Any improvements obtained using this technique would be over and above the performance figures presented in this report.

The system described below meets all of these criteria.

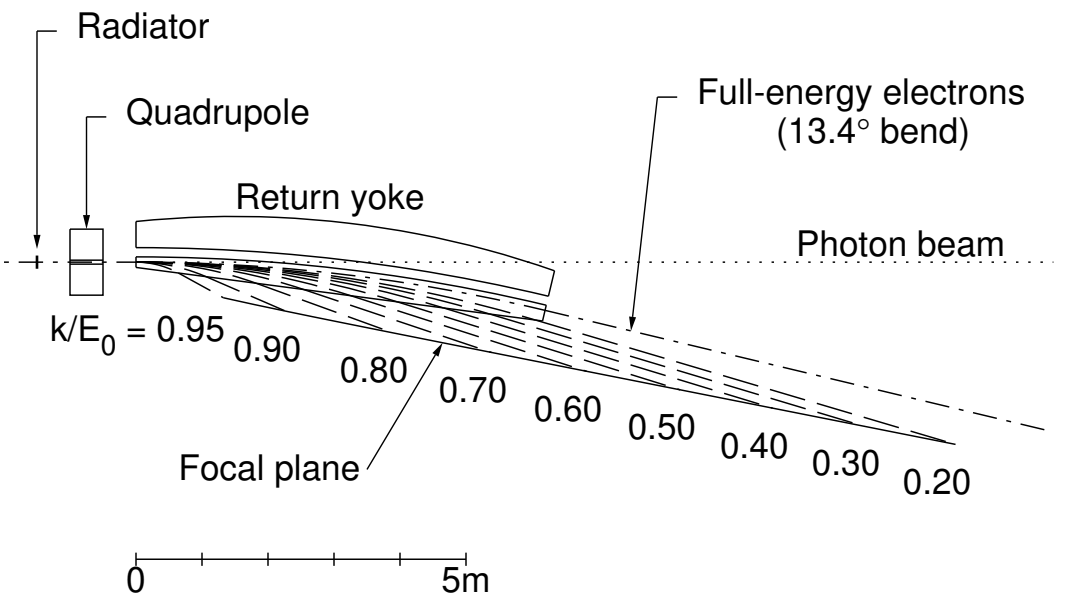

Figure 4.16: A plan view of the tagging spectrometer from above, showing the path of the primary beam and the trajectory of post-bremsstrahlung electrons of various recoil momenta.

4.4.2 Magnet

The tagger magnet (Fig. 4.16) is an Elbek-type spectrometer similar to the existing tagger magnet in Hall B of Jefferson Lab.[101] The higher energy of the HALL D beam is largely compensated for by going to smaller bend angles, so the sizes of the magnets are comparable, and much of the experience from Hall B can be carried over. Unlike the Hall B tagger, which bends vertically, the HALL D tagger will deflect electrons in the horizontal plane, with both the detector hall and the beam dump constructed above ground.

The parameters of the magnet are given in Table 4.4. The magnet poles themselves will form part of the vacuum system, and will be welded to a stainless steel vacuum chamber which terminates in a thin window along the length of the focal plane.

The detector package is divided into two parts: a set of 128 fixed scintillation counters spanning the full energy range from 25% to 92%, and a movable "microscope" of 64 narrow counters that is optimized for normal operation spanning the energy range from 70% to 75%.

Radius of curvature	26.7 m
Full-energy deflection	13.4^{o}
Field at 12 GeV	1.5 Tesla
Gap width	2.0 cm
Length of pole	6.1 m
Weight	100 tons
Length of focal plane (25% to 90% of E_0)	8.7 m
Coil power	800 A at 22 V

Table 4.4: Design parameters for the tagging spectrometer dipole magnet

The fixed array provides access to the full tagged photon spectrum, albeit at a modest energy resolution of 0.5% and reduced photon spectral intensity. These detectors are well suited for running with a broadband incoherent bremsstrahlung source. They enable experiments to be performed with the highest photon energies possible with the source. When running with a coherent source they play an essential role in the crystal alignment procedure, and provide a continuous monitor of the performance of the source. The microscope is needed in order to run the source in coherent mode at the highest polarization and intensities, and whenever energy resolution better than 0.5% is required. Using the microscope, the source is capable of producing photon spectral intensities in excess of 2×10^8 photons/GeV, although accidental tagging rates will limit normal operation to somewhat less than this.

4.4.3 Spectrometer optics

Table 4.5 and Table 4.6 give some of the beam optics parameters as functions of the photon energy. The energy resolution and transverse position resolution were calculated using the following assumptions for the beam at the radiator:

$$\Delta E/E_0 = 0.080\% \text{ r.m.s.}$$
$$\Delta x = 1.7\, mm \text{ r.m.s.}$$
$$\Delta y = 0.5\, mm \text{ r.m.s.}$$
$$\Delta x' = .020 \text{ mr r.m.s.}$$
$$\Delta y' = .005 \text{ mr r.m.s.}$$

The intrinsic energy resolution (i.e. the energy resolution independent of detector size) is limited in most cases by the 0.08% energy spread of the primary electron beam.

Table 4.5: Geometrical parameters of the tagging spectrometer for $E_0 = 12\ GeV$: Bend = deflection angle; Drift = distance from exit edge to focal plane; Angle = angle between electron path and focal plane; cm/%E_0 = dispersion in units of cm per percent of the incident energy

k (GeV)	Bend (deg)	Drift (m)	Angle (deg)	cm/%E_0 perp.to ray	cm/%E_0 along FP
6	17.270	3.7790	6.035	1.467	13.956
7	17.664	3.2039	6.428	1.568	14.008
8	18.28	2.6276	6.992	1.716	14.096
9	19.108	2.0485	7.872	1.954	14.264
10	20.695	1.4626	9.459	2.407	14.644
11	24.608	0.8560	13.372	3.668	15.860

At the focal plane, the characteristic bremsstrahlung angle corresponds to a few millimeters of transverse displacement. The vertical beam spot size at the radiator (0.5 mm r.m.s.) contributes a comparable amount because of the large transverse magnification in the dipole transport matrix. However, placing a quadrupole magnet between the radiator and the tagger dipole magnet reduces this magnification nearly to zero over a substantial range of photon energies without substantially changing the other optical properties. Including the quadrupole in the design makes possible a future upgrade of the photon source by employing tagging detectors with two-dimensional readout.

4.4.4 Tagger detectors

Focal plane microscope detectors

Since the intrinsic energy resolution along the focal plane is approximately 0.1% (Table 4.6), a detector width which spans an energy range of 0.2% could be used without seriously affecting experimental resolution (the r.m.s. deviation of a flat distribution of width W is $W/\sqrt{12} = 0.29W$. The principal limitation on detector size is imposed by the design goal of tagging collimated photons at rates up to 100 MHz over the coherent peak. The nominal collimated coherent peak has its highest intensity between about 8.5 and 9 GeV (see Fig. 4.6). However, the the tagger sees both collimated and uncollimated photons, and the total tagging rate in this region is about twice the collimated rate (see Fig. 4.6), so the actual tagging rate must be about 200 MHz. If a

Table 4.6: Optical properties and resolutions of the tagging spectrometer at the focal plane, for $E_0 = 12\ GeV$: (x x),(y y),(y y') = first-order transport matrix elements where x and y are radial and transverse coordinates respectively; the focal plane is defined by (x x')=0.; Δk_{beam} = r.m.s. energy resolution due to beam energy uncertainty; Δk_{spot} = r.m.s. energy resolution due to spot size on radiator; Δk_{tot} = total r.m.s. energy resolution excluding detector size; Δy_{tot} = transverse r.m.s. position resolution due to spot size on radiator; y_{char} = transverse size corresponding to one characteristic electron angle $\theta_{Ce} = (m/E_0)(k/(E_0 - k))$.

k	(x x)	(y y)	(y y')	Δk_{beam}	Δk_{spot}	Δk_{tot}	Δy_{tot}	y_{char}
(GeV)	(mm/mm)	(mm/mm)	(mm/mr)	($\%E_0$)	($\%E_0$)	($\%E_0$)	(mm)	(mm)
Without quadrupole:								
6	-0.701	2.737	18.882	0.080	0.081	0.114	1.372	0.804
7	-0.667	2.708	16.538	0.080	0.072	0.108	1.357	0.986
8	-0.625	2.670	14.178	0.080	0.062	0.101	1.337	1.207
9	-0.569	2.617	11.788	0.080	0.050	0.094	1.310	1.506
10	-0.494	2.539	9.341	0.080	0.035	0.087	1.270	1.989
11	-0.389	2.402	6.745	0.080	0.018	0.082	1.201	3.159
With quadrupole: (length = 50 cm, gradient = -0.4 kGauss/cm)								
6	-0.628	0.451	17.622	0.080	0.073	0.108	0.242	0.750
7	-0.583	0.348	15.121	0.080	0.063	0.102	0.190	0.901
8	-0.526	0.202	12.535	0.080	0.052	0.095	0.119	1.068
9	-0.449	-0.024	9.792	0.080	0.039	0.089	0.050	1.251
10	-0.338	-0.427	6.699	0.080	0.024	0.083	0.216	1.426
11	-0.162	-0.416	2.474	0.080	0.008	0.080	0.708	1.159

single phototube can count reliably at 5 MHz, then the energy range detected by a single scintillation counter should be 5 MHz / 200 MHz * 600 MeV = 15 MeV= 0.12% of E_0. Thus a detector width of 0.1% would satisfy the requirements of both resolution and rate. According to Table 4.5, such a detector would have a width of 3 mm perpendicular to the electron direction, and detectors for individual channels would be spaced about 30 mm apart along the focal plane.

Fixed focal plane array

Tagging of photons over the full range from 25% to 90% of E_0 is not required as part of the physics program here proposed for HALL D, but is desirable for two separate reasons. First, it will increase the flexibility of the source by allowing other possible experiments using highly polarized photons below 8 GeV, or incoherent bremsstrahlung up to 11 GeV. This capability is not available elsewhere at JLab, since the Hall B tagger will not handle beam energies above 6 GeV and its photon polarization will be quite low for photon energies above about 4.5 GeV. Second, the process of aligning the crystal radiator for coherent bremsstrahlung requires rotation about several axes and rapid observation of the resulting energy spectra, as described in section 4.2.6. The low-energy portion of the spectrum, between about 25% and 50% of E_0, is most sensitive to these rotations, and experience with the coherent bremsstrahlung beam at Mainz [102]-[103] indicates that the alignment process would be severely compromised if photon energies below 0.5 E_0 were not measurable.

A high energy resolution in the tagger is not deemed necessary for these purposes. A counter width spanning 0.5% of E_0 is considered sufficient in most cases. For operations with an amorphous radiator, these counters would be capable of running a broad-band photon beam with the highest intensities compatible with tagging. Crystal alignment procedures are not normally carried out at full source intensity, so rate capacity is not a limitation in that application. If a need arose to operate the source in collimated-coherent mode at lower photon energies, for example to obtain increased polarization, then full-intensity operation would always be possible by repositioning the microscope on the focal plane. In this case, the fixed array would be useful in fixing the energy calibration of the moveable segment. When used as the primary tagging detectors, the fixed array would be capable of pre-collimated intensities up to 80 MHz/GeV.

4.4.5 Beam dump optics

Although the full-energy beam leaving the tagger magnet is diverging in both directions, the range of angles is small enough that the beam does not blow up rapidly. For a dump distance of 30 m the r.m.s. beam size is 6.3 mm horizontal (dominated by the 0.08% beam energy spread) and 0.7 mm vertical (combination of vertical spot size and multiple scattering in a 10^{-4} radiation length radiator.) These values scale approximately linearly with distance from the magnet to the dump, and are not very sensitive either to the quadrupole or to small rotations of the exit edge of the tagger magnet. Thus the beam dump design is quite insensitive to the beam optics, and depends only on the lateral and longitudinal spread of the shower.

4.5 Polarimetry instrumentation

The major part of produced photons will be cut out in the proposed collimator system. In case the radiator and collimator system are well aligned, the expected photon spectrum behind the collimators is dominated by the coherent peak. The beam parameters can be determined by using the intensity spectra of the tagging channels.

Nevertheless, in order to monitor the polarization parameters – grade (P_γ) and direction (ϵ_γ) – of the collimated photon beam it is crucial to have an independent method, either a photon polarimeter detecting the asymmetry of a process that is well understood within theory (QED) or a well known hadronic process so that the measured beam asymmetry can be compared with theoretical (or experimental) expectations. At photon energies above 5 GeV, the forward production of vector mesons is described by VMD, thus resulting in a $sin^2\theta_{hel}cos(2\psi)$ dependence of the vector meson's decay distribution where θ_{hel}, ϕ_{hel} are the polar and azimuthal decay angles in the helicity frame and $\psi = \phi_{hel} - \epsilon_\gamma$. Acceptance studies have to be performed in order to estimate the time needed to collect sufficient statistics for these processes.

The other method, measuring the photon polarization by means of a polarimeter, can be realized by a pair polarimeter or a triplet polarimeter. It involves additional hardware components on the beamline between the collimator system and the spectrometer magnet. Both types of polarimeter require a thin radiator and a detector in a field free area followed by a dipole magnet and counters for the trigger.

QED based calculations for the latter process show that the angle and energy of the soft (triplet) electron is almost independent of the energy of the

incident photon ($\bar{E}_{triplet} \approx 0.7 - 0.9$ MeV). The low rate of this process and the technical challenge for a counter device measuring accurately the angular distribution of low energy electrons do not favor this type of polarimeter.

For pair production, on the other hand, the opening angle between the produced electron and positron decreases with increasing energy making the measurement more complicated at higher energies. A magnetic separation is not desirable because the deflection cannot be determined very accurately. The proposed polarimeter consists of a thin scintillator (d=50 μm) as an active target, 1.5 m in front of a silicon microstrip detector arrangement, followed by a dipole magnet and two scintillators 10 cm apart from the beamline for triggering on symmetric e^+e^- pairs. The microstrip detector consists of four layers having 512 channels each of silicon wafers with a spatial width for a single channel of 25 μm. The second and third layer are oriented at $\pm 60°$ with respect to the first layer, the fourth perpendicular to one of the previous layers, thus allowing to measure the full angular range of produced e^+e^--pairs without any gap in the acceptance. A Monte Carlo simulation of this device including multiple scattering in the target, the microstrip detector, and foils in the vacuum system (using GEANT) shows that an analyzing power of 25% is achievable (cf. fig 4.17). QED calculations predict an angular distribution for pair production proportional to $(1 + P_\gamma \alpha \cos 2(\phi - \epsilon_\gamma))$ with an analyzing power of $\alpha = 0.28$ for incident photons in the range of 6-10 GeV. Because of the thickness of the microstrip layers (300μm) it is convenient to measure the beam polarization for fifteen minutes every time the orientation of the crystal radiator or the electron beam parameters have changed. The scintillator target as well as the detector device have to be mounted on motor driven stages so that they can be removed from the beamline.

4.6 Operating beam intensity

Table 4.7 brings together the diverse set of parameters that must be considered in evaluating the optimum beam intensity at which an experiment using the coherent bremsstrahlung beam should operate. All four columns of numbers were obtained for the same beam conditions, except that the crystal orientation was adjusted to align the coherent intensity peak at the energy listed in row one. The second row, labeled N_γ, gives the integrated rate of beam photons in the coherent peak downstream of the collimator. Note the sharp decrease in the intensity of the coherent peak as the energy approaches the end point. By contrast, the incoherent bremsstrahlung flux is approximately constant over this range of energies. The third and fourth row show the height and width of

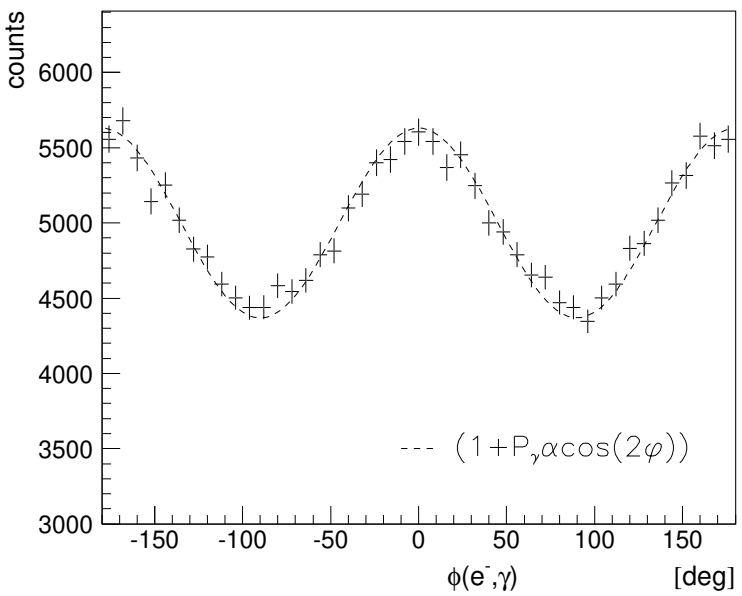

Figure 4.17: Angular distribution for pair production by linearly polarized photons as measured by a polarimeter in comparison with theoretical prediction (it dashed line). The count rate corresponds to 15 min data taking.

the peak in the polarization spectrum of the beam. Rows five and six report the height and width of the peak in the tagging efficiency spectrum. The tagging efficiency is defined as the number of beam photons of a particular energy reaching the target divided by the corresponding rate in the tagging focal plane. Large tagging efficiencies are required in order to make effective use of tagging. The width of the peak in the tagging efficiency spectrum determines the width of the focal plane that would be active when running with collimation. The peak integral reported in row two is summed within the f.w.h.m. tagging efficiency window. Rows seven and eight give the photon beam power that is incident on the experimental target (and photon beam dump) and the photon collimator, respectively.

The last two rows in Table 4.7 give the inclusive and tagged rates for hadronic triggers from a 30 cm liquid hydrogen target placed in the beam following the collimator. Note that the total hadronic rate is dominated by background (*i.e.* non-tagged) events associated with the low-energy compo-

E of peak	8 GeV	9 GeV	10 GeV	11 GeV
N_γ in peak	185 M/s	100 M/s	45 M/s	15 M/s
peak polarization	0.54	0.41	0.27	0.11
(f.w.h.m.)	(1140 MeV)	(900 MeV)	(600 MeV)	(240 MeV)
peak tagging efficiency	0.55	0.50	0.45	0.29
(f.w.h.m.)	(720 MeV)	(600 MeV)	(420 MeV)	(300 MeV)
power on collimator	5.3 W	4.7 W	4.2 W	3.8 W
power on target	810 mW	690 mW	600 mW	540 mW
total hadronic rate	385 K/s	365 K/s	350 K/s	345 K/s
tagged hadronic rate	26 K/s	14 K/s	6.3 K/s	2.1 K/s

Table 4.7: Operating parameters for an experiment using the coherent bremsstrahlung beam. The calculation assumes a 12 GeV electron beam energy and a 3.4 mm collimator 80 m downstream from a radiator of thickness 10^{-4} radiation lengths. The electron beam current is taken to be 3μA. The rates in the detector (last two rows) are calculated for a 30 cm hydrogen target and an open hadronic trigger.

nent of the beam. This is why the total trigger rate is essentially constant while the flux in the coherent peak varies with peak energy over an order of magnitude. This table illustrates the value of having an electron beam energy well above the photon energy needed for the experiment.

Chapter 5

The Hall D Detector

5.1 Overview

The goal of the HALL D experiment is to search for gluonic excitations with masses up to 2.5 GeV/c^2. The identification of such states requires knowledge about their production mechanism, the identification of their quantum numbers J^{PC} and their decay modes. The production mechanism and J^{PC} determination require a partial wave analysis which in turn depends on the kinematic identification of exclusive reactions. The decay products of produced mesons must be identified and measured with good resolution and with full acceptance in decay angles. In many cases the decays of mesons involve a chain of particle decays. The HALL D detector must therefore be hermetic with 4π coverage and have the capability of measuring directions and energies of neutral particles (γ, π^0, η) and momenta of charged particles with good resolution. Particle identification is also required.

The partial wave analysis technique depends on high statistics and in the case of incident photons, also requires linear polarization. As discussed in Chapters 3 and 10, the latter is needed to identify the production mechanism. The linear polarization is achieved by the coherent bremsstrahlung technique. The degree of linear polarization and flux of photons in the coherent peak fall dramatically as the photon energy approaches the endpoint energy. On the other hand, it is desirable to have photon energies high enough to produce the required masses with sufficient cross section and with sufficient forward boost for good acceptance. For a fixed incident momentum and a fixed resonance mass, it is also desirable to have a fairly constant t_{min} over the natural width of the resonance. This also requires sufficiently high incident photon energy.

An operating photon energy between 8.0 and 10.0 GeV produced from a

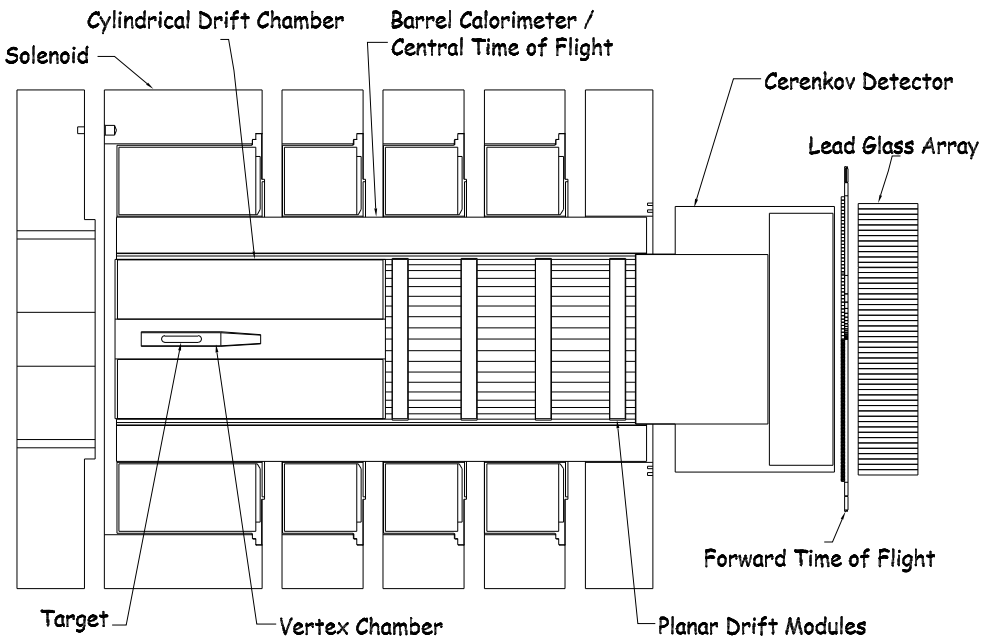

Figure 5.1: An overview of the HALL D detector. The major subsystems are labeled and are discussed individually in the text.

12.0 GeV electron beam represents an optimization of beam flux, cross–section and degree of polarization. The HALL D detector is therefore optimized for this energy range. Figure 5.1 is a schematic representation of the proposed HALL D detector. The individual subsystems are discussed in more detail below.

5.2 The solenoid

Momentum analysis of charged particles will be achieved using a superconducting solenoid and tracking chambers. The superconducting solenoid already exists. It was built for the LASS detector at SLAC and later moved to LANL where it was used for the MEGA experiment. The magnet is described in a technical note [104] and some relevant portions of that description are quoted below. Table 5.1 summarizes important magnet parameters. The refrigeration units are not currently available, and alternatives will need to be found. Additional information on the magnet can be found in Appendix B of this report.

The LASS solenoid magnet provides a 22.4 kG magnetic field parallel to the beam direction. The inside diameter of the magnet is 185 cm and its overall

Inside diameter of coils	80 *inches*
Clear bore diameter	73 *inches*
Overall length (iron)	183 *inches*
Inside iron diameter	116 *inches*
Outside iron diameter	148 *inches*
Coil-to-coil separation	11 *inches*
Total iron weight	200 *tons*
Central field	25 kG
Conductor current	1800 A
Total stored energy	36 MJ
Inductance	22 H
Total helium volume (including reservoir)	5,000 *liters*
Operating heat load (liquid He)	30 *liters/hour*
Operating heat load (liquid nitrogen)	30 *liters/hour*
Cool-down time	2 *weeks*
Copper to superconductor ratio	20:1 (grade A) 28:1 (grade B)
Total conductor length	117,600 *feet*
Total conductor weight	29,000 *lbs*
Turn on time	20 *minutes*
Turn off time (normal)	20 *minutes*
Axial load per coil due to magnetic forces	280 *tons*

Table 5.1: Summary of characteristics of the solenoid as used in the LASS configuration.

length is 465 cm.

The fiducial region within the bore is 320 cm in length and 75 cm in radius. Within this region the field homogeneity is better than $\pm$ 3.1%. Along the beam axis the homogeneity improves to $\pm$ 0.9%.

The solenoid is constructed of four separate superconducting toroidal coil-Dewar units [105] in order to permit inter-coil placement of planar proportional chambers. A 200 ton iron flux return path, similarly split in four places surrounds and supports the coil assemblies. A common liquid helium reservoir is located atop the solenoid providing the gravity feed of the liquid to the coils.

The superconductor used is a stabilized, composite, twisted, multi–filament niobium–titanium wire. The wire is made by soldering the superconductor composite between two copper strips to form a rectangular cross section 0.763 x 0.533 cm^2. The coil is wound directly on the liquid helium vessel inner cylinder wall. As the coil is wound, a 0.20 $inch$ thick stainless steel support band and a mylar insulating strip are wound along with it for mechanical support and insulation. Cooling by the liquid helium is accomplished from the edges. Each of the four toroidal windings has its own predetermined number of turns, the configuration being selected for optimum central field homogeneity consistent with the requirement of the inter-coil gaps and the large downstream end opening.

The liquid helium vessel is surrounded by a liquid nitrogen cooled radiation shield and this assembly is centered in the vacuum tank by a circumferential series of tie bolts designed for minimum conductive heat flux to the helium bath. Radial centering and support are achieved by four low conductance hangers arranged in a spiral pattern. Various tie rods and hangers are instrumented with stress bolts to measure the tremendous forces on the assembly caused by the magnetic fields.

The inductance of the coil is 25 $Henries$, and the magnet is run at 1600 $Amperes$. The liquid helium volume is $\approx$ 5000 $liters$ and the heat load is $\approx$ 60 $l/hour$. Refrigeration is supplied by two C.T.I. refrigerators, one a nominal 100 $watt$ refrigerator, the second nominally 70 $watt$. Either refrigerator alone is capable of supplying the liquid helium required by the magnet while operating under current. However, when operated together at half speed they can handle the magnet and supply additional liquid to a reserve tank. This conservative design, both of the refrigeration system and of a superconductor itself, has produced a stable, reliable and safe superconducting magnet.

5.3 The target

A 30 cm long liquid hydrogen target will be used. It will be contained in the same vacuum jacket as the photon tagger radiator and will be constructed of low mass materials. The collimated photon beam will be contained within a radius of 2.5 cm from the beam axis. This will allow adequate space between the hydrogen vessel and the innermost detector element for insulation, a vacuum pipe and any plumbing and wiring required to instrument the target. Safety is, of course, a very serious concern for any hydrogen target and we will be consulting with the appropriate lab groups early on in the actual design of the target.

It may be desirable, during some running of the experiment, to use compact, nuclear targets. For this reason it is anticipated that the liquid hydrogen target will be removable from the apparatus. It is assumed that it will be inserted from the upstream end of the solenoid through the hole in the upstream flux return.

5.4 Barrel calorimetry

Electromagnetic (EM) calorimetry in the barrel region of the HALL D detector covers the approximate polar angular range $14^\circ < \theta < 138^\circ$. Exact specifications depend on the final size and location of the liquid hydrogen target, the effective thickness of the calorimeter and its readout scheme on both the upstream and downstream ends of the solenoid. It will be positioned immediately inside the solenoid, which constrains the outer radius to be 90 cm. This allows 2 cm for supports and cabling. The outer surface area is approximately 23 m^2. This device is a key component of a hermetic system, and is crucial for fully reconstructing all the photons in many physics reactions. The large size also implies that it will be a challenge to build and instrument at reasonable cost.

The goal of the calorimetry is to detect and to measure photons from the decays of π^0's and η's which, in turn, can come from the decays of an excited baryon (N^* or Δ) and/or from the decays of produced mesons. The positions and energies of the photons must be determined to sufficient accuracy to allow for a complete kinematic reconstruction of the event. Finally, for events with only charged particles, it is essential to be able to veto on neutral missing energy. Here, nearly hermetic coverage is critical. For selected triggers, neutral energy requirements (or vetoes) are relatively easy to implement.

5.4.1 Design considerations

For the tracking elements inside the magnet to perform optimally, the barrel calorimeter must be thin, perhaps no more than 25 cm. The length of the solenoid is 4.5 m. These geometrical constraints lead to a long, narrow tube-like design. In this geometry, readout is easiest at the ends where space exists. However, at the upstream end a magnetic field-shaping plug will need to be modified. The choice of readout device must bear in mind the considerable magnetic field (22.4 kG) inside the bore and the rapidly varying fringe field at the ends. Conventional photomultiplier tubes (PMTs) will work only outside of the solenoid and even there considerable attention must be paid to shielding.

We have considered a number of candidate calorimeter designs. The leading design utilizes scintillating fibers embedded in a lead matrix (Pb/SciFi) to make a relatively high–resolution sampling calorimeter. Advantages include speed, cost, ease of readout, and the fact that it is based on a proven technology. The second, *high–end* option is based on the relatively new lead tungstate ($PbWO_4$) crystals which are being developed as the main EM calorimetry for the CMS experiment at the LHC. They offer superior resolution, good light output and the density to make them very compact. Unfortunately, the very large channel count probably makes this option cost–prohibitive. A hybrid design mixing two technologies for different parts of the polar coverage is possible. The very forward angles ($\theta < 14°$) will be covered by an existing lead glass detector (LGD) used in the E852 experiment at BNL and restacked to meet the geometrical acceptance criteria for HALL D. Based mostly on the cost considerations, we are only considering the Pb/SciFi option at the moment.

The very strong magnetic field in the immediate vicinity of the SciFi ends in each section leave only two options for read out. First, magnetic field resistant PMTs can be used coupled to fiber optic light guides to place the PMTs in regions of reduced field and with an appropriate orientation to further minimize signal loss. This option has the drawback that there is a loss of light associated with the long light guides. A second option is to take advantage of the new hybrid PMTs (HPMT) available now which have been developed for CERN applications. These HPMTs have very fast rise time of 6 ns or less, fast fall time of less than 10 ns, and excellent energy resolution. They are immune to magnetic fields up to 2 T and their power supplies are very compact due to the fact that they draw virtually no current even under maximum bias. It appears that their only drawback is the higher cost compared to that of conventional magnetic field resistant PMTs.

We are currently evaluating both options. Static tasting of several makes of single– and multi–clad SciFi strands is underway to be followed by in-

beam testing in the presence of high magnetic fields. Based on such testing, a decision will be made on the final SciFi type and manufacturer as well as the choice of PMT based also on performance and cost.

5.4.2 Pb/SciFi barrel calorimeter

Scintillating fibers embedded in a matrix of lead or other high-Z materials have been used in calorimeter design and operation for more than a decade. The ratio of the active scintillator to the passive high-Z material, as well as the diameter of the fibers, can be tuned to enhance resolution, to determine the radiation length, and to achieve uniformity in the electromagnetic to hadronic response (the e/h ratio). For high-resolution EM performance, the Jetset detector developed at Illinois [106] was the first detector designed specifically to optimize EM resolution. The recipe produced a detector comparable to lead glass at a considerably lower cost and with approximately half the radiation length. It utilizes 1 mm fibers spaced uniformly (close packed) on specially grooved plates of lead. The lead is alloyed with $3-6\%$ antimony to provide mechanical stiffness. Tooling was developed in order to groove the plates. A second machine was built to guide spools across stacks of the plates taking care to properly align each fiber spool with a groove in the lead. The assembly of a module consisted of a repeated layering of fibers and plates, all held together with an optical epoxy. A finished module was machined into final shape, polished and outfitted with a plastic lightguide for readout.

The resolution for an array of prototypes subjected to electrons in the range from $0.3-1.5\ GeV$ was represented by the function $\sigma/E = 6.3\%/\sqrt{E}$ with E in GeV. The constant term was negligible. In the Jetset Forward Calorimeter, the beam entered nearly parallel to the fiber direction. The energy resolution was also measured with tagged photons below $0.1\ GeV$ and improved to $\approx 5\%/\sqrt{E}$; the detector gave a resolvable signal all the way down to $0.02\ GeV$. Monte Carlo studies done for the HALL D configuration [107] show that this $20\ MeV$ threshold is important for hermeticity of the detector. Figure 5.2 show the fraction of lost photons as a function of this threshold for several reactions of interest.

In Jetset, a Barrel Gamma Veto detector with thickness $6X_0$ was made in a barrel-like fashion with 24 modules of length 80 cm each forming the sides of the barrel. Here, with the interaction point centered in the barrel, gammas entered the modules at normal incidence for polar angles of 90°. For other angles, the detector is effectively thicker. Our design for HALL D follows this concept but would be a full $12.5-15X_0$ thick at normal incidence and considerably longer. Realization of these changes fortunately can be based on

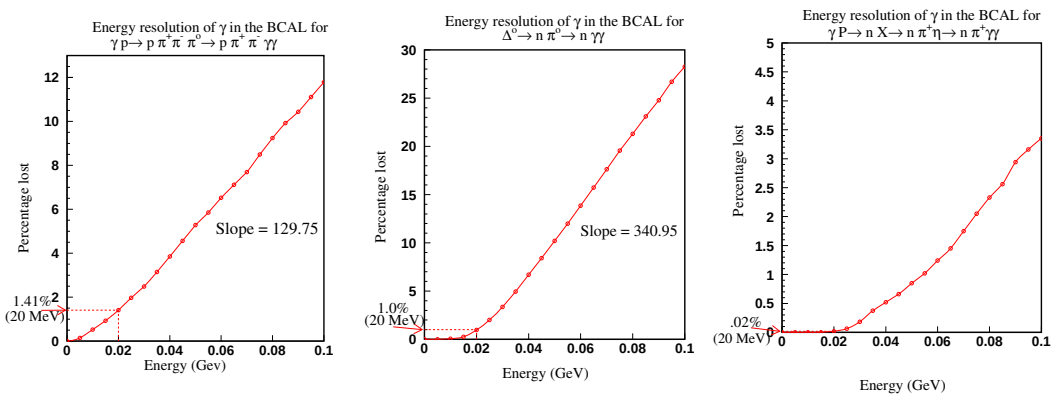

Figure 5.2: Photon detection efficiency as a function of the low energy photon threshold in the barrel calorimeter for three typical reactions. For a 20 MeV photon threshold, the losses are typically less than 1.5%.

the KLOE calorimeter at DAΦNE where they have built a device of this length with an even larger inner diameter. The KLOE collaboration has taken the development of Pb/SciFi a step further. They have developed better tooling for the production of long grooved plates, have pushed the technology for excellent, fibers with long attenuation lengths[1] and have produced prototypes with excellent energy and timing characteristics[2]. We intend to follow much of this development and therefore describe some of the aspects below.

Like Jetset, the KLOE design utilizes 1 mm diameter scintillating fibers embedded in a lead matrix with a fiber to lead to glue ratio of approximately 48 : 42 : 10. Prototype modules, 2 m in length, were produced with PMT readout at both ends. An excellent energy resolution parameterization of $\sigma/E \approx 4.4\%/\sqrt{E}$ was found. In the actual experiment the module length was increased to 4.3 m (which is similar to HALL D) and therefore special efforts were made to develop and to test scintillating fibers with very long attenuation lengths. Tested fibers had attenuation lengths in the range from $2.3 < \lambda < 3.2$ m which is far superior to the average λ of 1 m for the Jetset fibers. This aspect of the design is critical because there exists a significant coupling between the position of impact (essentially the polar angle, θ) and the interpreted energy. Light collected on each end must be corrected for

[1] A discussion of the properties of the fibers considered for KLOE can be found in [108]. Included are measurements of propagation velocity, attenuation length, light yield and decay time.

[2] Energy, time and position resolutions of a 2.03 meter KLOE prototype calorimeter are discussed in [109].

attenuation length before conversion to energy units.

An important feature of these detectors is the signal risetime and overall duration. Because fast plastic scintillator[3] is used, integrated signal time can be kept below 100 ns, with shorter times possible if deemed necessary for rate considerations. At the expected maximum luminosity, no problems are anticipated. With risetimes of a few ns, excellent timing can be expected for each of the PMT's involved in collecting the light from a shower. The time difference from the two ends produces the z coordinate of the hit. Because we will use an array of PMT's on each end (segmented in azimuth and depth), redundant measurements are made of the z coordinate. These measurements of z correspond to different average radii and therefore help to establish the angle of the incoming photon.

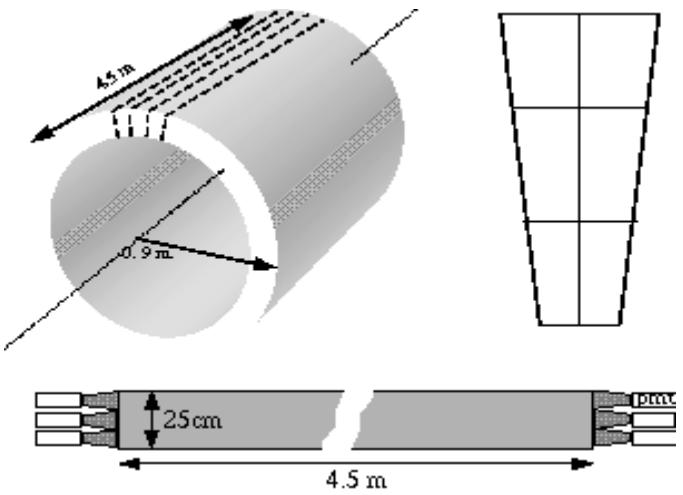

Figure 5.3: Sketch of Barrel Calorimeter made from bars of Pb/SciFi material. (a) perspective view; (b) closeup of end with suggested readout segmentation for one of 48 bars; (c) side view showing approximate locations of PMTs.

The fractional volume of scintillator in the detector naturally makes it efficient for detecting charged hadrons. The mean light collection time of the two readout ends can be used to determine the particle time-of-flight (TOF). TOF coupled with the track length and momentum then yields particle mass. Therefore, this design for a Barrel Calorimeter can be expected to play an important role in the overall barrel PID scheme. In the KLOE design timing of ≈ 250 ps (RMS) was achieved, and improvements are possible. The same can be expected for HALL D as long as PMT's and discriminator chains are selected

[3]Decay times are 2.0 – 2.5 ns.

carefully.

In order to form grooved plates and construct modules 4.5 m long, we plan to study the KLOE tooling development. We would either replicate or borrow their successful devices. This proof of principle gives us confidence that the daunting mechanical task can be handled. For HALL D we expect to build 48 modules each 4.5 m in length and 20–25 cm deep. Variants on this theme are being considered; in particular, half length modules with intermediate readout will be studied. The readout scheme takes advantage of the fact that all fibers run parallel to the axis of symmetry of the solenoid and therefore all light piped to the ends of the modules retains its azimuthal and radial information. The polished ends of the detectors can be coupled with multiple independent lightguides. In Figure 5.3, 6 segments are suggested. This gives a minimum of 96 independent azimuthal slices, each with three dual-ended readouts at varying depths. The transverse size of a module is approximately 4 cm at impact. Because the EM showers spread across these azimuthal boundaries, algorithms for finer positioning of the shower are employed. In Jetset, one finds a typical weighted position resolution of $\delta x \approx 5\, mm/\sqrt{E}$. For the HALL D design, this would lead to an azimuthal resolution of $\approx$ 10 mrad. Using the z position resolution of approximately 1 cm obtained from the time difference leads to a polar angular resolution at 45° of $\approx$ 8 mrad. As the design of the barrel calorimeter is further refined, it will be important to keep these numbers balanced.

In Figure 5.3 several views are shown for the barrel calorimeter including an overall perspective, a side view of one module, and an end view indicating how a single module could be segmented with six independent readouts. In this design, there are $48 \times 6 \times 2 = 576$ PMT's. Each channel requires high voltage, a flash ADC, discriminator, TDC and cabling. A calibration system is critical and can be based in part on the use of Nichia blue LED's glued directly to a short lightguide stub at the end of each module. An LED driver system is also required. The choice of ADC and TDC systems depends on the overall readout coordination for HALL D. To estimate costs, we can imagine packaging typical of existing Fastbus–based systems with 64 or 96 channels per unit.

5.5 Tracking chambers

The system of tracking chambers in the HALL D detector must cover as close to a 4π solid angle as possible over a wide range of particle momenta and must have sufficient momentum resolution to be able to identify missing particles. In the solenoid region, the chambers are inside the barrel calorimeter. This defines

a maximum keep–out radius of about 65 cm. For purposes of this report, the active volume has been limited to 60 cm in radius. This provides 5 cm of space for support systems and cables. The chambers also must extend as close to the beam line as possible. Near the target this will provide very accurate vertex information, which will be important in identifying decaying particles (e.g. K_S, Λ, Σ, ...). In the forward region this is needed to reconstruct very fast small angle particles (down to nearly 0°). Finally, it is necessary that near the target the tracking be able to separate π's and K's up to momenta of about 0.5 GeV/c — a regime where dE/dx measurements will work.

5.5.1 Design considerations

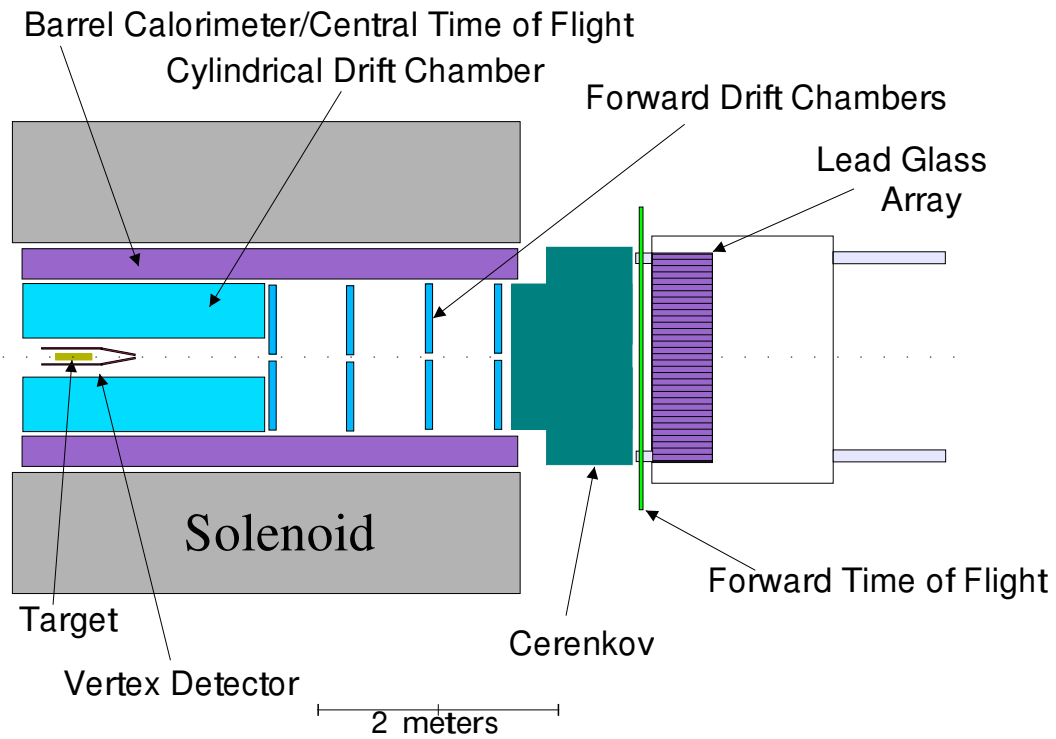

Figure 5.4: The HALL D detector. The tracking elements are the cylindrical drift chamber (CDC), which is a straw tube chamber. The forward drift chambers (FDC), are planar circular shaped planar chambers. The vertex detector (VTX) is a fiber tracking device which doubles as a start counter. The small gap indicated in the middle of the FDCs are deadened wires rather than an actual hole.

To satisfy the tracking requirements a starting point based on the LASS detector [104] was examined where we have taken a series of different tracking elements. Each of these elements has been optimized for a particular region in the detector. An example of such a design is shown in Figure 5.4, where there are three different tracking regions. Just around the target is a *vertex system*, VTX. This is likely to be several layers of scintillating fiber, which would allow it to be used for both track reconstruction and triggering. Around this is a cylindrical drift chamber (CDC) which provides very good $r-\phi$ information and moderate to good z information. This chamber will also provide dE/dx information. In the forward region are planar forward drift chambers (FDC). These chambers physically fill the tracking volume, but have regions in the beam line deadened.

System	*Radius*		*Length*		*Resolution*	
	$r_{\min}$	$r_{\max}$	z_{min}	$z_{\max}$	$\sigma_{r-\phi}$	σ_z
VTX	5.0 cm	5.5 cm	10. cm	90. cm	500 μm	stereo
CDC	15.0 cm	60.0 cm	0. cm	200. cm	200 μm	stereo
FDC	3.5 cm	60.0 cm	210. cm	400. cm	150 μm	fixed

Table 5.2: A summary of the tracking chamber parameters. The z values under *Length* give the smallest and largest z of the combined system. The z measurement starts at the upstream end of the magnet. The z resolution for the CDC comes from $\pm 6^\circ$ stereo layers. The VTX chamber is expected to measure z resolution using stereo layers. The z resolution of the planar chambers is assumed to be given by their position in space.

The charged particle system within the solenoid must be optimized for both overall acceptance and momentum resolution. A detailed study using the *HDFast* framework (see Chapter 9) has been performed to examine this [110]. The results of this study indicate that the above combination of cylindrical drift chambers and planar drift chambers with typical $r-\phi$ position resolutions of 200 μm in the central region and 150 μm in the forward region would satisfy these requirements. A plot of resolution as a function of angle is shown in Fig 5.5 where we have zoomed in on the forward angles in the right-hand part of the figure. Note that the current Monte Carlo does not fully deal with the degradation in resolution as the tracks become parallel to the CDC wires. An exact optimization between CDC and FDC has not been fully performed.

The 22.4 kG solenoid field determines the physically measurable quantities, and hence, the momentum resolution. The transverse momentum, $p_\perp$ and the dip–angle, λ, ($\lambda = \frac{\pi}{2} - \theta$) are measured from the curvature of the tracks and

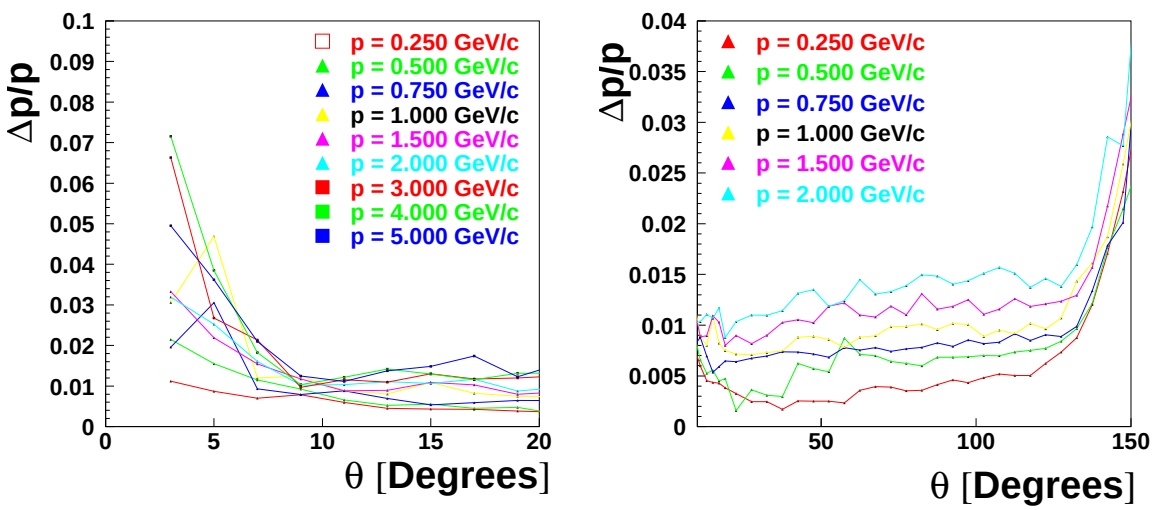

Figure 5.5: The resolution as a function of angle plotted for several total momenta. The plots correspond to the detector design shown in Figure 5.4. For polar angles larger than 70°, the maximum detected momentum will be well under $1 GeV/c$ so even though the resolution for high momentum tracks is poor in this large angle region, it will not affect the overall tracking of physics events.

their initial direction. The total momentum and the longitudinal momentum are then obtained from these as $p_{total} = p_\perp \sec\lambda$ and $p_\parallel = p_\perp \tan\lambda$. The accuracy of the $p_\perp$ measurement is completely dominated by the $r-\phi$ resolution of the tracking chambers, while the λ measurement relies on an accurate measurement of both z and the distance traveled.

Track reconstruction effects also play a very important role in the design of the system. In particular, track matching between different detectors and the associated inter–calibration problems often limit the ultimate resolution. In addition, the high magnetic field strength of $22.4\,kG$ means that tracks may spiral significant distances between measurement planes. Ultimately, one would like each measurement along a track to be a full space point, rather than a single coordinate. The magnetic field is known to be nonuniform near the ends of the magnet, particularly due to the lack of a mirror plate at the downstream end. To achieve the ultimate resolution, sufficient space points must be available in the nonuniform region. In addition, particle identification will require projecting charged tracks forward to both the time–of–flight (TOF) wall and the forward calorimeter, again a requirement for good tracking near the end of the magnets.

As an example, one particular all charged final state is considered. In Figure 5.6 is shown the distribution of charged particles in p versus θ space for both $E_\gamma = 6\ GeV$ and $E_\gamma = 10\ GeV$. The events are generated according to reaction 5.1 where the X has masses between 1.7 and 3.2 GeV/c^2.

$$\gamma p \to X p \to K^+ K^- \pi^+ \pi^- p \tag{5.1}$$

Table 5.3 summarizes the maximum momentum as a function of angle for both photon energies. From the plots in Figure 5.6, several important features which drive the design of the detector are observed. In particular, particles

θ [°]	$p_{\max}$ [GeV/c]	
	$E_\gamma = 6\ GeV$	$E_\gamma = 10\ GeV$
20°	3.00 GeV/c	5.00 GeV/c
50°	1.00 GeV/c	1.50 GeV/c
70°	0.50 GeV/c	0.50 GeV/c
100°	0.25 GeV/c	0.25 GeV/c

Table 5.3: Maximum total momentum as a function of angle for both E_γ of 6 and 10 GeV for all particles in reaction 5.1.

that emerge at angles larger than 90° have momenta less than 0.2 GeV/c. To measure these slow particles accurately, good z–resolution will be needed near

the target. Additionally, these particles will not make it to any time of flight system. The only particle identification will come from a dE/dx measurement. On the other hand, good tracking resolution for high–momentum particles in the backward angle region is not required.

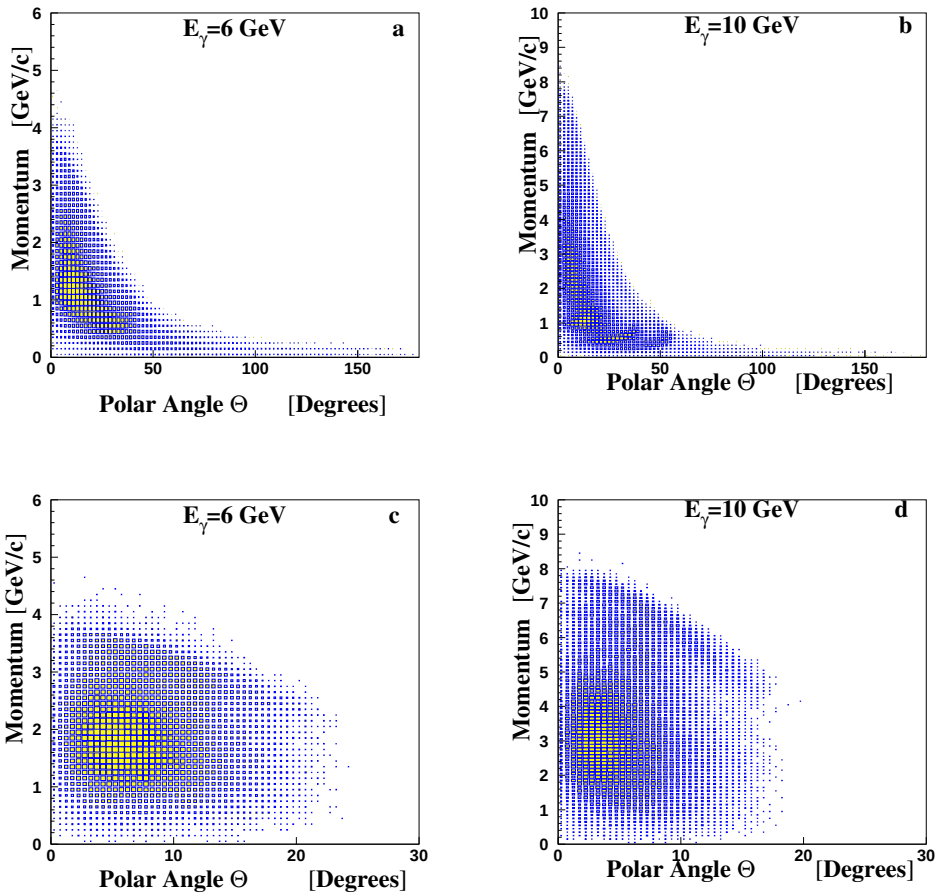

Figure 5.6: Momentum versus polar angle for all charged particles in $\gamma p \to K^+K^-\pi^+\pi^-p$ data sets. Figures (a) and (b) are the distributions for all particles for $E_\gamma = 6\ GeV$ and E_γ=10 GeV respectively. Plots (c) and (d) show momentum versus angle for the most forward particle in both cases.

Next, most events have at least one particle moving in the forward direction at high momentum. In Figure 5.6(c) and (d) are shown the momentum versus angle for the most forward particle in each event. Good tracking will be needed as close to the beam line as possible, hopefully extending down to 1°.

Many of the charged particles in HALL D will produce spiraling tracks in the solenoid. Figure 5.7 shows the p versus θ plane for tracks in the solenoid. Tracks which fall above the hyperbolic curve cannot spiral in the 60 cm radius region containing the tracking chambers. Below the hyperbola are a series of approximately horizontal lines. Tracks below these lines spiral the number of times indicated. Based on the p versus θ distributions in Figure 5.6, it can be easily seen that most tracks at angles larger than 50° will always spiral at least once in the detector.

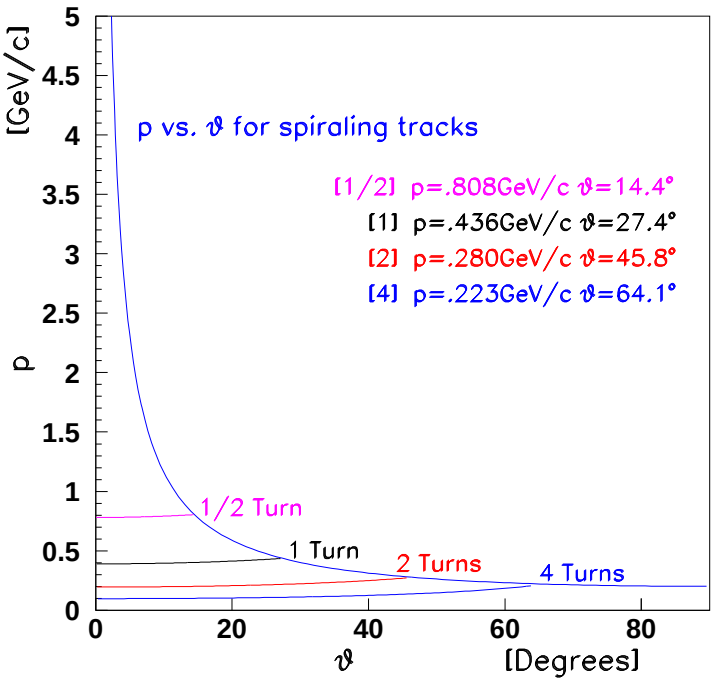

Figure 5.7: This figure shows the number of full circles made by charged particles in the magnetic field. The limit line corresponds to $p_\perp = 0.2\ GeV/c$ tracks. The approximately horizontal lines indicate when the particle can make the indicated number of turns without leaving the magnet.

To study the missing mass resolution, reaction 5.2 has been examined.

$$\gamma p \rightarrow K^+K^-\pi^+\pi^-\pi^0 p \tag{5.2}$$

For this study, the nominal detector as shown in Figure 5.4 with 200 μm resolutions is assumed. It is also assumed that the π^0 in 5.2 is not detected. Using

the reconstructed charged tracks, the known beam energy, and the assumption that the reaction took place on a proton target, the square of the missing mass is computed and shown in Figure 5.8(a) for a nominal 0.1% beam energy resolution. The distribution is centered at the square of the π mass, but it has a non–negligible width. In Figure 5.8(b) the width of the peak in (a) is plotted as a function of the beam energy resolution. For this particular reaction with a missing π^0, a beam energy resolution of 0.1 to 0.2% is well matched to the 200 μm resolution of the tracking system.

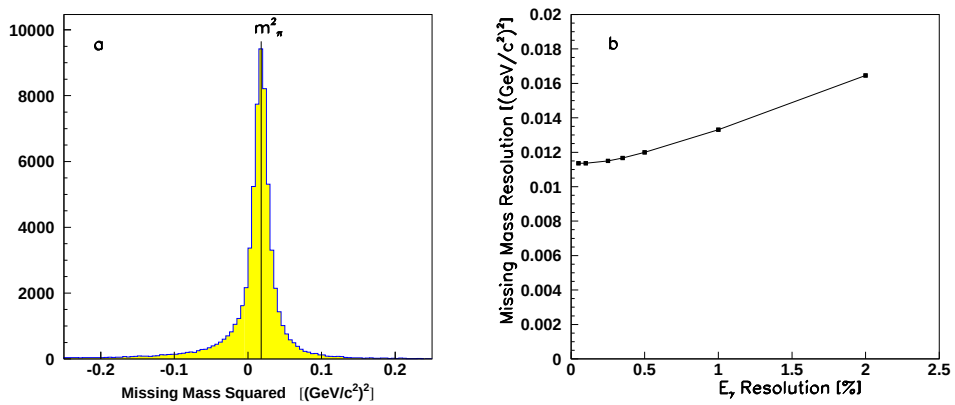

Figure 5.8: Missing mass squared from the reaction 5.2 where the π^0 is assumed missing. (a) is for 0.1% beam energy resolution, while (b) is a plot of the missing mass resolution as a function of the beam energy resolution.

5.5.2 Central drift chamber

The central drift chamber (CDC) is used to track particles between polar angles of 20° back to 170°. To minimize material in the forward end plate of the chamber, one would like a self–supporting chamber. This leads to a straw chamber, where the straw walls support much of the wire tension The disadvantage of this design is the difficulty of making dE/dx measurements in a circular straw tube. It is in principle possible, but additional research must be done to determine how to correct for the total path length in a tube. An example of this is shown in Figure 5.9a where two nominally identical tracks have very different path lengths through the straw.

The planned design has the chamber filled with 5200 1 cm diameter straw tubes arranged in 22 layers as shown in Figure 5.10. The tubes are assumed

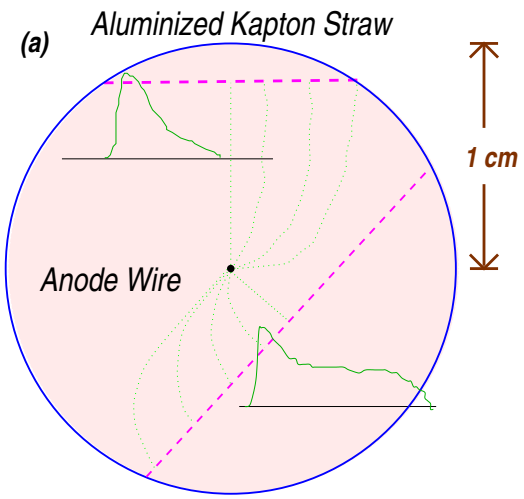

Figure 5.9: A end view of one straw-tube in the the CDC. The two dashed lines indicate charged tracks with quite different path lengths in the tube, which then lead to different electronic pulse shapes as shown. For accurate dE/dx measurements, this path length must be known.

to have an $r-\phi$ resolution of 200 μm, while resolution along the wire length will be obtained by placing about half of the layers at a 6° stereo angle. A typical hydrocarbon drift gas will have a drift speed v_d on the order of 50 $\mu m/ns$, meaning maximum drift times will be on order of 100 ns. In this case a 4 ns drift time corresponds to 200 μm of drift. Many of the charged particles will not reach the TOF system in the calorimeter, requiring the use of dE/dx information in the chamber for particle identification. This requires both TDC and ADC readout on the chamber. This is likely to be better accomplished with a flash ADC system. To achieve the required 200 μm resolution, this system must run at 200 to 250 MHz (5.0 to 4.0 ns time bins). Time fitting algorithms matched to the pulse shape in the chamber usually yield intrinsic time resolutions around 20% of the time bin width.

In Figure 5.5 is shown the momentum resolution as a function of angle corresponding to the detector layout in Figure 5.4. The most striking feature of this plot is the two upward spikes at forward angles. The first is due to very stiff particles at small angles. The second (at around 15°) is due to the interface between CDC and FDC. This feature leads us to believe that the CDC chamber should be as long as possible. This is, however, not the complete picture. The current Monte Carlo assumes a CDC position resolution which is independent of the dip angle. This is not the case; the resolution will deteriorate like $\tan\lambda$. On the other hand, the FDC chamber resolution will

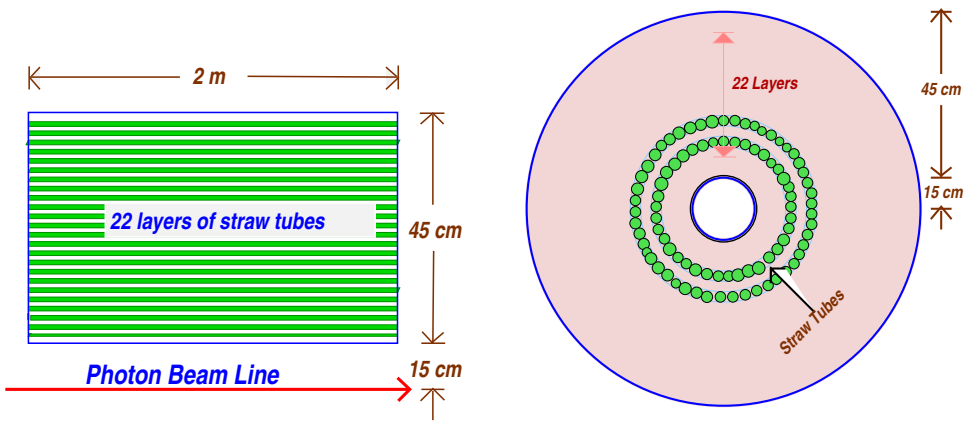

Figure 5.10: (a) A side view sketch of the CDC assuming a straw tube arrangement. (b) An end-view picture of the straw tube arrangement. Two of the 22 layers of straw tubes are shown.

be optimum for tracks parallel to the beam axis, and deteriorate for tracks at small values of λ. In any case, intermediate angles have somewhat worse resolution than indicated by this design. Finally, one drawback of this design is the large amount of material in the tracking volume. While this material has been put into the Monte Carlo, it is still worrisome based on the large number of scattering surfaces within this critical tracking volume. Preshowering of photons within the tracking volume is also only partially described by the current Monte Carlo.

The resolution studies in this report are based on such a straw tube chamber. The chamber is built out of $2\,cm$ thick aluminum end plates with a $2\,mm$ thick carbon fiber shell on the inside, and a $4\,mm$ outer carbon fiber shell. The straw tubes are $100\,\mu m$ thick aluminized kapton, and have $20\,\mu m$ diameter gold–plated tungsten wires.

5.5.3 Forward drift chambers

The forward drift chambers, FDC, are disk shaped drift chambers. The basic drift package is a plane of wires with $150\,\mu m$ spatial resolution between two planes of cathode strips. The strips are arranged in a u and v geometry with respect to the wires, allowing the reconstruction of a 3–D space point from each hit. The chambers are arranged in packages of six to provide a small track segment to facilitate later linking of tracks. Given the number of spiraling tracks, it is critical that these chamber packages not only provide good spatial

resolution but also reasonable direction information.

The basic chamber element is a disk of outer radius 60.0 cm, the wires strung as chords across the chamber as shown in Figure 5.11(a). With a 1.0 cm wire spacing, each chamber will contain 119 wires. In addition, there will be an equal number of cathode strips on each face. These are arranged in a u–v pattern with respect to the wires as shown. This leads to 357 channels per chamber. Figure 5.11(b) shows the six chambers in side view forming one FDC package leading to about 2200 channels per package. Adjacent planes will be rotated by 60° with respect to each other to improve the overall resolution. The wires that cross through the beamline will be deadened out to a radius of about 3.5 cm by placing material such as Styrofoam in the chambers.

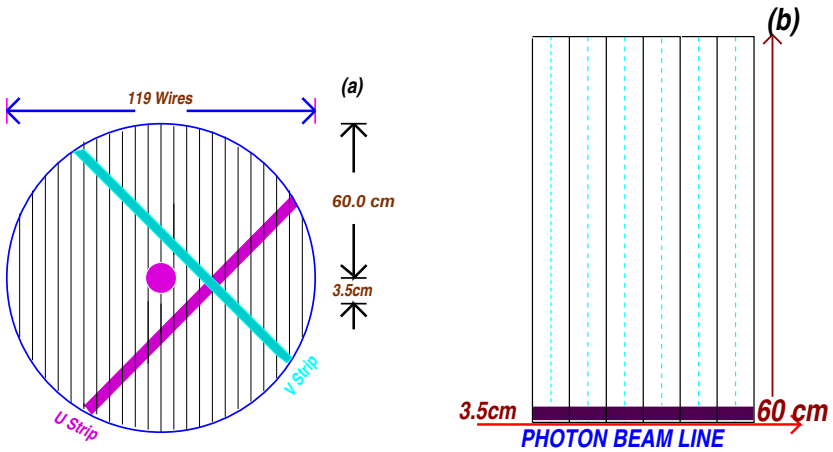

Figure 5.11: A front, (a), and side, (b) sketch of an FDC package. In (a) the wires are schematically indicated as the vertical lines. The u cathode strips are in front of the wires and the v cathode strips are behind the wires. In (b) is shown a side view of the upper half of a six–chamber package. The wire planes are shown as the dashed lines, while the cathode planes are the boxes. Ground planes between adjacent chambers are not shown.

5.5.4 Vertex chamber and start counter

The central vertex chamber has several purposes. First it will be used to provide accurate tracking information very close to the target. These track elements must be sufficiently well defined to be connected to the other tracking chambers. Secondly, this chamber must provide a fast signal which can be used in the level–1 trigger of the experiment, in particular a start signal for

the event. It may also be desirable to trigger on secondary vertices from Λ or K_S decays. In terms of the overall tracking resolution (see Figure 5.5) the vertex chamber has a non–negligible contribution. In Figure 5.12 are shown the overall resolutions for 200 μm and 1000 μm spatial resolution. Forward of 50° (where the particles have larger momenta) the chamber must have at least 500 μm resolution. In addition, the chamber must have a position resolution along the beam direction, z, on the order of 1 mm to facilitate track matching.

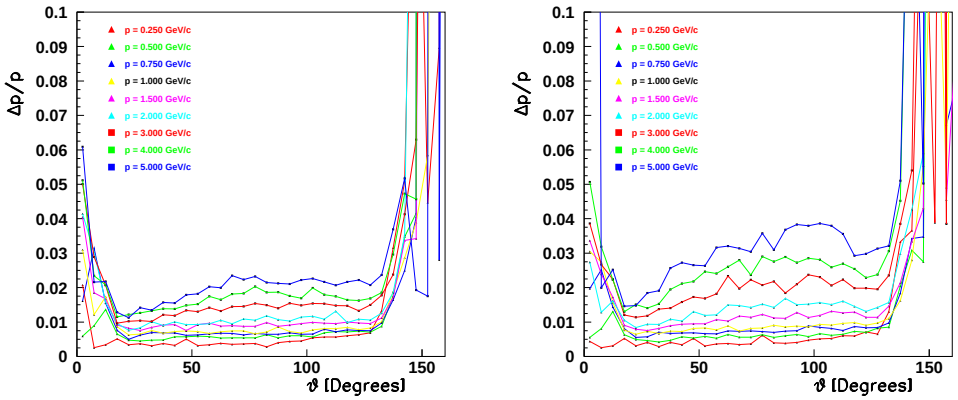

Figure 5.12: Tracking resolution as a function of angle and momentum. The left–hand figure has 200 μm resolution in the VTX, while the right–hand one has 1000 μm resolution.

The vertex detector will consist of two detector packages. One will be optimized for timing purposes and the other one will provide fast tracking information.

The timing detector will consist of a cylindrical array of 10 scintillator paddles. This will cover scattering angles between 1° and 90° for the full length of the target. The acceptance for large angles could be extended by increasing the length of the detector into the backward area. The scintillators have a thickness of 5 mm which reduces to 2 mm in the forward direction. This will provide a good light output and therefore a good timing signal. The paddles will be coupled to phototubes at the upstream end via light guides which lead out of the high magnetic field region. Figure 5.13 shows the cross section of the scintillator array parallel and perpendicular to the photon beam. Using Bicron BC-404 scintillating material in combination with fast photomultipliers we expect to achieve better than 120 ps overall timing resolution.

The fast tracking detector will consist of three super–layers of fibers, each

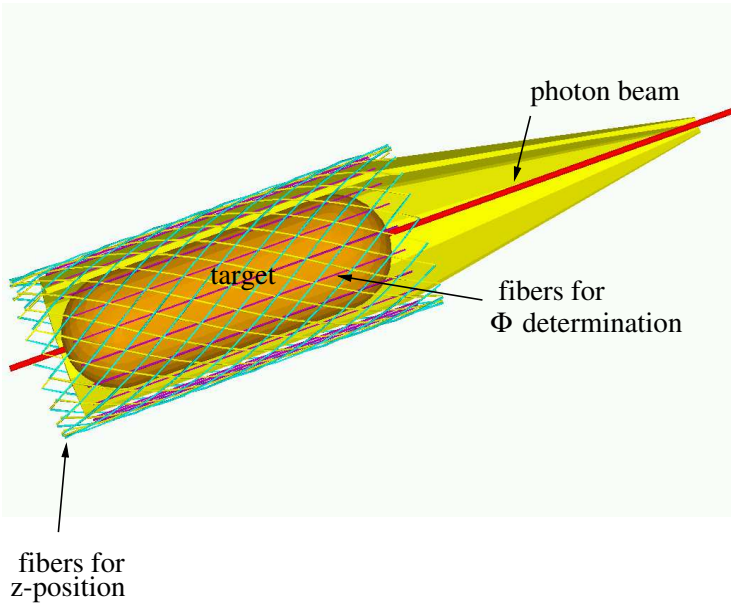

Figure 5.13: Conceptual design of the start detector with the target area surrounded by the cylindrical and conical array of scintillator paddles and the three super-layers of scintillating fibers. Note that the fibers do extend forward over the conical section of the detector.

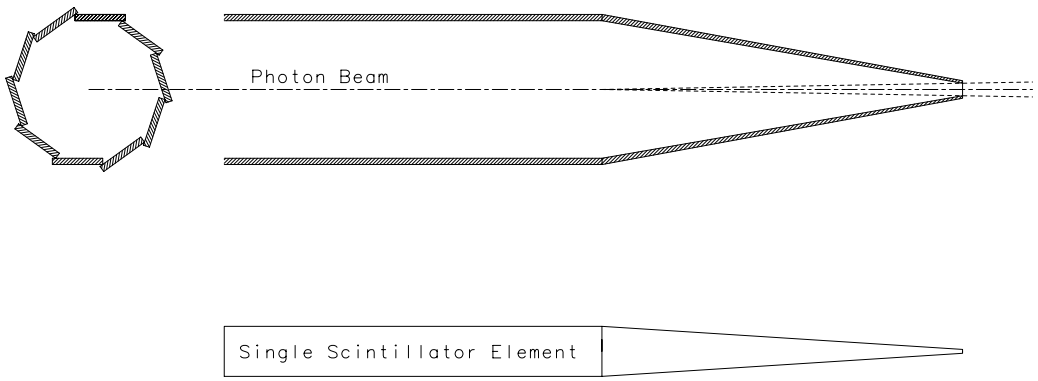

Figure 5.14: Cross sectional view of the scintillator array (timing detector) perpendicular to the beam (left) and parallel to the beam (right) and the top view of a single paddle.

containing two layers to minimize dead space. The central layer will be arranged around the target and parallel to the beam. It will determine the azimuthal angle. The z position is deduced from the two outer layers. They

will be wound in two opposite helixes around the first layer. Since this detector will be at 5 cm radially outward from the target the conventional solution using position sensitive photo multipliers (PPMT) together with blue scintillating fibers and light guides will not work for the following reasons. PPMTs will not properly function in high magnetic field areas, therefore necessitating long light guide fibers to an area where the field is low enough for the PPMTs to operate successfully. However the absorption length of clear light fibers in the blue area, where the photo cathodes have a maximum in quantum efficiency (at best 18 %) is only of the order of 2 meters. As an additional factor one has to consider that blue scintillating fibers are highly susceptible to radiation damage, leading to an additional decrease in photoelectrons. Even excluding radiation damage these combined effects will result in approximately two to three photoelectrons per minimum ionizing particle (mip), making a position determination by charge distribution on the PMT anodes impossible. One therefore cannot resolve multiple hits in one PMT.

In order to circumvent the problems mentioned above, we are studying the possibility using Visible Light Photon Counters (VLPC) developed by Rockwell in collaboration with Fermilab [111]. The spectral sensitivity of the VLPCs require us to use SCSF-3HF multi clad scintillating fibers from Kuraray which are also the least susceptible to radiation damage. One of the main advantages of using VLPCs is their large quantum efficiency of approximately 80% [112] for the light produced by the fibers together with a very high rate capability of 10^8 single photoelectrons per second. Another advantage of using the Kuraray fibers is the long attenuation length of 5.5 m for the scintillating fibers and 10.4 m for the clear ones [113] allowing us to position the readout electronics well outside the region of the magnetic field. The design of the whole detector system will closely follow the prototype system developed [114] by the D0 collaboration at FNAL for the central tracking facility of D0 detector. The expected position resolution will be at least 1 mm.

5.5.5 Chamber infrastructure and alignment

Because the tracking system is built out of several different elements, good reconstruction relies on accurate positioning of the individual detector components. In designing such a system, it is important to build accurate, reproducible positioning of the detectors directly into the system. It is also desirable for cabling and servicing that all the tracking elements within the solenoid are removable as a single package. This will require some sort of rail structure on the inner surface of the barrel calorimeter and mounting supports on the inner surface of the CDC or the TPC. The current design allocates a 5 cm

space between the CDC and the barrel calorimeter for this. There is also a rather large logistical problem of getting all the cables out from the detector elements. The CDC or TDC will be read out only at the upstream end, and high voltage can be connected there as well. The FDC chambers can be read out at the outer radius, and the cables can pass between the tracking chambers and the barrel calorimeter. The scintillating fiber VTX chamber must be read out using phototubes. It is possible to extend the fibers outside of the magnet at the upstream end, and attach the photo tubes there. The most difficult readout design problem is presented by the BVT chambers; most obvious readout schemes introduce additional mass in the form of cables directly in the center of the tracking volumes. It will be necessary to do some research to multiplex, or preprocess the chamber information to minimize cables and high voltage connections.

5.5.6 Electronics

Table 5.4 summarizes the numbers of ADC and TDC channels needed in the basic drift chamber configuration. The only chamber that requires dE/dx information is the CDC, where many of the slow tracks will not reach the time–of–flight systems. Here it is possible to replace the ADC/TDC pair with flash ADCs.

Detector	*Anodes*		*Cathodes*	
	FADC	TDC	FADC	TDC
VTX	0	2000	0	0
CDC	5200	0	1000	0
FDC	0	3570	7140	0
total	5200	5570	8140	0

Table 5.4: A summary of the electronic channels in the detector components..

5.6 Particle identification

Identification of particle types will be achieved in several detector subsystems. Photons and electrons will be identified by means of the photon detectors described elsewhere in this chapter. Charged hadrons and muons will also register low pulse heights in these detectors. Charged particle identification will be made primarily on the basis of time-of-flight, TOF, measurements in conjunction with the output from a threshold Čerenkov detector and dE/dx

information from the tracking chambers. The TOF signals will come from the barrel calorimeter and from a scintillator hodoscope located directly behind the Čerenkov detector. The designs of the scintillator hodoscope and the Čerenkov detector are described in this section, and their expected performance levels are discussed.

In order to understand the demands to be placed on the performance of the particle identification system, simulations have been performed for typical reactions involving pions, kaons and protons in the final state. The reaction

$$\gamma p \to Xp \to K^* \bar{K}^* p \to K^+ \pi^- K^- \pi^+ p \tag{5.3}$$

has been simulated with a 9 GeV incident photon beam. All events are assumed to arise from the decay of a meson X having a mass of 2 GeV/c^2 and a width of 300 MeV/c^2. The momentum spectra for the final state particles are shown in Figure 5.15. The average proton momentum, $0.55 GeV/c$, is sufficiently low that protons can be distinguished from mesons using both dE/dx and TOF combined with momentum information from traversing the magnetic field. However separating pions from kaons is more challenging. The meson momenta span the range from about 0.1 to 6 GeV/c. The part of this spectrum below 3 GeV/c can be accommodated with time-of-flight measurements. The remainder will be addressed by the Čerenkov detector. When these are combined with constrained kinematic fitting the overall efficiency is quite high.

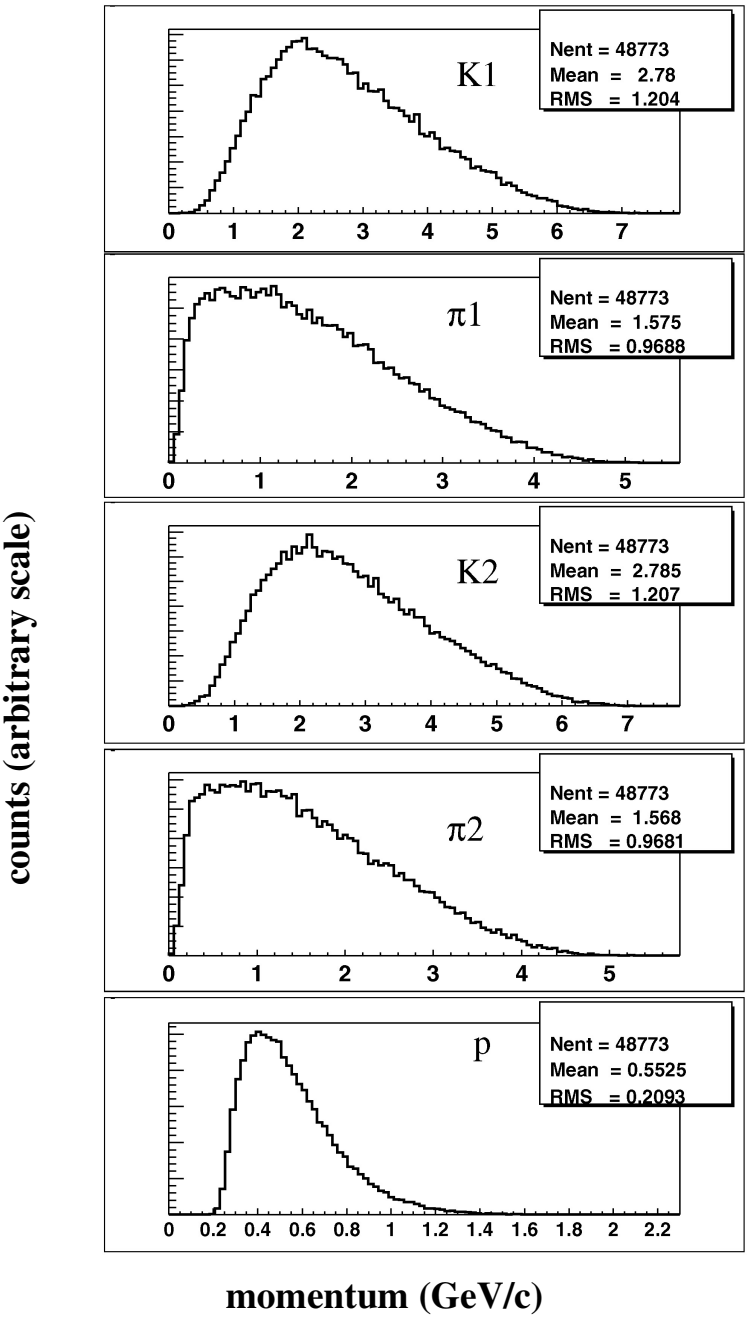

Figure 5.15: The momentum distributions for charged particles from the reaction $\gamma p \to K^+K^-\pi^+\pi^-p$ for $9GeV$ photons.

5.6.1 Time-of-flight

The design of the barrel calorimeter is dictated primarily by the available space inside the magnet and the method chosen for photon conversion. Charged particles emitted at large angles to the beam often have low velocity so even moderate time resolution is sufficient to distinguish pions from kaons. The lead/fiber design of the barrel calorimeter provides a large number of scintillator samples as a particle traverses the individual fibers. The KLOE collaboration has demonstrated [115] an RMS time resolution of $252\,ps$ for minimum ionizing particles traversing 19 layers of lead and fiber. This value will be used as an estimate of the performance that can be achieved in the TOF measurement from the calorimeter in HALL D.

In the forward region, two orthogonal arrays of 80 scintillators each will be placed immediately in front of the downstream photon detector. Each detector element will be about one inch square and will have a photomultiplier at each end. The primary design constraints for the TOF hodoscope are the high ambient magnetic field and the necessity of using thin scintillators to minimize reactions in the detector. We are currently using computer models (including TOSCA) of the magnetic field to predict the ambient field using different assumptions for the magnetic shielding of all detector components. Depending on the final design, the TOF photomultipliers will either use standard passive shields, high-field photomultipliers, or fiber bundle light guides (to move the detectors to a low field environment). We have fabricated a $1.0\,m$ long fiber bundle from 492 clear $1.2\,mm$ diameter fibers and will be measuring its light attenuation. Reference [116] describes the performance of a prototype high-field detector. Scintillator bars $2\,m$ in length were instrumented with mesh photomultipliers, achieving an RMS time resolution of $81\,ps$. In the Monte Carlo simulations described below, we have taken this result as the expected value. This resolution is sufficient to have a 2.5 standard deviation separation between pions from kaons for momenta of 3 GeV/c and lower, as indicated in Table 5.5.

Momentum	Time Difference
2 GeV/c	463 ps
3 GeV/c	207 ps
4 GeV/c	117 ps
5 GeV/c	75 ps

Table 5.5: Flight time difference between a π and K for a $5\,m$ flight path.

To optimize the forward region TOF time resolution a prototype system

has been fabricated at Indiana University. The prototype scintillator is fast (≈ 2 ns decay time), has a large signal, and possesses an attenuation length that is long compared to the element length of approximately $2\,m$. The other scintillator dimensions are $2.54\,cm$ by $2.54\,cm$. The *XP2020* photomultipliers on each end have a rise time of $2\,ns$.

Using cosmic rays, time resolutions of $90\,ps$ per phototube have been achieved. The results are shown in Figure 5.16 where a Gaussian is fit to the distribution in the difference in time from the two phototubes at the ends of the scintillator. The σ of this fit corresponds to $160\,ps$. Taking into account the finite size of the trigger counters ($\sigma \approx 97\,ps$) and accounting for the two phototubes results in the quoted time resolution.

These studies have shown that the resolutions are quite sensitive to the scintillator pulse height and to the manner in which the analogue pulses are discriminated in the TOF leg of the electronics. This prototype system is being shipped to IHEP in Protvino for a week of tests in a beam line at IHEP in November 2000. Several other types of photomultipliers, including the ultrafast XP2020/UR, will be tested. In addition, the fiber bundle mentioned earlier will be installed and its performance characteristics studied.

5.6.2 dE/dx in the chambers

There will be a subset of the low momentum charged particles which will not reach a time of flight counter, or will reach them after spiraling so many times in the magnet that the TOF information will be very difficult to use. For these particles, dE/dx information from the CDC and the FDC chambers will be the primary source of particle identification. Fortunately, these particles all have momenta smaller than about 400 MeV, which is exactly where dE/dx will work the best.

5.6.3 Čerenkov counter

TOF measurements alone will not provide particle identification above $3GeV/c$, and thus TOF does not suffice for typical reactions of interest. Therefore a threshold Čerenkov detector has been included in the HALL D design. The primary function of this detector is to signal the presence of pions over a large part of the expected momentum range (see Figure 5.17). Several radiator materials have been considered for the design. A pressurized gas radiator has the advantage of allowing one to match the index of refraction to the desired momentum range. A prototype of such a detector was developed for CLEO-III [117]. However this method requires the use of thick gas containers in the

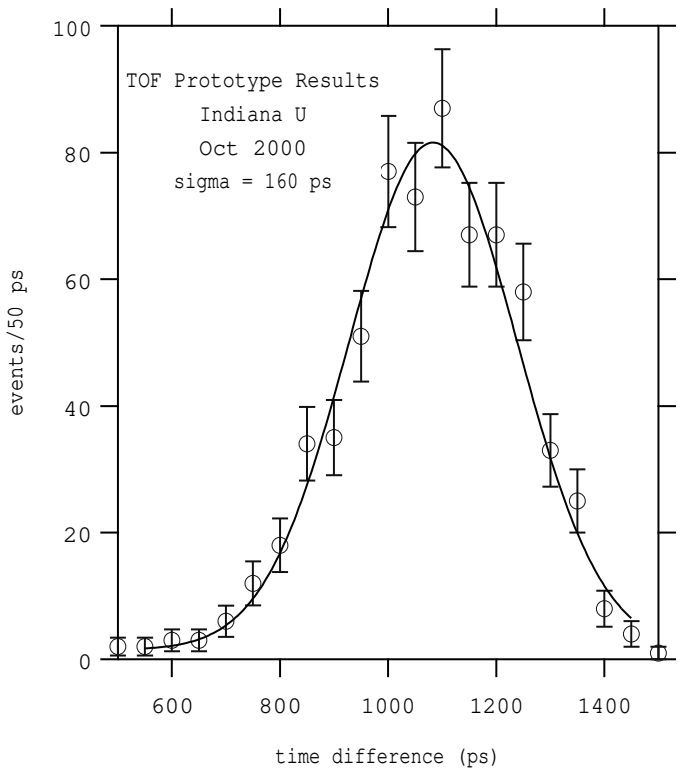

Figure 5.16: Time difference achieved using prototype TOF bar of 2 m length with phototubes at each end.

downstream detector region. This results in unwanted photon conversions and hadronic interactions, as well as safety concerns. Two atmospheric-pressure radiators were found to produce high acceptance rates: aerogel ($n = 1.008$), and C_4F_{10} gas ($n = 1.00153$). The C_4F_{10} gas radiator has been chosen for HALL D because it is has a threshold momentum of 2 GeV/c for pions, which complements the TOF system's useful range of 3 GeV/c and below. The kaon threshold of 9 GeV/c in this gas is nicely above the momenta that will be encountered in the experiment, overlapping less with the TOF system.

Gas filled Čerenkov detectors have been used in many particle physics experiments. The original LASS spectrometer [104] used a freon radiator in a design similar to the one in HALL D. The primary changes we will make in the LASS design are the use of an environmentally friendly gas (freon is no longer available) and mirrors made of low-density carbon-fiber composite materials. The gas handling system will be patterned after a similar system now in use on the JLab CLAS spectrometer. The detector will be segmented into six-

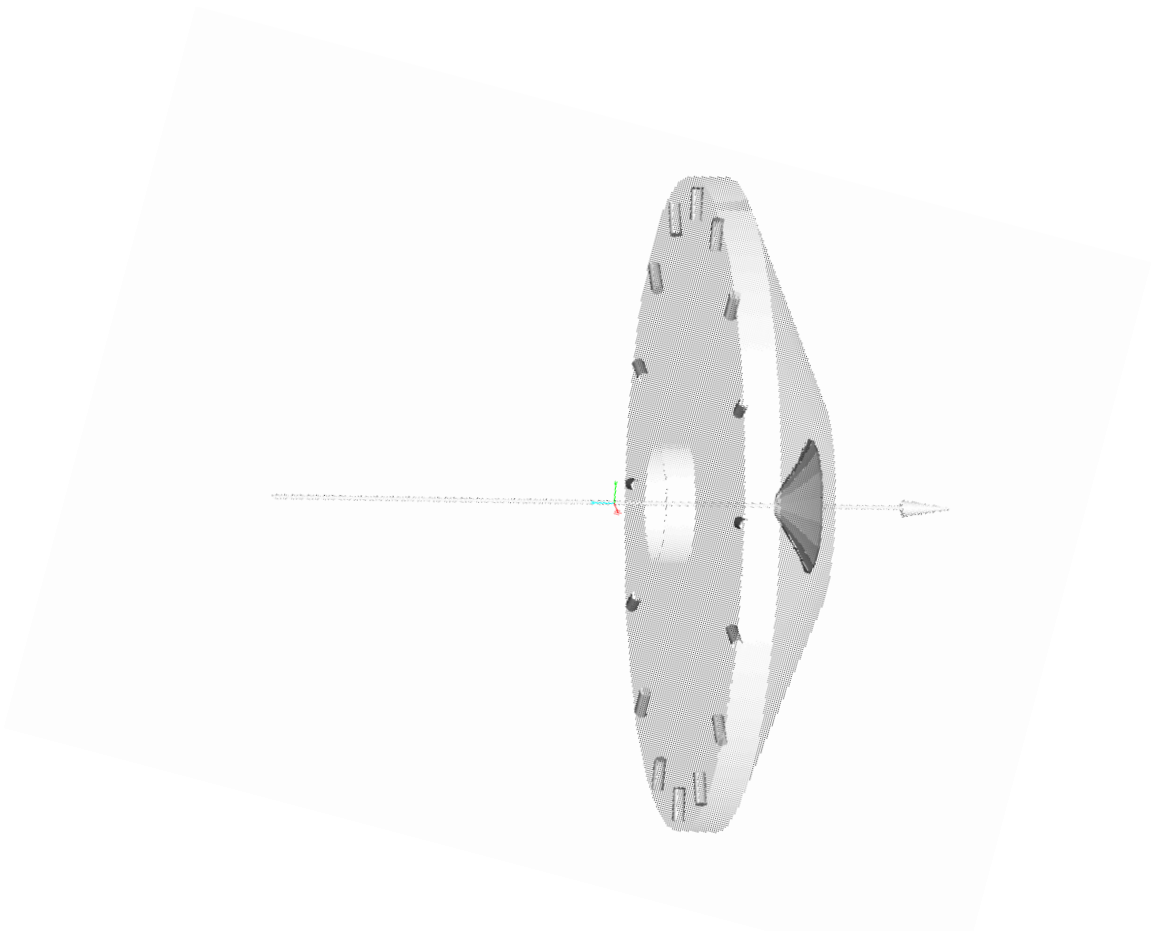

Figure 5.17: A schematic drawing of the HALL D Čerenkov detector system. The particles enter from the left into the gas volume in the center. The Čerenkov light is then reflected off the mirrors in the center (shown in dark) into the phototubes at the outer rim (shown as dark cylinders).

teen azimuthal regions, each housing a single mirror that focuses light onto its own photomultiplier tube. Light emitted into the region within 10 cm of the beam axis will not be collected in order to suppress accidental coincidences in the detector. A sketch of the optical design is shown in Figure 5.17. The minimum radiator thickness encountered by a particle traversing the detector is approximately 90 cm. The measured performance of the JLab CLAS Čerenkov detector was used to estimate the photoelectron yield of the HALL D design, adjusting for radiator length and the number of mirror reflections. This results in an expected average yield of 5.0 (3.3) photoelectrons for 5.0 (2.9) GeV/c pions. Particles that traverse thicker regions of the detector will

register proportionately larger signals.

5.6.4 Acceptance of the particle identification system

The overall acceptance of the particle identification system is determined by the performance of the TOF systems and the Čerenkov detector, and the effectiveness of constrained kinematic fitting. The latter allows one to compensate for incomplete particle identification in an event by determining the assignment that best agrees with energy, momentum conservation and strangeness conservation. For some reactions other constraints, for example the neutral pion mass, can be placed on the fit. Monte Carlo simulated events for reaction 5.3 were analyzed to determine the overall acceptance of the particle identification system. The events were generated using 9 GeV photons, and each event had 2 π's and 2 K's in the final state. All three detector systems were included in the simulation: TOF from the barrel calorimeter ($\sigma = 250$ ps), TOF from the downstream hodoscope ($\sigma = 80\,ps$), and a 2.9 GeV/c effective threshold momentum for the Čerenkov detector. Proton identification was assumed to be 100 percent efficient. Smeared flight times, momenta and path lengths were used in the calculations. Figure 5.18 shows the fraction of π's, K's, and p's identified as K's by a combination of the Čerenkov detector and the TOF wall. The left hand figure is for a gas index of $n = 0.0014$, while the right hand figure has a material index of $n = 1.0024$.

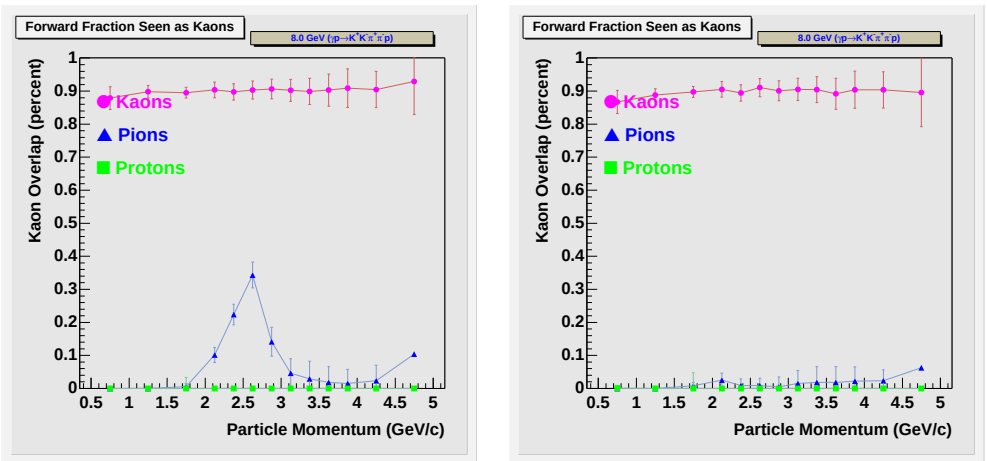

Figure 5.18: The fraction of π's, K's and p's from the reaction $\gamma p \rightarrow K^+K^-\pi^+\pi^-p$ as a function of the particle momentum. The TOF wall is assumed to have a resolution of 100 ps. The left hand plot has a Čerenkov index of $n = 1.0014$, while the right hand has $n = 1.0024$.

However, Figure 5.18 is not the entire story as far as correct identification goes. The TOF acceptance for charged tracks is determined by examining the flight time difference between π's and K's of the same momenta. If this difference is less than 3 times the σ of the TOF detector, then the particle is said to be unidentified. This 3σ limit will suppress π contamination in the K signal by a factor of 25. The ambiguities in the particle identification arise from both the non-hermeticity of the detector as well as from inherent limitations of the TOF and Čerenkov systems. A given $\pi\pi KK$ event can have 0 to 4 particles incorrectly identified. Table 5.6 shows the percentage of all events having 0 1, 2, 3 and 4 ambiguous particles for both the aerogel and the C_4F_{10} gas Černekov detector. With the proton identified, most events with either 0 or 1 ambiguous

	0	1	2	3	4
aerogel	15%	39%	33%	11%	1%
C_4F_{10} gas	26%	43%	25%	5%	1%

Table 5.6: Percentage of $\gamma p \to K^+K^-\pi^+\pi^-p$ events with ambiguous tracks in the HALL D detector.

particle can be recovered using simply strangeness conservation. By using a kinematic fit, it will be possible to also recover most of those events where 2 particles are ambiguous. This leads to the results shown in Table 5.7 which shows the percentage of correctly reconstructed events as a function of the number of ambiguous particles.

	0 or 1	0, 1 or 2
aerogel	52%	83%
C_4F_{10} gas	66%	88%

Table 5.7: Percentage of events with N ambiguous particles than can be correctly reconstructed using strangeness conservation and kinematic fitting. Events with 3 or 4 ambiguous particles are not resolved.

The variation of PID acceptance with TOF resolution is shown in Figure 5.19. It is important to keep this resolution as good as possible. The pure detector resolving power decreases rapidly with worsening timing resolution, and even though the combined results using kinematic fitting are less sensitive, the right plot shows a hint to a slope as timing resolutions get worse than 80 ps .

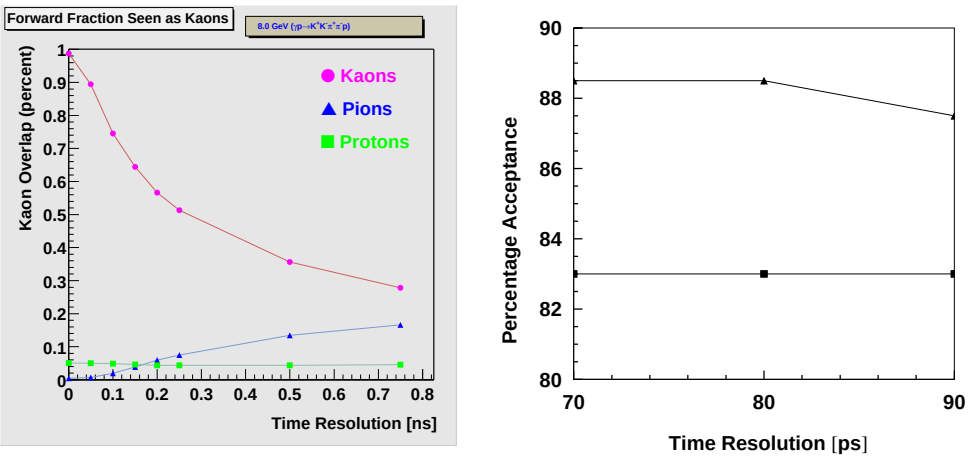

Figure 5.19: The fraction of K's from the $K^+K^-\pi^+\pi^-$ events which are correctly identified as K's as a function of the timing resolution in the TOF wall. The left plot shows the identification using only the TOF and Černekov information, while the right figure is an expanded view around the expected TOF resolution using kinematic fitting as well as detector information.

5.7 Forward calorimetry

A circular lead glass array will serve as the forward electromagnetic calorimeter for the HALL D detector. An existing detector, the LGD used in the Brookhaven E852 experiment, has been moved from Brookhaven to JLab and will be configured for use in the HALL D experiment. Several modifications to the detector are needed to optimize its performance for HALL D.

- The horizontal motion will be perpendicular to the existing configuration, that is, horizontal motion will be along the beam axis.
- A platform behind the LGD darkroom will be added. This platform will carry the electronics associated with the LGD.
- The inner frame will be stretched vertically to allow a circular array of lead glass blocks. Shim structures will be built to support the stack in uninstrumented areas.

Figure 5.20 shows the E852 LGD as modified for use in HALL D. A large range of z–motion is required to allow removal and servicing of the solenoid region components. The addition of the platform makes the detector self-contained, as all cables and electronics are contained on this platform and move with it. The circular stack matches the aperture of the solenoid and mimimizes the number of detector channels while maximizing the target to LGD distance.

5.7.1 Calorimeter performance

The calorimeter on which the HALL D detector will be based was used as a detector and a trigger element in BNL E852 and has been described previously [118]. Good position and energy resolution allowed for the reconstruction of multi-photon final states. Figure 5.21 gives some examples. We anticipate similar performance in the HALL D environment.

A trigger processor[119] allowed the calorimeter to be used as a trigger device. The total energy deposited and the effective mass of the photon system were calculated by this trigger processor. This allowed selection of well contained events or the rejection of relatively uninteresting final states. When used in conjunction with a charged track counting trigger element, final state topologies like, for example, $\pi^+\pi^-\eta$ (with $\eta \to \gamma\gamma$) could be selected while the $\pi^+\pi^-\pi^0$ topology was reduced. Figure 5.22 shows the result when events are selected by such a trigger.

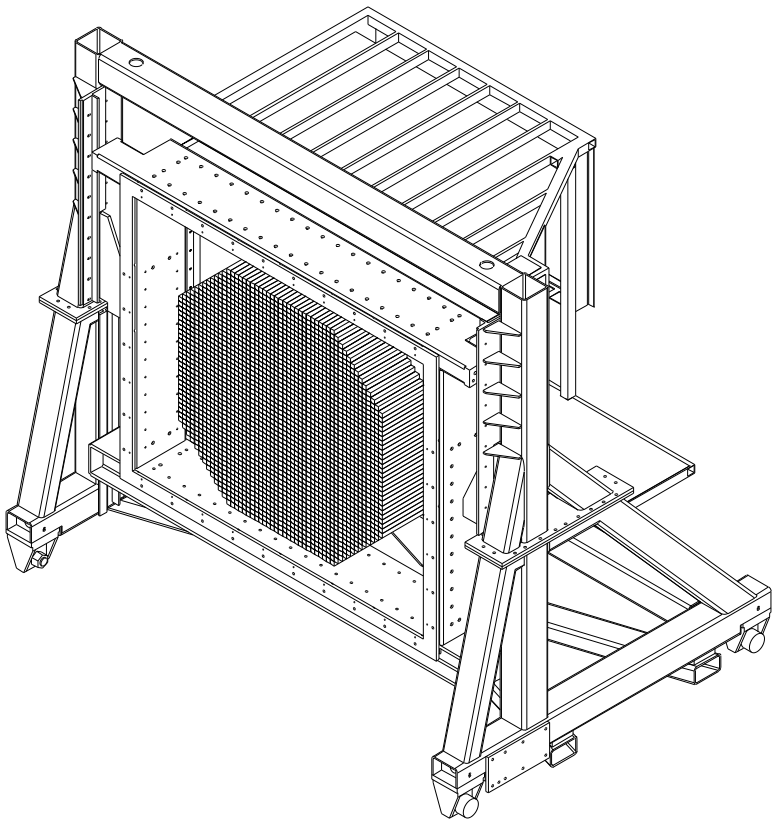

Figure 5.20: The lead glass detector as modified for use in HALL D.

5.7.2 The radphi experience

Operating an electromagnetic calorimeter, like the LGD, near a photon beamline could be a concern given the backgrounds one might expect with a tagged bremsstrahlung photon beam. For this reason, the recent experience with the LGD used in the RADPHI experiment during a recent data run in the Hall B photon beam is of particular relevance. Because of the high quality of the photon beam, beam-associated backgrounds were manageable, even when operating at an endpoint energy of 5.5 GeV. At higher energies the beam spot size will be even smaller and the LGD energy resolution will improve.

This goal of the RADPHI experiment is the measurement of rare radiative decays of the ϕ meson. The RADPHI experiment uses an LGD similar to the proposed HALL D detector with 700 similar lead glass blocks arranged in a roughly circular arrangement around the beam. A two block by two block hole allows for passage of the beam. The PMT bases are of the Cockcroft-Walton [120]

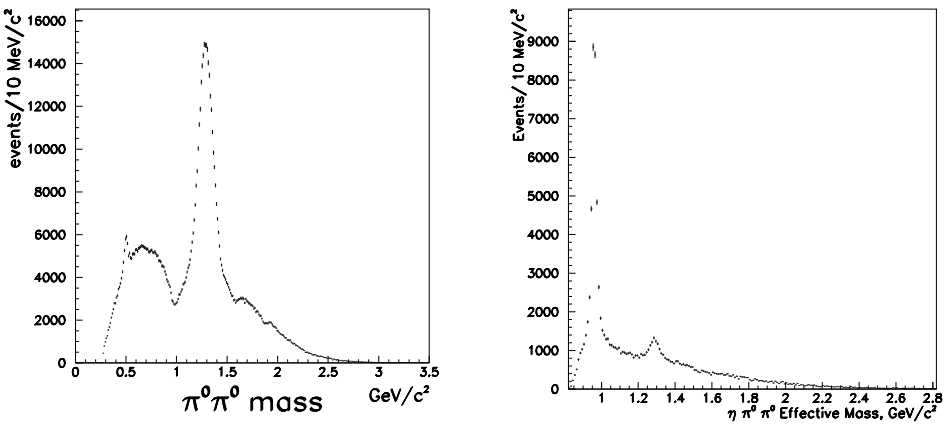

Figure 5.21: Effective masses as reconstructed using the lead glass detector in the Brookhaven E852 experiment. Left: The $\pi^0\pi^0$ mass from 4 photon events. Structures for the K_S, $f_0(980)$ and $f_2(1270)$ are seen. Right: The $\eta\pi^0\pi^0$ effective mass as reconstructed from 6 photon events. Clear structures associated with the $\eta'(958)$ and $\eta(1295)/f_1(1285)$ are seen.

type and the same ADCs and trigger processor used in the E852 experiment were used in this test run as well. The RADPHI experiment is located in Hall B downstream of the CLAS detector. The tagged photon beam operated at an endpoint energy of 5.5 GeV and the photon beam passed through the CLAS target before reaching the RADPHI experiment. A cylindrical beryllium target was used (1 *inch* long and 1 *inch* diameter) placed about 1 m from the front face of the LGD wall.

The data shown here are from 15M triggers collected in the data run. The events were passed through a cluster finder which looks for showers in the LGD array due to photons. The π^0 signal was used to calibrate the LGD by adjusting the gains of each of the modules to yield the nominal mass and to minimize the width of the π^0 seen in the 2γ mass distribution.

The 2γ effective mass spectrum from two cluster events in shown in Figure 5.23. Clear peaks at the π^0 and η are observed. The calibration procedure ensures that the centroid of the peak occurs at the nominal mass. The observed width of the peak is 0.014 GeV/c^2. A fit of the η peak, show in Figure 5.23, yields a mass of 0.547 ± 0.0044 GeV/c^2 and a width of 0.064 GeV/c^2.

The 3γ effective mass spectrum from three cluster events is also shown in Figure 5.23 for events in which two of the photons are consistent with coming from the decay of a π^0. The decay $\omega \to \pi^0\gamma$ is clearly evident.

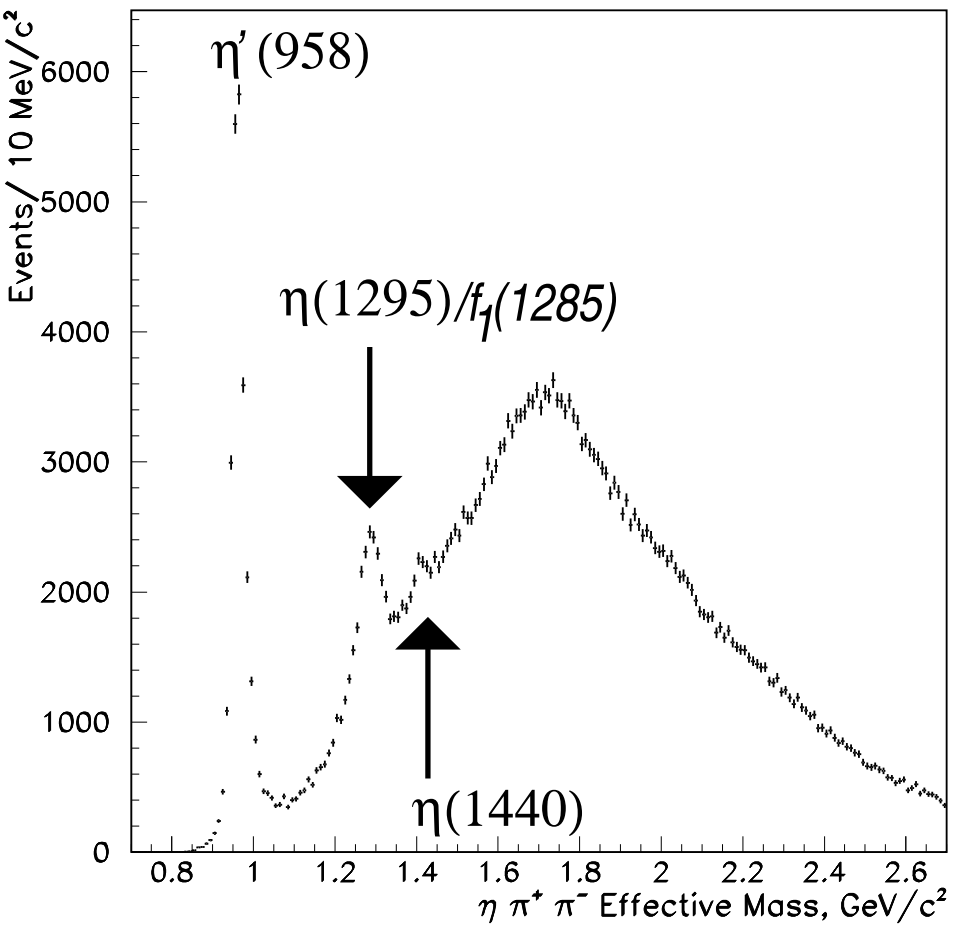

Figure 5.22: The $\eta\pi^+\pi^-$ effective mass distribution as seen in E852 as reconstructed from two charged tracks plus $\eta \to \gamma\gamma$ events. Clear structures associated with the $\eta'(958), \eta(1295)$ and $\eta(1440)$ are seen.

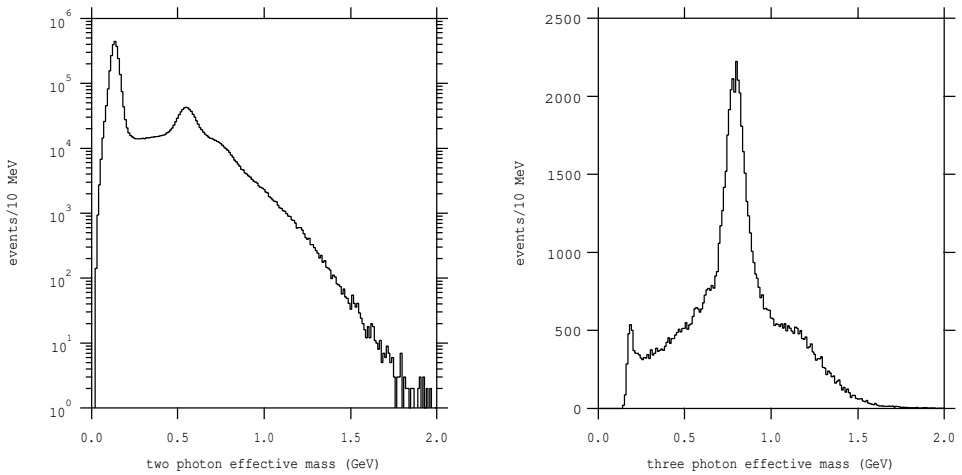

Figure 5.23: Effective mass distributions observed in the RADPHI experiment. (left) Two photon mass distribution in two-photon events. The peaks correspond to the π^0 and η. Note the log–scale. (right) Three photon mass distribution in three-photon events. The peak correspond to the $\omega \to \pi^0\gamma$.

The ϕ radiative decays, including those resulting in the final state $\pi^0\pi^0\gamma$ decaying into 5 photons, are the focus of the RADPHI experiment. Figure 5.24 shows the $\pi^0\gamma$ effective mass distribution from 5γ events identified as $\pi^0\pi^0\gamma$ events. The $\omega \to \pi^0\gamma$ is clearly visible in this distribution. Figure 5.24-right shows the same distribution with the additional requirement that no energy be deposited in the cylindrical calorimeter surrounding the RADPHI target. The ω signal/background improves indicating that high multiplicity, well contained events with a radiative decay can be selected and that an electromagnetic calorimeter can be successfully operated in the proposed environment.

RADPHI ran in a high intensity photon beam. The intensity of this beam was similar to intensities anticipated for HALL D, that is, 5×10^7 photons per second in the energy range between 75% and 95% of the electron beam energy.

The RADPHI calorimeter was radiation damaged during this high intensity run. It was shown [121] that this damage occured gradually over the run period and was limited to the region immediately surrounding the beam hole in the center of the calorimeter. Curing these central blocks *in situ* with a high intensity (100 watt) UV lamp with a UV transmitting light guide was effective in recovering the performance of this region of the detector.

Similar effects could be anticipated for HALL D and UV curing will remain an effective remedy should unacceptable damage occur. However, several important differences between the conditions of RADPHI and HALL D lead us to

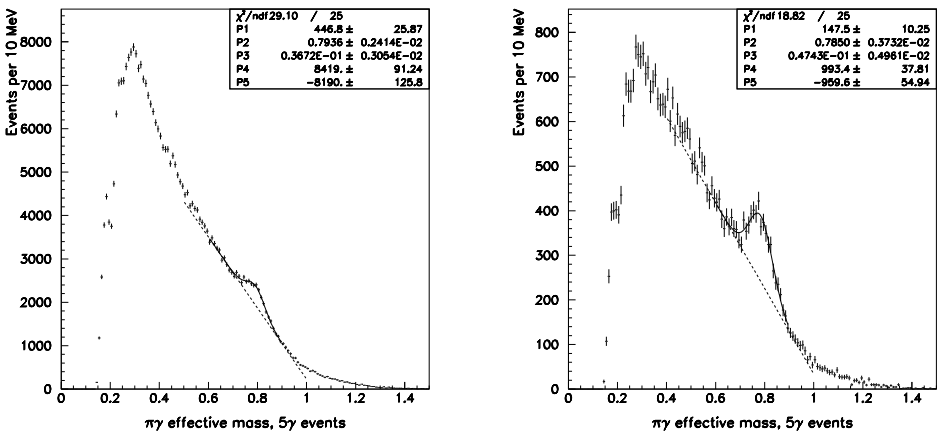

Figure 5.24: The $\pi^0\gamma$ effective masses from 5γ events identified as $\pi^0\pi^0\gamma$ from the RADPHI experiment. The figure on the left is for all events, while that on the right is for events in which no energy is detected in the barrel region.

conclude that the effect of radiaton damage rate will be smaller in the HALL D environment:

- The beam energy is higher, leading to smaller dose rates at fixed angle for HALL D than for RADPHI.
- The HALL D beam will be more tightly collimated than the RADPHI beam.
- The LGD is shielded from charged particles produced in the target by the solenoidal field.

These effects, plus the availability of an effective treatment, lead us to conclude that radiation damage will not be an issue for HALL D.

Chapter 6

Civil Construction

The meson spectrometer will be in a new experiment hall (HALL D) located at the end of a new beamline off the stub at the east end of the North Linac. Figure 6.1 shows an overview of the accelerator and of the proposed HALL D location.

Civil construction includes breaking through the accelerator stub, tunnel construction, beam transport system and instrumentation. Aabove ground facilities including the tagger building, HALL D service buildings, beam dumps, control room, roads, and parking area. Basic infrastructure for all utilities is also included.

We have had numerous meetings with JLab civil construction, accelerator, and RadCon staff, and conclude that there are no serious civil construction problems. The main problem is to minimize cost while satisfying HALL D requirements. In particular, the beamline and hall will fit on DOE/SURA land, building construction should be straightforward, and RadCon problems can be handled by standard techniques. A formal agreement to use a portion of land owned by SURA for the HALL D project is under consideration.

Figure 6.1 shows the plan and elevation views for the HALL D beamline and associated buildings.[1] Figure 6.4 shows more detail of the tagger building and HALL D complex.

6.1 General requirements

Requirements and specifications assuming a maximum electron beam energy of 12 GeV are given in Table 6.1 and below:

[1] The elevation is for a beamline 1.5 m above grade. The option of a beamline which is 3.0 m below grade is also under consideration, but appears to be more expensive.

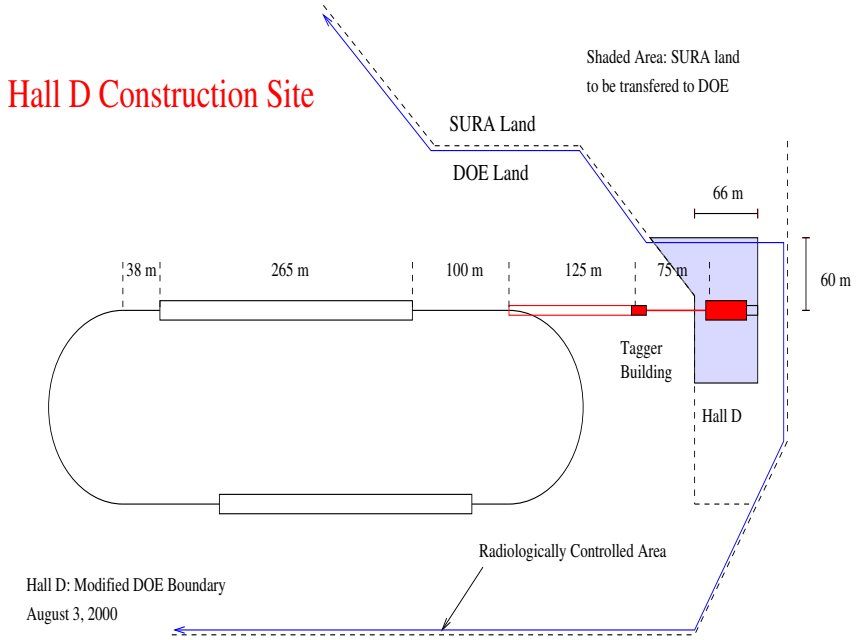

Figure 6.1: An overall view of the accelerator site and HALL D.

- Single electron energy available for the D line
- HALL D is designed for a photon beam only (i.e. no primary electrons into HALL D)
- Civil construction compatible with 24 GeV beam (e.g. 80 m bend radius)
- Accelerator tangency point to radiator = 125 m
- Radiator to collimator distance = 75 m
- Tagger building = 6 m x 15 m x 3.5 m (height). Nominal beam height above tagger floor = 1.5 m. Beam is nominally 4.5 m from the south wall and 1.5 m from the north tagger wall.
- Housing for sideways electron beam dump = 3 m x 5 m x 3 m (height)
- Detector building = 15 m x 30 m x 11 m (clear hook height). The collimator enclosure upstream is 12 m). The nominal beam height above the HALL D floor = 3.5 $\pm$ 0.3 m. Beam is nominally 10 m from the south wall and 5 m from the north wall in HALL D.

Parameter	Operating Value	Design Max
Max Electron Current	3 μA	5 μA
Min Electron Current	$\sim$0.0001 μA	0.0001 μA
Electron Energy	12 GeV	12 GeV
Power	36 KW	60 KW
Photon Power (Collimator)	7 W	10 W
Photon Power (Detector)	1 W	1.5 W

Table 6.1: Beam parameters for a 12 GeV electron beam.

- Permissible building settlements: 1 *inch* initial; 2 *inches* max over lifetime

6.1.1 Compatibility with future upgrades

The allocation of space for the beamline instrumentation and layout of the site is designed such that an accelerator upgrade to 24 GeV would be possible using proposed buildings and tunnels. We assume that during 12 GeV operation HALL D would only receive 5.5-pass beam. For 24 GeV operation HALL D would receive 4.5, 3.5 or 2.5-pass beam; the number of passes will be switched at most annually. This implies that conditioning for the HALL D beam cannot start before the tangency point and no recombiner area is required. For 24 GeV operation, an east two-way RF separator would be used to extract the beam; the configuration could be changed during long shutdowns by relocating extraction and transport elements.

6.2 Personnel protection

The Jlab Beam Containment Policy requires that personnel be protected from accidental beam loss by at least three independent devices built using at least two different technologies.

6.2.1 Failure scenarios

The following failure scenarios were identified:

- Failure of vertical beam transport, shooting electron beam into the sky.
- Poor tuning or steering of electron beam.

- Excessive current in electron beamline.
- Tagger magnet failure, directing electrons down the photon line.
- Excessive photon flux (resulting from obstructions in the electron beamline, poor vacuum, etc).

6.2.2 Beam containment proposal

In the following we list the active and passive safety devices that assure the primary electron beam reaches the diamond radiator and the electron dump. We believe these devices satisfy the Laboratory beam containment rules as well as the SLAC beam containment rules, where there are currently two "above ground" primary electron beams in operation. See Ref. [122].

Electron beam on diamond radiator

1. There should be a beam current monitor near the exit from the linac which will turn off the beam if the current exceeds the Hall D requirement.
2. The bend string, which brings the beam up from the accelerator and back to horizontal, must be in series on the same power supply.
3. The bend string power supply should be equipped with a "meter relay" which shuts off the primary beam if the supply current varies by $\pm 10\%$ from its desired value.
4. Preceding the diamond radiator there should be a small aperture protection collimator with a burn-through monitor and a beam-loss detector, such as an ion chamber, which will shut off the beam if it hits the protection collimator.

Electron beam on the dump

1. There should be a meter relay on the tagger magnet power supply to turn off the beam if the supply current varies by more than $\pm 10\%$ from its desired value.
2. There should be a beam current monitor set to a low threshold in the photon beam line just downstream from the tagger magnet which will shut off the primary beam if it detects a charged beam in the photon line.

3. Following the current monitor there should be a permanent magnet to bend a charged beam downward.

4. There should be small aperture protection collimators with burn-through-monitors on either side of the permanent magnet with ion chambers or other type of beam loss detectors near the protection collimators.

5. There should be a beam current monitor just upstream of the 60 KW electron dump. This current reading can be compared to the current reading at the exit of the accelerator and shut off the beam if the readings differ by more than a few percent.

6.3 Environmental and radiation concerns

The civil construction includes shielding for all buildings which are obtained from preliminary, but conservative, estimates of expected radiation doses. They are based on original calculations by Lewis Keller, who has served as a consultant on this project. The Jlab RadCon group has refined his estimates using GEANT based simulations and a realistic geometry for the buildings.

6.3.1 Site dose limits

On–Site The design goal at Jefferson Lab is 250 mrem/year which may include occupancy as a factor and is based on guidelines from the Jefferson Lab RadCon Manual. This implies an average dose rate of less than 0.1 mrem/hour. There is also an instantaneous accident dose rate limit which is identified in the Jefferson Lab Beam Containment Policy as 15 rem/hour based on maximum credible beam loss conditions.

Site boundary The integrated dose limit at any point on the site boundary is 10 mrem/year.

6.3.2 Beam on radiator

For the purpose of estimating dose rates, RadCon assumes that losses along the transport line are of order 0.1%. After the beam is horizontal, two burn-through monitors with small apertures preceding the radiator are needed. In addition there should be a 1-2 m steel wall downstream from the last vertical bend, as in the beam lines to the other halls.

6.3.3 Tagger building

Jlab rules require that the instantaneous dose rate outside HALL D during a beam accident be less than 15 R/hr, assuming the beam will be turned off in less than 1 second. To shield photons and neutrons, 3.0 m of earth shielding is sufficient.

6.3.4 Tagger hodoscope

Assuming the dump is 60 m from the hodoscope elements and that there is a 5 cm vacuum pipe leading to the dump, the neutron rate coming backward from the dump is 3×10^6/s, and the photon rate is 0.9×10^8/s for a 60 KW beam on the dump.

6.3.5 Electron beam dump

The electron beam dump proper will be based on a design similar to the existing BSY 120 kW dump [2] at Jlab. Beam dumps with similar characteristics are in use at SLAC [123]. We have extensive operational experience with the BSY dump and detailed calculations [124] of neutron production and ground water activation for this geometry. This dump is designed so that all the primary beam energy is dumped in solid metal. The closed water circuit for cooling sees only thermal energy, not beam energy, and there is no hydrogen generation. The dump will require regular service, which can generally be performed from outside the building itself. The absorption of longitudinal showers, including muons, will be accomplished with the beam dump proper, aided by an additional 10 m of Fe downstream to insure containment. JLab requires that the dose rate must be less than 0.1 mrem/hour outside the building. Therefore, the lateral containment of photons and neutrons resulting from the 60 KW beam, also requires 1 m of steel and 5 to 6 m of earth on the top and sides of the building.

6.3.6 Collimator enclosure

Assuming a limit of 0.1 mrem/hr outside the building and a 10 W photon beam, 1.2 m of steel is needed on the top and sides of the collimators for high-energy neutrons, and 1.7 m of earth or concrete is needed in the backward

[2] An identical dump is available, which is located in the north linac "stub" and was used in commissioning days, but must be removed during the construction of the HALL D transport tunnel. It has its closed circuit water system attached, along with steel shielding for neutrons.

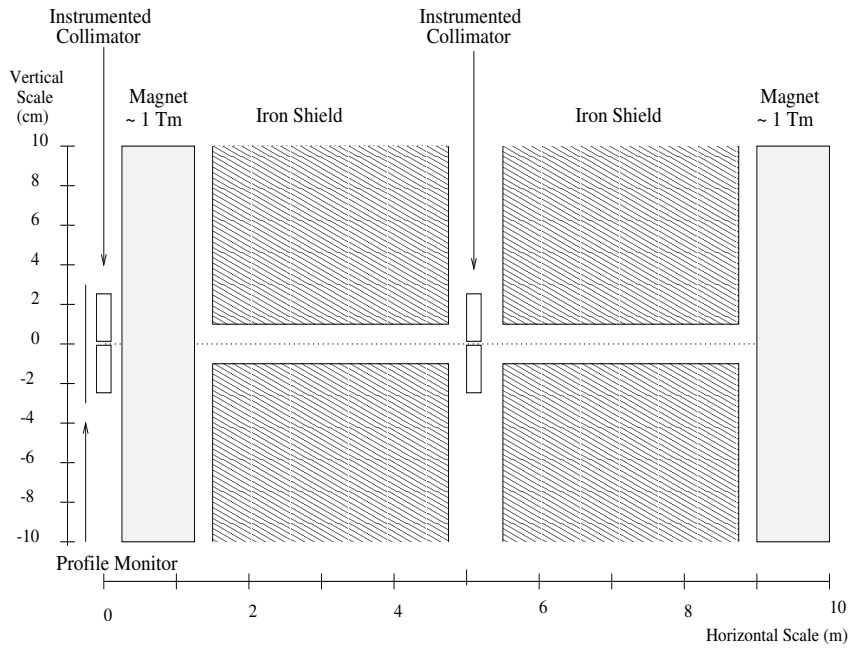

Figure 6.2: Schematic of space allocated for the collimator enclosure which includes limiting apertures, sweeping magnets and passive iron shielding. Details of photon beam generation are contained in Chapter 4.

direction for the giant-resonance neutrons. The general layout is given in Figure 6.2. The design and specifications of the photon beam are given in Chapter 4.

6.3.7 Detector building

To shield against low energy neutrons, the wall thickness must be 40 cm up to 5 m above grade level and 10 cm above that. The roof must be at least 10 cm thick. The calculated radiation doses, using realistic GEANT Monte Carlo input geometry, are 5-10 μrem/hr in the Counting House, 30-50 μrem/hr in the parking lot, and 1.6 μrem/hr at the site boundary. Assuming an annual operation of 30%, the integrated dose at the site boundary is estimated at less than 5 mrem/year.

6.3.8 Photon beam dump

The photon beam dump is required to absorb up to 1.5 W of photons which survive collimation and are used for experiments in HALL D. The photon beam must be transmitted to the interior of the dump in order to minimize the flux of secondaries scattering back into HALL D. A few meters of steel is adequate to contain the residual muon production, covered by earth to stop neutrons. Most of the muons produced in the collimation enclosure are absorbed before entering HALL D[125, 100].

6.3.9 Ground water activation

Based on the present design, there are no concerns about surface water, ground water, or soil activation in the vicinity of the end station itself. Any concerns for groundwater and soil activation are limited to the beam transport line up to and including the structures containing the photon tagger assembly and the electron beam dump. Procedures in place for current operation will be used to address these.

6.4 Geotechnical analysis

Engineering Consulting Services, Ltd. has completed a subsurface exploration and geotechnical analysis to understand the foundation conditions for building construction for the Hall D site on the east end of the accelerator. Details of their findings can be found in their report [126]. We briefly summarize their work and review their conclusions which are of direct interest to the project.

Eleven borings were taken which covered the intended construction site. Each boring obtained nine samples down to a depth of 10 m. The samples were analyzed and classified according to the unified soil classification system. In Figure 6.4 we have summarized the composition of the soil from the samples. They indicate that the soil above the Yorktown Formation, starting at depths of 5 to 6 m below grade, would not provide stable support for construction.

Based on the amount of expected settlement and the low allowable bearing pressure, a mat foundation was found unsuitable for above-ground construction. To limit settlements, Engineering Consulting Services recommends a pile foundation system be used to support the buildings, including walls, columns, floor slabs and detector crane rails. Foundation settlements for pile supported structures should be less than 3/4 $inch$.

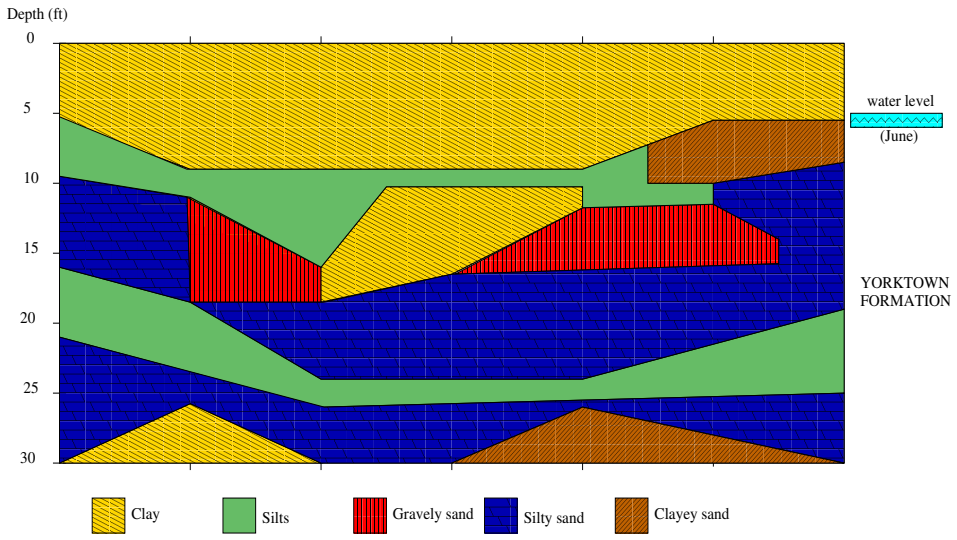

Figure 6.3: Typical composition of soil under the HALL D contruction site as a function of depth. The result of the geotechnical analysis shows that buildings at grade level will require support piles, driven approximately 15-20 m into the ground.

6.5 Costs

Preliminary designs, optimizations, and cost estimates have been performed and are summarized in Chapter 12 [127].

6.6 Schedule

Jlab engineers estimate that civil construction will take a minimum of 27 months (including design time) from project start until we can gain beneficial occupancy of the detector hall and control room.

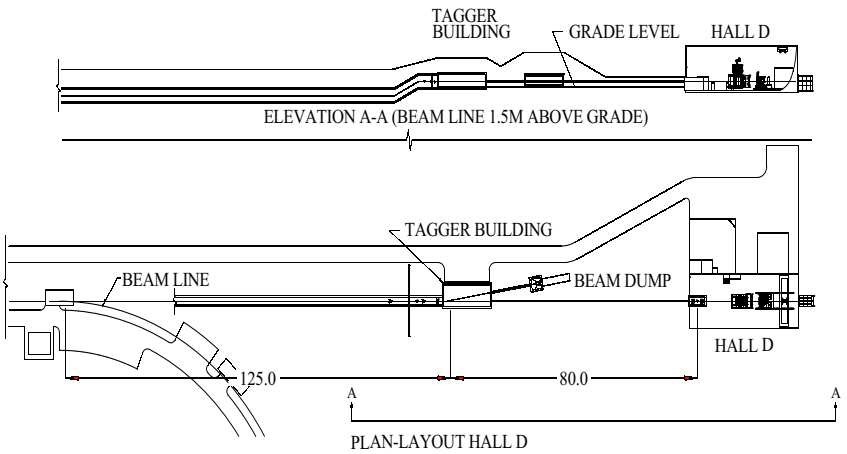

Figure 6.4: Elevation and plan view of the tagger and HALL D buildings.

Chapter 7

Rates, Trigger and Data Acquisition

7.1 Expected rates

7.1.1 Overview

We estimate trigger and background rates in HALL D using measurements of the hadronic cross section combined with the CLAS experience. The hadronic rate between any two photon energies E_1 and E_2 can be written as

$$R = \int_{E_1}^{E_2} n\sigma(E)\frac{dN}{dE}dE$$

where n is the number of target protons per unit area, $\sigma(E)$ is the hadronic cross section as a function of energy, and dN/dE is the photon energy spectrum. The photon flux is composed of a coherent and incoherent sum as detailed in Chapter 4. Background rates are dominated by the broad-band incoherent flux. The signal rates result from the photon flux in the coherent peak, which will depend on the radiator crystal structure and its orientation. The coherent peak will be optimized to the specific physics program. For our rate estimates, we use the typical case for the flux computed on a diamond radiator with the coherent peak at $\mathrm{E}_\gamma = 9\ GeV$.

Both coherent and incoherent fluxes are proportional to the electron beam current and radiator thickness. Multiplying the number of electrons per second by the radiator thickness in radiation lengths gives the product N_0 which we will use in the following calculations. For conditions which we will refer to as "low intensity" (300 nA beam on a 10^{-4} radiator), $N_0 = 1.9\times\ 10^8$/s. For the coherent peak at 9 GeV the tagged photon flux between 8.4 and 9.0 GeV is

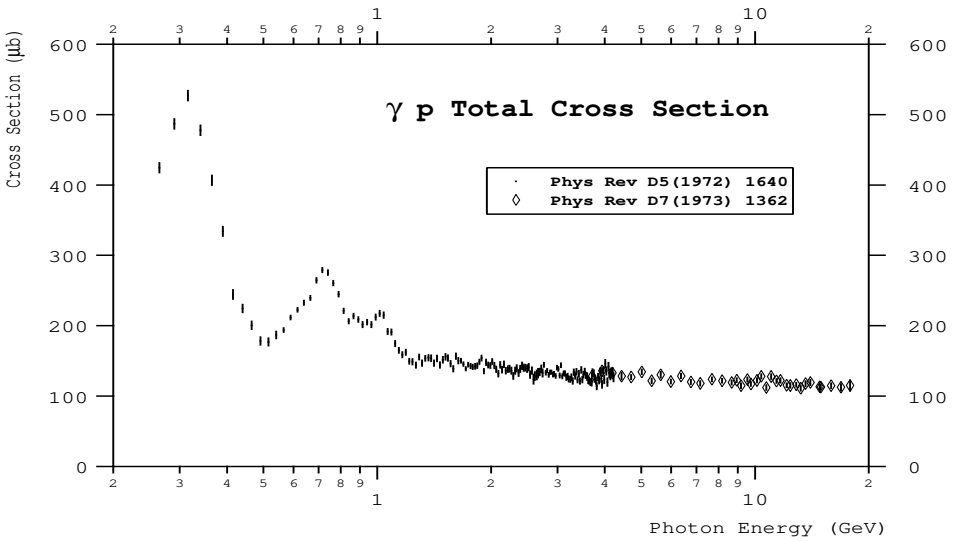

Figure 7.1: Total cross section for $\gamma p \rightarrow$ *hadrons* as a function of photon energy.

$R_{tag} = 0.14\ N_0$. The average tagging efficiency over this interval is 0.375, so the tagged photon flux on target is 1.0×10^7/s. "High intensity" running, where the tagger becomes ineffective as part of the level 1 trigger, nominally corresponds to $N_0 = 1.9 \times 10^9$/s and yields 10^8/sec tagged photons on target.

The total hadronic γp cross section[1] is plotted in Fig. 7.1. For the experimental conditions defined above and a 30 *cm* liquid hydrogen target, the total hadronic rate in the detector is

$$R_0 = 2 \times 10^{-4} N_0 \tag{7.1}$$

and a tagged hadronic rate

$$R_T = 7.4 \times 10^{-6} N_0 \tag{7.2}$$

For low intensity, the expected total hadronic rate is 37 *kHz* and the tagged hadronic rate is 1.4 *kHz*.

7.1.2 Trigger elements

We make some rudimentary assumptions about the trigger elements in order to estimate various rates. These assumptions are discussed further in the

[1] We use measured cross sections [128, 129] with actual data obtained from the Durham Data Base [130]

Trigger section of this document. Initial commissioning of the detector at low rates will use a level 1 trigger to select events of interest. At higher rates a sophisticated level 3 software trigger [2] is required. We concentrate here on discussion of rates at lower photon beam fluxes.

The trigger consists of coincidences between several counter elements of the detector. It must select the tagged hadronic rate in the presence of accidentally coincident backgrounds. The first trigger element is the photon tagger, essentially a segmented scintillation counter. The rate in this counter is determined by N_0, which is controllable (within limits) by the experiment.

The second trigger element is the start counter. A start counter similar in design to that used in CLAS would suffice for low intensity running, although modifications will likely be needed to handle high intensity conditions. One possible design might use several layers of scintillating fibers. Such a counter would also provide position information with sufficient resolution for track reconstruction. In comparing the demands of the HALL D start counter to the CLAS experience, it is useful to note that the HALL D target is inside a solenoidal magnetic field which will protect the start counter from the flux of low-energy Compton scattered electrons emerging from the target. The CLAS start counter does not enjoy this protection.

The tagger and start counters are small, and are therefore the best candidates for determining the precise event timing. For this discussion, we will assume that coincidences between them can be identified within a time window $\Delta T_1 = 15\,ns$.

Interesting events will have particles in the final state other than the one that satisfied the start counter requirement. These particles may be energetic, forward-going charged particles, forward or large angle photons, and/or charged particles with sufficient transverse momentum to reach the bore of the solenoid. Any particles of this type will be registered in other elements of the detector and these signals can be used as further requirements in the trigger. This refines the loose interaction definition given above. We refer to this collection of signals as the global level 1 trigger. As its elements are counters of extended size, we take a coincidence time window $\Delta T_2 = 100\,ns$ when the global level 1 trigger is required.

7.1.3 Accidental rates

The rate of interesting events given by Eq. 7.2 is $1.4\,kHz$ ($N_0 = 1.9\times\ 10^8$/s) and $14\,kHz$ ($N_0 = 1.9\times\ 10^9$/s) for low and high intensity beams respectively.

[2] We are reserving level 2 for a possible intermediate level hardware trigger

However, various other processes will form accidental coincidences at the different trigger stages, and we need to recognize these. It is most important that these do not form the bottleneck for the data acquisition system, regardless of our ability to reject them offline.

We consider two sources of accidental background. They are not entirely mutually exclusive, but we consider them separately for ease of explanation. The first (A_1) of these comes from purely random time coincidences between the trigger elements, in which case we compute the time overlap based on the various counter singles rates. The second (A_2) is more "physical", considering hadronic photoproduction that is outside the tagging range, but in accidental coincidence with the tagging system.

First consider purely random coincidence events. A coincidence between the tagger and start counter loosely defines an interaction in the target. The rate A_0 of this coincidence is given by

$$A_0 = SR_{tag}\Delta T_1 \tag{7.3}$$

where S is the total rate in the start counter. Based on the experience in CLAS, we take $S = 0.03N_0$, scaled using appropriate factors for collimation and beam intensity. This is most certainly an upper limit because of the solenoidal shielding effect. For $R_{tag} = 2.7 \times 10^7$/s we find $A_0 = 2.3 \times 10^6$/s, considerably larger than the tagged hadronic rate $R_T = 1400$/s. Further refinements are achieved by the global level 1 trigger.

The rate of the global level 1 trigger, $f_{L1} \times R_0$, is taken to be the total hadronic rate[3] reduced by the rate for single pion production for $E_\gamma \leq 0.5$ GeV ($f_{L1} = 0.5$). A loose trigger which uses a charged particle track count in the start counter and requires neutral energy in the barrel and/or forward calorimeter (see Section 7.2.2 below) should easily be able to eliminate these low energy events. The accidental rate using both the interaction and global level 1 triggers is

$$A_1 \;=\; A_0 f_{L1} R_0 \Delta T_2 = S f_{L1}(0.28 \times 10^{-4}) N_0^2 \Delta T_1 \Delta T_2 \tag{7.4}$$

where we have substituted from Eqs. 7.1 and 7.3 and used $R_{tag} = 0.14 \times N_0$. The second accidental background comes from true hadronic events, and therefore would pass the global level 1 trigger. They are out of time with the precise RF signal, but that is much smaller than the online resolving time ΔT_1 of the interaction coincidence. Ignoring the "true" events that are part of this rate, one calculates

$$A_2 = f_{L1} R_0 R_{tag} \Delta T_1 = f_{L1}(0.28 \times 10^{-4}) N_0^2 \Delta T_1 \tag{7.5}$$

[3]The cosmic-ray rate is small and has been neglected.

In order to evaluate the total accidental contribution numerically, correlations must be taken into account. This reduces the sum of the above estimates. For $N_0 = 1.9 \times 10^8$/s, the accidental contribution to the trigger is $7.3\,kHz$, and the tagged hadronic rate is $R_T = 1.4\,kHz$. We note that as the photon flux increases, the start counter and tagger lose their effectiveness in reducing trigger rates, so the trigger rate asymptotically becomes proportional to the hadronic rate. At higher currents, a DAQ system with a software level 3 trigger is required. A summary of the rates is shown in Fig. 7.2 as a function of electron beam current.

7.1.4 Rates in tracking chambers

At the high photon flux anticipated for HALL D, one concern is that the occupancy rates in the drift chambers may be too high to allow reconstruction. In order to estimate these occupancies, a test of high intensity running with photons was performed in the CLAS detector.[4] Measurements were taken at 10, 80, 250 and 320 nA with a 10^{-4} radiator, and rates were measured in the forward TOF scintillators (7.5-12.5 deg), the electromagnetic calorimeter (8-45 deg), and the drift chambers. The drift chamber occupancies at the highest current (320 nA) are given in Table 7.1.

Table 7.1: Drift chamber occupancies for each superlayer (in percent) for run 21998 at the maximum beam current of 320 nA (logbook entry #7031).

Beam	Region 1 S1	Region 1 S2	Region 2 S3	Region 2 S4	Region 3 S5	Region 3 S6
Photon	2.3%	2.3%	0.3%	0.4%	0.7%	0.9%

Although the conditions of the test did not duplicate precisely the conditions expected in HALL D, reasonable estimates can be made by appropriate scaling. In Table 7.2 we compare the differences in target, collimation and beam energy. As the majority of background results from lower energy photons, we assume the energy dependence of the measured rates is small. The rates are scaled by a factor of 1.7 (ratio of target lengths) and the beam current is scaled up by a factor of 5.33, which is the expected collimation ratio. The drift chambers in region 1 are completely unshielded by any magnetic field in CLAS, whereas the drift chambers in region 2 are shielded by the field of the

[4] This information is taken from CLAS-NOTE-2000-004 High-Rate-Test by Elton Smith.

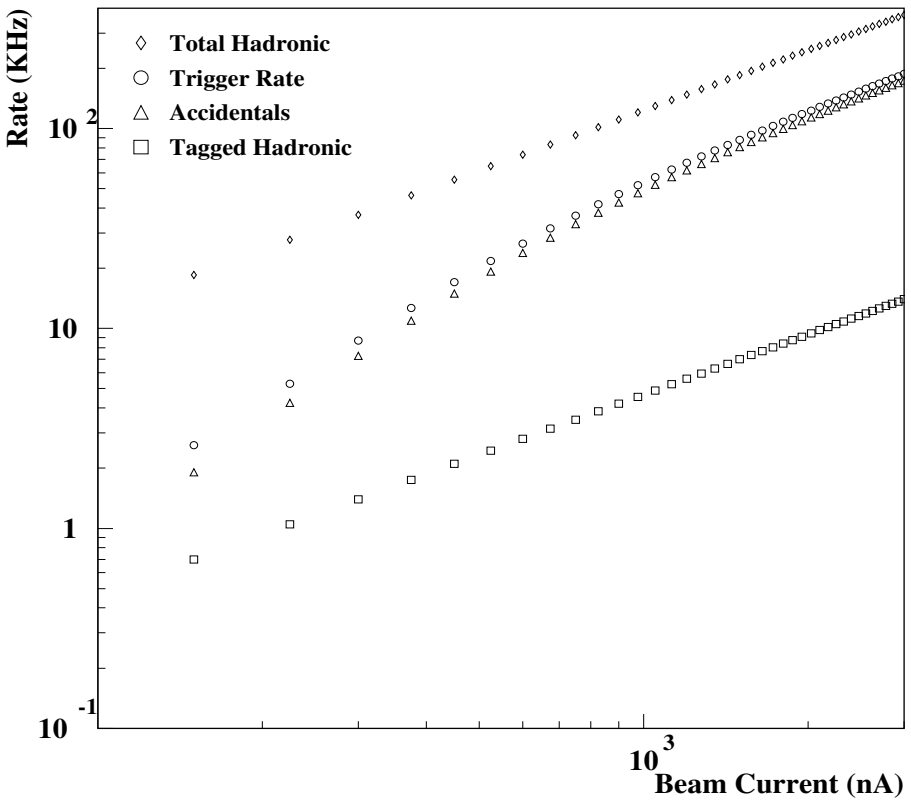

Figure 7.2: Estimated rates as a function of electron beam current. Plotted is the total hadronic rate and the estimated trigger rate, which is the sum of accidental coincidences and the tagged hadronic signal.

CLAS torus. The 2.2 T solenoidal field for HALL D is expected to be at least as effective as a shield as the CLAS torus. Therefore, we expect the oocupancies in the HALL D drift chambers to be as low or lower than those in CLAS for comparable granularity.

Table 7.2: Comparison between conditions in Hall B during high rate test and anticipated running parameters for HALL D. A current of 3 μ A in HALL D corresponds to 10^8 photons/s in the coherent peak.

	Hall B Test	Hall D
Beam Current	80 nA $\rightarrow$ 320 nA	300 nA $\rightarrow$ 3 μ A
Radiator	10^{-4}	10^{-4}
Collimation keeps	80%	15%
Target Length	18 cm	30 cm
Beam Energy	2.4 GeV	12 GeV
Trigger	Restricted	Open

Extrapolating measured occupancies in region 2 to a current of 3 μA (HALL D with 10^8 photons/s in the coherent peak), we expect an occupancy of 0.6%. The rates are plotted versus electron current scaled to HALL D in Figure 7.1.4. This is well below the typical operational limits of 2.3% imposed for the region 1 drift chambers in CLAS during electron beam running, a rate at which tracks can still be reconstructed with reasonable efficiency. We note that the extrapolated rates in region 1 for a beam current of 3 μA is approximately 5%, exceeding usual operational limits by a factor of 2, but this figure is for a configuration which is completely unshielded by any magnetic field whatsoever and thereby represents an absolute maximum to the expected rates. We note that the operation of a polarized target in Hall B (which replaces the mini-toroid with a solenoidal field) allows running at twice the normal luminosity. Thus we expect that for comparable segmentation, raw rates in the HALL D detector at the maximum design current will be similar to the current experience with CLAS. The conclusion is that the HALL D detector should be able to handle rates up to 10^8 photons/s.

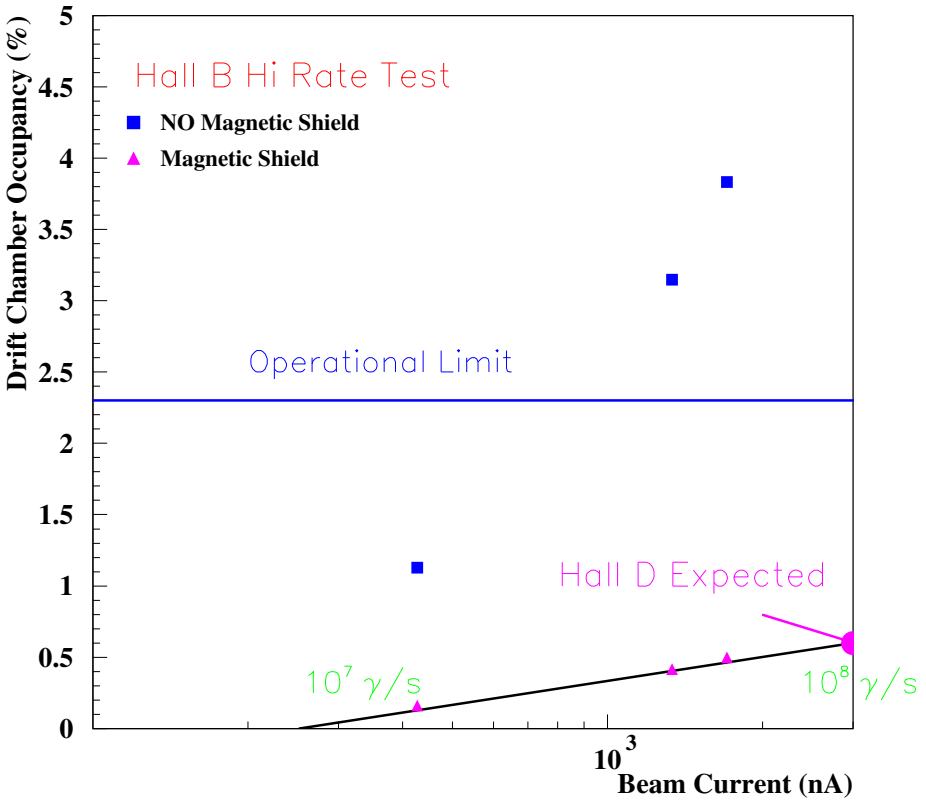

Figure 7.3: Drift chamber occupancies (scaled by target thickness = 1.7) plotted versus beam current (scaled by collimation factors = 5.33) expected for HALL D operation. The drift chambers in region 1 (squares) are completely unshielded by any magnetic field in CLAS, whereas the drift chambers in region 2 (triangles) are shielded from backgrounds by the main torus field. The nominal low current operation in HALL D (10^7 photons/s in the coherent peak) corresponds to 300 nA. The 2.2 T solenoidal field for HALL D is expected to be at least as effective as a shield as the CLAS torus.

7.2 Trigger

7.2.1 Overview

In order to achieve the roughly 20-1 reduction in event rate, Hall D will use a two-stage trigger, combining a hardware-based level 1 trigger with a software (reconstruction) based level 3 trigger. An essential feature of the HALL D design is to build pipelining into the entire trigger, digitizer, and data acquisition systems at the outset. This has the twin virtues of allowing adequate time for the level 1 trigger to do its job, while eliminating signal degradation involved in delaying the signals while the trigger operates. Pipelining in this way also allow us to upgrade from initial photon fluxes of 10^7 photons/sec to eventual fluxes of 10^8 photons/sec without any significant changes to the trigger/DAQ architecture. Eliminating conversion deadtimes will allow us to acquire events which occur very close together in time.

Figure 7.4 shows a schematic of the implementation of the HALL D level 1 trigger. The level 1 trigger makes a decision based on detector elements which

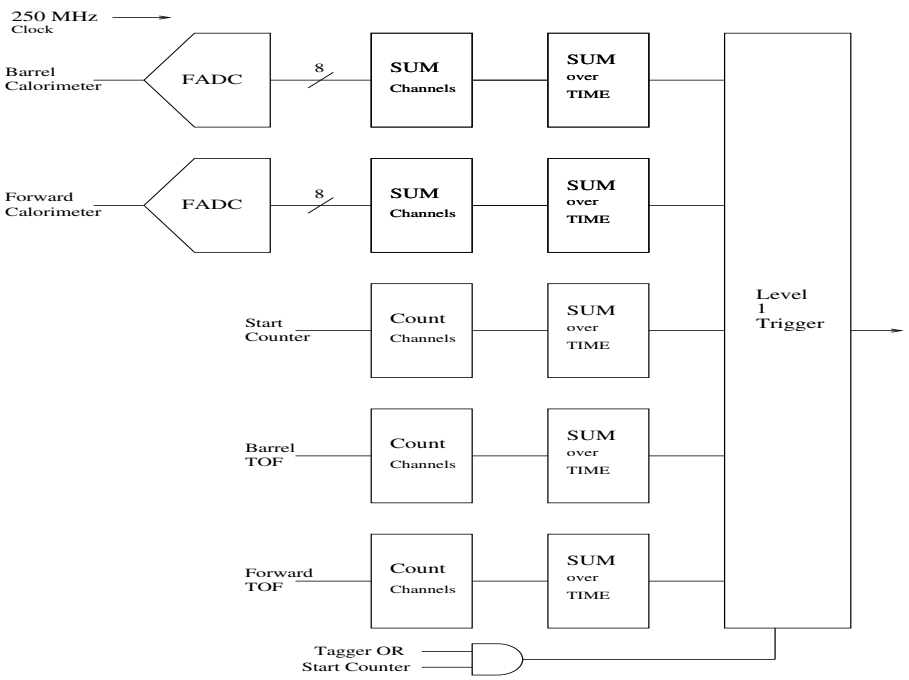

Figure 7.4: A schematic diagram of the HALL D trigger.

measure hadronic multiplicities (track counts) and energies. In the schematic

shown, the start counter and barrel calorimeter and forward TOF detectors provide the track count while the barrel and forward calorimeters determine the energy. A tight tagger OR/start counter coincidence is used as input to the level 1 trigger for low photon fluxes of $\approx 10^7$ photons/sec.

For high photon fluxes ($\approx 10^8$ photons/sec), the tagger OR/start counter coincidence is not a useful requirement, and the level 1 trigger will probably only be able to cut the rate down from 385 KHz to around 180 KHz. Most of this background comes from multi-pion events caused by untagged (low energy) photons. In order to reduce this rate by a factor of 10, a very accurate reconstruction of the photon energy is required. Because of the complexities involved in accurately determining track momenta and then linking information from the different detectors, we believe the best approach is to use a software level 3 trigger embedded in the DAQ architecture, rather than to build a series of specialized level 3 trigger processors. This level 3 trigger will do a simplified full reconstruction of the event, using all of the data, in order to throw out events from low energy photons.

7.2.2 Level 1 trigger

The level 1 trigger consists of five subsystems, and a global trigger processor (GTP) which combines these five outputs into the global level 1 trigger. Each of the subsytems continuously (via a digital pipeline) computes a parameter, then compares it against a number of programmed value/function pairs. A value function pair might be an energy value and a $<$, $=$, or $>$ function. When any of the value/function requirements is satisfied, the subsytem sends a timestamped subsystem event report (SER) to the GTP. The GTP is programmed with a number of different level 1 trigger configurations, each combining different value/function pairs from the subsystems, along with a trigger coincidence window (TCW) specifying the maximum time window for coincidence of the different trigger requirements.

The five level 1 trigger subsystems are:

1. **A track count** - obtained from the start counter. The start counter discriminator signals are used to create the prompt OR for coincidence with the tagger, but are also sent into a *track count pipeline* to determine the number of tracks. The sample rate for the pipeline would be $4\,ns$ ($250\,MHz$). Two different track counts may be programmed, each with a $<$, $=$, or $>$ criterion attached.

2. **A track count** - obtained from the barrel calorimeter. The discriminator signals from the central calorimeter are sent into another *track count*

pipeline which determines the number of tracks. This pipeline runs synchronously with the start counter track count pipeline. Two different track counts may be programmed, each with a $<$, $=$, or $>$ criterion attached.

3. **An energy sum** - obtained from the barrel calorimeter. The barrel calorimeter will be digitized by 8 bit, 250 *MHz* flash ADCs (FADC). All channels are then digitally added together (in a pipeline tree) to form the barrel calorimeter energy sum. These adders are pipelined at the same 250 *MHz* rate, giving an energy measurement every 4 *ns* for use in the *Level 1 Trigger*. The energy sum then passes through a shift register thus making available a time window. Successive samples within this time window are added together. This is analogous to the gate width in a conventional charge sensitive ADC. Two different energy values may be programmed, each with a $<$, $=$, or $>$ criterion attached.

4. **A track count** - obtained from the forward TOF. Discriminator signals from the forward TOF are sent into a *track count pipeline* which determines the number of tracks. This pipeline runs synchronously with all the other level 1 pipelines. Two different track counts may be programmed, each with a $<$, $=$, or $>$ criterion attached.

5. **An energy sum** - obtained from the forward calorimeter. This sum is constructed in the same manner as for the central calorimeter, except that the selection of which digitized analog sums are added together to form the forward energy sum, is programmable. Two different energy values may be programmed, each with a $<$, $=$, or $>$ criterion attached.

As mentioned above, the GTP may be programmed with several different triggers. Programming a single trigger means selection of

1. Either a minimum, maximum, or exact number of tracks in the start counter.

2. A minimum, maximum, or exact number of tracks in the barrel calorimeter.

3. A minimum, maximum, or exact number of tracks in the forward TOF.

4. A minimum or maximum for the global energy in the barrel calorimeter.

5. A minimum or maximum for the global energy in the forward calorimeter. Certain areas might be programmed out of this sum.

6. The appropriate boolean combination of elements 1-5.

The trigger will have the capability to have at least eight simultaneously defined triggers. This trigger is very flexible and can be programmed to be very loose (say one track in the start counter) or very tight (specific track counts and energy thresholds in each detector). Examples of triggers which can be programmed in this model include:

1. At least two tracks in the start counter AND at least one track in the downstream TOF.

2. At least one track in the start counter AND a minimum energy in the downstream calorimeter.

3. At least two tracks in the start counter AND at least one track in the barrel calorimeter AND a minimum requirement of energy in the barrel calorimeter AND a minimum requirement in the forward calorimeter.

All subsystems will run synchronously and will be timed so that the time stamps from average momentum tracks ($\sim$ Ebeam/3) will match at the GTP. Higher and lower momentum tracks will be slightly out of time, but this effect should be less than 20 ns, and this is compenstated for by programming the TCW value. The synchronous output of the level 1 trigger will then be ANDed with the coincidence of the tagger OR and the start counter OR. This allows the timing to be determined by the tagger and start counter, and removes the synchronous nature of the trigger.

The rate of the global level 1 trigger, $f_{L1} \times R_0$, is taken to be the total hadronic rate[5] reduced by the rate for single pion production for $E_\gamma \leq 0.5$ GeV ($f_{L1} = 0.5$). A loose trigger which uses a charged particle track count in the start counter and requires neutral energy in the barrel and/or forward calorimeter should easily be able to eliminate these low energy events. The resultant level 1 trigger rate is about 180 kHz. We note, however, that 80% of the hadronic rate comes from photons with energies below 2 GeV. This energy cut, which would require a more sophisticated trigger, would reduce the level 1 rate to 70 kHz.

[5]The cosmic-ray rate is small and has been neglected.

7.3 Data acquisition

7.3.1 Overview

The data acquisition goal for HALL D is to accept the level 1 trigger rate without incurring any DAQ system deadtime. The high rate of 70-180 kHz drives the design of the trigger, the front-end electronics, and the DAQ system. Both the FADC and the TDC digitizing modules must store data for several microsecond so that the level 1 trigger can be processed. When the level 1 trigger is satisfied these devices must be read-out without deadtime. When the level 1 trigger is asserted, a time slice of each ring buffer will be copied, compressed and stored. Events will be buffered into groups of at least 64 on each electronics board and then transferred first across a backplane to be built into crate event fragments and then to a computer farm to be built into complete events. The farm will perform a quick analysis to reduce the event rate by approximately a factor of ten before recording to magnetic media. This design allows HALL D to start running with a modest tagged photon rate and then to scale-up by an order of magnitude.

The DAQ system will be an important part of the whole HALL D data analysis system. The rates and complexity of the DAQ system for HALL D are challenging, nevertheless we will provide a flexible system that will allow different modes of read-out:

- production physics events,
- full FADC and TDC time window events, and
- several microseconds streams of raw FADC and TDC data for the whole detector.

Additionally, since demand for access to a DAQ system during accelerator down-time is very high, we propose that the system should allow independent trigger, control and read-out of sub-systems so that effective use of this time can be made. Each of the components of the data acquisition system will be discussed below.

7.3.2 Data flow

Two basic types of digitizing electronics will be used in HALL D, ADCs and TDCs. Channels which measure energy will be continuously sampled with flash ADCs. These boards would be designed by our collaboration; a conceptual design is shown in Fig. 7.5. A dual-port RAM running at the full FADC speed

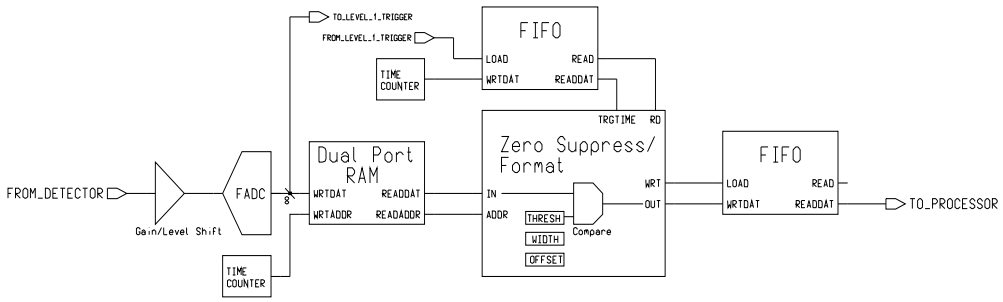

Figure 7.5: Block diagram of FADC board.

continuosly stores the FADC data. The level 1 trigger signal will copy data from the time window of interest to an output queue. A prototype of this board is currently being designed. The general philosophy is to use commercial FADC integrated circuits and programmable gate arrays. Suitable FADC ICs are being developed by industry for fully digital radio receivers. An 8 bit, 200 MHz FADC IC is available today for ~$20 each. Programmable gate arrays with internal dual-port RAM are also available today for ~$20 each. These ICs are used in high speed computer network routers.

In HALL D there are approximately 16,000 FADC channels. If we assume a typical occupancy of 2%, a 250 MHz, 8 bit FADC, a time window of 100 nanoseconds, and that the full time window is read-out, then the total amount of FADC data would be: 16000 channels * 0.02 (% occupancy) * 25 bytes/channel = 8Kbytes per event.

The 25 bytes/FADC channel is used to get an energy and a time signal. Previous work [131] [132] indicates that a time resolution better than the FADC sampling interval can be achieved by fitting the FADC waveform. We are studying algorithms for determining energy from a FADC waveform. Figure 7.6. shows results obtained for a simulation in which a PMT of the type used in the forward calorimeter was modeled and digitized by an ideal FADC. The energy was determined by simply summing the FADC samples.

Reduction of the FADC data will be performed in real-time. The result will be an energy, a time, and a channel identifier. This would allow us to reduce the amount of data per hit to 10 bytes per FADC channel thereby lowering the total FADC data to 3.2 Kbytes per event. The computational resources required to achieve this reduced data rate are currently being studied. It may be possible to build this processing into the gate array, or to include digital signal processors on the FADC boards.

Channels which require precise time measurements will use a multi-hit

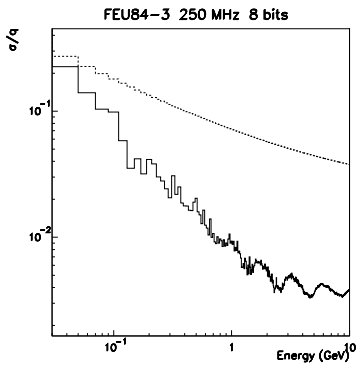

Figure 7.6: Resolution as a function of energy for simulated FEU84-3 PMT sampled at 8 bits, 250 MHz. LGD resolution is shown by dotted line. FADC samples are summed to determine energy.

TDC. We are evaluating a few sources of such boards. One company, "Acam Messelectronic Gmbh"[6], has a prototype board based on the "F1" ASIC developed for the COMPASS experiment at CERN. This design can provide up to 60 *ps* resolution and is designed for high rate, low deadtime experiments. The TDCs can store hits for several microseconds and are equipped with a filter and a muliple level buffering scheme so that only times from a region of interest are read-out. In HALL D there are approximately 8,000 TDC channels. The data volume for the TDCs would be: 8000 channels * 0.02 (% occupancy) * 4 bytes/channel * = 640 bytes per event. The total event size would be about 4 Kbytes; we assume 5 Kbytes per event for the DAQ design.

Once the event fragments have been selected from a stream in each channel and reduced, they must be built into complete events and pass a filter that will reject accidentals and low energy events. Board level event fragments will be read out over a VME backplane and crate level event fragments will then be assembled and sent to the level 3 trigger farm. One important detail of the DAQ design is that the boards would have to buffer 64 (or more) events locally before transferring this group of event fragments to the crate computer. This is necessary because the tasks that the crate computer is required to do can't be done today at a 100 *kHz* interrupt rate with a commercial real-time operating system. At 64 events per buffer, we will have to transfer about 23.5 KB in less than 640 microseconds. This transfer speed (36.7 MB/sec) is achievable with current VME technology. Depending on the CPU power available, the crate CPU may reorganize the crate event fragments so all data from one event is

[6]see www.acam.de for details on the "F1"

contiguous.

Using current technology this data transfer rate could be handled using either gigabit ethernet or ATM OC-12 network links. Regardless of the network hardware, significant CPU resources will be required at the crate level to transmit the data. A fast switch with a backplane bandwidth greater than 672 MB/second and more than 40 ports will also be required. This switch technology is under development by many networking companies[7] and in a few years it should be common and less expensive.

The architecture of the CPU farm which performs event building, filtering and recording is presented below. Event building and recording will be done in parallel on 10-20 computers. Each of these systems would send events to a sub-farm for filtering. The sub-farm nodes would send a pass/fail answer for each event received and the master node would record all events that passed the filter. It is possible that further information could be added to the event or that the events selected by the filter could even be reformatted before being sent to the recording computer(s).

7.3.3 Level 3 trigger

The goal of the level 3 trigger is to reduce the event rate given by the level 1 trigger to an acceptable rate to tape. In low intensity running (10^7 tagged photons/s) the level 1 trigger rate is expected to be $15\,kHz$. Since the DAQ system is being designed to handle this rate to tape, the level 3 trigger farm will not have to cut any events, although it may be used to reduce the event rate somewhat. In high intensity mode where the level 1 rate may be as high as 180 kHz, the level 3 trigger must be able to reduce the event rate by a factor of ten.

Most of these unwanted events result from an untagged (mostly lower energy) photon interacting in coincidence with a tagged photon. Rejecting these events means that level 3 must be able to calculate, with reasonable accuracy, the energy of the photon which produced the event. This involves accurately reconstructing tracks, matching them with the calorimeters, and adding additional energy deposited by neutral particles in the calorimeters.

Because of the accuracy requirements and the demands of linking information from different detectors, we have decided to use a processor farm architecture for level 3 instead of building a dedicated hardware processor. All events passing the level 1 trigger will be read into the level 3 processor farm where they will be reconstructed; events passing the cuts applied will then be

[7] One product from Cisco is described at http://www.cisco.com/warp/public/146/1971.html

written to tape. This approach allows for algorithmic flexibility and improvements, and the ability to adjust cost-effectively to higher rates, but it does put pressure on the DAQ system.

An estimate of the processing power required can be made as follows. The Hall-B full event analysis, with momentum resolution of less than 1%, requires approximately 45 milliseconds on a 21 SPECint processor (Pentium III - 500). We believe that HALL D will be similar and will require a similar amount of processing power. To perform the level 3 trigger analysis we think that 1/10 the number of instructions will be adequate because unlike the 1% precision required in a full reconstruction we are aiming for only 2-5% precision. In fact Hall-B has such a pattern recognition program in development; it is able to achieve 10% momentum resolution using only 3% as much processing power. Therefore we believe that approximately 5 milliseconds on a 21 SPECint processor will be required for the level 3 analysis of each event. This yields a figure of 0.105 SPECints/ev/s as a good estimate of the processing power required. This means an aggregate processing power of 18,900 SPECints is required for the level 3 analysis. Allowing for 50% processor utilization (due to I/O overhead etc.) this means that a farm composed of 200 computers each capable of 200 SPECints could handle the I/O and perform the level 3 analysis for the high intensity configuration.

Table 7.3 shows the rates, sizes, and processing requirements for the level 3 trigger.

7.3.4 Monitoring and control

Monitoring and control tasks include hardware configuration and control ("slow controls"), bookkeeping, online event monitoring, alarm systems,and messaging systems. These are less demanding tasks than data acquisition in HALL D, and should not present unusual challenges. We plan to follow some examples from Hall B, but to also make use of lessons learned there. In particular, we plan to integrate offline data analysis tools with the online software at the outset to reduce the total cost of software development.

The number of events that can be processed online is largely determined by the number of processors available. In HALL D a monitoring component can be added to the main event filtering code to gather statistics about both the event that is being written to tape and those being discarded by the level 3 farm. The choice of the type and number of processors can wait until soon before the system is installed, when prices are lower and performance is better known.

The framework for slow controls should be uniform for all subsystems in

	Low Rate	High Rate
Event Size	5 KB	5 KB
Event Rate to Farm	10 kHz	180 kHz
Data Rate to Farm	50 Mbytes/s	900 Mbytes/s
Num Links to Farm	20	20
Data Rate per Link	2.5 Mbytes/s	45 Mbytes/s
Link Technology	100 Megabit Ethernet	Gigabit Ethernet
Events/s per Link	500	9000
SPECints/ev/s for L2	0.105	0.105
Num SPECints/link	52.5 SPECints	945 SPECints
Num SPECints/link x 2	105 SPECints	1890 SPECints
Num 200 SPECint processors/link	1	10
Total Num 200 SPECint processors	20	200

Table 7.3: Rates, sizes, and processing requirements for the level 3 trigger.

HALL D, but the choice is not obvious. VME-based EPICS works in Hall B, but does not mesh well with the online requirements and has proven to be manpower intensive. In fact, a number of Hall B systems do not use EPICS or VME, but instead resort to CAMAC or other options. Other software possibilities include message-based systems and hardware alternatives include PC or mixed hardware systems. We believe that an open, message-based system that implements a uniform interface to diverse hardware is probably best. Commercial products are currently available that implement this at moderate cost.

Bookkeeping tasks include all recordable activities of the experiment other than raw and calibration data. We expect this will be done using relational and/or object-oriented databases. Current commercial and public domain database technology should be adequate.

The alarm and messaging framework allows sub-systems to communicate their state to monitoring programs and operators. This system needs to be integrated across the entire online, DAQ, and database systems in a simple, uniform manner. The scale and performance requirements of this system are modest, and similar to other projects in progress or completed at Jefferson lab.

Chapter 8

Data Handling and Offline Computing

8.1 Overview

In this section we present a conceptual outline of our plan for the HALL D computing activities in two parts. The first discusses how we intend to create the initial data record. The second discusses how we intend to manage and process the data once it has been acquired. In acquiring and recording the data, we plan to employ a data handling strategy similar to those currently used by many large experiments. Although handling the 100 MB/sec of data generated by HALL D is ambitious by today's standards, this should be achievable at a reasonable cost in the near future. The subsequent offline computing activities require a significant effort on the part of the HALL D collaboration, forcing us to examine emerging information technology and to develop an offline system that is significantly different from existing systems.

The CLAS experiment at Jefferson lab has run with a maximum rate to tape of about 10 MB/sec. Below we justify our approach by scaling up the CLAS experience to the HALL D rate of 100 MB/sec.

As is the case with CLAS, online data will be staged directly to tape silos residing in the Computer Center. The offline analysis will rely heavily on the tape silos and large disk farms to access the data for both track reconstruction and higher level analysis. It will also make use of computer facilities optimized for simulations, calibrations and partial wave analysis. Information on the condition of the detector, experiment and analysis will be maintained in a collection of databases.

We plan to integrate our online and offline software efforts, as our online

level 3 trigger farm will run essentially offline reconstruction and analysis code. Extensive online data quality checking is critical since the level 3 farm will (eventually) discard much of the online data. Database integration will be achieved using a common interface to access all of the distributed database information.

There are a number of labor intensive steps associated with the data analysis. In seeking to create an offline software that minimizes the effort required to complete these tasks, we have developed a "Grid-based" design that employs several computer systems that are customized for particular types of computations. The resulting collection of data and services are then integrated at the software level by a HALL D portal.

Discussed below are our projected hardware requirements, expected computer support, and software development strategy; first for the online and then for the offline analysis.

8.2 Data acquisition hardware requirements

Our data handling hardware requirements divide into five categories: bandwidth, tape speed, long–term data storage, CPU power, and disk space.

Jefferson Lab routinely handles CLAS data rates up to 10 MB/sec to tape. The lab provides a dedicated fiber optic link between the experimental hall and the computing center capable of transferring 100 MB/sec. Currently Gigabit Ethernet is capable of real bandwidths of better than 50 MB/s. Using multiple ("trunked") connections the necessary bandwidth could be available with today's technology. With 10-Gigabit Ethernet expected within one or two years, the required 100 MB/s data transfer rates will be easily achievable.

Data transferred to the computer center is written directly to tapes in a tape silo. Current tape speeds are 10 MB/sec onto 50 GB tape cassettes. Tape speeds will double in 2000-2001, and should exceed 40 MB/s before HALL D data taking begins. Accounting for tape mount times and redundancy, we will need about 5 tape drives dedicated to HALL D online data recording.

We are planning for a peak DAQ rate of 100 MB/sec to tape. At this rate we will accumulate 1000 TB of raw data per year, assuming a 1/3 duty cycle (same as CLAS). In addition, sufficient space will be needed to store processed data and Monte Carlo data. CLAS currently generates over 1.5 times more processed data than raw data (overall multiplication factor 2.5), and keeps the raw data in the silo for long periods. We anticipate requiring more simulations per raw event than CLAS, and are planning on accumulating approximately 3000 TB per year. To accommodate the larger accumulated data volume,

we are developing plans that do not require long storage times for the raw data. We plan to double, at most, the total accumulated raw data volume, and will move raw data out of the silo at the same rate it is generated. We are investigating compression algorithms, storage formats, etc. in the hope of generating as little as 0.5 times more processed data than raw data.

Currently tapes hold 20-50 GB, depending on tape technology. By 2005 we expect tapes holding 200 GB to cost around $100, about 5 times cheaper than current tape cassettes, although this is uncertain. A tape silo typically holds 6000 tapes, or 1200 TB at 200 GB/tape. Thus JLab will need to purchase 2 tape silos to store HALL D data, and will need adequate tape archive and storage facilities. Tape costs are likely to be a factor of 2 more than for CLAS, but might be comparable if we can find a way to store less processed data.

Events produced by the HALL D detector should be of comparable size and complexity as CLAS events (5 KB/event, ≈30K channels), and analysis should require about the same amount of CPU power per event. CLAS data are analyzed on 400-600 MHz Dual Pentium III Linux machines having high bandwidth access to the tape silo. Current processing rates are around 6 events/sec/cpu, or 480 events/sec on 40 dual processors.

Assuming Moore's law holds (doubling of cpu power every 18 months for the same cost), as is expected, we could purchase a factor of 10 more compute power than CLAS uses for the same cost. Thus HALL D processing should cost no more than CLAS processing.

How much disk space HALL D will be need is very uncertain at this time. Disk costs have been dropping dramatically, leading CLAS (and others) to store processed data on large online disk farms instead of tapes. Small RAID systems have already begun to appear on the desktop! HALL D also plans to follow this very efficient analysis strategy, and might need several hundred TB of online disk space. JLab currently has about 10 TB online. Clearly the balance we choose between tape and disk storage will depend on state of the art five or six years from now.

We note that upcoming RHIC, CERN and FNAL experiments will produce about the same amount of data as HALL D, but a few years earlier. Further, LHC is expected to start about the same time as HALL D, but with higher rates.

In summary, we anticipate that computing technologies needed for the HALL D initial data storage will be available, and that the costs for acquiring the new data handling systems will generally be about the same as those originally employed for CLAS. The exception is that offline storage might cost about a factor of 2 more, depending on the cost of tapes and disk farms, and on our ability to minimize the size of the processed data.

8.2.1 Computer center support for data acquisition and storage

The Computer Center plans to support HALL D in the same manner as is currently done for CLAS and other experiments, with the important distinction that the HALL D computing facilities will be logically separated from the other computing activities. This change is intended to improve our ability to schedule tape access. The Computer Center will provide data storage, networking and processing power for first-pass analysis of the data, and will support the data acquisition systems (including level 3 trigger farm) in collaboration with HALL D. In particular, HALL D will provide system managers for DAQ systems, while the Computer Center will provide system administration, software, and (24x7) hardware support.

8.2.2 Software development for data acquisition

It is essential that HALL D begin software development very early, earlier than most experiments. The level 3 trigger code is basically the offline analysis code; this must be written, debugged, and working a year or more before production startup. The Monte–Carlo simulation must be available years before startup in order to debug the level 3 code. Further, unlike most experiments, our analysis code must also be available a year or more before startup, as our optimal running strategy depends on the methods used in analysis. It is clear that close integration between online and offline code development is mandatory.

Software manpower estimates are notoriously difficult; here we assume our needs scale by the number of lines of code (loc). The CLAS online and offline software contains approximately 500 K loc, and we expect the same for HALL D .

Effective programmers in our field typically produce 10-20 K loc/year, although individual productivity varies greatly. The CLAS data acquisition effort alone required 25-50 programmer-years over a 5 year period, or about 5 to 10 full–time programmer–equivalents. Similar total efforts were devoted to developing simulations and reconstruction codes.

In order to minimize costs (loc, maintenance) we plan to use a carefully chosen subset of modern languages and tools, especially object oriented languages and modern database technology. We also will take an integrated approach, treating the entire software effort (online, offline, slow controls, etc.) as a complete system (common libraries, tools, databases, etc.).

Finally, existing software will be used when appropriate. For example the modern, object oriented partial wave analysis code that has been developed

for the analysis of CLAS data will be used in HALL D .

In summary, it is clear that HALL D requires a large group of experienced programmers, many of whom will need to be located at JLab. We believe a core group of at least 5 or 6 physicist/programmers, familiar with modern programming techniques and tools, should be hired early on in the project. They will need to start working 5-6 years in advance of production data taking.

8.3 HALL D Offline Computing

The range of computing activities required by HALL D are typical of experiments at most high-energy and nuclear physics facilities. However, in terms of data quantity and complexity, the activities fall somewhere between the proposed upgrade for CLAS and the planned CMS detector at CERN - which is expected to generate roughly 33% more data. The HALL D data size and complexity require that we develop automated, high level data management tools. The HALL D computing activities can take full advantage of the expertise gained at Jefferson Lab in data acquisition and analysis. Consequently, the efforts for other planned JLab projects, particularly for an upgraded Hall B are synergistic with the effort required for HALL D .

The computing activities required to carry out the HALL D program include: data acquisition and triggering, calibrations, data analysis, slow controls, physics analysis, simulations and all of the tasks associated with communicating information about the status of these activities to the members of the collaboration. General technical solutions and the expertise to conduct these activities exists within the collaboration; still the effort required to complete these tasks is significant and literally thousands of detailed technical decisions must be made and implemented as the computing environment is created. The resulting computing environment will have a fundamental impact on the quality of the scientific results from HALL D – the ease with which we can do our computing will play a critical role in the quality and timeliness of our physics program. To this end we intend to adopt a computing strategy that:

- Enables university-based physicists to play key roles and provide appropriate levels of leadership in all stages of computing related activities from the development of reconstruction programs and software infrastructure to the extraction of physics results.

- Is optimized for ease of use and broad participation in computing activities.

We intend to apply and to extend recent developments in information technology such as portals and distributed services to our scientific computing activities. In particular, we intend to:

- make information about the equipment status, experiment and the computing activities routinely available to collaborators where they work.
- design separate computer systems to perform specific tasks rather than trying to create one general purpose computing system. The general purpose computing system will be achieved by creating a single user interface to the different services.
- minimize data movement - bring the applications to the data and send the results to the user only when absolutely necessary.
- provide tools to aid the collaboration in distributed computing activities.

Estimates of the computing required to complete these tasks made this far in advance of the development of the required algorithms provide only general guidelines. We are fortunate that our estimates can be based roughly on the experience with CLAS. The table below summarizes the expected computing needs for HALL D based on the following assumptions:

1. The event rate into the level three trigger is approximate 180 Kevents/s.
2. The event rate out of the level three trigger is approximately 15 Kevents/s.
3. The processors will operate at the equivalent of approximately 5000 MHz computers.
4. The overall duty factor for the accelerator and detector operation is about 1/3.
5. The number of instructions for offline analysis is roughly equivalent to that of CLAS.
6. The number of instructions for detector simulations is roughly equivalent to that of CLAS.
7. We expect that the physics analysis of HALL D data will be limited by systematic uncertainties. Consequently we require extensive simulations (about 10 simulated events/real event).

8. These tasks are being carried out on computer systems dedicated to these activities.

Computing Process	Instructions CLAS/event (CPU-ms/ev)	Instructions HALL D/event* (CPU-ms/ev)	Num. of CPU's Needed	Data Produced (MB/s)
Online Trigger	N/A	0.5	100	75
Offline Analysis	50	5.0	50	50
Simulations	1000	100.0	500	25

* We are assuming a factor of 10 improvement in CPU performance over current systems.

Based on the above data production rates, HALL D should generate approximately three Pbytes of data annually, excluding detector and calibration information. These estimates probably underestimate the total computing and data slightly, since they exclude physics analysis, calibration and development activities.

8.3.1 Detector calibration

Data calibration requires the repeated analysis of a small subset of the experimental data. Retrieving these data from tape is often delayed due to long tape access times. To overcome this problem, we expect to create a second data output stream that duplicates a small fraction (0.5 to 1%) of the experimental data onto a dedicated calibration system. An inexpensive computer system will be created to maintain approximately two years worth of calibration data (about 30 TBytes) and to carry out the computing needed for detector calibrations.

8.3.2 First-pass event analysis

For the current experiments at Jefferson Lab, data location, efficiency and quality control issues have confined most first-pass analysis activities to Jefferson Lab. Jefferson Lab computing facilities will be expanded to meet the expanded archival and computing needs. However, we hope to make it possible for people who reside somewhere other than Jefferson Lab to contribute effectively to the first-pass analysis. This requires the development of routine methods for distributed collaborators to work together on the first-pass analysis and to stay informed of the analysis progress.

8.3.3 Event simulations

Event simulations play a key role in this project since we anticipate that the quality of our results will be limited by systematic errors. This means that understanding the detector is critical. Simulations are a relatively straightforward and compute limited task. Our plan, which is motivated by the CMS computing plan, is to distribute the simulation effort among several of the institutions within the HALL D collaboration. We are planning to operate several simulation centers (3-5) that will serve as both compute and data resources for the experiment. The main motivation for this choice is to relieve pressure on the Jefferson Lab tape systems. Such tape systems are inherently inefficient due to the number and variety of input/output requests they get and the difficulty with developing automated algorithms to schedule such heterogeneous systems. By creating relatively homogeneous environments for the calibrations, simulations, first-pass analysis and physics analysis, we hope to reduce the impact of the scheduling problem.

Distributing the simulations over several sites requires that we develop the infrastructure to manage such systems (there are several universities within the collaboration which currently operate smaller systems). We must also develop a transparent mechanism for running simulations on these facilities and for communicating the results of the simulations to the rest of the collaboration. If one adds enough resources to each site to allow the collaboration to manipulate the results of the simulations then it may never be necessary to transfer the simulation results from one site to another. To make such facilities usable, one must deploy software tools that enable the remote submission and tracking of jobs on any of the computer systems and that integrate the simulation database with the online and offline databases. Such systems are just now coming into common use.

8.3.4 Physics analysis

One of the key activities of the physics analysis is the partial wave analysis of the experimental data. This process relies on the determination of the maximum likelihood and has been essentially unchanged for decades. The problem is almost trivially parallel and therefore can be performed on a loosely coupled cluster of computers. We intend to perform this activity on a cluster created expressly for this purpose, to explore several alternative algorithms that are suitable for exploring alternative solutions and to develop 3-D visualization tools to help evaluate the quality of our results.

8.3.5 HALL D portal (myHallD.org)

The computing environment that must be constructed to complete this project will require a large effort by many people. The resulting system will be a complex, distributed computing system. The goals of the HALL D portal effort are to make the complex distributed nature of the computing system transparent to the users and to provide users with customized, collaborative access to all information about the detector, the experiment, the analysis and the services that the HALL D computing environment provides.

To this end we intend to describe as much of our data as possible in XML, with the goal of describing all data produced in the experiment, analysis, calibration, simulation and physics analysis processes in DTD or XML Schema. By integrating XML into the experiment from the detector to the physics analysis we create simple mechanisms for describing and accessing data within our applications. In particular we make the information accessible via the HALL D portal. This information will most likely be stored in a variety of databases. For example slow control information might be stored in a mySQL database on the online system, while run information and first-pass analysis information might be stored in a commercial database at Jefferson Lab and simulation information might be stored in databases at the simulation centers. It is the task of the HALL D portal software to provide users with an integrated view of this information.

8.3.6 Project timeline

While the data size is comparable to CMS, the size of the collaboration is approximately an order of magnitude smaller. Thus we have a premium on getting the most out of the people within the collaboration. Figure 8.1 provides an estimate of the time required to complete many of the major computing task. Most of the major tasks require several people working full time for several years. Consequently it is critical that key individuals be identified early in the project. These individuals must develop the detailed standards and structures for all future computing activities.

8.4 Conclusions

The data acquisition and storage needs of the HALL D experiment are achievable, even though they are a factor of 10 greater than those currently in place for CLAS, because of anticipated improvements in CPU power, bandwidth,

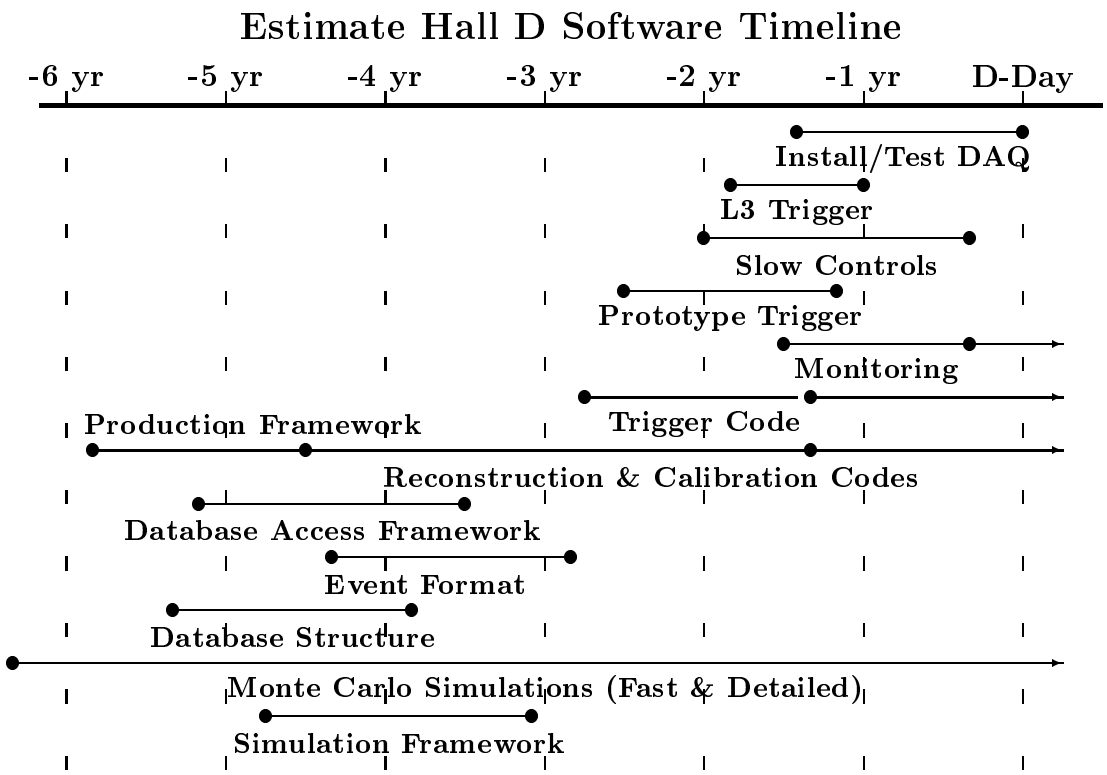

Figure 8.1: An overview of the software development times for the HALL D software project.

data storage speeds and capacities. Other approved or running experiments are planning to handle similar or larger data sets on the same time scale as HALL D.

The offline computing activities required to complete the HALL D project are significant. We have adopted an approach that employs several customized computing systems to meet each particular need. These data and computational services are then integrated at the user interface level by a HALL D portal. This has the significant benefits for the development, maintenance and use of the HALL D offline computing environment.

There is a critical need to begin the software effort early in the HALL D construction project both to insure that the level 3 trigger can be used reliably starting very early in the experiment and to provide a stable, efficient environment for offline computing activities.

Chapter 9

Monte Carlo Simulations

9.1 Introduction

Prelminary Monte Carlo work has been done to study the expected resolution of the charged particle detectors proposed for HALL D. Since significant experience in calorimetry exists from BNL E852 and JLab Radphi actual results from those experiments have been used for this report and Monte Carlo development in this area is not as complete. The emphesis in the work done to date is on creation of a useful and flexible system of programs that will allow design work to proceed quickly. Realistic models of detectors and materials are used so that expected resolutions can be estimated. An overview is presented below.

9.2 Monte Carlo framework

A Monte Carlo framework has been developed to understand the performance of key aspects of the HALL D detector systems. This framework is in general a collection of modules, each serving some particular function. These modules consist of individual programs and library routines which use common event I/O formats. Figure 9.1 illustrates this modular structure.

First, a Monte Carlo four-vector generator is used to create phase–space distributed events. Next is the detector simulation, *HDFast*, which is a fast and flexible simulation program based upon the MCFast framework developed by the simulation group at Fermilab. The Monte Carlo output includes (but is not limited to) the following data objects:

- generated event

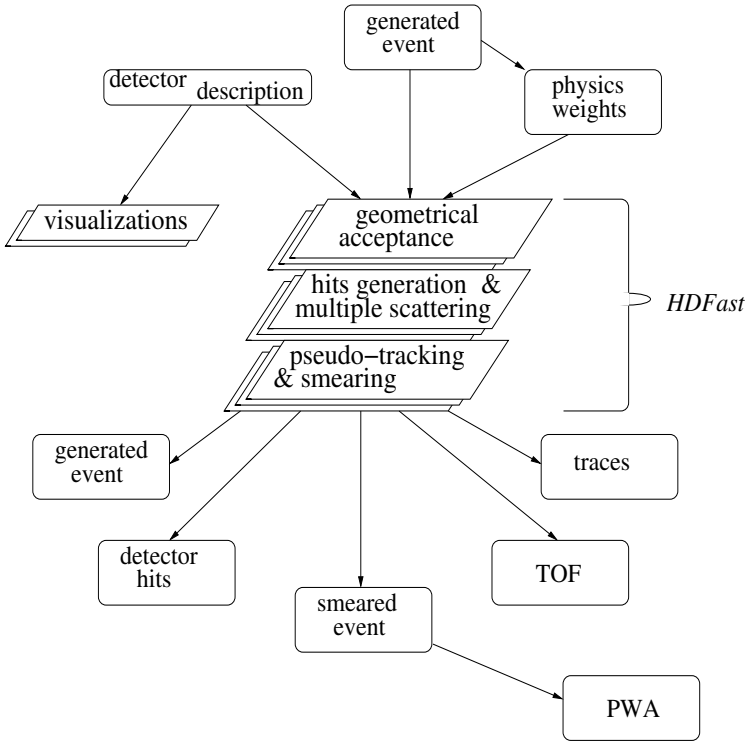

Figure 9.1: An illustration giving an overview of the HALL D Monte Carlo software which emphsizes its modular nature.

- detector hits
- resolution modified (smeared) event
- time-of-flight information
- dE/dx information
- threshold Čerenkov information
- particle trajectory information

Monte Carlo events can be generated using the program *genr8* [133] or *cwrap* [134]. Both programs generate peripheral phase space Monte Carlo events where events can be produced which describe a complex decay chain of intermediate states. Both meson and baryon decay chains are allowed, but with

a limiting assumption of a t–channel production process. The four–momentum transfer squared distribution follows that of

$$\frac{d\sigma}{dt} \propto e^{-b|t|}$$

where the user defines the t-channel slope or $d\sigma/dt$ can be specified by an input histogram.

HDFast is a fast and flexible simulation program based upon the MCFast framework developed by the simulation group at Fermilab[135]. MCFast consists of a set of modularized Monte Carlo library routines; it is designed to perform parameterized tracking by assembling a covariance matrix for each track that takes into account materials, efficiencies, and resolutions for all measurement planes, and use this matrix to smear the track parameters randomly. The covariance matrix is first diagonalized so as to properly account for effects due to correlations when parameters are smeared. In principle, the distribution of smeared tracks produced by this method would be similar to the distribution of real tracks that were measured by a real detector(with the same parameters) and analyzed with an idealized track fitting procedure[135].

HDFast is controlled via a set of user routines which act as an interface to the MCFast framework. They control the tracking and smearing of the four-vectors, in addition to the booking and filling of monitoring ntuples and histograms. The detector geometry is controlled by an ascii file which is read in during program execution. This allows the user to quickly create or modify the detector geometry without the need to recompile the executable. In addition, ROOT[136] was used to develop an event display which reads in the ascii geometry file and displays a two-dimensional visualization (see Figure 9.7) of the detector configuration and event track projections.

The motivation for using the MCFast framework is to facilitate the study of design changes and detector configurations. This does not exclude the use of a GEANT based simulation. MCFast provides routines for converting MCFast geometry to GEANT. Eventually, a GEANT4 based simulation will be incorporated into the HALL D Monte Carlo framework.

9.3 Acceptance studies

In order to better understand the effects of finite acceptance of a proposed detector configuration, a simple study of the acceptance as a function of total meson effective mass for various final states has been performed. In doing the Monte Carlo acceptance studies we considered the following reactions:

1. $\gamma p \to X^+ n$
   - $X^+ \to \pi^+\pi^+\pi^-$
2. $\gamma p \to X^+ n$
   - $X^+ \to \eta\pi^+\pi^+\pi^-$
     - $\eta \to \gamma\gamma$
3. $\gamma p \to X^+ n$
   - $X^+ \to \omega\pi^0\pi^+$
     - $\omega \to \pi^+\pi^-\pi^0$
     - $\pi^0 \to \gamma\gamma$
4. $\gamma p \to X^0 p$
   - $X^0 \to \eta\pi^0\pi^0$
     - $\eta \to \gamma\gamma$
     - $\pi^0 \to \gamma\gamma$

The acceptance studies were performed with total effective meson masses ($Mass(X)$) of 1.4, 1.7, and 2.0 GeV/c^2. At each $Mass(X)$, events were distributed according to a Breit-Wigner of width $\Gamma = 0.250\ GeV/c^2$. In generating the Monte Carlo events, the following assumptions were made:

- peripheral production where $\frac{d\sigma}{dt} \propto e^{-b|t|}$ and $b = 5.0\ (GeV/c)^{-2}$;
- events distributed according to phase-space; and
- isotropic decay angles.

For each reaction, 30000 events (10000 for each $Mass(X)$) were generated for different photon beam energies of: 5, 6, 8, 10, and 12 GeV.

9.3.1 Detector geometry

The generated events were processed through *HDFast* with the assumed detector configuration listed below and scematically shown in Figure 9.7. This configuration is comprised of the following assumptions:

- 2.24 Tesla solenoid magnet –LASS magnet,

- 5-layer Vertex Chamber (VTX),
- 22-layer Central Drift Chamber (CDC),
- 5 6-layer Forward Drift Chambers (FDC),
- Barrel Calorimeter which also acts as central TOF(BCAL),
- Cerenkov Detector,
- Forward time-of-flight (FTOF),
- Forward Lead Glass Detector (LGD) 172x172 cm with 8x8 cm beam hole,
- target-beam vertex distribution at $r = 0.0\,cm$, $z = 50\,cm$ with $\sigma_r = 0.3\,cm$, $\sigma_z = 15.0\,cm$ ($\hat{z}$ is along the magnet axis; the origin is located at the upstream face of the solenoid).

9.3.2 Acceptance performance

In the simulation, an event was accepted if the following minimum conditions were met:

- all charged tracks were found with a minimum of four hits per track, and
- all gammas were detected in either the BCAL and/or LGD.

The acceptance as a function of total effective meson mass is shown in Figure 9.2. It is important to note that at higher beam energies the forward boost results in more forward going high momentum tracks. And Even though the mass acceptance is seemingly good, the resolution of the forward going higher momentum tracks degrades. This issue has been studied in detail and is discussed greater in HALL D Note #7[137].

In Figure 9.3 through Figure 9.6, we show the acceptance for the Gottfried-Jackson decay angles (the particle decay angles often used in the partial wave analysis). It is clear that the Gottfried-Jackson angular acceptance is quite good. The acceptance for gammas is also rather high, but it suffers more from holes in the forward and backward regions. The hole in the backward region results from backward going gammas which is the dominant factor at lower beam energies. The forward hole, due to gammas hitting the beam hole in the LGD, becomes a factor (and effectively gets larger) for higher beam energies. Figure 9.7a displays a lost event for $\gamma p \to p\eta\pi^0\pi^0$ at $Mass(X) = 2.0\ GeV/c^2$ and beam of 5 GeV. For this channel 75% of the lost events were of this

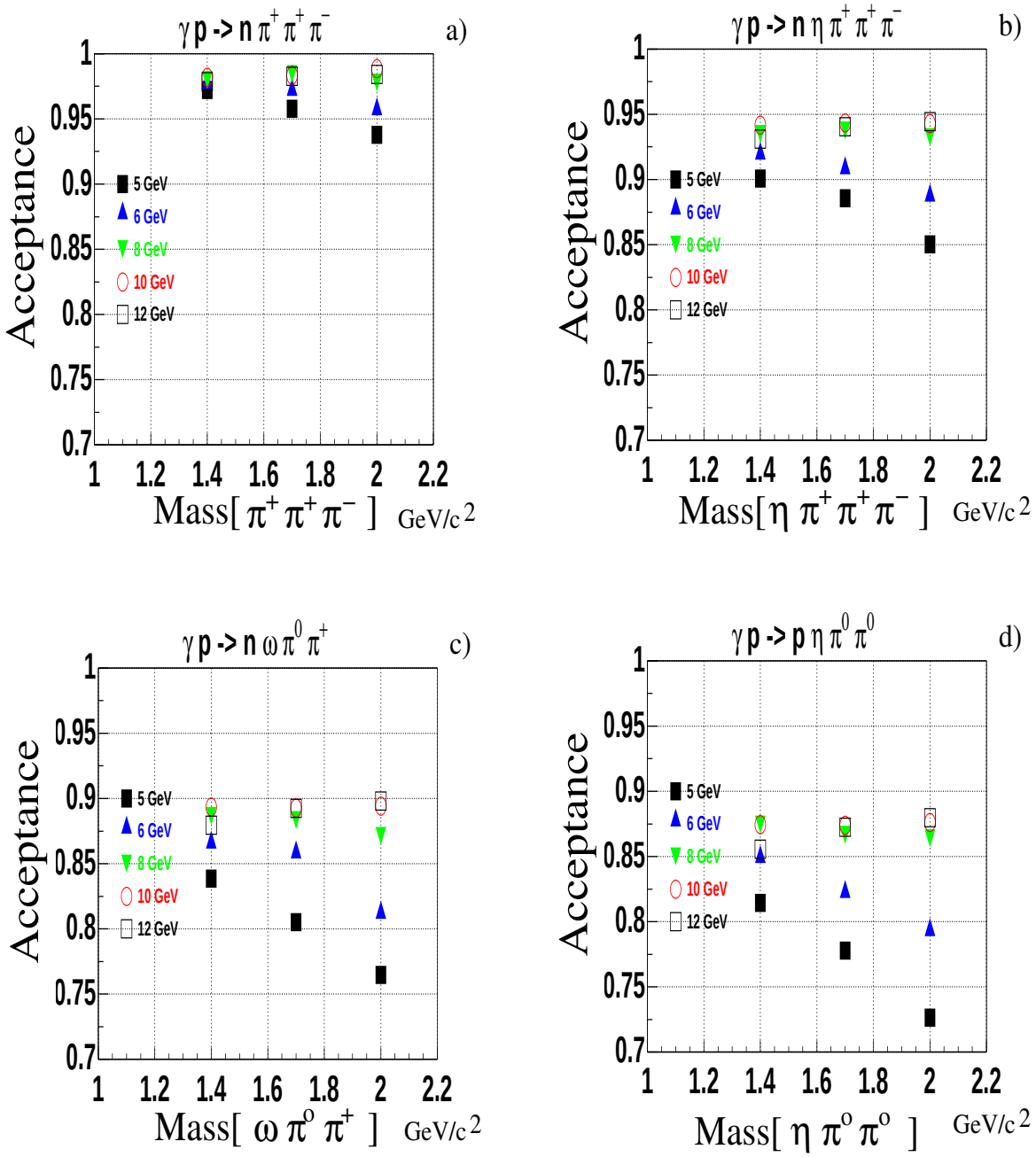

Figure 9.2: The acceptance as a function of total effective meson mass: a) $X^+ \to \pi^+\pi^+\pi^-$, b) $X^+ \to \eta\pi^+\pi^-\pi^+$, c) $X^+ \to \omega\pi^0\pi^+$, d) $X^0 \to \eta\pi^0\pi^0$. The acceptance studies were performed for effective meson masses of 1.4, 1.7, and 2.0 GeV/c^2, and at each mass point the photon beam energy was varied from 5 to 12 GeV.

type. One the other hand, for a 12 GeV beam and the same final state about 50% of the lost events are due to the beam hole(See Figure 9.7b). While the beam hole is a necessity, the hole in the backward region suggests the need at the lower beam energies for a backward gamma veto. More importantly, the acceptance for the Gottfried-Jackson decay angles is flat and not strongly dependent on $Mass(X)$ or the beam energy. Even though the method of partial wave analysis can account for effects of finite detector acceptance, a small misunderstanding of the detector acceptance can be greatly amplified by the need for large acceptance corrections and thus produce false or misleading results.

9.4 Monte Carlo Study of Photon Energy Resolution

In this study the GENR8 program was used to generate the events. Four different exclusive reactions were studied, two with photons produced at the baryon vertex:

$$\gamma p \rightarrow N^*(1500)\pi^+ \rightarrow (n\eta)\pi^+ \rightarrow n\pi^+\gamma\gamma \tag{9.1}$$

$$\gamma p \rightarrow X^+(1600)\Delta^0 \rightarrow (\pi^+\pi^+\pi^-)(n\pi^0) \rightarrow \pi^+\pi^+\pi^- n\gamma\gamma \tag{9.2}$$

The Δ^0 reaction (reaction 9.2) has a 3π-meson mass of $1.600 GeV/c^2$, and a width of 300 MeV/c^2. The two meson vertex reactions are:

$$\gamma p \rightarrow X^+(1600)n \rightarrow (\eta\pi^+)n \rightarrow n\pi^+\gamma\gamma \tag{9.3}$$

$$\gamma p \rightarrow X(1600)p \rightarrow (\pi^+\pi^-\pi^o)p \rightarrow p\pi^+\pi^-\gamma\gamma \tag{9.4}$$

In both reactions 9.3 and 9.4, the meson systems were generated with a Breit–Wigner distribution of mass $1.6 GeV/c^2$and a width of $0.3 GeV/c^2$.

Each of the above reactions were simulated using a beam energy of $8 GeV$, and a t-channel slope of $5 GeV/c^2$. The production and decay vertex was assumed to be at the center of the target. For each system, 10,000 events were generated. The direction and energy of the photons were recorded and analyzed.

9.4.1 Photon Detector Energy Resolution

The photons produced in the above decays were traced into the Barrel Calorimeter and the Lead Glass Detector. Figure 9.8 and 9.9 show the

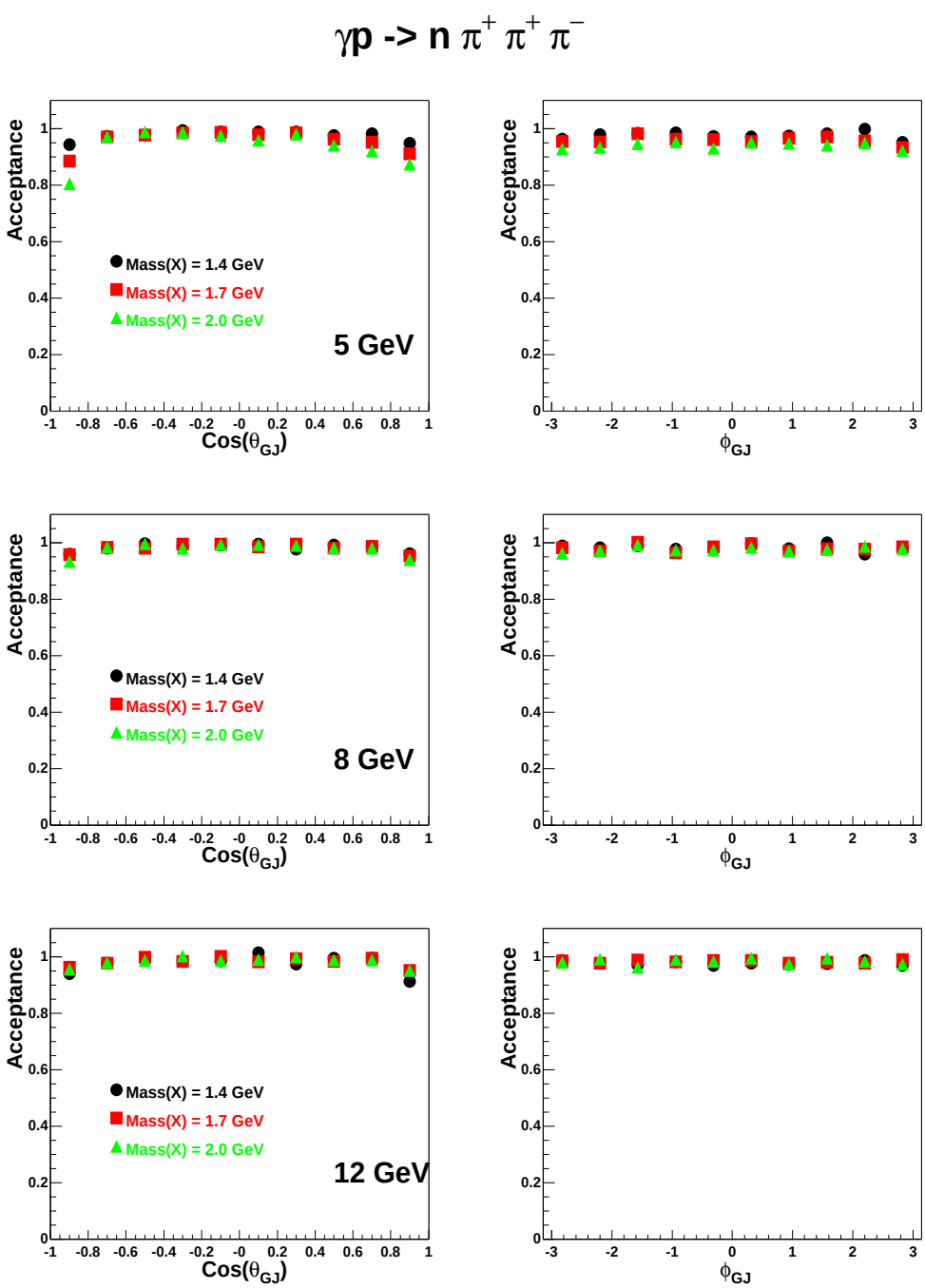

Figure 9.3: The acceptance in $cos(\theta_{GJ})$ and ϕ_{GJ} for $X^+ \rightarrow \pi^+\pi^+\pi^-$. The acceptance was studied for the different meson system effective mass of 1.4, 1.7, and 2.0 GeV/c^2, and for different photon beam energies of $5GeV$ (top), $8GeV$ (middle), and $12GeV$ (bottom).

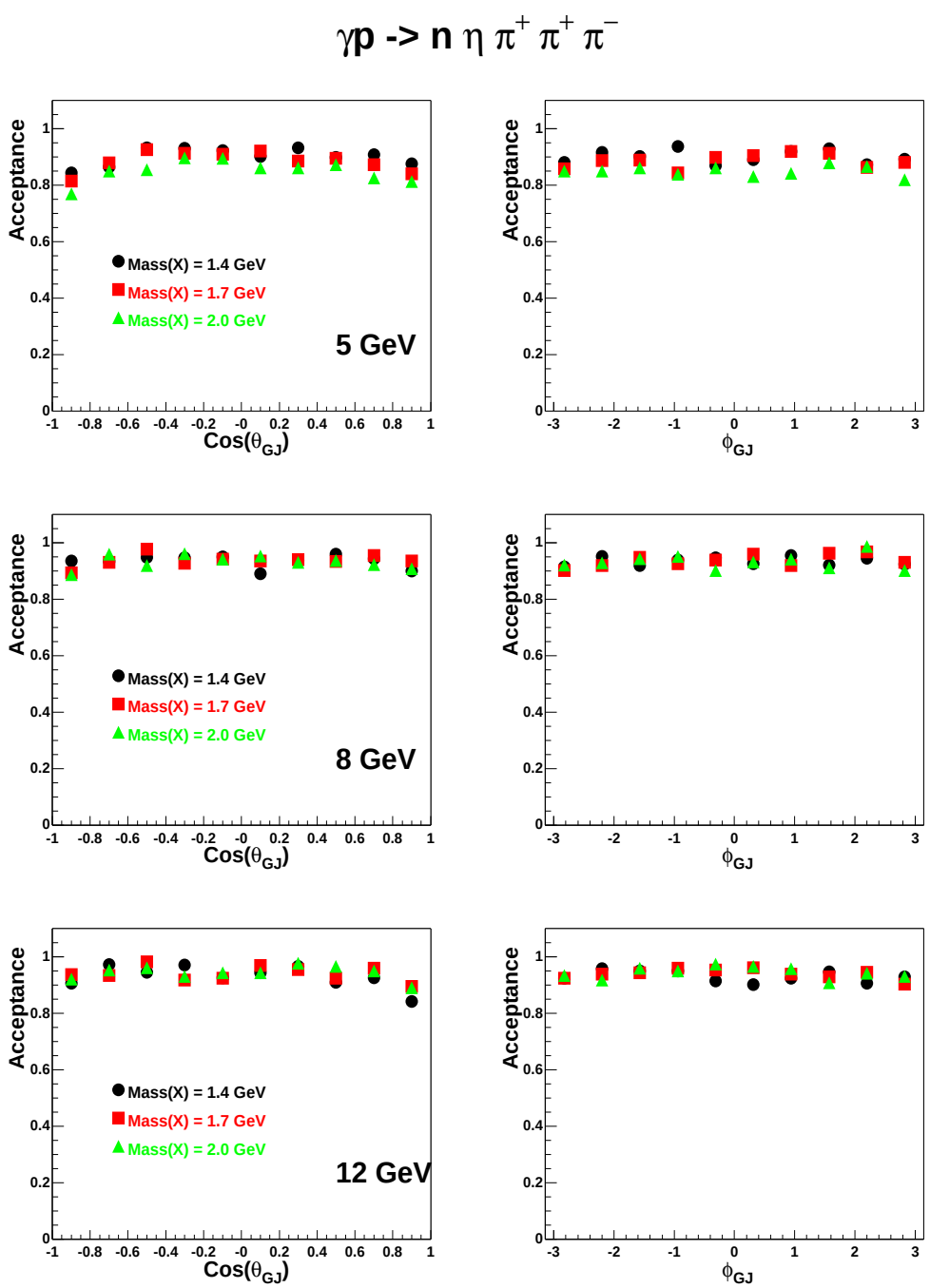

Figure 9.4: The acceptance in $cos(\theta_{GJ})$ and ϕ_{GJ} for $X^+ \rightarrow \eta\pi^+\pi^+\pi^-$. The acceptance was studied for the different meson system effective mass of 1.4, 1.7, and 2.0 GeV/c^2, and for different photon beam energies of $5GeV$ (top),$8GeV$ (middle), and $12GeV$ (bottom).

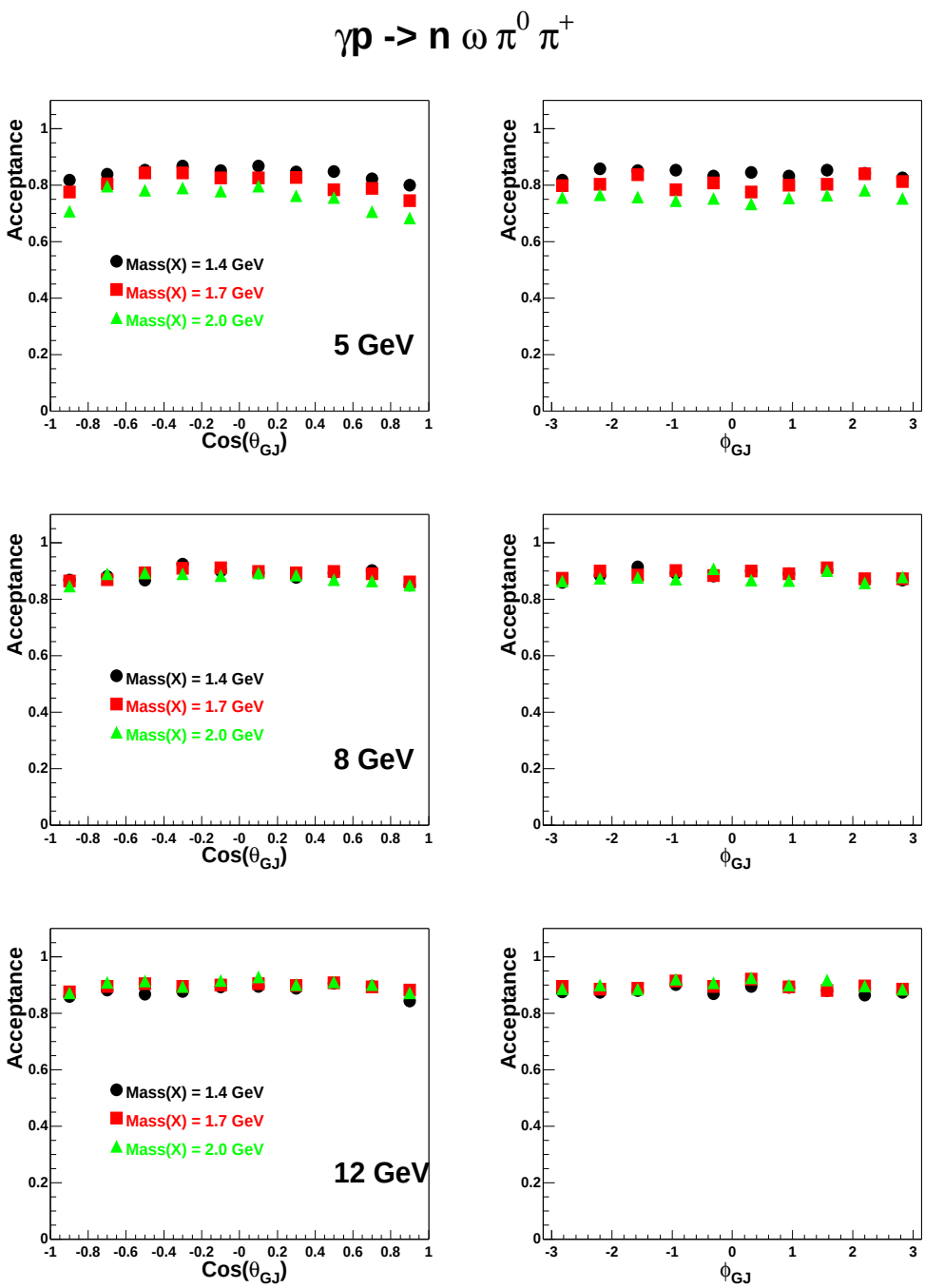

Figure 9.5: The acceptance in $cos(\theta_{GJ})$ and ϕ_{GJ} for $X^0 \rightarrow \omega\pi^0\pi^+$. The acceptance was studied for the different meson system effective mass of 1.4, 1.7, and 2.0 GeV/c^2, and for different photon beam energies of $5GeV$ (top), $8GeV$ (middle), and $12GeV$ (bottom).

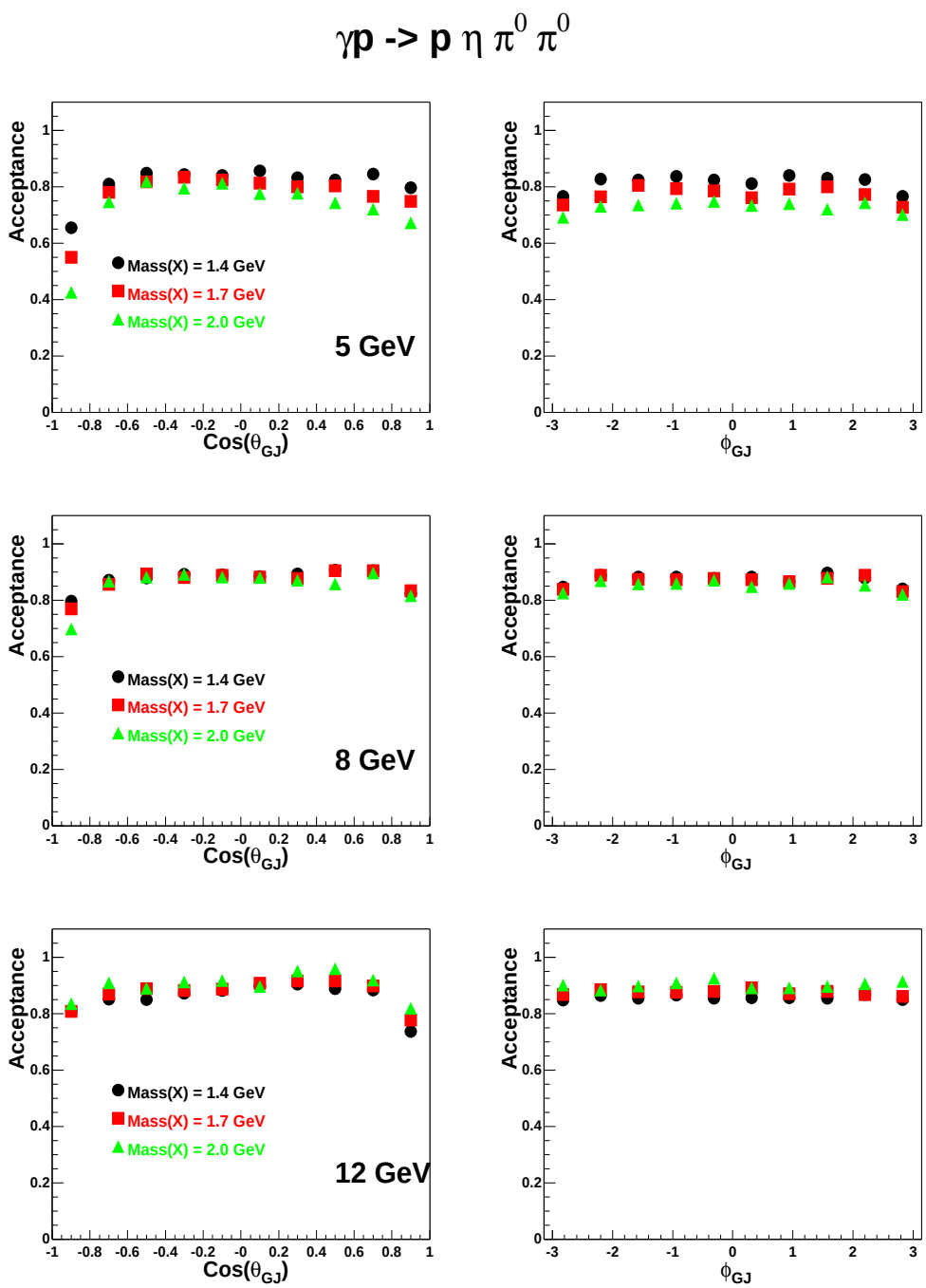

Figure 9.6: The acceptance in $cos(\theta_{GJ})$ and ϕ_{GJ} for $X^0 \rightarrow \eta\pi^0\pi^0$. The acceptance was studied for the different meson system effective mass of 1.4, 1.7, and 2.0 GeV/c^2, and for different photon beam energies of $5GeV$ (top), $8GeV$ (middle), and $12GeV$ (bottom).

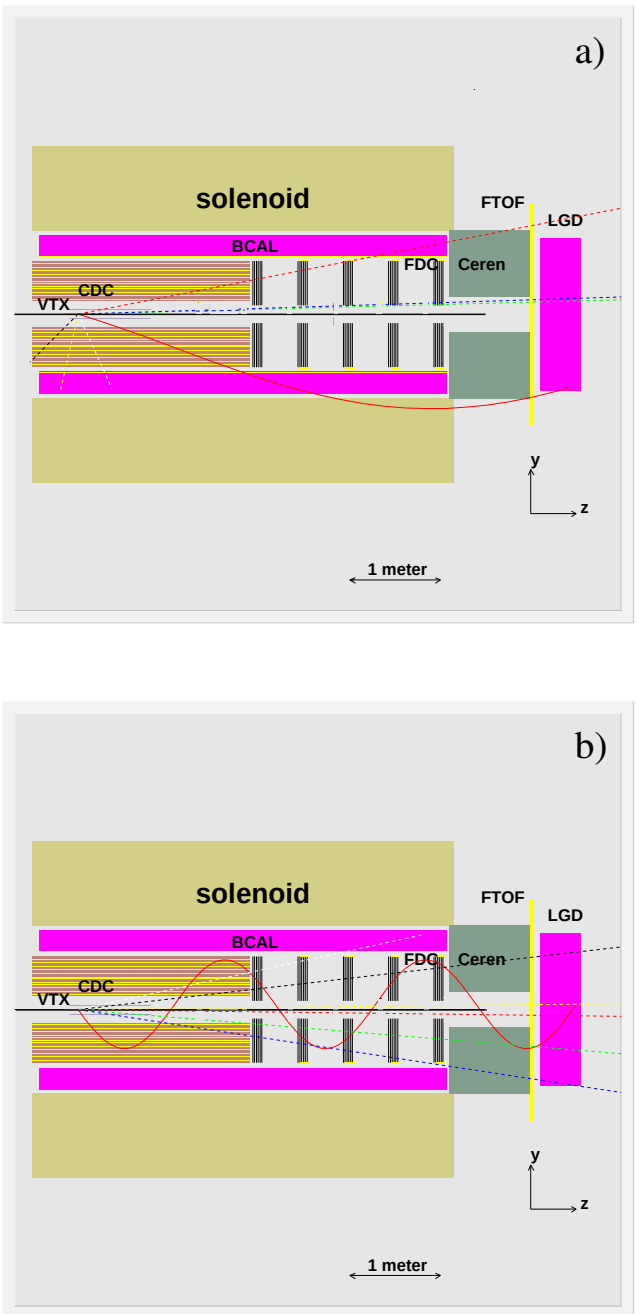

Figure 9.7: Event displays of lost events for $\gamma p \to p\eta\pi^0\pi^0$ for $Mass(X) = 2.0$ GeV/c^2: (a) backward missed gamma at for a beam energy of 5 GeV, and (b) forward missed beam hole gamma at a beam energy of 12 GeV. The events shown contain both charged particles (solid lines) and photons (dashed lines).

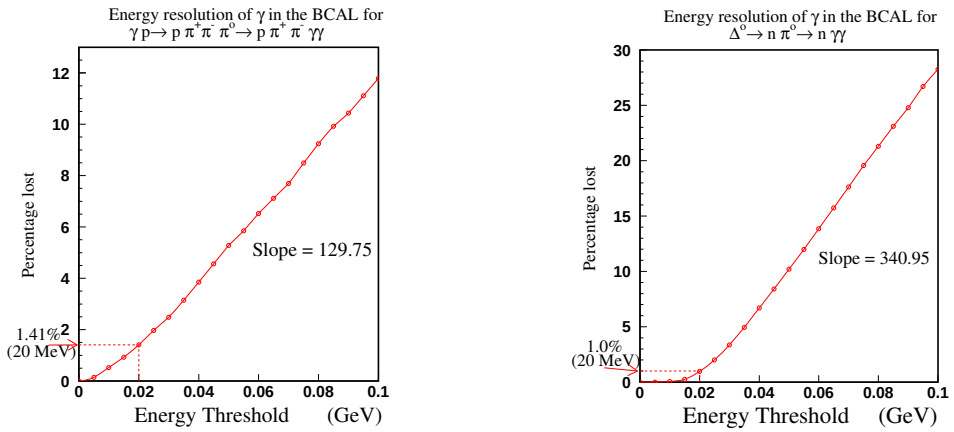

Figure 9.8: The percentage loss due to the energy threshold of the BCAL. Left is for reaction 9.4, while the right figure is for the Δ^0 decay from reaction 9.2. The percent of the total photons entering the Barrel Calorimeter for reaction 9.4 is 57% and reaction 9.2 is 87%.

percentage of photons that would enter, but not be detected by the Barrel Calorimeter due to the minimum energy thresholds.

Currently, the design calls for the energy sensitivity of 20 MeV for the Barrel Calorimeter. One can see that this results in around a 1% loss of photons which is quite acceptable. However, if this energy can not be met, the percentage of photons lost rises rapidly with the increased energy threshold, especially for the Δ^0 (reaction 9.2) decay. For example, if the threshold is 50 MeV, then 5% of the 3π reaction is lost, and 10% of the Δ^0 reaction is lost. The situation for the η reactions is not so severe, as would be expected from the higher energy photons in the η decay (figure 9.9).

The results for the Lead Glass Detector are similar, but the percentage rise is not so significant at higher energy thresholds. The only system with significant loss in the lead glass array is the 3π (reaction 9.4) decay. At the sensitivity threshold of 100 MeV, the lead glass detector will not see 0.718% of the photons. The design calls for a $150MeV$ detection minimum in the LGD. At this energy, the detector will miss 1.86% of the photons (figure 9.10).

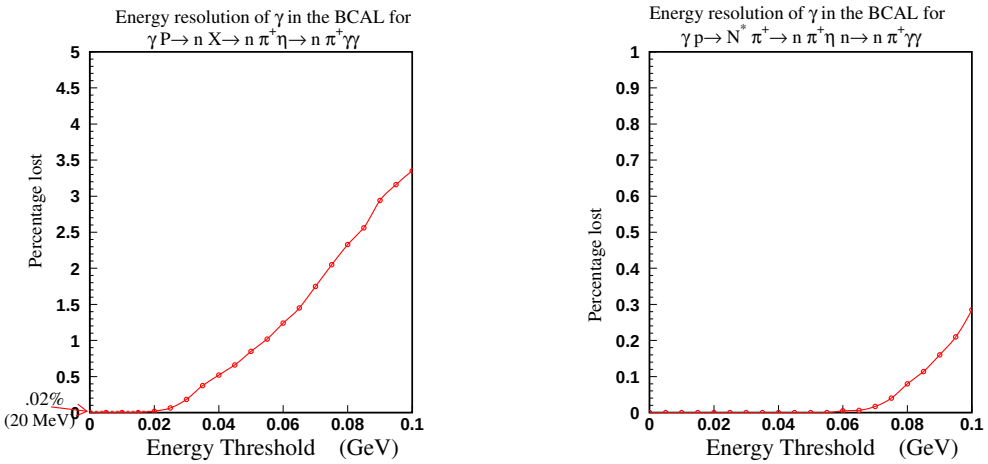

Figure 9.9: The percentage loss due to the energy threshold of the BCAL. The left plot is for reaction 9.3, and right is for reaction 9.1. The percent of all the photons entering the Barrel Calorimeter for the η X (reaction 9.3) and the η N^* (reaction 9.1) are 55% and 88% respectively.

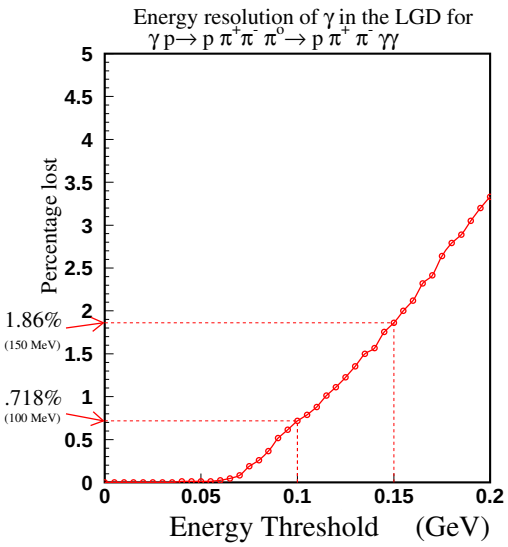

Figure 9.10: The percentage of undetected photons for a given energy threshold of the lead glass detector. From reaction 9.4.

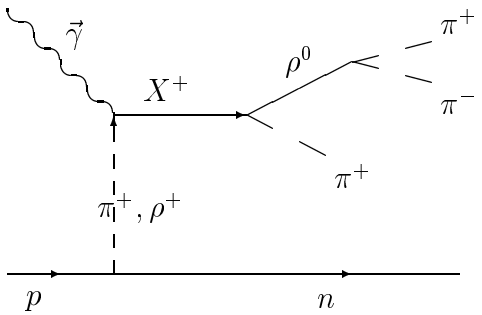

Figure 9.11: A schematic diagram of the photoproduction amplitude via one–π or ρ exchange. The state X^+ then decays via $\rho^0\pi^+$, and the ρ subsequently decays into $\pi^+\pi^-$.

9.5 Physics Event Weighters

In addition to the phase space event generators mentioned earlier in this chapter, it is also important to be able to simulate the expected photoproduction physics that will be studied. To this end, an event generator for the 3π final state has been written using the one–pion charge–exchange mechanism as discussed in reference [33] for reaction 9.5.

$$\vec{\gamma}p \to X^+n \quad \left(X^+ \to \left[\rho^0 \to \pi^+\pi^-\right]\pi^+\right) \tag{9.5}$$

A schematic of this process is shown in Figure 9.11. One–π charge exchange requires both a spin–flip at the nucleon vertex, and that the X^+ particle carry the helicity of the incoming γ, ($M_X = 1$). Any number of resonances X^+ with different masses, widths and production strengths can be included in the generator. In addition, the photon beam can have any polarization desired. An extension to this program allows for ρ–exchange under the same conditions as the π exchange. These two amplitudes represent *unnatural* and *natural* parity exchanges resepctively. Events produced using one of the phase space generators can then be weighted according to the physics weighter, and then passed through the HALL D Monte Carlo program. These can then be used as input to the partial wave analysis as described in the next chapter.

A sample of the output of this generator is shown in Figure 9.12. These events have been generated with four resonances: $a_1(1260)$, $a_2(1320)$, $\pi_2(1670)$ and an exotic $\pi_1(1600)$. The masses and widths are all consistent with current accepted values. In addition, one can see the ρ^{circ} in the $\pi^+\pi^-$ invariant mass spectra. A full list of known resonances [138] that could be put in this generator is given in table 9.1.

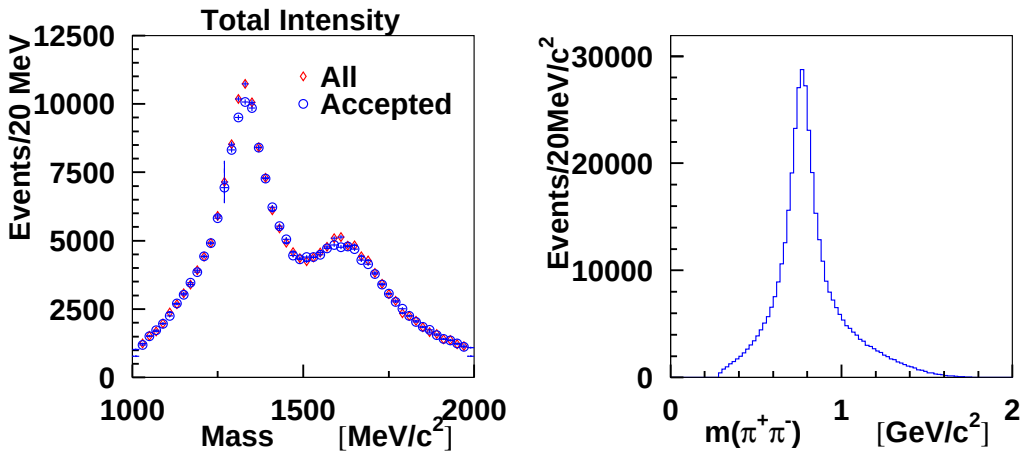

Figure 9.12: (Left) The genrated 3π mass spectrum using four intermediate resonances, X^+. The diamonds correspond to all generated events, while the circles correspond to events which have been run through the HALL D Monte Carlo program. (Right) The $\pi^+\pi^-$ invariant mass from the 3π events. The peak corresponds to the $\rho^0(770)$.

Resonance	Mass	Width	$L_{\rho\pi}$
$a_1^+(1260)$	$1.230 GeV/c^2$	.250 to $.600 GeV/c^2$	$L = 0, 2$
$a_2^+(1320)$	$1.318 GeV/c^2$	$.105 GeV/c^2$	$L = 2$
$\pi_1^+(1600)$	$1.593 GeV/c^2$	$.168 GeV/c^2$	$L = 1$
$a_1^+(1640)$	$1.640 GeV/c^2$	$.300 GeV/c^2$	$L = 0, 2$
$a_2^+(1660)$	$1.660 GeV/c^2$	$.280 GeV/c^2$	$L = 2$
$\pi_2^+(1670)$	$1.670 GeV/c^2$	$.259 GeV/c^2$	$L = 1, 3$
$a_2^+(1750)$	$1.752 GeV/c^2$	$.150 GeV/c^2$	$L = 2$
$a_4^+(2040)$	$2.014 GeV/c^2$	$.361 GeV/c^2$	$L = 4$
$\pi_2^+(2100)$	$2.090 GeV/c^2$	$.625 GeV/c^2$	$L = 1, 3$
$a_6^+(2450)$	$2.450 GeV/c^2$	$.400 GeV/c^2$	$L = 6$

Table 9.1: A list of known charged 3π resonances that could be produced in photoproduction and decay via $\rho\pi$. The column $L_{\rho\pi}$ are the allowed orbital angular monetum between the ρ and the π when the resonance decays. Because we require non–zero isospin, many states can not be produced.

Chapter 10

Partial Wave Analysis

10.1 Introduction

To identify the J^{PC} quantum numbers of a meson it is necessary to perform a *partial wave analysis* (PWA). In the simplest terms, a partial wave analysis determines production amplitudes by fitting decay angular distributions. The fit includes information on the polarization of the beam and target, the spin and parity of the resonance, the spin and parity of any daughter resonances and any relative orbital angular momenta. The analysis seeks to establish the production strengths, production mechanisms and the relative phase motion of various production amplitudes. Phase motion is critical in determining if resonance production is present.

While the implementation of a partial wave analysis is in principle straightforward, there are both empirical and intrinsic difficulties. Empirically, instrumentation effects, such as detector acceptance and resolution, can conspire to make one distribution look like another. These similar distributions lead to *leakage* in the partial wave analysis. Here, cropping, smearing, or incorrect acceptance corrections of two physically different distributions may lead to distributions which are apparently indistinguishable. These difficulties can be minimized by properly designing the experiment. Full angular coverage in the distributions can be achieved by using a nearly 4π detector with excellent resolution. In addition, high statistics are critical to be able to separate these partial waves with accuracy. Thus, thorough partial wave analysis requires nearly 4π coverage, excellent resolution, high statistics and a very good understanding of the detector.

The PWA method is subject to intrinsic mathematical ambiguities for certain final states. Two or more different choices of amplitudes lead to identical

observables, *e.g.* moments. Here there are at least two approaches. The first assumes some *a priori* physics knowledge that allows one to choose one solution over another, *e.g.* at threshold low angular momentum waves should dominate high angular momentum waves. The second is to examine simultaneously several final states to which the resonance can decay. While the distributions may be confused in one final state, such as $\eta\pi$, they are likely to be different in a second such as $\rho\pi$. This latter approach assumes that the detector has been optimized for many different final states and that relative normalizations between these are understood.

This latter approach of looking at multiple final states not only allows one to separate different waves, but in itself yields key information about the relative decay rates of mesons. It is this latter information that is critical to understanding the underlying wave functions of the mesons — their content and mixing with other states. This ability to measure accurately many final states and to perform a simultaneous partial wave analysis is a key feature of the HALL D spectrometer.

The use of photon polarization will also allow one to simplify the analysis and to access additional information on the production of mesons. This will provide key checks on the stability of the analysis itself. While a circularly polarized beam may yield some information in a few special cases, the true gain comes from linear polarization. Linear polarization defines a *new spatial direction* beyond the photon direction, which is not the case for circular polarization. Linearly polarized light can be expressed as a coherent sum of helicity (circular polarization) states which leads to interference terms not present for unpolarized light. This yields additional angular dependence which simplifies the PWA analysis. Furthermore, linear polarization is necessary to discriminate between different production mechanisms.

Backgrounds are always a problem in a partial wave analysis. These limit one's ability to measure phase motion, and can be particularly severe in a region of dense overlapping resonances. Backgrounds involve a different final state accidently reconstructing as the channel under study. Either a particle is missed by the detector or, when putting the final state back together, multiple interpretations are possible. This can be minimized with a good 4π detector with high efficiency for detecting all final state particles with good resolution. One needs all particles to be reconstructed well enough to allow for a complete kinematical identification of a specific final state.

Finally, while the PWA is in principle straight forward, the machinery itself can become rather cumbersome. There are several different equivalent bases in which the analysis can be done. In addition, small coding errors can lead to errors which may not be easily detected in the results. As such, the HALL D

collaboration is developing independent PWA packages. Currently two such packages have been implemented. These use two different formalisms (one uses the so called reflectivity basis and the other helicity basis), which can be used to cross check results of fits.

10.2 Beam and final state normalizations

It will be necessary to show, in the first results from HALL D, that our experiment produces results that are consistent with previous investigations, albeit with much greater statistical precision. These will include total cross sections (at various photon energies) for various inclusive multi–particle photoproduction reactions [139], invariant mass distributions and differential cross sections for exclusive reactions [140, 27] and density matrix element determinations in processes for which polarized beams have been available [141].

Each of the measurements cited above has been carried out with relatively low flux photon beams (for which the beam normalization is rather straightforward) and using bubble chambers for particle detection (which therefore provide excellent, flat acceptance functions). Moving to high intensity beams and sophisticated electronic detectors, while leading to enormous gains in statistical precision, makes it more difficult to determine normalizations. Since one of our main goals is to determine such things as relative branching ratios and production cross sections of new states, it is important to establish consistent connections with these previous measurements. Furthermore, it is likely that our experiment will run with different triggers for different running periods, and these data sets need to be merged as seamlessly as possible. All of these goals will need accurate controls of beam normalization and detector acceptance, as well as a clear determination of their inherent systematic uncertainty.

Beyond demonstrating that earlier measurements can be reproduced, an accurate normalization plays a critical role in the physics of HALL D. To measure relative decay rates of mesons it is critical to have accurate normalizations between different final states. This requires the ability to count incident photons and also the ability to understand systematics due to the trigger hardware and software on the event rates.

10.3 A partial wave analysis study

To study the design of the HALL D detector, and to help in understanding the limits of the Partial Wave Analysis, a study was undertaken to perform

a PWA on simulated data. The goals of the study are twofold: to both qualitatively and quantitatively understand the role of the photon polarization in the partial wave analysis and, to determine what limits are placed on the PWA due to the finite acceptance and resolution of the detector. The aim is to ultimately perform such a study over many different final states but, to develop the tools to perform this, the initial studies have concentrated on the reaction 10.1 for $E_\gamma = 8.5\ GeV$.

$$\gamma p \to \pi^+\pi^+\pi^- n \tag{10.1}$$

This is a good candidate reaction for exotic π_1 searches. If a $\pi^+\pi^-$ pair comes from the decay of a ρ^0 meson then the 3π final state has $G - Parity = (-1)$ and is an isovector. Thus, a resonant $\rho^0\pi^+$ P-wave would correspond to a charged member of the $J^{PC} = 1^{-+}$ exotic multiplet.

10.3.1 The Role of Linear Polarization

Monte Carlo studies have been made with unpolarized, 100% linearly polarized and fractionally polarized photons. The data can best be examined by looking at the 3π system in the Gottfried–Jackson (GJ) frame, (see Figure 10.1). The GJ frame is the rest frame of the 3π system with the z axis chosen to be along the photon beam direction. The y axis is defined as the normal to *neutron*–3π production plane (which is invariant under boost to the rest frame of the 3π system). The photon polarization is fixed in the lab frame. However, in the GJ frame it is at some angle α with respect to the y axis (where α varies on the event–by–event basis). The 3π system decays into a 2π system, and a spectator π. In the GJ frame, the orientation of this decay is given by $\theta_{\rm GJ}$ and $\phi_{\rm GJ}$ as shown in Figure 10.1. In the case of linearly polarized photons, one expects there to be a dependence on both the angle α and the azimuthal angle ϕ. This would not be true for unpolarized photons.

The 3π data have been generated using a phase–space Monte Carlo, and the events have been weighted using a one–pion exchange (OPE) production mechanism that includes 3π resonances decaying via $\rho\pi$ [33]. All known $\rho\pi$ resonances in the with mass less than $2GeV/c^2$ that can be produced in OPE have been included. (These are listed in Table 10.1). At low momentum transfer, OPE is expected to be the dominant production mechanism [140, 27].

The effect of polarization can be directly seen in Figure 10.2. In the absence of polarization, there is nothing to define a ϕ direction in the GJ frame. As such, a plot of ϕ versus α is flat, (in the unpolarized case, α is taken as the

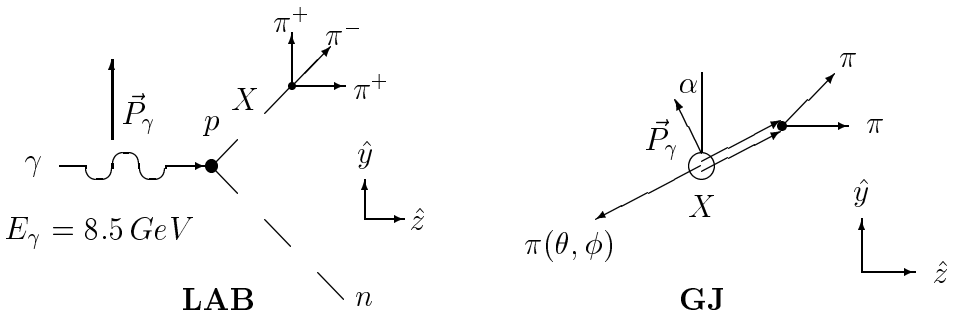

Figure 10.1: The reaction $\gamma p \to \pi^+\pi^+\pi^- n$ as seen in the lab frame and in the Gottfried–Jackson, (GJ), frames. The y direction in the GJ frame is defined as the normal to the reaction plane. The angle α locates the photon polarization direction with respect to the y axis in the GJ frame.

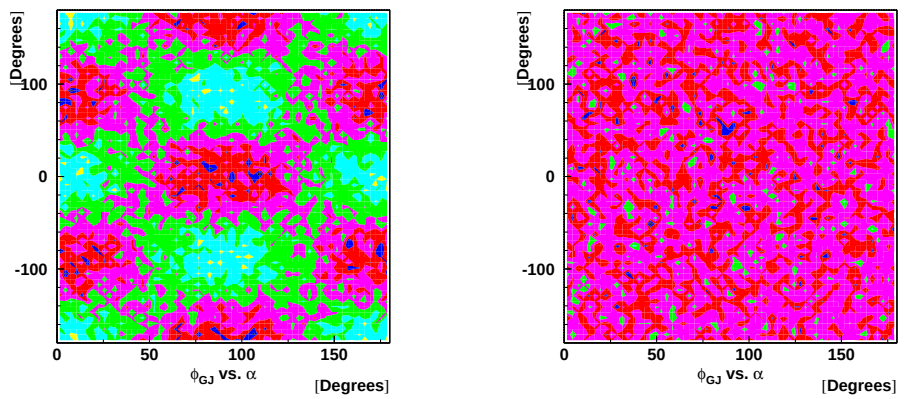

Figure 10.2: Plots of ϕ_{GJ} versus α in the Gottfried–Jackson frame for a band of 3π masses near the peak of the $a_2(1320)$. The left hand figure is for 100% polarized photons, while the right hand figure is for unpolarized photons.

angle between the y axis in the GJ frame and the y axis in the Lab frame). However, if photon polarization in non-zero, there is clear structure in the ϕ versus α plots. Near $\alpha = 0°$, the ϕ distribution is $\sin^2\phi$, whereas near $\alpha = 90°$, the distribution is $\cos^2\phi$, consistent with the expected $(1 - \cos[2(\alpha - \phi)])$ dependence.

Because the only production mechanism used is OPE, all particles are produced, it is also possible to get additional information about the naturality of the produced resonances. Pion exchange corresponds to unnatural parity exchange, so depending on the naturality of the produced 3π system, the

	Resonance					J^{PC}	L	Wave
		Mass $[GeV]$	Width ($\Gamma[GeV]$)	$\Gamma_{3\pi}/\Gamma$	σ_γ $[nb]$			
1	a_1	1260	400	99%	30	1^{++}	0	S
2				1%			2	D
3	a_2	1320	110	70%	500	2^{++}	2	D
4	π_2	1670	110	30%	20	2^{-+}	1	P
5				1%			3	F
6	π_1	1600	170	50%	20	1^{-+}	1	P

Table 10.1: The resonance contributions to the weighting function. The column labeled L corresponds to the relative angular momentum between the ρ and the π in the decay of the 3π resonance.

$\sin^2\phi$ and $\cos^2\phi$ will flip (the dependence on ϕ changes to that of $90^o - \phi$). For natural parity, (0^+, 1^-, 2^+, $\cdots$), it will be like the a_2, while for unnatural, (0^-, 1^+, 2^-, $\cdots$), it will be opposite to that. This behavior can be seen in Figure 10.3 which shows ϕ versus the 3π mass for α near 90°, (left) and α near 0° (right). These figures show a clear band at the a_2 mass, which is $\cos^2\phi$ in the left, and $\sin^2\phi$ on the right. There is also a second band visible near a mass of 1.7 GeV/c^2, which if one looks carefully, has the opposite angular distributions as the a_2. Since in this test, the exchange mechanism is known, the opposite structure means that the naturality of the particle at 1.7 GeV/c^2 is opposite that of the a_2. In the real experiment the exchange mechanism will not be known. However, the PWA can determine the naturality of the produced particle, and this can then be used to determine the naturality of the exchange.

There is still additional information in these plots. For masses below that of the a_2, there is a diffuse band that has the opposite angular distribution as the a_2. This corresponds to the $a_1(1260)$ in the data. Finally, for masses just below the π_2, there is an even more diffuse structure whose angular distribution is opposite that of the π_2. This most likely corresponds to the π_1. The fact that the photon beam is linearly polarized allows us to read significant information about the resonances and their production directly from such a plot.

10.3.2 The PWA Formalism and Results

There are several equivalent formalisms in which the PWA can be performed. All of these initially look at the decay of the meson state in the GJ frame, and require that the polarization be expressed in that frame. The spin density matrix of a linearly polarized photon in the helicity basis can be

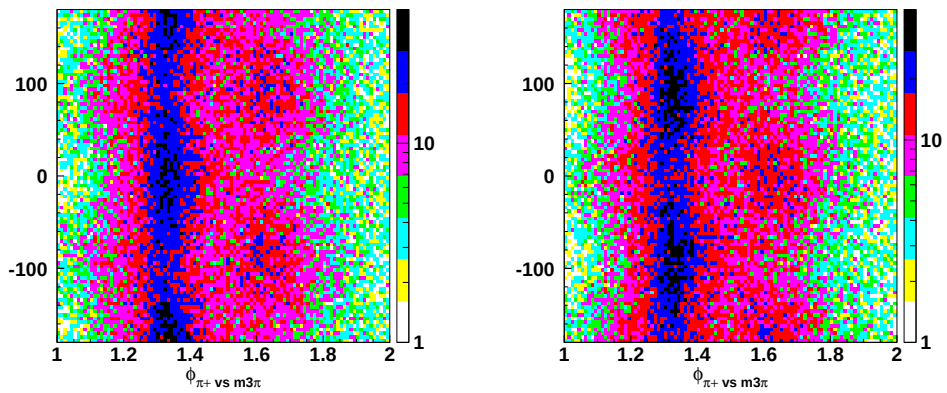

Figure 10.3: Plots of ϕ_{GJ} versus 3π–mass for 100% polarized photons. The figure on the left is for α near 90°, while that on the right is for α near 0°.

written in terms of the angle α in the GJ frame as in equation 10.2.

$$\rho_{\lambda_\gamma \lambda'_\gamma} = \begin{pmatrix} \frac{1}{2}(1 + Psin2\alpha) & \frac{P}{2}\cos 2\alpha \\ \frac{P}{2}\cos 2\alpha & \frac{1}{2}(1 - Psin2\alpha) \end{pmatrix} \tag{10.2}$$

$$\rho_{\epsilon_\gamma \epsilon'_\gamma} = \begin{pmatrix} (\frac{1}{2} - \rho_{1-1}) & (\frac{1}{2} - \rho_{-1-1}) \\ (\frac{1}{2} - \rho_{-1-1}) & (\frac{1}{2} + \rho_{1-1}) \end{pmatrix} \tag{10.3}$$

One particular choice for the analysis is the reflectivity basis. The eigenstates of reflectivity are eigen–states of reflection in the production plane. The density matrix of a linearly polarized photon in the reflectivity basis expressed in terms of the helicity basis elements is given in equation 10.3. In the reflectivity basis, photons polarized along either the x axis or the y axis in the GJ frame are eigenstates of reflectivity. However, photons that are polarized in some other direction are coherent mixtures of the two eigenstates. The eigenvalues of reflectivity depend on the naturality of particles involved in the reaction. For a given produced resonance, linear polarization enables one to distinguish between naturalities of the exchanged particles. This is the main handle on the production mechanism. Second, if the production mechanism is known (*e.g.* from momentum transfer or energy dependence), linear polarization enables one to filter resonances of different naturalities, as shown in the study of ϕ dependence discussed above. In the case of a known production mechanism, the same quality PWA can be done with about 50% as much

polarized data as with unpolarized data.

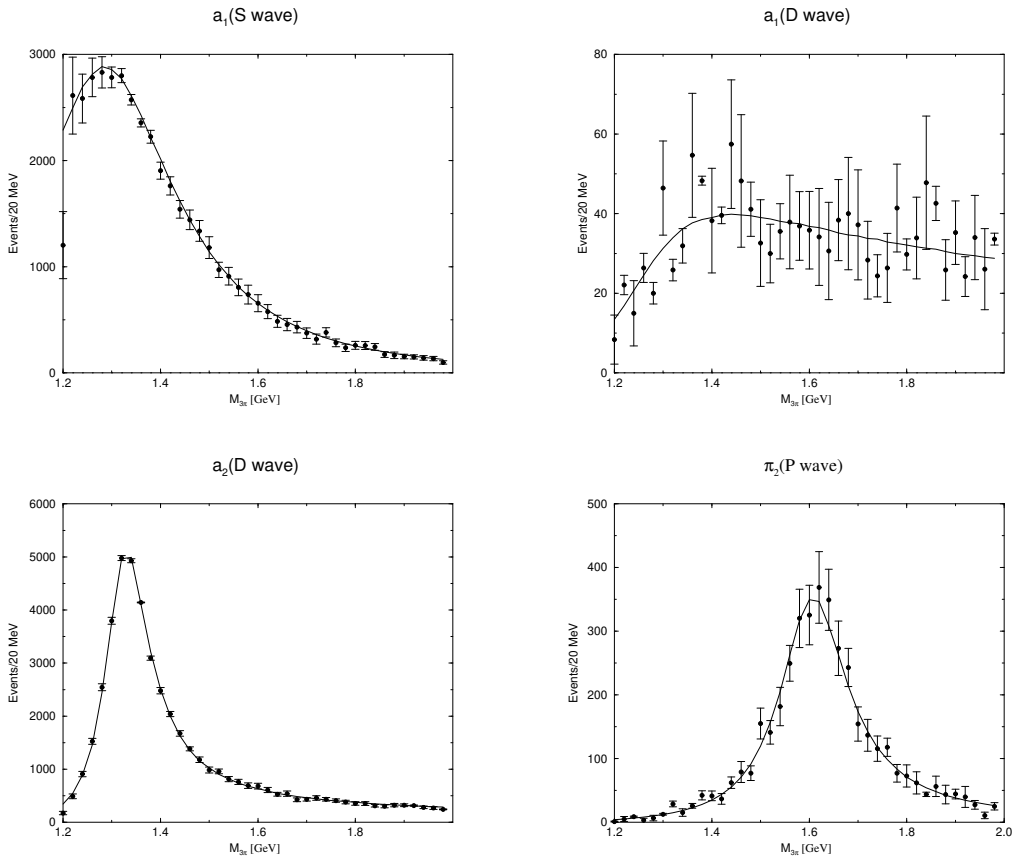

Figure 10.4: Fits to a 4π acceptance data set showing the four of the six partial waves from table 10.1. The error bars arise purely from the statistics of the data set which is about 1% of one year's running.

To date, independent fits have been carried out using two different codes. Ones using the reflectivity representation, and the other using a moments fit. Both return the same results, and have provided a very good cross check of our understanding of the procedure. In fact, the development of two parallel versions of the PWA code, and cross checking results against each other will be an important handle on systematic errors in the HALL D experiment. The results in Figure 10.4 are from the latter fit using the same formalism as in the weighting function. (These fits do not use input modified by the acceptance or resolution). What is of particular interest is the sensitivity limit in these data. The two extremely weak waves (at well less than 1% of the total intensity)

are just at the limit of being resolved in this data set. This is seen in the a_1D wave in Figure 10.4. The data set used in these fits represents about 1% of the reconstructed statistics from one year of running at $10^7\,\gamma/s$. The statistics of the experiment will clearly be large enough to resolve such small signals. They will also be large enough to provide statistically meaningful sample on much rarer final states. (The 3π mode chosen for this study is one of the largest contributors to the total γp total cross section.)

The second fitting procedure is done in the reflectivity basis. In the reflectivity basis, the total amplitude for some final state can be written as in equation 10.4. The subscript β refers to a given partial wave, $(J^{PC}M^{\epsilon})$. The indices ϵ_x and ϵ_γ refer to the reflectivities of the state X and the γ respectively. The indices λ and λ' refer to the initial and final state nucleon spin–states. Parity reduces the total number of helicity amplitudes by a factor of two and connects the reflectivity of the beam and exchange particles to the reflectivity of the produced state $(\epsilon_\gamma * \epsilon_e = \epsilon_X)$.

Additionally, in the case of OPE only the nucleon helicity–flip amplitude contributes and the λ and λ' indices are suppressed as in 10.4.

$$R_\beta^{\epsilon_x,\epsilon_\gamma} = V_{\beta,\lambda,\lambda'}^{\epsilon_x,\epsilon_\gamma} \times A_\beta^{\epsilon_x,\epsilon_\gamma} \tag{10.4}$$

The set of complex parameters, V's, are known as the production strengths. These are usually determined by fitting to the data. The A's are decay angular distributions which are functions of the angles in the various frames as well as resonance parameters of any daughter resonances into which the state X decays. The amplitude, A, for the decay of a particle with spin J and $|J_z| = M$ into two particles with helicities λ_1 and λ_2 $(\lambda = \lambda_1 - \lambda_2)$ in the resonance rest frame is given by [142]:

$$A = < \vec{p}\lambda_1; -\vec{p}\lambda_2 \mid \mathcal{M} \mid JM > = F^J_{\lambda_1\lambda_2} \mathcal{D}^{*J}_{M\,\lambda}(\phi,\theta,0) \tag{10.5}$$

Calculation of the decay amplitudes for a resonance is done recursively within the isobar model, regarding the n–body final state as a result of a series of sequential, generally 2–body, decays through intermediate isobar states. The total decay amplitude is the amplitude for the resonance to decay into its intermediate daughters times the amplitude for each of its daughters to decay.

This total amplitude, R can then be used to predict the intensity distributions of the final state particles. For a particular point in phase space, τ, the intensity is given as in equation 10.6. Finally, for amplitudes that do not interfere, (denoted by α) *e.g.* from production via different initial and final

spin configurations, a sum over these

$$I(\tau) = \sum_{\alpha} \text{Trace}\left[\sum_{\epsilon_\gamma,\epsilon'_\gamma}\left[\left(\sum_{\beta'} R_{\beta'}^{\epsilon_{x'},\epsilon_{\gamma'}}\right)^{\dagger} \rho_{\epsilon_\gamma,\epsilon_{\gamma'}} \left(\sum_{\beta} R_{\beta}^{\epsilon_x,\epsilon_\gamma}\right)\right]\right] \quad (10.6)$$

gives the intensity.

The data are binned in mass of X and the momentum transfer t and a fit is performed for the full set of V's in each bin. The results for such a fit for 100% linearly polarized photons are shown in Figure 10.5. In this fit, a comparison is made between the generated data and the Monte Carlo corrected data. In the 3π channel, the acceptance corrections are fairly small. The data shown are only for the positive reflectivity solutions, but a more or less identical set for the negative reflectivity are also produced. While visible, the acceptance effects are small, and do not hinder the extraction of the partial waves. It is

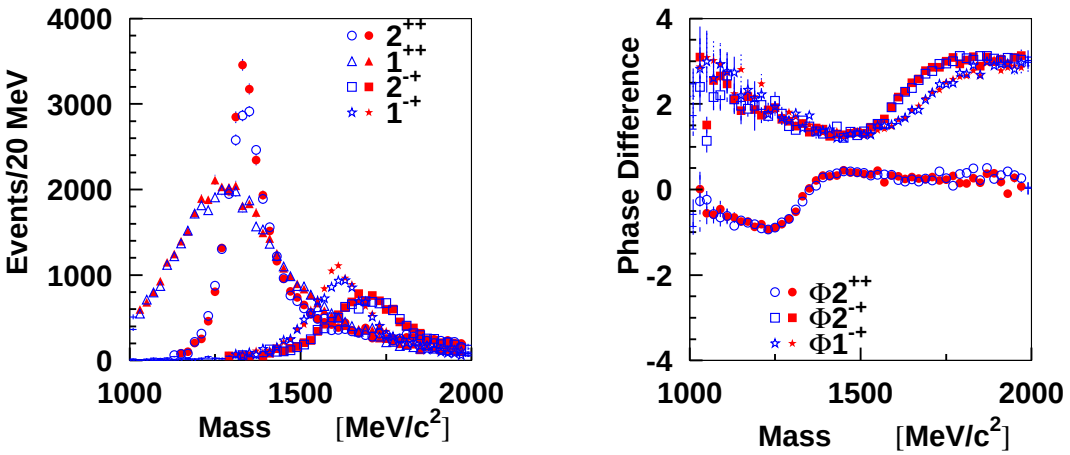

Figure 10.5: Fits to the weighted data using wave 1,3,4 and 6 from table 10.1. These fits compare generated data (solid shapes) to data that has been run through the HALL D Monte Carlo, (open figures). The left figure compares the fits to the intensities of four waves, while the right figure shows the phase differences between the listed waves and the 1^{++} wave.

also possible to extract the two rather small waves that are in the generated data set. These correspond to a second decay for each of 1^{++} and 2^{-+} waves. The main decays proceed with orbital angular momentum between the ρ and the π, $L_{\rho\pi}$ of 0, (S-wave), and 1, (P-wave) respectively. In addition, decays

could occur via $L = 2$, (D-wave) and $L = 3$, (F-wave), respectively. The relative rates between the two decays of a given resonance is an important quantity which can be compared to several models. Its extraction will be an important HALL D measurement. Figures 10.6 and 10.7 show the fits to these two waves. In each case, the left plot is the intensity of the positive reflectivity wave, while the right hand figure is the phase difference between the two decays of a given resonance. In the absence of final state interactions, the phase difference should be either 0° or 180°, which both fits show in the region where the intensity is non–zero.

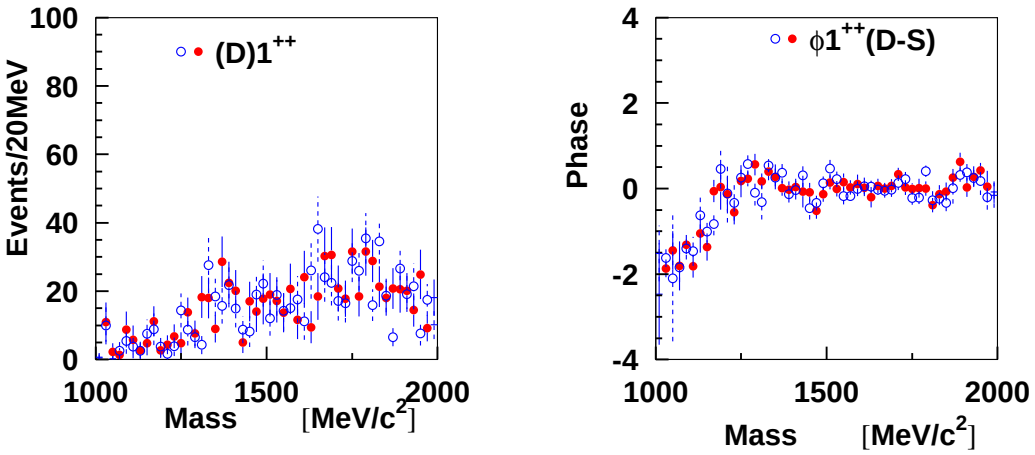

Figure 10.6: Fits to the D–wave decay of the 1^{++} wave from table 10.1. The figure on the left shows the intensity for the positive reflectivity wave. The right hand figure shows the phase difference between the S and D–wave decays. The open markers correspond to data that has been run through the HALL D Monte Carlo, while the solid markers are the generated events.

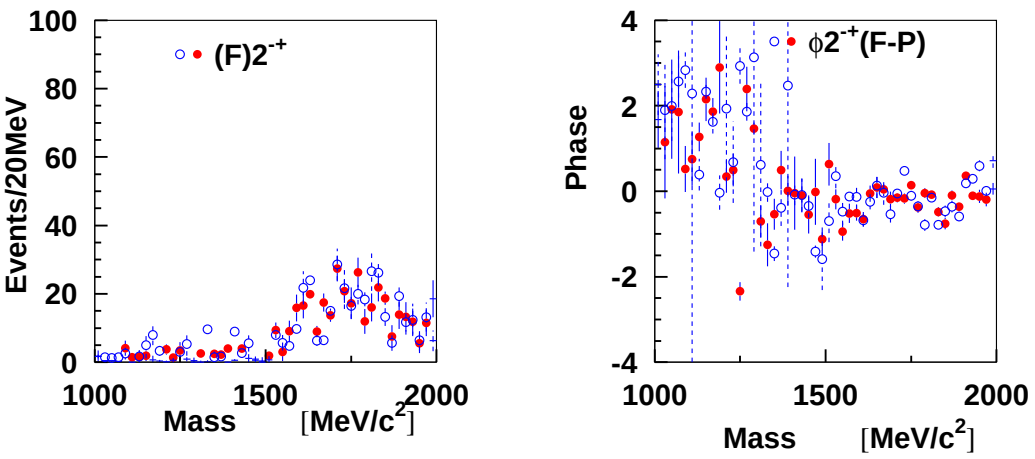

Figure 10.7: Fits to the F–wave decay of the 2^{-+} wave from table 10.1. The figure on the left shows the intensity for the positive reflectivity. The right hand figure shows the phase difference between the P and F–wave decays.The open markers correspond to data that has been run through the HALL D Monte Carlo, while the solid markers are the generated events.

In addition to the small waves, another common problem in PWA is leakage from one wave into another wave. A small distortion in the acceptance that is not fully understood can cause one wave to look like a different wave. This has been examined by adding six additional waves which were not in the generated data set, and repeating the fits with these waves in them. These waves correspond to $J^{PC}(M^{\epsilon})$ of $3^{++}(1^{+})$, $3^{++}(1^{-})$, $2^{++}(2^{+})$, $2^{++}(2^{-})$, $2^{-+}(2^{+})$ and $2^{-+}(2^{-})$. Figure 10.8 shows the results for two of these. The main point is that there is virtually no intensity in any of these waves, and certainly no structure leaking in from one of the strong waves in the events. At least in this study, the leakage appears to be an insignificant issue.

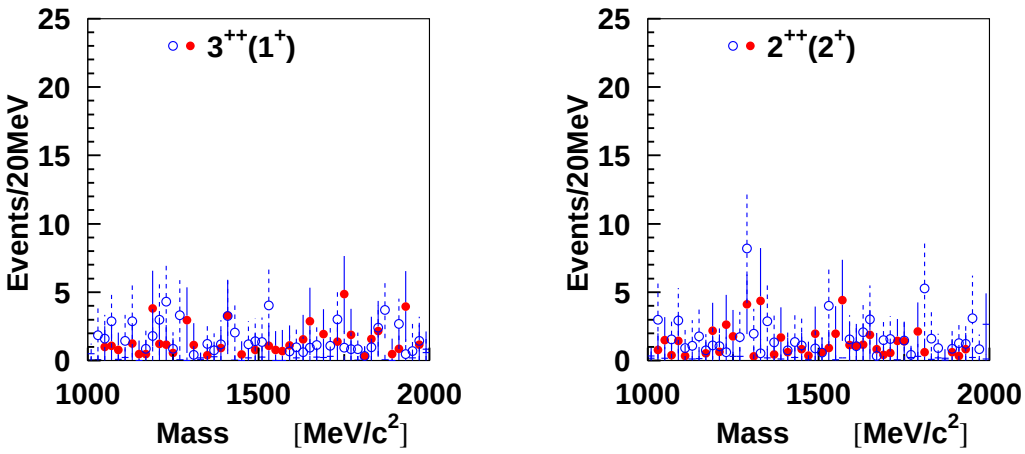

Figure 10.8: Fits to two partial waves which are not in the generated set. The figure on the left is a $J^{PC}(M^{\epsilon}) = 3^{++}(1^{+})$ wave, while that on the right is a $J^{PC}(M^{\epsilon}) = 2^{++}(2^{+})$ wave. There is virtually no leakage into these waves from resolution effects in the detector simulation.The open markers correspond to data that has been run through the HALL D Monte Carlo, while the solid markers are the generated events.

A comparison can also be made between an unpolarized data set and a 100% polarized data set. Because the positive and negative reflectivity distributions do differ in their $\cos\theta_{GJ}$ distributions, it is possible to separate them with unpolarized data. The separation is just not as clean as it is for polarized data and in the absence of information on the production mechanism, this separation becomes more difficult, especially if multiple production mechanisms are present. The best way to view these results is to look at the errors in the wave intensities for both the polarized and the unpolarized data sets.

These are shown in Figure 10.9. If one averages over all of the partial waves, the unpolarized errors are about $\sqrt{2}$ times larger than those for the polarized data set with the same number of events. Roughly speaking, in this test, the polarization reduces by a factor of 2 the statistics needed to achieve a given level of sensitivity. It should be pointed out that this is not the entire story as discussed below.

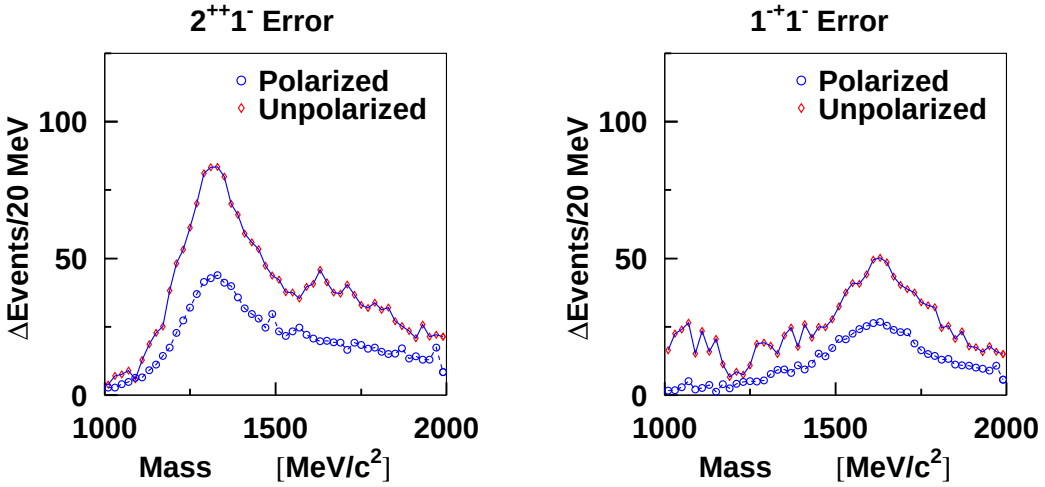

Figure 10.9: The errors in the fit results for two of the partial waves from the fit. The polarized and unpolarized data sets are the same size, and both sets are for generated data, (no acceptance corrections). The errors for the unpolarized data are on average about a factor of the $\sqrt{2}$ larger than those for the 100% polarized case.

Finally we have examined the case of simultaneous production via unnatural (π) and natural (*e.g.* ρ) exchange. The point is to illustrate the need for linear polarization. As discussed earlier at the nucleon vertex OPE flips helicity and is proportional to $\delta_{\lambda',-\lambda}$. At the meson production vertex the helicity structure is given by $\delta_{\lambda_\gamma,\lambda_X}$ for unnatural, and by $\tau^3_{\lambda_\gamma,\lambda_X}$ for natural resonances respectively. For the spin–1 ρ exchange, the number of different helicity couplings is quite large, however, if the nucleon helicity is flipped then coupling is proportional to $\tau^3_{\lambda',-\lambda}$ and if the helicity in the photon–resonance vertex is conserved, natural exchange leads to the $\delta_{\lambda_\gamma,\lambda_X}$ and $\tau^3_{\lambda_\gamma,\lambda_X}$ dependencies for the natural and unnatural exchanges respectively, *i.e.* opposite to the case of unnatural exchange.

In an additional study a ρ exchange intensity that is about 50% of the π exchange has been added to all six partial waves given in Table 10.1 using

Monte Carlo generated with 100%, 50%, 25% and 0% linear polarization. These two exchanges are incoherent, so the fit to the intensity is actually a fit to the sum of the two exchange mechanisms. As seen in Figure 10.10, this sum is well fit independent of the degree of linear polarization. One way in which the two can be separated is to fit the difference of the two exchanges (dashed curves in Figure 10.10). Here it is seen that the degree of linear polarization place a crucial role in a fit to this difference. With 100% polarization the difference is well fit, while for 0% polarization the difference is ambiguous. Any two values with the correct sum will work. Similar to this would be to examine the ϕ_{GJ} and α dependence of a given partial wave as in Figure 10.3.

To study on the effect of linear polarization in determining the production mechanism, data have been selected near $\alpha = 0°$ and near $\alpha = 90°$ in the Gottfried-Jackson frame of the resonance. These two states correspond to eigenstates of reflectivity. In the case of single pion exchange, (the naturality of the π is negative), the produced reflectivity state of the resonance is opposite to that of the photon. In the case of natural parity exchange, (such as ρ exchange), the two reflectivities will be the same. Partial wave analyses has been performed independently on the two data sets. Figure 10.11 shows the results for the 1^{-+} wave. The figure on the left shows the positive reflectivity 1^{-+} wave, $M^{\epsilon} = 1^{+}$. Only the events near $\alpha = 0°$ contribute, while the $\alpha = 90°$ gives nearly no contribution. The exact opposite happens in the $M^{\epsilon} = 1^{-}$ wave on the right. Had the production mechanism been of opposite naturality to the pion, these figures would have been reversed. If both mechanisms had been present, then the exact mixture could have been read directly off these plots as long as the degree of linear polarization in known. In the case of unpolarized photons, no such separation is possible. Of course the real data will involve a more general fit to this, but with linear polarization, the naturality of the exchange particle is trivially known, while for no linear polarization, there is no handle on this.

10.3.3 Joint production of excited baryons and mesons

In the kinematic region of HALL D it is probable that baryon resonances will be produced in addition to the meson states we have been discussing. Processes such as the two shown in Figure 10.12 will interfere with each other and they must be taken into account in the analysis. In general this could lead to ambiguities, since the baryon states can be described as an infinite sum over meson states. In practice, however, the sum over meson states is truncated to a finite number of resonances, and will not well describe the distribution due to the baryon resonance. Hence, in order to get a good description of the intensity

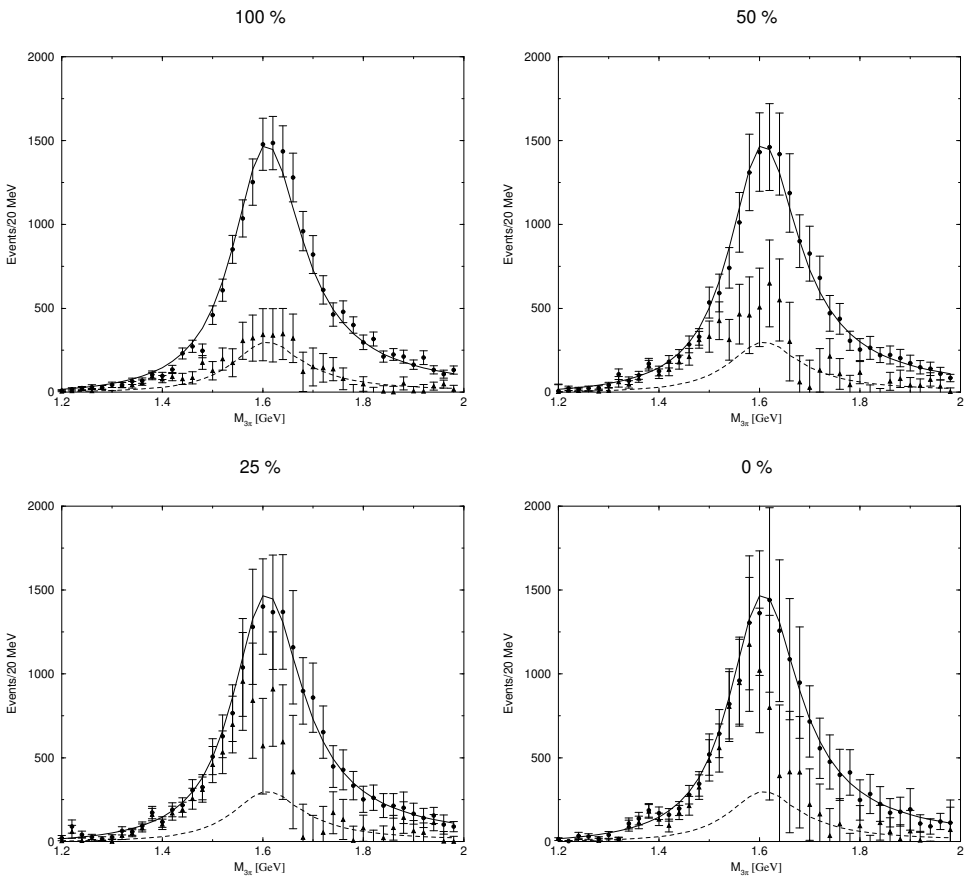

Figure 10.10: Fits to $\pi_1(1600)$, 4π acceptance data sets generated with a combination of π and ρ exchange mechanisms. The solid line is the sum of the two, while the dashed line is the difference. The four plots correspond to 100%, 50%, 25% and 0% photon linear polarization. The sum of the two is well fit for all values of polarization, while the difference becomes unclear as the polarization is decreased.

distribution, the baryon resonances must be included explicitly. Effects of ambiguities are mitigated at the cost of requiring a physically motivated *ansatz* of states *i.e.*, truncating the set of waves to the minimal set required by the fit. The impact of any ambiguities created will vary with the reaction being studied, but can be well determined using Monte–Carlo methods.

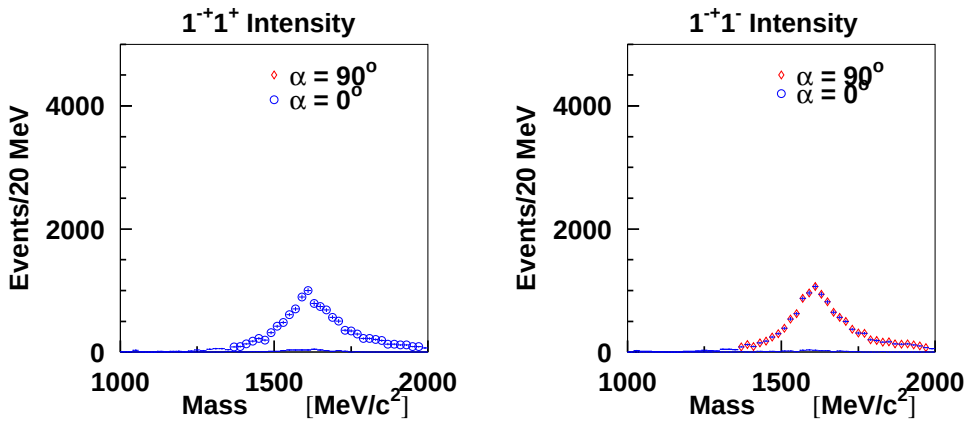

Figure 10.11: (Left) shows the fit to the positive reflectivity part of the 1^{-+} intensity for events near $\alpha = 0°$ and $90°$ degrees. (Right) shows the same for the negative reflectivity waves. They key point is that for π exchange, (negative naturality), only the positive reflectivity wave is produced near $\alpha = 0°$ while only the negative reflectivity is produced near $\alpha = 90°$. If the exchange mechanism had opposite naturality, then exactly the opposite would have occurred. These fits can lead to an exact decomposition of the exchange mechanism as long as one know the degree of linear polarization.

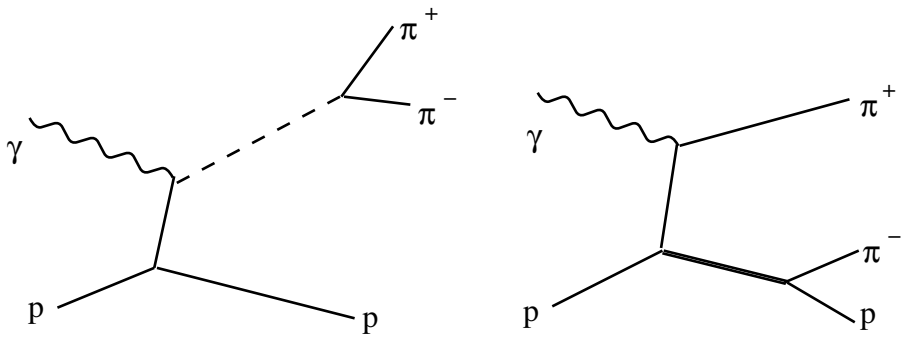

Figure 10.12: Example of interfering baryon and meson processes.

10.4 Summary

The HALL D collaboration is currently performing partial wave analyses on data that have been run through the HALL D detector simulation package. The initial studies have concentrated on the reaction $\gamma p \to \pi^+\pi^+\pi^- n$. The

collaboration has two different software packages under development. These use different formalisms and fitting procedures to perform the PWA. The comparison of the results from the two efforts will allow us to better understand the systematic problems associated with the procedures.

Fits have been performed with varying degrees of linear polarization to understand the balance between polarization and raw statistics when the production mechanism is known and to demonstrate the need for linear polarization in disentangling the natural and unnatural exchange mechanisms in resonance production.

These initial studies give us confidence that we are designing the appropriate detector with the capabilities needed to find and understand exotic mesons.

Chapter 11

Management Plan

11.1 Principles of the management plan

The task of the HALL D Collaboration, or simply the collaboration in this document, is to secure scientific approval and funding for the HALL D experiment at the Thomas Jefferson National Accelerator Facility (JLab) and to subsequently design, construct, and commission the beam-line and detectors and to complete the physics program leading to the publication of final results.

The governance of the collaboration is laid down in the Management Plan, MP, in such a way as to assure the timely and successful completion of the tasks above. It emphasizes teamwork and peer-review as essential to the successful execution of this plan. The framework is based on the formation of teams for each task with the autonomy and delegated authority needed for them to carry out their tasks within the integrated structure of the collaboration. Mechanisms of oversight and review of each team's work are implemented to assure that the goals of the collaboration are achieved in a timely, effective and coherent manner. An effective and unhindered liaison with JLab staff and management is paramount to the success of the project.

A collaboration is as good as the members that form it. The philosophy of the MP is to maximize the considerable talent and expertise available in its membership, while, at the same time, preserving a well defined order in decision making. Three principles guide this approach:

- First, the collaboration needs a strong and effective leadership. Such leadership ultimately resides with individuals who are identified with the physics and technical goals of the experiment and who have the confidence of their peers within the collaboration and the community

beyond. The MP endorses a multi-tiered structure designed to encourage and recognize such leadership at all levels within the collaboration.

- Second, the collaboration needs a clear and transparent decision making process, one that is open to every member of the collaboration who wishes to participate. This is accomplished by the principle of representative democracy, where the collaboration and all the teams and groups within it elect their own representatives to the next higher level of decision making. In parallel, the MP makes provisions which safeguard the effectiveness of the structure by outlining the process of conflict resolution at the various levels where such conflict may arise.

- Third, the MP proposes a structure that is both simple and flexible and able to adapt and change as experience and circumstances dictate.

As the collaboration progresses through the various stages of its program, the MP is an adaptable and flexible instrument of governance and can change to best serve the membership based on experience and environment. The basic principles enumerated above provide a reliable basis upon which the MP and its future developments will be founded.

11.2 The HALL D collaboration membership

The HALL D Collaboration membership consists of physicists and engineers who have signed a Memorandum of Understanding (MoU) specifying the expected contributions within the scientific and/or technical objectives of the HALL D Collaboration. Such contributions may be defined as any component of hardware, software, or any aspect related to the scientific basis of the experiment, and which the collaboration deems important to the pursuit of its objectives.

Membership for researchers within either an institutional or a task oriented group will also carry individual membership status. The list of individual researchers within the group brought forward for membership is the responsibility of the group leader. The list, drawn in good faith by the group leader, is a commitment by the individuals named to fulfill the obligations outlined in the MoU and to be active members of The collaboration in all its aspects.

Membership entails specific contributions to the HALL D experiment in all its aspects. As such, a failure by any individual or group to meet the respective MoU commitments constitutes grounds for removal of the individuals or groups from the HALL D Collaboration membership list. The rules governing

such matters will be defined in the appropriate sections of the MP and by the introduction of by-laws to be defined after the adoption of this MP.

Finally, all members in good standing will enjoy equal rights, opportunities for advancement, voting and decision making rights. the collaboration membership is the source of all decision making by elected representation and general voting procedures on the HALL D governance, as stated in the following sections. Even though the collaboration is a layered structure for organizational and functional efficiency, Collaboration members may bring concerns, ideas, and suggestions to any group, team, or representative within the collaboration. Thus, accessibility is an implied doctrine throughout this MP.

11.3 The HALL D governance structure

The governance structure of the HALL D Collaboration consists of five bodies. These are:

- The HALL D Collaboration Membership.
- The Working Groups (WG).
- The Technical Review Committee (TRC).
- The Executive Group (EG).
- the collaboration Board (CB).

The schematic diagram of the structure is shown in Figure 1.

11.3.1 The HALL D collaboration membership structure

Based on the general principles of the HALL D membership in Section 11.2, specific issues of membership structure are listed below which help define the membership, introduce grandfather clauses, and outline the mechanisms to be followed for introduction of new members. Purpose-specific by-laws may be added after the adoption of this MP to enhance and refine the process.

- When this MP is voted into existence by the existing membership, it will create the HALL D Collaboration by the current membership, as listed elsewhere in this document. This includes the posts of Spokesman, Deputy Spokesman, and HALL D Leader, as they are listed in this document. This article constitutes the formal grandfather clause of the collaboration.

- It is expected that all current members who wish to remain as Collaboration members will provide an MoU or equivalent document outlining undertaken commitments, for each individual or for each group of individuals, as stated above in Section 2.
- New applicants for membership, after the adoption of this MP, will be admitted into the HALL D Collaboration upon submission of an MoU, or equivalent, to the CB and Spokesman, and voted upon by both the CB and the Collaboration membership.
- The CB and/or the Spokesman may reject or return the application for further actions to be taken by the applicants. It is expected that the CB will communicate with the applicants the reasons of rejection or deferral.
- JLab physicists and/or technical staff will be assigned to HALL D tasks consistent with the objectives of the collaboration. This assignment will be done by JLab management in consultation with the CB Chair and the Spokesman.

11.3.2 The working groups

The WG s address themselves to the core of the reason of existence of the HALL D Collaboration and are the main means of reaching its objectives. The WG concept encompasses groups of Collaboration members working together on specific components of the experiment based on expertise, interest, and MoU obligations. The WG concept foresees an open architecture where members can contribute to more than one WG and where WG s may be added or dissolved as the need arises. Furthermore, members within a general WG may create sub-groups depending on need and work load.

Although new WG s may form as the needs arise and work progresses, it is clearly desirable to establish an initial structure of working groups to allow the installation of a critical structure to the HALL D project. Any changes in the structure and numbers of working groups after the MP is adopted will require the approval of the TRC in consultation with the EG. This will ensure that the needs of the project as a whole are taken into account in such restructuring. Each WG will select a representative to the next higher technical level, that of the TRC. The method of selection is left up to individual working groups.

The seven initial working groups upon approval of this MP are listed below:

- WG-M: is the group responsible for the assembly, installation and operation of the LASS/MEGA magnet and the liquid hydrogen target and their cryogenic infrastructure.

- WG-B: is the group responsible for the construction, installation and operation of the beam line elements, including the tagger, thin diamond radiator and the collimators leading to the delivery of tagged polarized photon beams of quality and intensity necessary to meet the objectives.
- WG-D: is the group responsible for the elements comprising the tracking, calorimetry, ToF, and all particle identification devices in the detector.
- WG-P: is the group responsible for the development and all related tasks necessary to pursue the PWA of the data. This is the working group developing and refining the scientific (Physics) case and looking into future experiments and new ideas that can be pursued by the collaboration. It is a natural working group for the theory group, but not exclusive to theorists.
- WG-C: is the group responsible for overall civil construction, the infrastructure needed to build the beam line, the end-station, control room, roads and radiation control procedures.
- WG-E: is the group responsible for coordinating the read-out electronics, trigger and DAQ hardware. Close cooperation with WG-D and WG-S will be needed.
- WG-S: is the group responsible for integration of all software issues, including simulations, data handling and online analysis. Close working relationships with WG-D and WG-P will be required.

11.3.3 The technical review committee

trc mandate

Although interaction between working groups is not only desirable but necessary, practical matters point to the necessity for a committee of representatives of the various WG s to form a review panel with the EG members and to oversee the total progress and integration, as it unfolds from the WG s. This is a very important committee on technical terms alone, since integration problems and solutions, element compatibility and delivery schedules of the total system will be examined and reviewed and recommendations will be made.

Other tasks may include the approval of prototypes before actual construction of the final elements begins, and addressing budget issues affecting construction and deliveries. Generally, the TRC is the body responsible for decision making on any and all technical and scientific issues concerning the

HALL D experiment. The TRC will also act as a source of technical expertise to the EG members.

Finally, the TRC will also act as the panel of final technical judgement on actions to be taken if a WG or an MoU signatory fail to meet progress milestones which affect other WG s and/or the project overall. In such a case, the TRC will recommend to the CB whatever action is deemed necessary to rectify the situation, including loss of Collaboration membership status.

trc structure

The TRC consists of the representatives of each working group (chosen by their respective WG members) and the three members of the EG. The TRC will be chaired by the Spokesman, who can also invite any other member of the Collaboration to attend, based on a specific issue of need and expertise. In order to preserve flexibility and effectiveness, the Spokesman may invite experts outside the Collaboration to attend specific meetings.

All reasonable freedom of action should be given the TRC to accomplish the Collaboration's objectives. The Spokesman has the authority to replace the representative of a WG, for cause, with another member of the same WG selected by its members. Such action by the Spokesman must be preceded by consultation with the CB Chair and the membership of the TRC in an effort to resolve the issue prior to removal.

11.3.4 The executive group

The EG consists of three members, the Spokesman, the Deputy Spokesman, and the HALL D Leader.

The experiment spokesman

The experiment spokesman is the Collaboration's central scientific figure to the world. The spokesman is expected to act as the principal investigator (P.I.) on the main funding application, present most of the presentations (at least initially), and be familiar, but not necessarily an expert, with all physics and technical aspects of the experiment. Furthermore, and just as importantly, the Spokesman must provide leadership, encouragement, and continuity without undue interference, together with the ability to take charge of and motivate individuals.

As the P.I. of the experiment, the Spokesman is responsible for all scientific, technical, and financial affairs of the HALL D Collaboration. On financial

matters, the Spokesman's duties must be consistent with all the requirements of the funding agencies and JLab structure. The Spokesman is the primary contact and ambassador between the HALL D Collaboration and JLab management and is expected to consult often and effectively with the CB Chair, the HALL D Leader, and the TRC. Finally, the Spokesman will chair the TRC and will nominate the Deputy Spokesman to the CB for approval.

The position of Spokesman is a term position. The initial stages of the HALL D Collaboration's objectives, such as the funding approval and the construction phases, require conditions of stability and continuity which are consistent with a longer term of tenure than later phases of data taking and analysis. Thus, the initial term is fixed at four years from the date of adoption of this MP

The term for Spokesman is renewable without any restriction on number of consecutive terms served. Upon the expiration of the stated term, the CB will call for nominations among the collaboration. The CB will act as an initial search committee to select no more than two candidates, based on technical, scientific, personality traits and, most importantly, leadership qualities, from among the pool of nominees. The CBendorsed nominee(s) will be presented to the the Collaboration membership for final vote.

The deputy spokesman

The Deputy Spokesman is the Spokesman's load-sharing, stand-in during absence and close advisor. The Deputy Spokesman will generally carry duties and responsibilities assigned by the Spokesman. In case the Spokesman is either removed from office or resigns, the Deputy Spokesman will be assigned as Spokesman (acting) until the collaboration elects a new Spokesman.

The Deputy Spokesman will be selected by the Spokesman from among the Collaboration membership and presented to the CB and JLab management for confirmation only. In the case of the CB, there should be important and overriding concerns in order to reject the selection by the Spokesman. A rejection will require a two-thirds vote by the CB members.

The normal term for the Deputy Spokesman coincides with that of the Spokesman. There is no limit on the number of consecutive terms the Deputy Spokesman serves.

The HALL D leader

The HALL D Leader is a JLab staff physicist appointed by JLab management in consultation with the Spokesman, Deputy-Spokesman, and the CB Chair.

The HALL D Leader must be either a Collaboration member, or become one immediately upon acceptance of the position.

The duties of the HALL D Leader are as diverse as they are important. The person will be the official representative of JLab management within the collaboration. The coordination of the civil construction and that for all elements necessary to deliver a high quality electron beam to the tagging facility, are primarily the responsibility of the HALL D Leader. All safety related administrative and engineering procedures and controls are also within the HALL D Leader's direct responsibility and authority.

The HALL D Leader is an important member of the TRC and is expected to interact and consult with members of the relevant Working Groups.

11.3.5 The collaboration board

The structure of the cb

The elected representative body of the collaboration is the CB. Its membership will consist of six voting members called CB Officers. The CB Officers will be elected directly by the Collaboration membership and they will choose their own chair. The Spokesman, Deputy-Spokesman, and the HALL D Leader, who cannot be elected to the CB, can attend CB meetings upon invitation by the CB Chair. No more than one voting member per institution or MoU group may serve on the CB. The CB membership tenure will be two years, with no more than two terms served consecutively for any member.

The mandate of the cb

The role of the CB is to address all issues related to the overall framework of the collaboration. It will decide on new membership applications in committee with the Spokesman. It will ratify the proposed by-laws for the collaboration and vote on proposed amendments. On major issues which affect the structure of the collaboration and the MP, both the CB and the general membership vote will be required. The exact mechanism will be defined in the by-laws, to be defined after the adoption of this MP.

Another important role of the CB is the management of issues related to graduate students. The very nature of the HALL D experiment, which is also a Collaboration as well as a facility, presents challenges and opportunities for the allocation of theses material for graduate students among the university based members of the Collaboration. A set of by-laws will be needed to govern such matters and to ensure fairness and objectivity to students and faculty.

The CB represents the interests of the membership in all aspects relating to the objectives of the HALL D Collaboration. It is expected that the CB Chair will play an active role in the governance of the collaboration and will bring issues of interest and concern of the membership to the attention of the EG and JLab management. The CB may recommend to the membership the removal of either the Spokesman or Deputy Spokesman by a two-third majority in the CB vote. The CB will meet regularly as conditions and needs arise and not less than three times within a calendar year.

The CB, like the EG, is entrusted with essentially the well being of the collaboration. It is self evident that all avenues of communication and substantive exchange of views will be pursued among these two committees and that electronic polling and conference calls will be employed to enhance the time response and frequency of contact between these two groups, over and above formal CB meetings a few times a year.

The chair of the collaboration board

The Chair will be responsible for calling CB meetings. However, any CB Officer can request to the Chair that a meeting be held. The Chair will consult with the other Officers and decide on the merit of such a request. The Chair will announce general Collaboration meetings in consultation with the Spokesman.

The CB Chair, like the Spokesman, is a position of high responsibility and sensitivity because the role is primarily that of human interaction rather than technical aspects. It is expected that Robert's Rules of Order are followed. On the issue of voting, the Chair will not vote on routine matters where simple or absolute majority is required, thus eliminating the possibility of split decisions in the six member committee. If the Chair wants to vote on such matters, an alternate Chair from among the other CB Officers must chair the meeting. On issues that require two-thirds majority, all members of the CB are eligible to cast a vote.

General duties of cb officers

The assigned duties of the other five CB Officers, as delegated by the Chair in consultation with the Officers of the Board, reflect the mandate of the CB Thus, CB Officers will be assigned one or more of the following duties:

- Dealing with membership issues.
- Dealing with nominations issues.

- Dealing with publication issues.
- Coordinating the speaker bureau.
- Keeping accurate records and minutes as the CB Secretary.
- Coordinating graduate student projects and theses.

If the need arises, either due to special circumstances or due to load factor, one or more Officers may request from the Chair the formation of subcommittees to assist in specific tasks. Such subcommittees are advisory to the CB and are to be recruited among Collaboration members. If necessary, non-Collaboration members may be invited to participate due to expertise and specific skills. Such subcommittees are of limited time duration and scope.

11.4 Summary

A management plan should create the minimum structure necessary to accomplish the ultimate objectives of the collaboration. It should preserve flexibility, while, at the same time, create a structure which is well defined and maximizes the individual talent and contribution of its membership. Due to the unique character, within the JLab structure, of HALL D as an experiment, but with a clear facility component, the MP could not necessarily be a direct or slightly modified copy of present models. The role of JLab management and structure for HALL D remains to be defined outside this MP, however, it should be an easy task to integrate new elements into this basic structure. Finally, the structure of the MP can be modified by the two-thirds majority vote rule in both the CB and the HALL D general memberships.

Appendix A

The report of the Cassel committee

Review of the Jefferson Laboratory "Hall D Project": December 6& 7, 1999

Review Committee:

David Cassel	Cornell University
Frank Close	Rutherford Laboratory
John Domingo	Jefferson Laboratory
William Dunwoodie	Stanford Linear Accelerator
Donald Geesaman	Argonne National Laboratory
David Hitlin	California Institute of Technology
Martin Olsson	University of Wisconsin
Glenn Young	Oak Ridge National Laboratory

Report Date: January 12, 2000

Executive Summary

The Committee was asked to address three principal questions, whose answers were to be based on the answers to more detailed questions. This Report contains the Committee's response to these questions, and advice to the Jefferson Laboratory management and the Hall D collaboration. Our answers to these questions are summarized in this Executive Summary and then given in more detail in the following Sections of this Report.

1. Evaluate the Scientific Opportunities Presented by the "Hall D Project"

This collaboration proposes to explore systematically the light mesons (with masses up to about 2.5 GeV) with capabilities far beyond those of previous experiments. The copious spin and flavor initial states produced by photon beams will be an extremely useful tool in this endeavor. Thorough study of the masses, spins, parities, and charge conjugation states of these light mesons will require a complete partial wave analysis. This will provide a much deeper understanding of quark-antiquark states, and will permit a definitive search for mesons with exotic quantum numbers, particularly hybrid states and glueballs. This search is very high priority physics; since the states involving excited glue, as well as quarkless glueball states, must exist if QCD is the correct theory of the strong interactions.

JLab is unique in being able to provide high quality, low emittance, CW photon beams that are required for this experiment. In addition, JLab and a significant segment of the JLab physics community are committed to this physics program. Together these provide a unique opportunity for exploring light meson states and making definitive searches for exotic states in this mass region.

2. Review the Collaboration's Approach to the Realization of that Facility

The general design of the detector is technically sound. This is verified by a detailed comparison (included in the Appendix of this Report) of the capabilities of the proposed Hall D detector with those of the successful LASS detector. This comparison leads to the conclusion that the proposed detector and beam combination will be able to realize the physics goals of the Project.

However, substantial effort must be invested to optimize the detector design and minimize the cost. The items requiring optimization that we have identified are described in detail in Section 2 of this Report. These optimizations are part of the R&D required to prepare a Conceptual Design Report for the Hall D Project. Preparation of a CDR with the associated WBS and resource-loaded cost and schedule will require a Project Office at JLab with a Project Director and a well-structured organization designed to address the necessary R&D and optimization efforts.

3. Recommend R&D Needed to Optimize the Facility Design and to Minimize the Overall Project Cost.

The R&D item of greatest concern is ensuring that the magnet is still functional, particularly the fourth coil, which has not been used for at least 15 years. R&D should also include construction of prototypes to optimize detector design, to validate mechanical, electronic, and software choices; and ensure the feasibility of the proposed coherent bremsstrahlung system.

Conclusions

In conclusion we find that:

- The experimental program proposed in the Hall D Project is well-suited for definitive searches for exotic states that are required according to our current understanding of QCD.
- JLab is uniquely suited to carry out this program of searching for exotic states.
- The basic approach is advocated by the Hall D Collaboration is sound.
- The Collaboration will be ready to begin work on a Conceptual Design Report once a Project Office with a Project Director is in place.
- An R&D program is required to ensure that the magnet is usable, to optimize many of the detector choices, to ensure that novel designs are feasible, and to validate cost estimates.

1 Evaluate the Scientific Opportunities Presented by the "Hall D"Project

1.1 Is this High Priority Physics That Must Be Done to Understand QCD?

Low energy QCD confines quarks into hadrons. Monte Carlo simulations of QCD demonstrate that the gluonic field (glue) collapses into a flux tube at large distances. Due to its self-interaction the glue should possess excited states which can be thought of as vibrations of the flux tube. Mesons with excited glue are called hybrids. Their existence is a firm prediction of QCD which has not yet been experimentally verified. In addition, quarkless mesons, known as glueballs, must also exist if QCD is the correct theory of the strong interactions.

These additional meson states should be plentiful in the mass range from 1 to 3 GeV. It would be important and in fact a crucial step in hadron physics to find these unconventional meson states as well as to identify the numerous conventional ones in this mass range. The proposed Hall D upgrade offers a unique opportunity to explore this mass region. The use of a photon beam is another special feature of the proposal, particularly since the photon beam carries both spin and flavor, which allows a large number of states to be excited.

The most convincing demonstration of the existence of hybrids and glueballs is likely to involve identification of exotic mesonic states — those with quantum numbers that cannot be formed by a quark-antiquark pair. A number of such exotic mesons are predicted to lie in the mass range that will be thoroughly mapped out as a result of this initiative.

Because of the nature of QCD, many hadron states are approximately degenerate in mass, so a detailed partial wave analysis must be done to disentangle them. A photon beam at JLab is particularly well-suited for this task, and the proposed linear polarization would substantially enhance the partial wave analysis by separating natural and unnatural parity contributions to t–channel exchanges.

1.2 Will the Facility's Capabilities be unique?

Photon beams bring the unique aspect of spin–aligned quarks to meson spectroscopy that is not available in the entrance channel with hadronic beams. This leads to the expectation of large cross sections for a number of states with exotic quantum numbers. While meson-production in baryon-baryon interactions , in principle, can populate the same states, the experimental situation is much more complicated.

The photon beam requirements for this project are initially 10^7 linearly polarized tagged photons per second in the energy range of 6–10 GeV with 100 percent duty factor and good emittance. The final goal is a tagged beam of 10^8 photons/s. JLab, with the energy upgrade, will be uniquely suited for providing such a beam. In particular, the excellent emittance of the JLab electron beam allows for strong collimation of the coherent bremsstrahlung radiation to enhance the polarization and ratio of tagged to untagged photons in the tagged photon beam. No other facility in the world will be able to provide a beam of this quality, with this combination of energy, duty factor, and emmitence. If such a project were pursued at other existing high-energy facilities, either the data taking rate would be dramatically reduced, compromising the physics goals, or a much more complicated detector would be required. We do not see any project at an existing accelerator complex (*e.g.* SLAC, CESR, DESY) which is likely to be able to compete with the Hall D initiative in this area.

2 Review the Collaboration's Approach to the Realization of that Facility

2.1 Is it Technically Sound?

- The technical solutions put forward in the proposal are, in the main, sound, but remain to be optimized
- It is worthwhile to spend time in optimizing individual component designs, in the context of the global scheme, rather than launching immediately into parallel prototyping efforts
- To this end, we recommend that, prior to assigning construction responsibilities, a set of "Task Force" efforts be launched to optimize the following detector systems:
  - Tracking
  - Calorimetry
  - Particle Identification
  - Trigger and Data Acquisition
- When specific approaches to detector design have been adopted, parametric studies should be carried out on items such as:
  - drift cell size,
  - support material distribution,
  - energy versus angular resolution in the barrel calorimeter,
  - particle ID capability, and
  - data acquisition concept and realization.
- Responsibility for each Task Force should be clear, and each Task Force should have an explicit charge and a definite reporting deadline.

2.1.1 Civil Construction

Since there was no detailed presentation of the civil construction, the Committee's comments are confined to the cost estimate and the brief outline in the document. The cost estimate provided by the JLab civil group appears reasonable for a project in this preliminary stage within the normal accuracy of 25% claimed by that group. We were more concerned by the 10–12 m of Fe shielding needed to range out the high energy muons from the photon collimator and the same amount probably required around the tagger dump. (The 1 m found in the document appears to be an error.) This suggest to the Committee that one should reexamine the decision to have a surface tagger dump and main building. By pointing the deflected electron beam downward

and placing the dump in the earth one could probably substantially reduce the required Fe shielding. In the same manner, placing the level of the hall floor below grade might also considerably reduce the required Fe shielding from the photon collimator. We suggest reexamining these questions in order to optimize costs.

2.1.2 Photon Beam

- The proposed tagger is essentially the same as that for Hall B and does not constitute a problem.
- Linear polarization from coherent bremsstrahlung is a well-understood phenomenon and the kind of beam proposed for Hall D has been used routinely in earlier experiments. However, achieving a beam of the quality desired for this experiment (*i.e.*, the flux, the concentration into a narrow band of photon energies, and the collimation needed to adequately enhance the fraction of photons that are linearly polarized) will require ongoing R&D efforts in conjunction with JLab Hall B developments. The R&D efforts that will be required include:
  - growth of synthetic diamond crystals of suitable thickness,
  - thinning of natural diamond crystals to the relevant thickness ($\leq 50\mu m$), and
  - a collimator feedback system to regulate photon beam targeting an polarization.
- Hall B tests indicate that the proposed Hall D incident flux will result in drift chamber occupancies well within acceptable range.

We conclude that the proposed photon beam design is compatible with the goals of the experiment, contingent on a successful R&D outcome.

Should it prove impossible to achieve the proposed level of linear polarization, it will be necessary for the collaboration to make the appropriate modifications to the proposed physics program.

2.1.3 Solenoid

- It is extremely important to ascertain very soon whether the MEGA/LASS magnet is still functional - especially the fourth coil, which has not been operated since $\sim$ 1982. If the potential Los Alamos collaborators can make such tests in situ, this should be done soon.

- If the magnet cannot be used, a reliable replacement cost estimate is needed to see if the experiment could still be funded. For example, if a replacement would cost $\sim$ \$ 10 million, would this be a showstopper?

- If the magnet is functional, experts, (*e.g.* John Alcorn, Steve Lorant) should be consulted to estimate anticipated lifetime and identify possible likely failure modes.

- A decision on coil configuration (*i.e*, gaps or no gaps?) is needed, since this has an impact on *e.g.*, the length of the barrel calorimeter to the extent of 60-80 cm.

2.1.4 Target

The cost estimate for the 30 cm hydrogen target system is based on the replacement cost for the Hall B cyrotarget. However, since the maximum power delivered by the photon beam is limited to 15 W, and the only cryogenic target envisaged is hydrogen (or deuterium), a small commercial closed cycle helium refrigerator would probably be much simpler and cheaper. We suggest that the collaboration investigate this option.

2.1.5 Barrel and Forward Calorimetry

Forward Calorimeter

The forward calorimeter design is based on:

- repackaging of the Pb Glass used successfully in E852/RadPhi and

- replacement of the balance of the PMT bases with a Cockcroft-Walton design already used in RadPhi.

The carriage, restacking, and acceptance match to the solenoid are all straightforward. In addition, the required manpower is clearly in place. Hence we expect that the Forward Calorimeter will not be a serious technical challenge.

Barrel Calorimeter

- The concept is sound. JETSET calculations and more recently KLOE experience provide proof-in-principle and proof-of-performance at the appropriate scale.

- Prototyping is needed, partly for reasons of technology-transfer and partly to show that the groups responsible can obtain the projected energy, time, and spatial resolutions at this detector length. This is likely to lead to development of the needed manufacturing technique. It will lend urgency to choices of scintillator configuration, metal, and sampling fraction, as well as coupling of photosensors to the calorimeter and their integration with the solenoid magnet and tracking chambers.

- Calibration and monitoring concepts need to be addressed in order to ensure that energy, time, and spatial resolutions can be maintained throughout the duration of the experiment.

- Further development of the requirements for front-end electronics is needed

- Manpower and group sizes still seem low for this effort, and engineering support needs to be identified for the structure, module manufacturing, supports, and front-end electronics.

2.1.6 Tracking Chambers

The overall geometry and anticipated performance of the tracking system appears to be reasonable. However, much work needs to be done to optimize the tracking system. This includes:

- A definite decision between the TPC option and the Central Drift Chamber needs to be made as soon as possible.

- The study of the TPC option must include an understanding of the problems that will be encountered with the non-uniform magnetic field of the solenoid and consideration of the data rate and volume issues that will arise from the anticipated very high occupancy.

- The overall design of the tracking system must be optimized. This optimization should include: studying the possibility of reducing the number of different types of chambers, optimization of cell sizes, and optimization of chamber geometry and locations. In addition, options for eliminating the separate Beam Vertex Chambers by combining them with the Forward Drift Chambers should be studied carefully.

- Prototyping of the selected drift chamber option(s) should be included in the R&D effort for a Conceptual Design Report.

- The proposed Vertex Detector system will require serious R&D effort.

2.1.7 Particle Identification Systems: Time of Flight, Cherenkov and dE/dx

The basic detector technologies for the ToF and Cherenkov systems are not a concern.

- ToF system:
  - Coupling of the active region to photosensors needs development, particularly a decision whether the photodetectors will be in the magnetic field and the resulting requirements on photodector design and magnetic shielding.
  - Prototyping of ToF elements would be useful to establish attainable timing resolution for chosen configuration and materials.
- Cherenkov system:
  - The proposed Cherenkov vessel would operate at pressures up to 5.6 atmospheres using an inert gas. This requires timely engineering attention to structural and safety issues.
  - The tradeoffs between threshold and imaging Cherenkov detectors should be examined.
- dE/dx system:
  - The proposed use of dE/dx information seems unsettled.
  - Extraction of dE/dx from straw tubes is possible but requires better understanding of the number of samples needed, electronics signal-to-noise, treatment of ambiguities in dE/dx versus momentum, and the resolution needed to obtain adequate $\pi/K/p$ separation without overdesigning this aspect of the spectrometer.
  - Prompt resolution of the choice of tracking system and whether a TPC would be employed will help in the timely resolution of these dE/dx issues.

Manpower is being addressed. Core institutions are identified for the ToF and Cherenkov detectors, while the effort on dE/dx is still a bit tentative.

2.1.8 Trigger System

- The basic concept for the Level-1 trigger is sound. This includes input from flash converters, a fully-pipelined formation of trigger primitives from several subsystems, appropriate front-end buffering during Level 1latency, feature extraction from a settable time window, and local event buffering, zero-suppression, and packet formation in response to issuance of a global Level-1.

- The choice of pipeline architecture is not clearly motivated. Within a pipelined architecture, the choice of 250MHz for TDCs to preserve drift chamber spatial resolution is clear, but it remains to be shown if this is the optimum choice, both in terms of cost and performance, compared to other systems. Similarly, choices of ADC and TDC step size and bit count should be optimized.

- There is some reliance on continued commercial development of high-speed FADCs, memories, and gate-array logic, but this does not seem to be an area for present concern.

- The speeds proposed will require that fully functional prototypes be developed soon to ensure proper performance at speed, handling of pipeline synchronization, and noise immunity of front-end sections.

Core manpower is identified for this subsystem

2.1.9 Data Acquisition

- The general Online effort would benefit from early appointment of a manager to promulgate and ensure a uniform approach to front-end electronics; data transmission to the event-building stage; and distribution of trigger, timing, and exception (*e.g.* calibration) events. This will yield significant benefits over the life of the project.

- The basic readout and event building architecture is sound. It depends somewhat on continued applicability of Moore's Law. The challenge will be to flesh this out to a buildable design.

Core technical staff are identified, but added manpower, especially in areas of online software is likely to be needed.

2.1.10 Computing Hardware and Software

- The partial wave analysis software developed by the collaboration makes a significant contribution to understanding the physics potential of the proposed experiment.

- The projections of computer hardware requirements appear to be reasonable. However, economic realization of these requirements depends on the continued validity of Moore's law.

- The principal software effort required for the Conceptual Design Report is the development of a Monte Carlo simulation of detector options that can aid the process of optimizing detector components while providing an upgrade path to a full simulation of the detector for physics analysis.

- In developing software infrastructure, the collaboration should be aware of similar efforts in other collaborations and should utilize the resulting software that matches collaboration requirements whenever possible.

2.2 Will the Detector/Photon Beam Combination be Able to Realize the Physics Goals in Terms of Rates, Resolution, etc.?

The proposed Hall D detector instrumentation is compared to that used in the LASS experiment in a table in the Appendix. The primary goal of the latter was the performance of partial wave analysis in the same mass region up to $\sim$ 2.4 GeV for forward-produced strange meson systems using incident $K^{\pm}$ beams. It is generally acknowledged that this endeavor met with a significant degree of success. Consequently, it provides proof of principle for the configuration proposed for Hall D. However, the proposed instrumentation is superior or equal to that employed in LASS in almost every instance.

Therefore — if the proposed Hall D detector capabilities are realized — it should be eminently possible to acquire data of sufficiently high quantity and quality that the collaboration can achieve its analysis goals.

2.3 Can the Approach to the Facility and Its Physics Program Be Improved Significantly?

While the committee saw several issues where substantial optimization and cost minimization studies are required, it did not identify significant alternative approaches that the collaboration should investigate before proceeding. The collaboration should continue to remain alert to new ideas and technologies as the project proceeds.

2.4 Is the Approach to Cost Estimation Sound, and Are the Cost Estimates Reasonable for a Project at this Early Stage of Development?

The equipment and material cost estimates appear reasonable for a project at this stage except for the absence of contingency assignments. The Committee was more concerned with the accuracy of the manpower estimates, in particular, with the absence of any explicit engineering manpower, except for the chamber frame system. While some engineering jobs can probably be met by technicians, professional engineers will undoubtedly be required for many of the detailed designs. The collaboration should work to make a detailed estimate of the various manpower requirements in order to proceed to a CDR.

2.5 Is the Collaboration Ready to Begin Work toward a Conceptual Design Report?

The physics motivation, detector design concept, and status of data-analysis methods all are mature enough for the collaboration to proceed to develop a CDR. However, we feel that:

- The detector design is not yet optimized, and the Collaboration would benefit from appointing the Task Forces described above to carry out these optimizations.
- It is important for the collaboration to establish how the detector resolution requirements determine the quality of the physics output in order to have verifiable criteria to understand the costs versus performance optimization.
- The organizations need to be put into place to prepare a CDR. Both Collaboration and Project organizations need to be fleshed out to support this. The effort will benefit from early identification of a Project Director and formation of a Project Office at JLab to support preparation of the CDR and associated WBS with resource-loaded cost and schedule.
- The Collaboration should work closely with JLab management to define
  - a prioritized R&D funding plan and
  - a Conceptual Design Report, working to a budget envelope.

2.6 Comments on the Contents of the CDR

The Conceptual Design Report should contain:

- reasonably detailed descriptions of the individual detector systems;
- parametric optimization;
- relationship of detector performance to physics goals;
- budget and schedule;
- assembly and commissioning plans; and
    - project organization,
    - Collaboration organization,
    - funding profile,
    - contingency allocation and management procedure,
    - use of planning, scheduling and cost-tracking tools,
    - detailed budget with a year-by-year profile,
    - resource-loaded schedule, and
    - system integration.

3 Recommend R&D Needed to Optimize the Facility Design, and Minimize the Overall Project Cost

When system designs have been optimized, prototype construction should begin on items such as:

- mechanical prototypes
- electronics prototypes, and
- prototypes for online and offline software.

R&D objectives and their relation to the construction project should be clearly defined. These include:

- proof of principle of novel designs,
- establishment of the project schedule,

- refinement of fabrication techniques,
- validation of cost estimates, and
- measurement of actual system performance in test beams.

Appendix: Comparison of LASS and Proposed Hall D Detectors

System	**LASS**	**Hall D**
Target	85 cm LH_2	30 cm LH_2
Magnetic Field (solenoid)	22.4 kG	$\sim$ same field coil configuration may differ
Cylindrical Chambers	6 PWC's $5 \leq r \leq 50$ cm $\sigma \sim 600\mu m$ 2 mm wire spacing and cathode strip readout dE/dx: limited π/p separation below $\sim$ 500 MeV/c Inner 2 cylinders used in definition of interaction trigger	Straw chamber $15 \leq r \leq 45$ cm $\sigma \sim 200\mu m$ dE/dx: capability proposed but needs optimization Dedicated start counter Scintillating fiber Immediately outside target
Planar Chambers	*Full Bore:* 6 PC's with 2 mm wire spacing 3 with (x,y,e) planes 3 with cathode strips $\sigma \sim 600\mu m$ (planes) $\sigma \sim 200\mu m$ (strips) *Beam Region:* 6 PC's with 1 mm wire spacing: all with (x,y,e) planes $\sigma \sim 300\mu m$ dE/dx: none First beam chamber package in trigger to close "target box"	5-6 drift chamber packages 6 planes in each package $\sigma \sim 300\mu m$ dE/dx: capability Configuration needs optimization
Cherenkov Counter	Segmented threshold counter Freon at atmospheric pressure π threshold $\sim$ 2.6 GeV/c	Segmented threshold counter Capable of pressures up to 5 or 6 atmospheres in order to vary threshold momentum
ToF	Pie-shaped 1 PMT per counter $\sigma \sim 500ps$ Large hole on axis ($r \sim$ 20–25cm) Downstream of Cherenkov Nothing in barrel region	Rectangular array 2 PMT's per counter $\sigma \leq 100ps$ Complete coverage except for small hole in beam region Downstream of Cherenkov EMC in barrel region capable of $\sigma \leq 250ps$
EMC	None	Barrel: Pb-scintillating fiber Downstream: Pb glass Almost hermetic coverage $\sigma(E)/E \sim$ 5–10%

Appendix B

The superconducting solenoid

B.1 Introduction

Momentum analysis in Hall D will be provided by a nominal 2 Tesla Super conducting Solenoid magnet. This solenoid was built at SLAC ca. 1970 for the LASS spectrometer , subsequently moved to LAMPF in 1985 for inclusion in the MEGA spectrometer and is expected to arrive at Jefferson Lab in the year 2001 for inclusion in the Hall D equipment. This magnet was designed and built using standards that today would be considered ultra conservative. The magnet is a cryostatically stable design and uses cryostats that were designed to be easily opened for service with hand tools. A recent inspection of the Magnet at LANL concluded that it is still in excellent condition and worthy of the use, time and cost involved.

B.2 Present condition

The LASS/MEGA solenoid was inspected in April 2000 by a team consisting of Hall D staff, JLab staff and two of the original designers of the magnet. This team met at Los Alamos with the MEGA staff and inspected the MEGA magnet installation and the fourth coil. The MEGA spectrometer was shut down in place in 1995. Except for two small mechanical vacuum pumps the system was completely intact. The fourth coil was found sealed in its original shipping crate. The fourth coil iron yoke ring, yoke stand and coil insertion tool were all found in storage. Several transportainers were found filled with magnet documentation including original drawings and micro film copies, log books, operating data, magnetic data, photo albums documenting all phases of the magnets life, manuals, calculations, and spare parts.

The committee rightfully concluded that "the condition of the magnet is excellent and if cooled down in place would in all likelihood work!" Thus Jefferson Lab has formally requested the property transfer from Los Alamos. The negotiations for this transfer have only just begun but at this time there appear to be no impediments to the eventual dismantling and shipment to Jefferson Lab. The entire magnet system has been requested and only two items are to be retained by Los Alamos. These items are the small Helium refrigerator (Not needed at JLab) and an Allen Bradly PLC (to be replaced at JLab). These items to be held back are required for another experiment at Los Alamos and as a spare for another installation respectively.

B.3 Dismantling and relocation

The MEGA setup is substantially unchanged since completion of the experiment. The magnet still contains all the physics equipment for the MEGA experiment and is still connected to various utilities and piped services. The magnet is still connected to its power source. Finally there are small quantities of activated materials and hazardous materials within the MEGA installation. Each of these conditions must be addressed by a comprehensive safety plan for the deactivation of the MEGA experiment installation. Furthermore work at Los Alamos is restricted to various trained and certified trades where there are specific hazards involved.

Electrical, piped -pressurized utilities, hazardous materials and activated materials may only be handled by certified personnel and use of Los Alamos cranes and lift vehicles is similarly restricted. These conditions will necessitate a careful safety and EH&S plan for all phases of MEGA system removal. The actual solenoid dismantling, removal and shipping can be performed by a private contractor with some on site LANL supervision. The related small items may also be dismantled by off site staff once the systems have been thoroughly deactivated by LANL certified staff. The Hazardous materials removal and activated materials removal may only be performed by LANL staff as well as the certification for "Free release."

Despite the long list of required items the process is straightforward and appropriate LANL professional staff who will oversee these steps have been tentatively identified.

JLab has contacted three rigging companies to determine the method and cost of the final dismantling, loading and shipment. We are fortunate in that there is good competition in Tidewater Virginia for such services. Preliminary estimates and schedules are available. It is estimated that two weeks will be

required at LANL for dismantling and loading. This work will require special equipment consisting of a lifting frame and a large (LANL owned and operated) fork truck. Shipment to JLab will be 14 truck loads common carrier.

Offloading at JLab into the Test Lab can be performed using JLab's crane and contract rigging staff.

Space in the Test Lab beginning in mid CY 2001 has been planned for the solenoid that will allow servicing and eventual re-assembly and test. The Test Lab was chosen due to the heavy lift capability, access to cryogenics and high bay-high load capacity floor.

Finally there are identified maintenance tasks that must be performed to insure continued reliability. Most of the items listed below are straightforward and require little explanation, consisting mostly of items that must be changed for basic compatibility with existing JLab systems and codes, or items that are obsolete and no longer serviceable. However the modifications required by the experiment have been the subject of some effort already and plans are by no means final. Further extensive efforts to calculate and understand the magnetic performance of the magnet will be made so an explanation of the present work is offered below.

B.4 Summary of proposed modifications

1. Experiment related modifications
    - Inclusion of "fourth coil"
    - Closing of yoke gaps
    - Thickening of fourth gap iron insert
    - Thickening of downstream "pole cap"
    - Alt 1- new upstream gap
    - Alt 2 - symmetric opening in upstream pole cap
2. JLab compatibility
    - Cryogenic interface
        - New JLab standard u-tube bayonet sockets
        - New JLab standard JT type valves and actuators
        - Cool down heat exchanger and controls
        - Relocated Helium reservoir

  - Burnout proof current leads
  - Replacement of LN2 reservoir
  - Replacement of LN2 and LHe level sensors
  - JLab standard U-Tubes
  - Transfer line to JLab CHL (not strictly part of magnet)
- Controls interface
  - Modern PLC and software
  - EPICS compatible controls and interface
- DC systems
  - NEC compatible DC Bus and energy dump
  - DC Power supply upgrade and controls interface
  - DC bus compatible with power supply relocation

3. Serviceability items

- Controls and instrumentation
  - Data Logger
    * Upgrade to instrumentation and signal processing electronics
    * Remote control power supply link
    * Replacement for interlock PLC retained by LANL
    * Upgrade to quench voltage and current lead voltage detection
    * Magnetic filed monitoring probe(s) and readout
    * Data cables as needed to allow relocation of controls
- Vacuum systems
  - Replacement of oil diffusion pump system with a modern turbo pump system.
  - Replacement of vacuum instrumentation as needed.

4. Maintenance items

- Replacement of vacuum system o-rings
- Repair of known leaks in LN2 shields
- Leak testing and repair of Helium space leaks as needed if found

- Maintenance of insulation systems as needed
- Test and maintenance of High Voltage insulation systems as needed
- Maintenance of DC power supply
- Maintenance of vacuum valves and gauges
- Maintenance of internal instrumentation and wiring
- Replacement of strain gauges known to be faulty
- Maintenance of existing electronics and signal conditioners
- Maintenance of existing data and instrumentation cabling
- Maintenance of existing instrumentation vacuum feed-throughs

B.5 Discussion of Magnetic modifications required by the experiment

The original SLAC configuration of the Solenoid allowed for gaps in the return yoke so that wire chambers could be inserted from the outside. Hall D does not have this requirement and thus it has been suggested to fill these gaps with iron rings. Further, in the LASS and MEGA installations the exit Cerenkov detector was required to be located at large radius due to the presence of high magnetic fields near the down stream end of the solenoid. The source of these high fields has been investigated using a 3D TOSCA model of the yoke and coil and various methods to reduce these "stray" fields have been explored.

The solenoid was originally designed with a segmented yoke with gaps and four cryostats with sub-coils inside. There are a total of thirteen sub-coils located within the four cryostats with the current density distributed by varying the number of turns. This was done to produce a more uniform internal field and to compensate for the gaps in the yoke and most prominently, for the asymmetric enlarged opening in the downstream pole cap. The thirteenth coil is very large, approximately four times the size of its neighbors. The other 12 coils vary by some few percent from each other. The thirteenth coil is needed to compensate for the large "Z" gradient in the field which is a natural consequence of the large opening in the yoke.

Furthermore, all coils have to operate at higher currents to drive the extra gap caused by the spaces originally designed in the yoke. The down stream pole cap is highly saturated in the original SLAC geometry due to the proximity of the thirteenth coil to the pole cap and the higher current required to drive the extra gaps. A solution for the high stray fields at the downstream end

presents itself in the form of the following set of yoke modifications. These modifications are all designed to reduce the saturation present in the pole cap which lowers the stray field in the region where the Cerenkov is to be located

1. Replace the air gaps with iron rings. This lowers the required operating current to achieve the same central field. The lowering of the local fields especially around coil thirteen helps reduce pole cap saturation.

2. Increase the distance in "Z" between the thirteenth coil and the downstream pole cap. This lowers the local field near the pole cap and thus lowers the saturation.

3. Increase the thickness of the pole cap by adding an iron disc to dilute the pole cap field and reduce saturation.

The above yoke modifications are shown to reduce the stray field levels in the Cerenkov region from ∼700 gauss down to ∼50 gauss, low enough to be shielded by thin iron and Mu-metal shields.

B.6 TOSCA simulations

B.6.1 Introduction

The Solenoid magnet for Hall D was designed without the benefit of modern 3D magnetic modeling. The magnet has worked long and has already lived two lives while meeting the requirements of two experiments. However there has been a persistent difficulty with stray fields in the vicinity of Photo Tubes and the required shielding. We have chosen to perform a 3D model of the solenoids fields to study the problem in detail and possibly design a remedy. Therefore a TOSCA model was created that allowed the calculation of the original geometry and the expected modifications. Further studies have been performed to study the effects of other modifications that may serve to lower the external fields.

B.6.2 TOSCA Model

The Solenoid has been modeled in 3D with an explicit accurate model of the iron yoke. The yoke has been modeled is such a way that the effect of closing the yoke gaps or creating new gaps or opening or closing the ends can be studied by simply changing the materials definitions for the relevant regions. This type of model has the benefit that the geometry is always the same. The

coils were approximated by the following stratagem. The last or 13th coil was modeled exactly because of its expected large effect on yoke end saturation and therefore external down stream fields. The other closely spaced 12 coils were approximated as a single uniform solenoid. The logic for this is that the 12 coils are all nearly the same size and uniformly spaced and that each has near equal current compared to coil 13 which is 4 times the average size of the other 12. Furthermore the 12 smaller coils are in a region where the yoke will be continuous and thus the external effects of this current distribution should be exceedingly small. The internal fields are expected to be affected by the exact distribution of current and the yoke details and modifications. The current distribution of the solenoid is not easily modified in any case and thus must be taken as a given. The modifications to the yoke are a mix of requirements from Physics, yoke improvements to lower external fields and modifications to provide new access for the Hall D detectors and their support. The current model is designed to evaluate the required yoke modifications and the need to lower external fields. The effect on internal fields will be the subject of a more detailed study.

The TOSCA model volume that has been modeled is a 45 degree slice of cylindrical geometry that contains a yoke segment and the surrounding air. The space modeled extends from -40 inches to + 600 inches along the z axis and out to a radius of 240 inches. This space is subdivided into regions that contain air or iron or reduced potential regions that contain currents. The volume modeled has 334,000 elements and the elements are all linear. With the high subdivision already present, one gets adequate accuracy with the extra computational time required using quadratic elements. The iron is a full nonlinear computation using the properties of generic 1006 steel which is similar to the actual 1010. The coil is represented by two solenoid coils one representing coil 13 and the other a uniform long coil that represents coils 1 thru 12. These coils are full 3D coil models that are superimposed on the 45 degree iron and air geometry. TOSCA uses symmetry to compute the fields in all space. The 45 degree segment of yoke is subdivided according to actual SLAC dimensions and all iron features and details are modeled. Furthermore the model can represent different geometries by changing materials definitions from air to iron for example. This can be used to study the effect of gaps or no gaps. Additional geometry has been programmed to simulate the extra gap on the upstream end that has been suggested for allowing cables to exit the yoke.

Also, by simply changing the iron to air on the upstream pole cap one can calculate the effect of a symmetric magnet, i.e. one with both ends open. The effect of extending the yoke geometry by adding extra iron to the downstream

end was studied by simply extending the existing geometry.

B.7 Initial results

The following 3D TOSCA models of the Hall D solenoid were evaluated : Hall D 107, Hall D 106, Hall D 103 and Hall D 105. These models are described below, and the original and last configurations are shown in FigureB.1. All four models use identical coil models and identical current density. The integral field increases by 2.6 % as a result of filling the gaps. The other modifications have no significant effect on the total field. This effect can be easily understood since most of the flux must return thru the original gaps. Thus filling them with iron must have a large effect on the field integral while only some of the flux is effected by the other changes and thus a minimal effect on field integral is seen.

Model Number	Max Field (G)	Min Field (G)	Low-Field Area (%)	$\int B \cdot dl$ (T·Inches)
Hall D 107	1067	523.0	none	302.8
Hall D 106	351	82.5	none	311.0
Hall D 103	241	56.7	17	311.3
Hall D 105	158	45.7	50	310.8

Table B.1: Field parameters for the region between 50 and 80 in radially, where Cerenkov photomultiplier tubes might be placed. The entries correspond to the maximum and minimum B fields, and fractional area with field below 75 Gauss. Also given is the on-axis field integral for each TOSCA model.

We briefly describe each configuration:

Hall D 107 has the iron yoke and coil configuration of the original LASS solenoid as it was used at SLAC. This model is to provide a baseline for comparison and to compare with historical calculations and measurements. The model has the original segmented yoke with the four original 6 inch air gaps. *This model should be used to measure the effectiveness of the yoke changes which are the subject of the other three models.*

Hall D 106 has the SLAC yoke but with the four 6 inch gaps filled with the same iron as the rest of the yoke. This was a requested change and it

a) Hall D 107

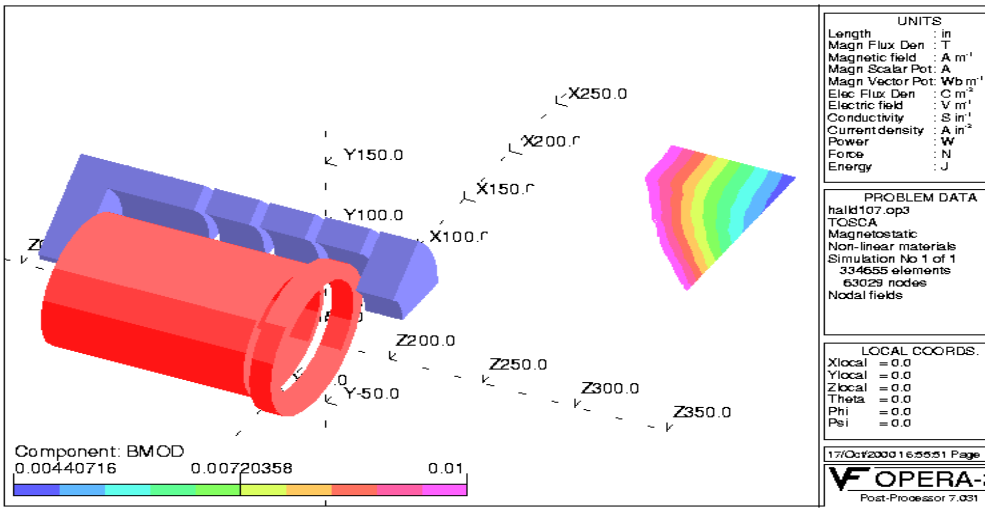

b) Hall D 105

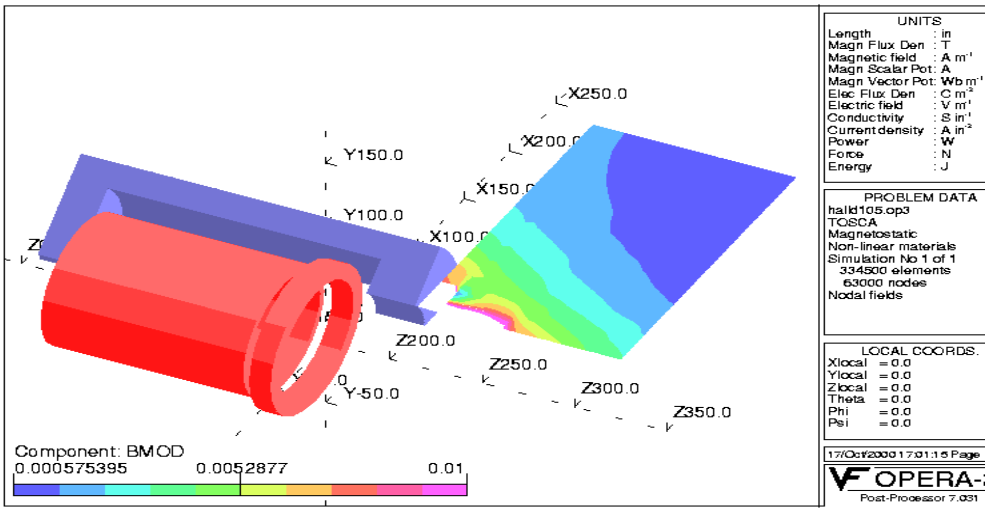

Figure B.1: TOSCA models for a) the original magnet configuration and b) configuration that fills the gaps with iron, extends the fourth gap and thickens the pole. Both figures show the model for the coils (solenoid and 13th coil ring) and a 45 degree pie slice of the yoke iron. Also shown is a contour plot of fields which are less than 100 G in the region of 50 to 240 in radially and 190 to 300 in along the axis. This is a region that could be considered acceptable for placing photomultiplier tubes. Note that in the bottom configuration the region of low field begins at the iron, allowing detectors to be mounted near

has the effect of lowering the external fields. You can clearly see that the external fields are in general lower especially in the regions where it would be desirable to locate photo tubes.

Hall D 103 has the four gaps filled with steel and gap four extended from 6 inches to 12 inches. This modification was selected because of the extreme saturation in the yoke that was observed around the 13th coil. Fields as high a 3 Tesla are observed near the 13th coil. Moving the yoke further away from the 13th coil will lower the yoke saturation and thus make the yoke more effective in collecting external flux and channeling it back within the yoke iron.

Hall D 105 has the down stream "pole cap" thickened from 20 inches to 26 inches. This is in addition to filling the gaps and extending the fourth gap. This modification was selected to further reduce saturation levels in the yoke and thus reduce further the external fields.

We studied the external fields in the region where Cerenkov photomultiplier tubes may be located. The region extends in z for 20 inches and in R from 50 to 80 inches. This 20 inch by 30 inch space is kept a constant 10 inches from the down stream yoke end for the four models discussed above. Models Hall D 107 and Hall D 106 have the patch of space located at from 199 to 219 inches in Z. Model Hall D 103 has the patch located at 205 to 225 in Z because the yoke has been lengthened by 6 inches overall. Model Hall D 105 has the patch located at 211 to 231 in Z due to the extended gap and the extra pole cap thickness adding 12 inches overall to the yoke length. Thus the four patches are a constant distance from the yoke end and clearly show the substantial improvements that are possible. The model Hall D 105 has a substantial volume ($\sim$ 50 %) with fields between 46 and 74 gauss (see Table B.1). These fields can be shielded by a combination of soft iron and Mu-Metal tubes. As this region extends from 65 to 80 inches in radius, the photomultiplier tubes for the Cerenkov could be located much close to the detection volume. A maximum distance of about 2 meters ($\sim$80 inches) is certainly possible. Figure B.2 plots the computed fields for the four models as a function of radial distance in the area where we expect to place sensitive detectors, and Table B.1 summarizes the characteristics for each case. Clearly there are large regions close to the detection volume where tubes could be located. It is also obvious that simply moving further out can have the same effect. Indeed the original solution chosen at SLAC was to locate the tubes at 4 meters where the fields are $\sim$75 gauss for the original SLAC /LASS geometry.

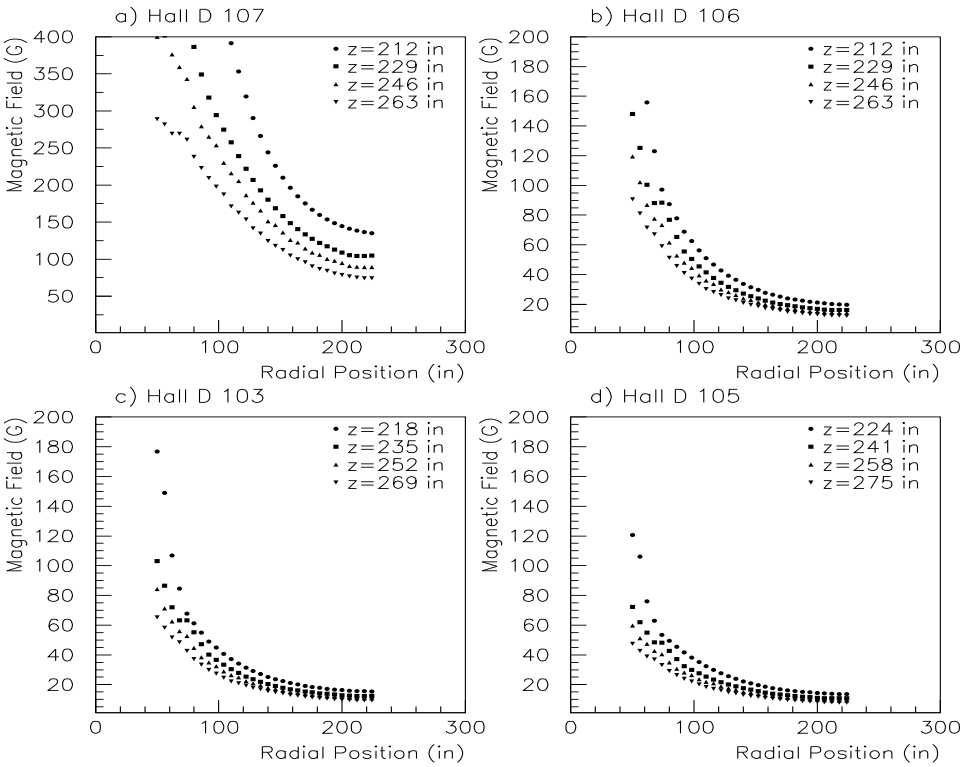

Figure B.2: Magnetic field as a function of radial distance at constant distance along the z axis for the four different configurations of the solenoid. Note the scale change for plot a).

The modifications computed above can achieve these field levels in a much more efficient manner.

Appendix C

Detailed Cost Estimates

This appendix contains the detailed cost estimates for HALL D.

Table C.1: Cost summary.
Table C.2: Detector overview.
Table C.3: Channel count summary.
Table C.4: Tracking.
Table C.5: Barrel calorimeter.
Table C.6: Cerenkov detector.
Table C.7: Forward calorimeter.
Table C.8: Time of flight.
Table C.9: Start counter.
Table C.10: Level 1 trigger.
Table C.11: Hydrogen target.
Table C.12: Data handling, experiment side.
Table C.13: Data handling, computer center side.
Table C.14: Civil.
Table C.15: Tagger.

C.1 Overview

The cost of this project includes the (1) civil construction associated with the beamline to Hall D, after the accelerator; (2) beam line elements; (3) photon tagger; (4) civil construction associated with Hall D; and (5) detector. The summary is shown in Table C.1 below. In preparing this budget we make the following assumptions:

1. Travel is not included.

2. Estimates of technician years, machinist weeks and student hours are given for each of the sub-systems. Throughout we assume $30,000/year for technicians, $1500/week for machinists and $9/hour for students. Fringe benefit and overhead rates vary from institution to institution and in the current budget we use the rates applicable at the institutions responsible for the individual sub-systems. In some cases, overhead is not charged on student labor. We assume that rates and applicability of overhead charges will be negotiated when funds are transferred to institutions.

3. Overhead is not charged on equipment or supplies and materials associated with constructing equipment.

4. Except for the tracking cost estimates, the cost of engineering has not been specifically included in the cost estimates. Rather, engineering costs are assumed to be part of some detector components.

5. Other assumptions, specific to the subsystem considered, are given below the cost breakdown table for that subsystem.

Item	Cost ($K)	Cost ($K) Including 30% contingency
Detector Package	17103	22235
Civil and Beamline	10285	13371
Total Cost	27389	35606

Table C.1: HALL D overall cost summary

Subsystem	Cost ($K)
Tracking	2591
Start Counter	1130
Barrel Calorimeter	2696
Cerenkov Counter	673
Forward Calorimeter	669
Time of Flight Wall	820
Computing	1232
Electronics	2901
Hydrogen Target	120
Solenoid	827
Photon Tagger	1940
Final Assembly	1500
Total	17103

Table C.2: HALL D detector cost summary

Channel Count	FADC	TDC (60 ps)	TDC (120 ps)	HV channels
Photon Tagger	0	250	0	250
Central Drift Chamber (Anodes)	5200	0	0	100
Forward Drift Chamber(Anodes)	0	0	2880	150
Forward Drift Chamber (Cathodes)	5760	0	0	150
Start Counter	10	10	2000	10
Barrel Calorimeter	576	576	0	576
Cerenkov Detector	38	38	0	38
Forward Calorimeter	2200	0		0
Time of Flight Wall	320	320	0	320
Total Number of Channels	14104	1194	4880	1594
Electronics Cost	**Number**	**Unit Cost ($)**	**Cost ($K)**	
FADC	14104	100	1410	
TDC (60 ps)	1194	75	89	
TDC (120 ps)	4880	50	244	
VME Crates	55	10000	550	
Racks for VME Crates	28	500	14	
Level 1 Trigger			295	
HV Channels	1594	187	298	
Total			2901	

Table C.3: Cost, electronics for detector and tagging spectrometer

Materials	Item	CDC	FDC	Total	Unit Cost ($)	Cost ($K)	
	Straws	5200	0	5200	10	52	
	Wire ($K)	10	40			50	
	Feed throughs	10400	0	10400	3	31	
	HV cables	100	300	400	100	40	
	Signal cables			865	100	86	
	Prints ($K)	15	100			115	
	Preamps			13840	20	276	
	Frames ($K)	80	30			110	
	Misc. parts ($K)	15	10			25	
	Support frame					75	
	Gas system					100	
	Calibration					150	
SubTotal						1111	
Labor		CDC	FDC	Frame	Total	Unit Cost ($)	Cost ($K)
	Technician years	10	5	0.5	15.5	30000	465
	Machinist weeks	50	25	20	95	1500	142
	Student hours	12000	6000	0	18000	9	162
	Engineer weeks	0	0	10	10	2500	25
	Shipping						60
	Subtotal (Fringe)						632
	Fringe (%)					25	158
	Subtotal (Overhead)						850
	Overhead (%)					55	467
SubTotal							1480
Total							2591

Table C.4: Cost, tracking detectors

Materials	Item	Number	Unit Cost ($)	Cost ($K)
	Scintillator Fiber			750
	Lead sheet			65
	Light Guides	576	150	86
	PMTs	576	1250	720
	PMT Bases	576	100	57
	Shields	576	100	57
	HV Cables	576	100	57
	Signal cables	576	100	57
	Glue and supplies			10
	Support structure			50
	Calibration system			100
SubTotal				2011
Labor	Item	Number	Unit Cost ($)	Cost ($K)
	Technician Yrs	10	30000	300
	Machinist Wks	50	1500	75
	Student Hrs	8000	9	72
	Shipping			20
	Subtotal (Fringe)			375
	Fringe (%)		16	60
	Subtotal (Overhead)			527
	Overhead (%)		30	158
SubTotal				685
Total				2696

Table C.5: Cost, barrel calorimeter

Materials	Item	Number	Unit Cost ($)	Cost ($K)
	Mirrors	38	630	23
	Mirror molds	3	2000	6
	Tooling			1.5
	Collector assemblies (material)	12	500	6
	Collector mirrors	38	290	11
	Lenses	12	250	3
	PMTs and bases	38	1971	74
	HV cables	38	100	3.8
	Signal cables	38	100	4
	Shields	38	200	7
	Gas (Cubic m C4F10)	36	380	13
	Gas system			100
	Calibration System			10
	Support structure			30
SubTotal				295
Labor	Item	Number	Unit Cost ($)	Cost ($K)
	Technician Yrs	2	30000	60
	Machinist Wks	55	1500	82
	Student Hrs	4000	9	36
	Shipping			10
	Subtotal (Fringe)			178
	Fringe (%)		32	57
	Subtotal (Overhead)			245
	Overhead (%)		54	132
SubTotal				378
Total				673

Table C.6: Cost, Cerenkov detector

Materials	Item	Number	Unit Cost ($)	Cost ($K)
	PMTs	2200	0	0
	PMT Bases	1500	100	150
	Lead Glass Blocks	2200	0	0
	Shields	2200	0	0
	Signal cables	2200	25	55
	Support structure			80
	Calibration system			20
SubTotal				305
Labor	Item	Number	Unit Cost ($)	Cost ($K)
	Technician Yrs	2	30000	60
	Machinist Wks	45	1500	67
	Student Hrs	10000	9	90
	Shipping			10
	Subtotal (Fringe)			127
	Fringe (%)		29	37
	Subtotal (Overhead)			264
	Overhead (%)		38	100
SubTotal				365
Total				670

Table C.7: Cost, forward calorimeter

Materials	Item	Number	Unit Cost ($)	Cost ($K)
	Scintillators	160	500	80
	Light Guides	320	100	32
	PMTs	320	1250	400
	PMT Bases	320	100	32
	Shields	320	100	32
	HV cables	320	100	32
	Signal cables	320	25	8
	Support structure			15
	Calibration system			10
SubTotal				641
Labor	Item	Number	Unit Cost ($)	Cost ($K)
	Technician Yrs	2	30000	60
	Machinist Wks	20	1500	30
	Student Hrs	1000	9	9
	Shipping			5
	Subtotal (Fringe)			90
	Fringe (%)		29	26
	Subtotal (Overhead)			130
	Overhead (%)		38	49
SubTotal				179
Total				820

Table C.8: Cost, time of flight detector

Materials:Timing	Item	Number	Unit Cost ($)	Cost ($K)
	Scintillators	10	500	5
	Light Guides	10	100	1
	PMTs	10	1250	13
	PMT Bases	10	100	1
	Shields	10	100	1
	HV cables	10	100	1
	Signal cables	10	100	1
	Connectors			3
	Support structure			3
SubTotal				29
Materials:Tracking	Item	Number	Unit Cost ($)	Cost ($K)
	VLPC Channels	5000	68	340
	Fibers	5500	3	16
	Clear Fibers	22000	3	66
	VLPC Mounting	5000	50	250
	Electronic Boards	5000	20	100
	Cryostat	1		140
	Support structure	1		12
SubTotal				924
Labor	Item	Number	Unit Cost ($)	Cost ($K)
	Technician Yrs	2	30000	60
	Machinist Wks	20	1500	30
	Student Hrs	1000	9	9
	Shipping			5
	Subtotal (Fringe)			90
	Fringe (%)		27	24
	Subtotal (Overhead)			128
	Overhead (%)		38	48
SubTotal				177
Total				1130

Table C.9: Cost, start counter

Components	Item	Number	Unit Cost ($)	Cost ($K)
	Crate level summation	35	5	175
	Subsystem level summation	5	10	50
	Level 1 Global Processor	1	25	25
	Clocks, synchronization, cables			25
	VME Crates	2	10	20
Total				295

Table C.10: Cost, level 1 trigger

Cryogenic Target	Item	Cost ($K)
	Gas Handling System	20
	Controls	30
	Isolation vacuum pumping system	20
	Outer vacuum chamber/scattering chamber	10
	Target cells, condenser, dewar, heat shields, etc	20
	Liquid helium supply/return	10
	Positioning/mounting system	10
Total		120

Table C.11: Cost, hydrogen target

Data Acquisition Item	Quantity	Unit Cost ($K)	Cost ($K)
Single Board CPU	35	3	122
Main Switch	2	20	40
DAQ Farm Switch	10	4	40
DAQ Sun SMP	10	20	200
DAQ FARM CPU	200	2	400
Misc. online computer	10	3	30
DAQ RAID disk	10	20	200
Racks, Desks, Misc			200
Total			1232

Table C.12: Data handling, experiment side

Data Analysis Item	Quantity	Unit Cost ($K)	Cost ($K)
CC RAID (TB)	100	4	400
CC Tape Drive	40	30	1200
CC Tape Silo	2	300	600
Analysis Farm	100	2	200
Tape Media (TB/Year)	3000	0.2	600
Racks, Desks, Misc			30
Total			3030

Table C.13: Data handling, Computer Center

Buildings	Item	Above Ground Cost ($K)	3.0m Below Cost ($K
	Construction	2152	2840
	Pilings	200	0
	Utilities	38	37
	Crane	164	164
	Access Control	42	42
	Fire Protection	83	83
	Mechanical, LCW, HVAC	1538	1538
	Electrical	1023	1023
	Overhead (30%)	1572	1719
Sub Total		6815	7449
Beamline		Cost ($K)	
	Diagnostics	470	
	Service Building	110	
	Elements	1180	
	Labor	1710	
Sub Total		3470	
Total		10285	

Table C.14: Cost, Civil construction

Spectrometer Magnet	Item			Cost ($K)
	Magnet Steel			200
	Machining			200
	Tagger Magnet PS			140
	Magnet Coils			200
Sub Total				740
Radiator/Hodoscope	Item	Number	Unit Cost ($)	Cost ($K)
	Vacuum Chamber			150
	Thin exit window			75
	Magnet support			50
	Hodoscope Support			30
	Scintillator/Light Guide	250	250	62
	Photomultiplier	250	400	100
	Base and mag shield	250	250	62
	Signal cables	250	100	25
	Goniometer			100
	Crystals			45
	Active collimator			30
	Discriminators			32
	Logic			10
	CAMAC Crate			5
	Scalars/VME Crates			30
Sub Total				807
Labor	Item	Number	Unit Cost ($)	Cost ($K)
	Technician Yrs	3	30000	90
	Machinist Wks	45	1500	67
	Student Hrs	8000	9	72
	Shipping			10
	Subtotal (Fringe)			157
	Fringe (%)		29	45
	Subtotal (Overhead)			285
	Overhead (%)		38	108
SubTotal				393
Total				1940

Table C.15: Tagger cost

List of Figures

2.1 QCD flux tubes 16
2.2 The Hall D detector. 18
2.3 The current CEBAF multipass electron accelerator at JLab, showing the three existing experimental Halls (A, B and C) and the planned Hall D. 18
2.4 Beam enery kinematics 22
2.5 Beam flux and polarization vs. electron energy 23
2.6 Figure of merit: relative meson yield as a function of photon beam energy for various meson masses. 23

3.1 QED and QCD fields 31
3.2 LQCD evidence for flux tubes 32
3.3 A level diagram showing conventional nonets and expected masses of glueballs, hybrids and molecular thresholds. The vertical axis is in units of GeV/c^2. For the $q\bar{q}$ boxes the L refers to the angular momentum between the quarks and each J^{PC} refers to a nonet of mesons. Note also that exotic J^{PC} occur only among the hybrids for the range of masses shown. 33
3.4 The $q\bar{q}$ spectrum 34
3.5 The process $\gamma p \to Xp$ proceeding via the exchange of a particle 40
3.6 Acceptance corrected effective mass distributions for the (left) $\pi^+\pi^-\pi^-$ combination and (right) $\pi^+\pi^-$ combination (two entries per event) from E852 [11]. 41
3.7 Combined intensities for all (a) 0^{-+} waves; (b) 1^{++} waves; (c) 2^{-+} waves; and 2^{++} waves from E852 [11]. 42
3.8 The intensities for the waves corresponding to 1^{-+} into $\rho\pi$. The shaded distributions are an estimate of leakage due to non-exotic waves – from E852 [11]. 42
3.9 Results of a coupled mass-dependent Breit-Wigner fit of the 1^{-+} and 2^{-+} waves showing the phase difference as well – from E852 [11]. 43

4.1 Generic diagrams for hard photon production. 62
4.2 Photon energy spectrum from the Compton back-scatter source 64
4.3 Photon power spectrum from an oriented diamond radiator. . 67
4.4 Schematic plan view of the photon beam line 69
4.5 Coherent bremsstrahlung spectrum 72
4.6 Coherent bremsstrahlung spectrum after collimation. 74
4.7 Linear polarization in the coherent bremsstrahlung peak . . . 77
4.8 Linear polarization of the coherent bremsstrahlung beam . . . 78
4.9 Maximum polarization *vs* radiator-collimator distance. 80
4.10 Collimated coherent bremsstrahlung spectrum 84
4.11 Schematic illustration of crystal mounted in goniometer 86
4.12 Temperature profile of crystal at full current 90
4.13 Coherent photon spectrum 96
4.14 Horizontal and vertical beta functions for electron beam . . . 98
4.15 Horizontal and vertical envelopes for the electron beam 99
4.16 Plan view of tagging spectrometer 102
4.17 Angular distribution for pair production by polarized photons 109

5.1 An overview of the HALL D detector. 112
5.2 Efficiency versus photon threshold 118
5.3 A sketch of the barrel calorimeter 119
5.4 The HALL D tracking elements. 121
5.5 Charged particle momentum resolution. 123
5.6 Particle distributions 125
5.7 Curl up in the magnetic field. 126
5.8 Missing mass resolution. 127
5.9 Tracks in a straw tube 128
5.10 Central drift chamber 129
5.11 A front and side sketch of an FDC package. 130
5.12 Momentum resolution versus VTX resolution. 131
5.13 The vertex detector. 132
5.14 Start counter scintillator element. 132
5.15 Momentum distributions for $K^+K^-\pi^+\pi^-$ events 136
5.16 Time differences in a prototype bar 139
5.17 The Čerenkov detector 140
5.18 Fraction of particles seen as K's 141
5.19 Percentage reconstructed 143
5.20 Modified lead glass detector 145
5.21 The $\pi^0\pi^0$ and $\eta\pi^0\pi^0$ effective masses 146
5.22 The $\eta\pi^+\pi^-$ effective mass. 147

5.23 RADPHI effective masses 148
5.24 The three photon effective mass 149

6.1 An overall view of the accelerator site and HALL D. 152
6.2 Schematic of space allocated for the collimator enclosure which includes limiting apertures, sweeping magnets and passive iron shielding. Details of photon beam generation are contained in Chapter 4. 157
6.3 Typical composition of soil under the HALL D contruction site as a function of depth. The result of the geotechnical analysis shows that buildings at grade level will require support piles, driven approximately 15-20 m into the ground. 159
6.4 Elevation and plan view of the tagger and HALL D buildings. 160

7.1 Total cross section for $\gamma p \rightarrow$ *hadrons* as a function of photon energy. 162
7.2 Estimated rates as a function of electron beam current. 166
7.3 Drift chamber occupancies (scaled by target thickness = 1.7) plotted versus beam current (scaled by collimation factors = 5.33) expected for HALL D operation. The drift chambers in region 1 (squares) are completely unshielded by any magnetic field in CLAS, whereas the drift chambers in region 2 (triangles) are shielded from backgrounds by the main torus field. The nominal low current operation in HALL D (10^7 photons/s in the coherent peak) corresponds to 300 nA. The 2.2 T solenoidal field for HALL D is expected to be at least as effective as a shield as the CLAS torus. 168
7.4 A schematic diagram of the HALL D trigger. 169
7.5 Block diagram of FADC board. 174
7.6 Resolution as a function of energy for simulated FEU84-3 PMT sampled at 8 bits, 250 MHz. LGD resolution is shown by dotted line. FADC samples are summed to determine energy. 175

8.1 An approximate time line for the HALL D software development. 188

9.1 Software overview 190
9.2 The acceptance as a function of total effective meson mass . . 194
9.3 Acceptance in $\cos\theta_{GJ}$ 196
9.4 Acceptance in $\cos\theta_{GJ}$ 197
9.5 Acceptance in $\cos\theta_{GJ}$ 198
9.6 Acceptance in $\cos\theta_{GJ}$ 199

9.7 Event displays of lost events for $\gamma p \to p\eta\pi^0\pi^0$ 200
9.8 Lost photons in the BCAL 201
9.9 Lost photons in the BCAL 202
9.10 Lost photons in the LGD 202
9.11 Physics event generation 203
9.12 Generated 3π spectra 204

10.1 $\gamma p \to \pi^+\pi^+\pi^- n$ 209
10.2 Photon polarization: ϕ versus α 209
10.3 Photon polarization: ϕ versus 3π mass 211
10.4 Fits to generated data 212
10.5 Fits to simulated data 214
10.6 Fits to the a_1 D-wave 215
10.7 Fits to the π_2 F-wave 216
10.8 Leakage to other waves 217
10.9 Fit errors 218
10.10 Two production mechanisms 220
10.11 PWA fits to two bins in α 221
10.12 Joint production of baryons 221

B.1 TOSCA configurations for the solenoid 257
B.2 Magnetic field as a function of radial distance 259

List of Tables

3.1 Photoproduction cross sections 38
3.2 Predicted partial widths 53
3.3 Predicted and observed partial widths (in MeV/c^2) of the two 1^{--} $s\bar{s}$ states $2^3S_1(1680)$ and $^3D_1(1850)$. 60

4.1 Figure of merit of various materials 79
4.2 Requirements for goniometer axes 85
4.3 Assumed and projected electron beam properties 92
4.4 Tagging spectrometer parameters 103
4.5 Geometry of the tagger 104
4.6 Optical properties of the tagger 105
4.7 Operating parameters for an experiment 110

5.1 The LASS solenoid. 113
5.2 The HALL D tracking design parameters. 122
5.3 Maximum momentum versus beam energy 124
5.4 Tracking electronics 134
5.5 K-π time-of-flight differences 137
5.6 Percentage Misidentified particles 142
5.7 Percentage of correctly reconstructed events 142

6.1 Beam parameters for a 12 GeV electron beam. 153

7.1 Drift chamber occupancies for each superlayer (in percent) for run 21998 at the maximum beam current of 320 nA (logbook entry #7031). 165
7.2 Comparison between conditions in Hall B during high rate test and anticipated running parameters for HALL D. A current of 3 μ A in HALL D corresponds to 10^8 photons/s in the coherent peak. 167
7.3 Rates, sizes, and processing requirements for the level 3 trigger. 178

9.1 Known 3π resonances. 204

10.1 Waves in the weighting function 210

B.1 Magnetic field in the region of Cerenkov detector 256

C.1 HALL D overall cost summary 262
C.2 HALL D detector cost summary 263
C.3 Cost, electronics for detector and tagging spectrometer 264
C.4 Cost, tracking detectors 265
C.5 Cost, barrel calorimeter 266
C.6 Cost, Cerenkov detector 267
C.7 Cost, forward calorimeter 268
C.8 Cost, time of flight detector 269
C.9 Cost, start counter 270
C.10 Cost, level 1 trigger 271
C.11 Cost, hydrogen target 271
C.12 Data handling, experiment side 271
C.13 Data handling, Computer Center 272
C.14 Cost, Civil construction 272
C.15 Tagger cost 273

Bibliography

[1] C. A. Meyer A. R. Dzierba and E. S. Swanson. The search for QCD exotics. *American Scientist*, **88**:406, 2000.

[2] A. R. Dzierba and N. Isgur. Mapping quark confinement by exotic particles. *CERN Courier*, **40 No. 7**:23, 2000.

[3] G. Bali *et al.* (SESAM Collaboration). Static potentials and glueball masses from QCD simulations with Wilson loops. hep-lat/0003012.

[4] A. Afanasev and P. R. Page. Photoproduction and electroproduction of $J^{PC} = 1^{-+}$ exotics. *Phys. Rev.*, D**57**:6771, 1998.

[5] S. Godfrey and J. Napolitano. Light meson spectroscopy. *Rev. Mod. Phys.*, **71**, 1999. Also available as hep-ph/981141.

[6] P. Minkowski and W. Ochs. Identification of the glueballs and the scalar meson nonet. hep-ph/9811518.

[7] C.Bernard *et al.* (MILC Collaboration). *Phys. Rev.*, D**56**:7039, 1997. hep-lat/9707008.

[8] K. Juge, J. Kuti, and C.J. Morningstar. *Nucl. Phys. Proc. Suppl.*, **63**:326. hep-lat/9709131.

[9] D. R. Thompson *et al. Phys. Rev. Lett.*, **79**:1630, 1997.

[10] A.Abele *et al.* (Crystal Barrel Collaboration). *Phys. Lett.*, **423B**:175, 1998.

[11] G.S. Adams *et al. Phys. Rev. Lett.*, **81**:5760, 1998.

[12] T. Barnes, F.E. Close, and E.S. Swanson. *Phys. Rev.*, D**52**:5242, 1995.

[13] C.J. Morningstar and M. Peardon. *Phys. Rev.*, D**56**:4043, 1997. hep-lat/9704011.

[14] G.S. Bali *et al. Phys. Lett.*, **309B**:378, 1993.

[15] J.Sexton *et al.* (IBM Collaboration). *Phys. Rev. Lett.*, **75**:4563, 1995.

[16] G. Bali *et al.* (SESAM Collaboration). *Nucl. Phys. Proc. Suppl.*, **63**:209. hep-lat/9710012.

[17] C.Amsler and F.E.Close. *Phys. Lett.*, **353B**:385, 1995.

[18] C.Amsler and F.E.Close. *Phys. Rev.*, D**53**:295, 1996.

[19] F. E. Close and A. Kirk. hep-ph/0004241.

[20] N. Isgur, R. Kokoski, and J. Paton. *Phys. Rev. Lett.*, **54**:869, 1985.

[21] N. Isgur and J. Paton. *Phys. Rev.*, D**31**:2910, 1985.

[22] F.E. Close and P. Page. *Nucl. Phys.*, **B443**:233, 1995.

[23] P.Lacock *et al.* (UKQCD Collaboration). *Phys. Lett.*, **401B**:308, 1997.

[24] J. Ballam *et al.* Vector-meson production by polarized photons from 2.8, 4.7, and 9.3 GeV. *Phys. Rev.*, D**7**:3150–3177, 1973.

[25] K. Abe *et al. Phys. Rev. Lett.*, **53**:751, 1984.

[26] Y. Eisenberg *et al. Phys. Rev.*, D**5**:15, 1972.

[27] G. Condo *et al. Phys. Rev.*, D**48**:3045, 1993.

[28] M. Atkinson *et al* (The Omega Collaboration). *Nucl. Phys.*, **B231**:15, 1984.

[29] M. Davier *et al.* The reaction $\gamma p \to \pi^+\pi^-\pi^+\pi^- p$ at high-energy and γ dissociation into 4π. *Nucl. Phys.*, **B58**:31, 1973.

[30] K. Abe *et al. Phys. Rev.*, D**32**:2288, 1985.

[31] M. Atkinson *et al* (The Omega Collaboration). *Nucl. Phys.*, **B243**:1, 1984.

[32] G. R. Blackett *et al.* The Photoproduction of the $b_1(1235)\pi$ System, hep-ex/9708032.

[33] A. V. Afanasev and A. P. Szczepaniak. Charge exchange $\rho^0\pi^+$ photoproduction and implications for searches for exotic mesons. *Phys. Rev. D*, **61**:114008, 2000.

[34] K.J. Juge, J. Kuti, and C.J. Morningstar. hep-lat/9809098.

[35] T. Schäfer and E. V. Shuryak. *Phys. Rev. Lett.*, **75**:1707, 1995.

[36] C. Roberts and A. Williams. *Prog. Part. Nucl. Phys.*, **33**:477, 1994.

[37] C. J. Burden and M. A. Pichowsky. J^{PC}-exotic mesons from the Bethe-Salpeter equation,in preparation.

[38] D. Horn and J. Mandula. *Phys. Rev.*, D **17**:898, 1978.

[39] S. Ishida, H. Sawazaki, M. Oda, and K. Yamada. *Phys. Rev.*, D**47**:179, 1992.

[40] E.S. Swanson and A.P. Szczepaniak. *Phys. Rev.*, D**59**:14035, 1999.

[41] A. Chodos. *Phys. Rev.*, D**9**:3471, 1974.

[42] T. Barnes. *Nucl. Phys.*, **B158**:171, 1979.

[43] T. Barnes and F.E. Close. *Phys. Lett.*, **B116**:365, 1982.

[44] M. Chanowitz and S. Sharpe. *Nucl. Phys.*, **B222**:211, 1983.

[45] M. Flensburg, C. Peterson, and L. Sköold. *Z. Phys.*, **C22**:293, 1984.

[46] P. Hasenfratz, R.R. Horgan, J. Kuti, and J.M. Richard. *Phys. Lett.*, **95B**:299, 1981.

[47] K.J. Juge, J. Kuti, and C.J. Morningstar. *Nucl. Phys. Proc. Suppl.*, **63**:543, 1998.

[48] V. A. Novikov, M. A. Shifman, A. I. Vainshtein, and V. .I. Zakharov. *Nucl. Phys.*, **B165**:67, 1979.

[49] J. I. Latorre, S. Narison, P. Pacual, and R. Tarrach. *Phys. Lett.*, **147B**:169, 1984.

[50] J. Govaerts. *Nucl. Phys.*, **B285**:674, 1987.

[51] J. Govaerts. *Phys. Rev. Lett.*, **53**:2207, 1984.

[52] I. I. Balitsky, D. I. Dyakanov, and A. V. Yung. *Z. Phys.*, **C33**:265, 1986.

[53] S. Perantonis and C. Michael. *Nucl. Phys.*, **B347**:854, 1990.

[54] T. Manke *et al.* (UKQCD Collaboration). *Nucl. Phys. Proc. Suppl.*, **63**:332. hep-lat/9709001.

[55] K.J. Juge, J. Kuti, and C.J. Morningstar. *Nucl. Phys. Proc. Suppl.*, **63**:513. hep-lat/9709132.

[56] T.J. Allen, M.G. Olsson, and S. Veseli. *Phys. Lett.*, **434B**:110, 1998. hep-ph/9804452.

[57] M. Tanimoto. *Phys. Lett.*, **116B**:198, 1982.

[58] A. Le Yaouanc, L. Oliver, O. Pene, J.-C. Raynal, and S. Ono. *Z. Phys.*, C **28**:309, 1985.

[59] F. Iddir, A. Le Yaouanc, L. Oliver, O. Pene, and J.-C. Raynal. *Phys. Lett.*, **207B**:325, 1988.

[60] E.S. Swanson and A.P. Szczepaniak. Decays of hybrid mesons. *Phys. Rev.*, D**56**:5692, 1997.

[61] P. Page, E.S. Swanson, and A.P. Szczepaniak. *Phys. Rev.*, D**59**:34016, 1999.

[62] Yu. S. Kalashnikova. *Z. Phys.*, C **62**:323, 1994.

[63] S. L. Zhu. hep-ph/9903537, 1999.

[64] S. Narison. QCD spectral sum rules. *Lecture Notes in Phys.*, Vol**26**:369, 1989.

[65] J. I. Latorre, S. Narison, and P. Pacual. *Z. Phys.*, C**34**:347, 1987.

[66] A. Le Yaouanc *et al. Phys. Lett.*, **205B**:564, 1988.

[67] H.G.Dosch and D.Gromes. *Phys. Rev.*, D**33**:1378, 1986.

[68] S.Godfrey and N.Isgur. *Phys. Rev.*, D**32**:189, 1985.

[69] D. V. Bugg. To be published in the proceedings of the World Hadron Symposium, March 1999, Frascati, Italy. T. Barnes, *ibid.*

[70] F. Iachello, N.C. Mukhopadhyay, and L. Zhang. Spectrum generating algebra for string-like hadrons: mass formula for mesons. *Phys. Lett.*, **256B**:295–300, 1991.

[71] F. Iachello, Nimai C. Mukhopadhyay, and L. Zhang. Spectrum generating algebra for string-like mesons. 1. mass formula for $q\bar{q}$ mesons. *Phys. Rev.*, D **44**:898–914, 1991.

[72] H.G.Blundell and S.Godfrey. *Phys. Rev.*, Dbf 53:3700, 1996.

[73] H.G.Blundell, S.Godfrey, and B.Phelps. *Phys. Rev.*, D**53**:3712, 1996.

[74] T.Barnes, F.E.Close, P.R.Page, and E.S.Swanson. *Phys. Rev.*, D**55**:4157, 1997.

[75] P.Lacock *et al.* (UKQCD Collaboration). *Phys. Lett.*, **401B**:308, 1997. hep-lat/9611011.

[76] Carl E. Carlson and Nimai C. Mukhopadhyay. Perturbative QCD signatures of hybrid hadrons in electroproduction at high Q^2. *Phys. Rev. Lett.*, **67** :3745–3748, 1991.

[77] C. Amsler *et al.* High-statistics study of $f_0(1500)$ decay into $\pi^0\pi^0$. *Phys. Lett.*, **342B**:433–439, 1995.

[78] C. Amsler *et al.* Coupled channel analysis of $\bar{p}p$ annihilation into $\pi^0\pi^0\pi^0$, $\pi^0\eta\eta$, and $\pi^0\pi^0\eta$. *Phys. Lett.*, **355B**:425–432, 1995.

[79] J.Weinstein and N.Isgur. *Phys. Rev.*, D**27**:588, 1983.

[80] J.Weinstein and N.Isgur. *Phys. Rev.*, D**41**:2236, 1990.

[81] N.N.Achasov and V.Ivanchenko. *Nucl. Phys.*, **B315**:465, 1989.

[82] F.E. Close, N. Isgur, and S. Kumano. Scalar mesons in ϕ radiative decay: Their implications for spectroscopy and studies of CP violation at ϕ factories. *Nucl. Phys.*, **B389**:513, 1993.

[83] N. N. Achasov *et al.* (The SND Collaboration). 1998.

[84] H.G.Blundell and S.Godfrey. *Phys. Rev.*, D**53**:3700, 1996.

[85] T.Barnes and N.Black. in preparation.

[86] D.Aston *et al. Phys. Lett.*, **215B**:199, 1988.

[87] A.Abele *et al.* (Crystal Barrel Collaboration). High-mass ρ-meson states from $\bar{p}d$-annihilation at rest into $\pi^-\pi^o\pi^o p_{\rm spectator}$. *Phys. Lett.*, **391B**:191, 1997.

[88] U.Thoma *et al.* (Crystal Barrel Collaboration). *AIP Conf. Proc.*, **432**:322, 1998.

[89] D.Weingarten. *Nucl. Phys.*, **B** (Proc. Suppl.) **34**:29, 1994.

[90] C.Michael. Liverpool report LTH 370, hep-ph/9605243 (May 1996).

[91] F.E.Close and M.J.Teper. On the lightest scalar glueball. RAL-96-040 / OUTP-96-35P (July 1996).

[92] J.Adomeit *et al.* (Crystal Barrel Collaboration). *Z. Phys.*, C **71**:227, 1996.

[93] C. Keppel. Development of a Compton-backscattered photon source for Hall B at Jefferson Lab. In *Physics with 8+ GeV Photons Workshop*. Workshop in Bloomington IN, July 14-16 1997, proceedings available from Jefferson lab.

[94] W. Kaune, G. Miller, W. Oliver, R.W. Williams, and K.K. Young. Inclusive cross sections for pion and proton production by photons using collimated coherent bremsstrahlung. *Phys. Rev.*, D **11**(3):478–494.

[95] H. Bilokon, G. Bologna, F. Celani, B. D'Ettorre Piazzoli, R. Falcioni, G. Mannocchi, and P. Picchi. Coherent bremsstrahlung in crystals as a tool for producing high energy photon beams to be used in photoproduction experiments at CERN SPS. *Nuclear Inst. and Meth.*, **204**:299–310.

[96] G. Diambrini-Palazzi. *Revs. Mod. Phys.*, **40**:611, 1968.

[97] U. Timm. *Fortschr. Phys.*, **17**:765, 1969.

[98] J. Kellie. University of glasgow. Private Communication.

[99] J. Benesch. Hall D Preliminary Optics Design. Technical report, 2000. JLab TN 00-011.

[100] L. Keller. Muon calculation results. Technical report, 2000. Hall D Internal Report 33 available at `http://www.phys.cmu.edu/halld/notes_main.html`.

[101] D. I. Sober, *et al. Nuclear Inst. and Meth.*, A**440**:263, 2000.

[102] Anthony, *et al. Nuclear Inst. and Meth.*, A**3**01.

[103] J. Hall, *et al. Nuclear Inst. and Meth.*, A**3**68.

[104] D. Aston *et al.* The LASS spectrometer. Technical report, 1987. SLAC-Report-298 Copies available from the SLAC publications office, at http://www.slac.stanford.edu/pubs/.

[105] J. S. Alcorn, H.O. Peterson, and S. St. Lorent. In *Applied Superconductivity Conference - 1972*, page 273.

[106] D.W. Hertzog *et al. Nuclear Inst. and Meth.*, **A294**:446, 1990.

[107] Graham McNicoll. A study of photon sensitivity in the Hall D detector. Technical report, 2000. Hall D Internal Report 36 available at `http://www.phys.cmu.edu/halld/notes_main.html`.

[108] A. Antonelli *et al. Nuclear Inst. and Meth.*, **A370**:367, 1996.

[109] A. Antonelli *et al. Nuclear Inst. and Meth.*, **A354**:352, 1995.

[110] C. A. Meyer. Tracking resolution requirements in the meson spectroscopy facility at Jefferson Lab. HALL DNote **7**, linked from http://www.phys.cmu.edu/halld/notes_main.html, 1998.

[111] M. D. Petroff and M. Atac. *IEEE Trans. Nucl. Sci. NS-36*, page 163, 1989.

[112] M. R. Wayne. *Nuclear Inst. and Meth.*, **A386**:278, 1997.

[113] M. Ambrogiani *et al. Nucl. Phys. B* **B61**, page 384, 1998.

[114] B. Baumbaugh *et al. IEEE Trans. Nucl. Sci. 43*, page 1146 and references therein, 1996.

[115] A. Antonelli *et al.* A Pb SciFi EM calorimeter for an experiment on CP violation at DAPHNE. LNF-91-073-P, 1991.

[116] E. Chen, M. Saulnier, W. Sun, and H. Yamamoto. Tests of a high resolution time-of-flight system based on long and narrow scintillator. hep-ex/9606007.

[117] M. Sivertz *et al.* A compact gas Čerenkov detector with novel optics. *Nuclear Inst. and Meth.*, **A385**:37, 1997. hep-ex/9607013.

[118] R. R. Crittenden *et al. Nuclear Inst. and Meth.*, **387**:377, 1998.

[119] S. Teige. In Howard A. Gordon and Doris Rueger, editors, *Proceedings of the Fifth International Conference on Calorimetry in High Energy Physics*, pages 161–166. World Scientific, 1995.

[120] A. Brunner *et al. Nuclear Inst. and Meth.*, **A414**:466–476, 1998.

[121] Craig Steffen and Scott Teige. Beam related radiation damage in radϕ. Technical report, 2000. Hall D Internal Report 43 available at `http://www.phys.cmu.edu/halld/notes_main.html`.

[122] E.S. Smith L. Keller and E. Wolin. Beam containment proposal. Technical report, 2000. Hall D Internal Report 32 available at `http://www.phys.cmu.edu/halld/notes_main.html`.

[123] A. McFarlane D.R. Walz and E. Lewandowski. Beam dumps, stoppers and faraday cups at the slc. In *Physics with 8+ GeV Photons Workshop*, 1989. IEEE Particle Accelerator Conference, Chicago, IL, March 20-23, 1989 (SLAC-PUB-4967).

[124] P. Degtiarenko. Neutron flux and ground water activation at bsy dump. Technical report, 1997. Intenal memo to R. May and G. Stapleton.

[125] SLAC-PUB-6385, Muon Background in a 1.0-TeV Linear Collider.

[126] Engineering Consulting Services Ltd. Report of subsurface exploration and geotechnical engineering analysis – hall d construction. Technical report, 1999.

[127] Details of the preliminary civil design and cost can be obtained from Suresh Chandra, Jlab Engineering.

[128] Armstrong *et al. Phys. Rev.*, D**5**:1640, 1972.

[129] Caldwell *et al. Phys. Rev.*, D**7**:1362, 1973.

[130] The Durham online database is located on the WWW at http://durpdg.dur.ac.uk/HEPDATA.

[131] J. Va'Vra. *Nuclear Inst. and Meth.*, **A244**:391–415, 1986.

[132] D.G.Cussans. *Nuclear Inst. and Meth.*, **A244**:277, 1995.

[133] P. Eugenio. *Genr8*: A general monte carlo event generator. Carnegie Mellon University, 1998.

[134] S. Teige. A monte-carlo user guide. Indiana University, 1998.

[135] Information on MCFast may be optained via the WWW at http://fnpspa.fnal.gov.

[136] Information on ROOT may be optained via the WWW at http://root.cern.ch.

[137] C. A. Meyer. Tracking resolution requirements in the meson spectroscopy facility at Jefferson Lab. HALL DNote **7**, linked from http://www.phys.cmu.edu/halld/notes_main.html, 1999.

[138] D. E. Groom, *et al.* (Particle Data Group). Review of particle physics. *Eur. Phys. Jour. C*, **15**:1, 2000.

[139] ABBHHM Collaboration. *Phys. Rev.*, **175**:1669, 1968.

[140] G. Condo *et al. Phys. Rev.*, D**41**:3317, 1990.

[141] J. Ballam *et al.* Bubble-chamber study of photoproduction by polarized photons. *Phys. Rev.*, D**6**:454, 1972.

[142] S.U. Chung. Spin formalisms. CERN Report 71-8, March 1971, Lectures given in the Academic Training Program of CERN 1969-1970.